Large scale plasma density perturbations in the polar F-region ionosphere

A Thesis Submitted to the
College of Graduate Studies and Research
in Partial Fulfillment of the Requirements
for the degree of Doctor of Philosophy
in the Department of Physics and Engineering Physics
University of Saskatchewan
Saskatoon

By
Gareth William Perry

©Gareth William Perry, February, 2015. All rights reserved.

Permission to Use

In presenting this thesis in partial fulfilment of the requirements for a Postgraduate degree from the University of Saskatchewan, I agree that the Libraries of this University may make it freely available for inspection. I further agree that permission for copying of this thesis in any manner, in whole or in part, for scholarly purposes may be granted by the professor or professors who supervised my thesis work or, in their absence, by the Head of the Department or the Dean of the College in which my thesis work was done. It is understood that any copying or publication or use of this thesis or parts thereof for financial gain shall not be allowed without my written permission. It is also understood that due recognition shall be given to me and to the University of Saskatchewan in any scholarly use which may be made of any material in my thesis.

Requests for permission to copy or to make other use of material in this thesis in whole or part should be addressed to:

Head of the Department of Physics and Engineering Physics
116 Science Place
University of Saskatchewan
Saskatoon, Saskatchewan
Canada
S7N 5E2

Abstract

The most compelling evidence of the complex interaction between the geomagnetic field of the Earth and the magnetic field of the Sun is found in the polar ionosphere. Large scale F-region plasma density perturbations result from the coupling between the two fields. Plasma density enhancements known as ionization patches, and depletions can have lifetimes of several hours in the F region and are almost always present everywhere throughout the nighttime polar ionosphere. The perturbations can seed ionospheric irregularities that severely hamper communication and navigational networks, even during times of subdued geomagnetic activity. Up until recently, it has been difficult to study the perturbations due to the remoteness of their location. In the past decade an array of optical and radio instruments have been deployed to the Canadian sector of the Arctic, enabling a more thorough sampling of the polar ionosphere and the large scale perturbations therein.

In this work, common volume measurements from the Rankin Inlet Super Dual Auroral Radar Network (SuperDARN), Resolute Bay Incoherent Scatter Radar - North (RISR-N) and Optical Mesosphere and Thermosphere Imagers (OMTI) system at Resolute Bay are employed to investigate the generation mechanisms, transport properties, and optical and radio signatures of the large scale perturbations. A model connecting the optical signatures of patches to their velocity profile through the ionosphere is introduced and applied to OMTI data. In addition, an algorithm is developed to detect the presence of patches using RISR-N. Using the algorithm, a survey of patches sampled over several days is conducted, providing a comprehensive account of the variable polar ionosphere in terms of its plasma state parameters. Furthermore, the algorithm is used to diagnose patches as a primary source of coherent backscatter for the Rankin Inlet SuperDARN radar. Lastly, the generation of a deep plasma density depletion is analyzed using the three aforementioned instruments. Using a model, it is shown that such perturbations can be forged by intense frictional heating events in the polar ionosphere on a time scale of 15 minutes, and can subsequently be transported through the region.

Acknowledgements

First, I would to like to thank my supervisor Dr. Jean-Pierre St. Maurice. I am eternally grateful for his candour, guidance and patience. It has been a pleasure to study under him.

I owe a debt of gratitude to Dr. Hanna Dahlgren. She has been an amazing colleague, friend, and mentor. Her tenacity and energy has kept me honest and has been inspirational.

I have had the pleasure of meeting and interacting some magnificent people on campus, at conferences, workshops and other gatherings. They have provided me with great advice, encouragement and empathy. I wish to give special recognition to a few: Dr. Robin Kleiv, a great friend who also made the trip from Abbotsford to Saskatoon for graduate school. The faculty, researchers and staff in the Institute of Space and Atmospheric Studies: Drs. George Sofko, Kathryn McWilliams, Glenn Hussey, Dieter André, Pasha Ponomarenko, Sasha Koustov, Chad Bryant, as well as Kevin Krieger, Bill Marshall, Jan Wiid, Naas Van Rensburg, and Cindy Jelinski. My co-authors: Drs. Mike Nicolls, Josh Semeter, Keisuke Hosokawa, Kazuo Shiokawa, Torbjörn Sundberg, Craig Heinselman, Mike Greffen, Steven Chen, Matt Zettergren, and Hasan Bahcivan. Thank you to a subset of my co-authors, the "Kananaskis Crew": Bill Archer, Matthew Patrick, Beate Humberset, Jone Reistad, Hossna Gharaee, and Drs. Johnathan Burchill, Stein Haaland, and Lasse Clausen. Thanks to Dr. Roger Varney for his valuable comments on this work. Thank you to Drs. Megan and Rob Gillies for being great friends. Thank you to Dr. Derek Harnett, for encouraging me to pursue graduate studies. Finally, thank you to my fellow graduate students: Ashton Reimer, Matthew Wessel, Sidd Choudhury, Hasan Chowdhury, Arpi Barua, Devin Huyghebaert, Blessing Iserhienrhien, Lindsay Goodwin, Dr. John McLeod, Eamon McDermott, Sarah Purdy, Zahra Abooalizadeh, Mohsen Ghezelbash, Kateryna Yakymenko, Sarah Toderian, and Clifford Ridley.

I would be nowhere without the hard work and dedication of all of my teachers. At times I was a difficult student, but they never faltered.

To Mom, Dad, Michael and Quinn: a person couldn't ask for a more supportive and loving family. Thank you.

To my wife, Janelle, my sunrise and my sunset, my wind and my fire: I am in your debt forevermore.

The smartest thing I have ever done was to ask for Janelle's phone number. This is for her.

Contents

List of Tables

List of Figures

List of Abbreviations

ACF	Autocorrelation Function
AMISR	Advanced Modular Incoherent Scatter Radar
AU	Astronomical Unit
EISCAT	European Incoherent Scatter Scientific Association
EMCCD	Electron-multiplying charged coupled device
ESR	EISCAT Svalbard Radar
FAI	Field-Aligned Irregularity
FOV	Filed Of View
FTE	Flux Transfer Event
GPS	Global Positioning System
GSM	Geocentric Solar Magnetospheric coordinate system
HF	High Frequency
GDI	Gradient-Drift Instability
IGRF	International Geomagnetic Reference Field
IMF	Interplanetary Magnetic Field
IRI	International Reference Ionosphere
ISR	Incoherent Scatter Radar
MI	Magnetosphere-Ionosphere
MLT	Magnetic Local Time
MSIS	Mass Spectrometry and Incoherent Scatter
OCB	Open-Closed Field Line Boundary
OMTI	Optical Mesosphere Thermosphere Imagers
PFISR	Poker Flat Incoherent Scatter Radar
PolarDARN	Polar Dual Auroral Radar Network
RISR-C	Resolute Bay Incoherent Scatter Radar – Canada
RISR-N	Resolute Bay Incoherent Scatter Radar – North
SuperDARN	Super Dual Auroral Radar Network
TEC	Total Electron Content
UHF	Ultra High Frequency
UT	Universal Time

Chapter 1

Introduction

1.1 A Short History of Space Physics

Figure 1.1: Plains Cree for "The ghost dancing in the skies" [M. Boyce, Personal Communication, 2014].

Records and artefacts from many cultures and societies spanning thousands of years and vast expanses in the northern and southern high-latitude regions exhibit a rich history of splendour, curiosity and mysticism regarding the aurora. The term *aurora borealis*, the "dawn of the north", is attributed to Galileo Galilei, who believed the aurora was due to sunlight reflecting off the atmosphere that had risen beyond the shadow of the Earth [*Kivelson and Russell*, 1995]. However, by the time Galileo coined the term, the aurora already had many names and interpretations. Some Indigenous cultures associated the aurora with otherworldly happenings. The Plains Cree in North America referred to the aurora as "the ghost dancing in the skies", written in Figure 1.1. Some Aboriginal cultures in Australia believed that the aurora were bush-fires in the spirit world; others, as a fire set by an ancestral hero, warning of a coming catastrophe [*Hamacher*, 2013]. Many reviews exist which chart the historical development of our understanding of the physics of the aurora, the upper-atmosphere and the near-Earth geospace environment. The following description is based on works by *Kivelson and Russell* [1995], *Schunk and Nagy* [2000], and *Brekke* [2012].

Significant developments in our understanding of the aurora and the greater geophysical environment were made as a result of solving problems caused by its effects on navigational

instrumentation. The first connections between the aurora and its organization by geomagnetic field were established by Edmund Halley after he conducted surveys of the geomagnetic field in the north and south Atlantic Ocean. The influence of the aurora on magnetic compass perturbations was first established by Olof Hiorter, after he identified a diurnal variation in measured magnetic perturbations. This result was interpreted as the Earth rotating under a fixed current source. He correctly attributed the perturbations to auroral activity.

Balfour Stewart 1882 is credited with being the first to claim that the currents responsible for the geomagnetic disturbances measured on the ground and the aurora are both located in the upper atmosphere. This was supported by Arthur Kennelly and Oliver Heaviside who hypothesized that a layer of charged particles in the upper atmosphere could be responsible for the transatlantic radio experiments performed by Guglielmo Marconi. They postulated that in order to transmit radio waves over the horizon, a reflecting layer of charged particles must exist in the upper atmosphere. Their theory was not verified until 1925 when Edward Appleton and Miles Barnett used radio instruments, the first radar systems, to detect and measure the height of layers which reflected the transmitted radio waves. Together, they discovered and labelled the D-, E- and F-regions of the ionosphere.

In the mid-nineteenth century, the connection between solar activity, the aurora and geomagnetic fluctuations was made by Edward Sabine. He compared geographically distributed magnetic observatory data to the sunspot cycle, the inversion of the solar magnetic field, and noted a correlation between the two. The 11-year sunspot cycle had already been known about since the development of the telescope, yet the connection between solar activity and its effects on the Earth were not considered to be significant until the work of Sabine and later, Richard Carrington. Carrington, in a true instance of serendipity, witnessed and recorded a solar flare and the subsequent geomagnetic disturbances. In that event, now referred to as the "Carrington Event", auroral displays were recorded as far south as the Caribbean. Meanwhile, a strong relation between the sunspot cycle and the occurrence of aurora had also been recorded, independently, by Sophus Tromholt in Scandanavia. A plot of his work is shown in Figure 1.2.

To further explain the link between geographically distributed geomagnetic disturbances and solar activity, both Kristian Birkeland and Sydney Chapman advanced the idea that a

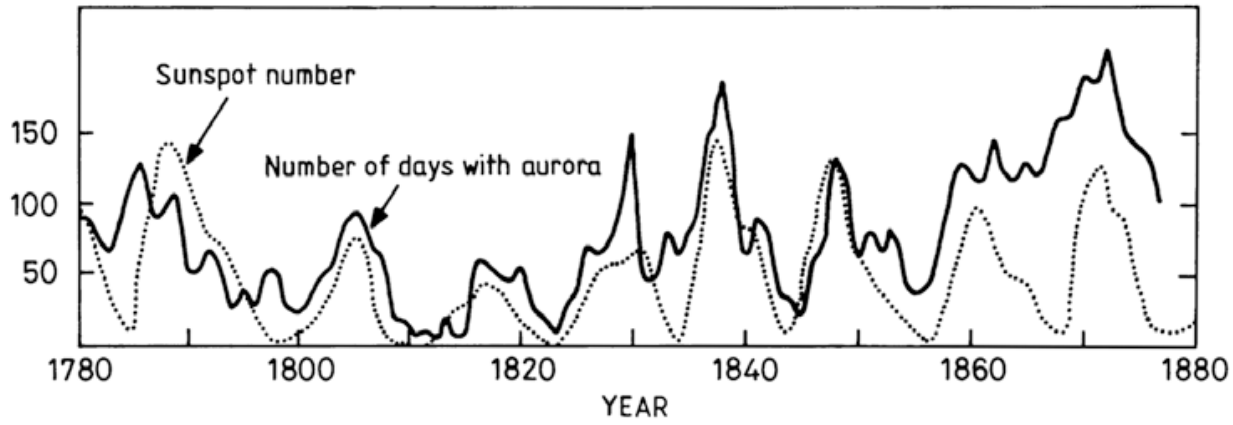

Figure 1.2: A plot comparing the occurrence of aurora observed in Scandanavia and the sunspot cycle, recorded between 1780 and 1877, by Sophus Tromholt. Reproduced from *Brekke* [2012].

stream of electrons originating from the Sun was responsible for the disturbances and auroral displays. Originally, this idea was refuted by others in the scientific community who noted that such a stream of electrons could not exist since the beam should disperse due to the like charge of the electrons. The idea was modified by Frederick Lindemann, who suggested that a stream of electrons from the Sun could reach the Earth if the stream contained equal amounts of electrons and positive charge, preventing the dispersion of the beam. In essence, Lindemann described the quasineutrality condition of a plasma. Arguably, this development marked the beginning of plasma physics, the theory of the solar wind and its relation to geomagnetic disturbances.

Chapman and Vincent Ferraro recognized that if the stream of charged particles originating from the Sun was extremely tenuous and the space through which it travelled was tenuous as well, the stream would have a nearly infinite conductivity. Thus, if one approximated the stream as an infinite plane of infinite conductivity, a dipole magnetic field would be induced in it as the stream approached the geomagnetic field. The superposition of the geomagnetic field and mirror field would distort the geomagnetic field, and divert the solar plasma stream around the geomagnetic field. This would create a cavity around the Earth, distinguished by the absence of solar plasma within it, now known as the magnetosphere. Despite the absence of in-situ measurements (satellites had not yet been invented) many characteristics of the

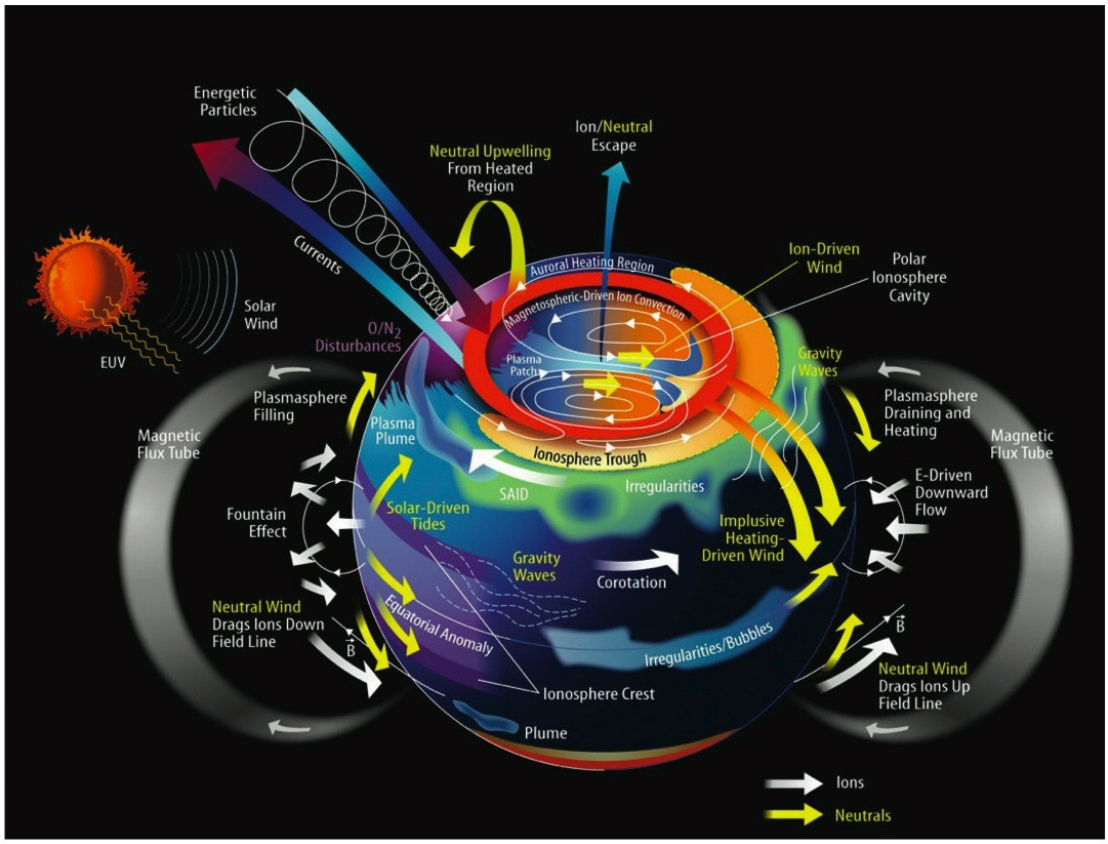

Figure 1.3: A graphic depicting the complex nature of the near-Earth geospace system, its phenomena, drivers and coupling mechanisms. Reproduced from *Committee on a Decadal Strategy for Solar and Space Physics (Heliophysics); Space Studies Board; Aeronautics and Space Engineering Board; Division of Earth and Physical Sciences; National Research Council* [2013].

Chapman-Ferraro model for the magnetosphere proved accurate, including the generation of current systems due to the interaction of the solar wind and magnetosphere, responsible for magnetic perturbations measured on the ground.

Space physics: the physics of the ionosphere, magnetosphere and Sun-Earth geospace system has undergone significant advances during the twentieth and twenty-first centuries. The progress has been closely linked to the development of radio instruments such as radar, optical instrumentation, rocketry and satellite exploration. Along with the experimental branch of the field, the theoretical branch has advanced our understanding of plasma physics, the terrestrial atmosphere, the ionosphere, and their coupling mechanisms, with clever phenomenology, the aid of sophisticated computer modelling and experimentation to guide their progression. A snapshot of the near-Earth geospace is given in Figure 1.3, and shows the

complexity and richness of only a portion of space physics, the near-Earth geospace, as it is understood today. An abundance of neutral atmospheric and ionospheric phenomena, their coupling mechanisms and their drivers is depicted. The region of focus in this work is the polar region, and the large scale ionosphere plasma density perturbations therein. A more detailed description of the solar wind, magnetosphere and ionosphere is now given.

1.2 The Solar Wind and Magnetosphere

1.2.1 The Solar Wind

The Interplanetary Magnetic Field (IMF) produced by the Sun is transported into the solar system by the solar wind, the super-sonic expansion of the atmosphere of the Sun. The solar wind is a fully ionized plasma, primarily composed of protons and electrons [*Baumjohann and Treumann*, 1997; *Chen*, 2010]. The state parameters of the solar wind vary depending on the activity of the Sun, which is strongly coupled to the 11-year solar cycle – the period of the solar magnetic field inversion. Table 1.1 provides information on the plasma density n, proton temperature T_p, electron temperature T_e, solar wind speed u, Alfvén speed V_A, and sound speed V_S, for three solar wind speeds with colloquial descriptors of "slow", "average" and "high" speed.

An electromagnetic description of the solar wind may be obtained if we consider the Maxwell-Faraday equation:

$$\nabla \times \mathbf{E} = -\frac{\partial \mathbf{B}}{\partial t}, \tag{1.1}$$

where $\mathbf{E}$ and $\mathbf{B}$ are the ambient electric and magnetic field, respectively. Substituting in Ohm's law gives:

$$\frac{\partial \mathbf{B}}{\partial t} = \nabla \times \left(-\frac{\mathbf{J}}{\sigma} + \mathbf{u} \times \mathbf{B} \right), \tag{1.2}$$

in which $\mathbf{J}$ is the current density, $\mathbf{u}$ is the velocity of the plasma and σ is the conductivity of the plasma. Substituting in Ampère's law (the static case) gives:

Parameter	Average	Low-Speed	High-Speed
n (m^{-3})	8.7×10^{-6}	11.9×10^{-6}	3.9×10^{-6}
u (ms^{-1})	468×10^{3}	327×10^{3}	702×10^{3}
B (T)	5.9×10^{-9}	6.0×10^{-9}	7.3×10^{-9}
T_p (K)	1.2×10^{5}	0.34×10^{5}	2.3×10^{5}
T_e (K)	1.4×10^{5}	1.3×10^{5}	1.0×10^{5}
V_A (ms^{-1})	44×10^{3}	38×10^{3}	66×10^{3}
V_S (ms^{-1})	63×10^{3}	44×10^{3}	81×10^{3}

Table 1.1: Solar wind parameters near the Earth, under various solar wind conditions, distinguished by the radial velocity. Reproduced from *Schunk and Nagy* [2000].

$$\frac{\partial \mathbf{B}}{\partial t} = \nabla \times \left(-\frac{\nabla \times \mathbf{B}}{\mu_0 \sigma} + \mathbf{u} \times \mathbf{B} \right), \tag{1.3}$$

which is equivalent to:

$$\frac{\partial \mathbf{B}}{\partial t} = \nabla \times (\mathbf{u} \times \mathbf{B}) - \frac{1}{\sigma \mu_0} \nabla^2 \mathbf{B}, \tag{1.4}$$

in which μ_0 is the permeability of free space. The first term on the right hand side of Equation 1.4 describes the motion of the plasma, perpendicular to the direction of the ambient magnetic field. The second term on the right hand side describes the diffusion of the magnetic field, in which the diffusion coefficient is $D_\perp = 1/\sigma\mu_0$. The density of the solar wind is low; the mean-free-path of a solar wind particle is extremely large, of the order of 10^{11}m (approximately 1 AU), and therefore, the conductivity of the solar wind is extremely large. The right hand side of Equation 1.4 is dominated by the first term.

Next, consider the total magnetic flux, Φ, passing through a surface S specifically,

$$\Phi = \int_S \mathbf{B} \cdot \hat{\mathbf{n}} \, dS, \tag{1.5}$$

in which $\hat{\mathbf{n}}$ is the unit vector normal to the surface S. Taking into account that $\nabla \cdot \mathbf{B} = 0$ everywhere, it can be shown that [e.g., *Siscoe*, 1983]:

$$\frac{\partial \Phi}{\partial t} = \int_S \left(\frac{\partial \mathbf{B}}{\partial t} - \nabla \times (\mathbf{u} \times \mathbf{B}) \right) \cdot \hat{\mathbf{n}} \, dS, \tag{1.6}$$

where once again $\mathbf{u}$ is the velocity of the plasma. Combining Equations 1.4 and 1.6, and considering the case of the solar wind where $\sigma \to \infty$ yields:

$$\frac{\partial \Phi}{\partial t} = 0, \tag{1.7}$$

which is *Alfvén's theorem* [*Alfvén*, 1942], also known as the *frozen in condition*. Alfvén's theorem states that for a perfectly conducting plasma (such as the solar wind) the magnetic flux through any closed surface remains constant. An implication of the theorem is that the IMF carried by the solar wind remains unchanged throughout its propagation through the solar system. For our applications in this work, the closed surface is of a cylindrical shape and bounded by magnetic field lines, and is referred to as a flux tube. For a flux tube,

$$\Phi = \int_S \mathbf{B} \cdot \hat{\mathbf{n}} \, dS = 0. \tag{1.8}$$

1.2.2 The Magnetosphere

Alfvén's theorem breaks down in regions in which current sheets are present. In the Sun-Earth system, this occurs when the solar wind encounters the plasma contained within the magnetosphere, the geomagnetic cavity of the Earth [*Schunk and Nagy*, 2000; *Hargreaves*, 1992]. The magnetosphere is a region enclosing the Earth in which the geomagnetic field is the predominant magnetic field. When a solar flux tube and magnetospheric flux tube are incident on one another a current sheet may be generated depending on the orientation of the magnetic field associated with tubes, according to Ampère's Law. Using Ohm's law to describe the induced current: $\eta \mathbf{J} = \mathbf{E} + \mathbf{u} \times \mathbf{B}$, in which $\eta = 1/\sigma \simeq 0$ – the normal case for a highly conducting plasma. However, according to the Sweet-Parker model for reconnection [*Parker and Krook*, 1956; *Sweet*, 1958], there is a point at which antiparallel magnetic field lines are sufficiently close such that the current, $\mathbf{J}$, becomes large enough that the product $\eta \mathbf{J}$ is no longer negligible. The ions and electrons become unmagnetized, they are no longer gyrating around the magnetic field, to first order. $D_\perp \not\simeq 0$ and the magnetic flux can diffuse

between flux tubes. The diffusion of flux is a fundamental step in *magnetic reconnection*, also known as *magnetic merging*. During magnetic reconnection, a reconfiguration of magnetic field topologies occurs whereby magnetic field lines can merge with other magnetic field lines [*Schindler and Hornig*, 2001; *Yamada et al.*, 2010]. Magnetic reconnection is not only found in the Sun-Earth system, it is also used to explain solar flares, and many other cosmic processes. Magnetic reconnection is not completely understood, and investigating any further into it is beyond the scope of this work. Nevertheless, for this work, it is sufficient to describe it as the interaction between two flux tubes: one of solar origin and the other of geophysical origin, resulting in either an IMF line connecting with a geomagnetic field line, an IMF line connecting with another IMF line, or a geomagnetic line connecting with another geomagnetic field line. Reconnection is the main driver for many complex systems of current, charged particle drifts, plasma transport and interaction in the magnetosphere.

Within a radial distance of 2 to 3 Earth radii (R_e), the geomagnetic field can be approximated as a dipole field [*Hargreaves*, 1992]. Complex interactions, including the reconnection process as well as the magnetic pressures from the solar wind and the magnetosphere, distort the dipole field, compressing it in regions between the Sun and the Earth, i.e., the dayside, and stretching it out on the nightside. This is illustrated in Figure 1.4, which is plotted in the Geocentric Solar Magnetospheric (GSM) coordinate system, in which the x-axis is the Sun-Earth line, and the x-z plane contains the geomagnetic dipole axis of the Earth [*Kivelson and Russell*, 1995].

The geomagnetic field lines at the edge of the magnetosphere – the magnetopause – map down to higher geographic latitudes. The field lines labelled 1 and 6 in Figure 1.4 undergo magnetic reconnection. In this process, a geomagnetic field line is disconnected from one of the two geomagnetic poles and reconnected to the IMF. This is shown with line $1'$ and 1 reconnecting to create line 2 in the northern hemisphere ($1'$ and 1 become $2'$ in the southern hemisphere). In the nightside, lines 6 and $6'$ also undergo reconnection creating lines 7 and $7'$. From this, we can categorize two types of magnetic field lines connected to a geomagnetic pole: those which are connected to the opposite geomagnetic pole, referred to as "closed" field lines, and those which are connected to the IMF, referred to as "open" field lines. In Figure 1.4, lines 1, 7, 8 and 9 are closed field lines, while lines 2, 3, 4, 5 and 6, and their

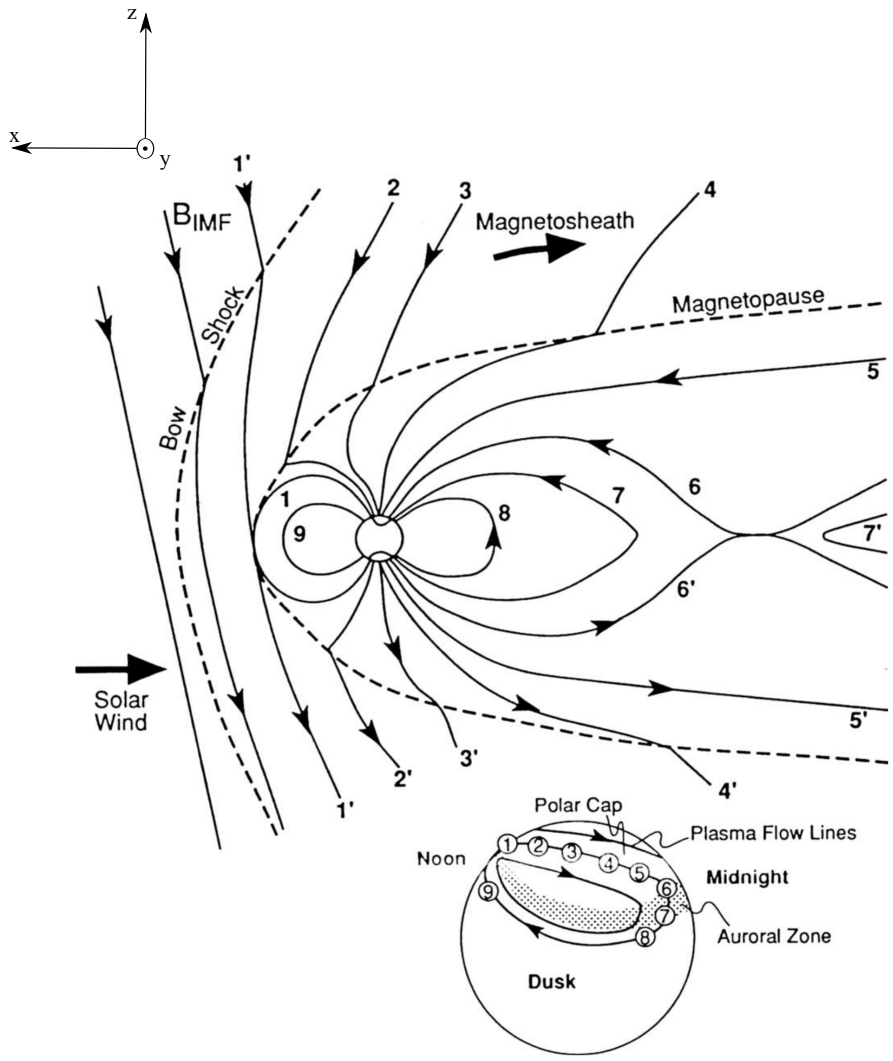

Figure 1.4: The interaction of the IMF and the geomagnetic field [*Kivelson and Russell*, 1995].

equivalents in the southern hemisphere, are open field lines. The footprints of the field lines in Figure 1.4 are connected to the ionosphere, whose role will be introduced in more detail shortly. As a field line transitions from 1 to 9 in Figure 1.4, its footprint in the ionosphere traces out a path, as shown by the inset in Figure 1.4.

There are many regions and features of interest in the magnetosphere, which may be distinguished by the characteristics of the plasma present there, and the dynamics of the plasma motion involved. A selection of the more significant regions and their plasma populations is shown in Figure 1.5. Two regions that are closely related to this work are now described.

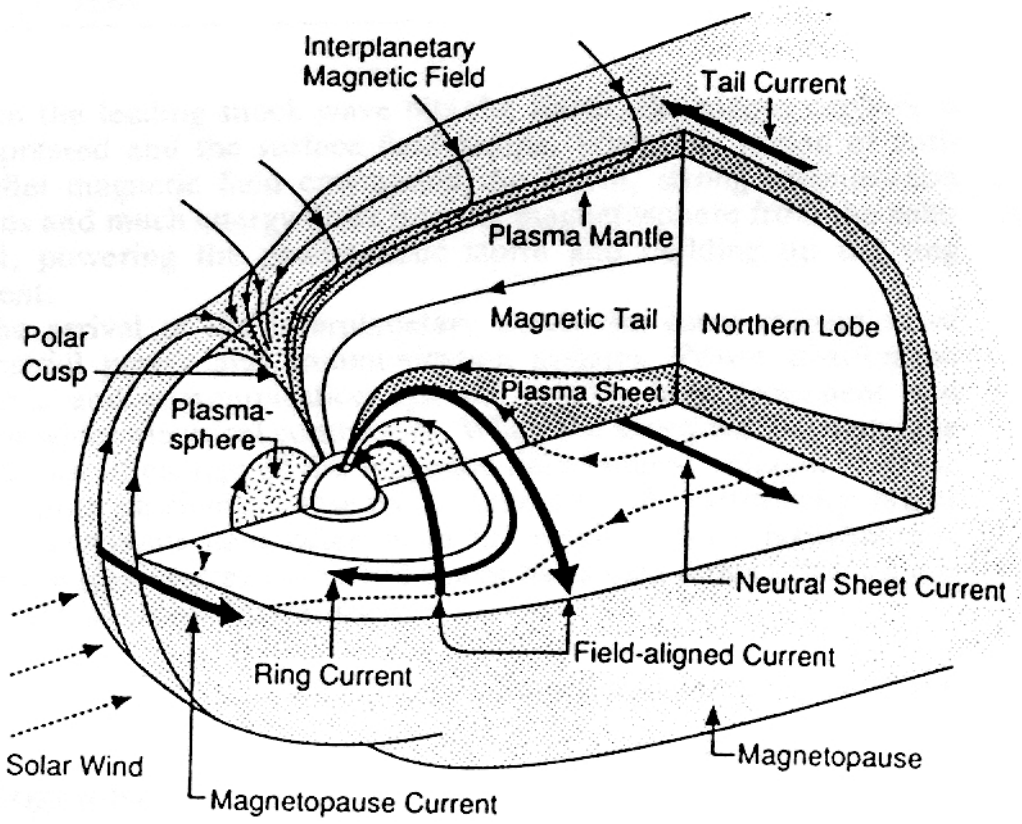

Figure 1.5: A depiction of the current systems and different regions of the magnetosphere [*Russell and Luhmann*, 1997].

Magnetosheath

The bow shock (depicted in Figure 1.4) is a region located approximately 12 R_e in front of the sunward side of the Earth [*Schunk and Nagy*, 2000]. The magnetosheath is the region in between the bow shock and the magnetopause (the outer boundary of the magnetosphere). At the bow shock, the solar wind plasma is suddenly decelerated and turbulent. The loss in kinetic energy of the plasma is converted into thermal energy, increasing the temperature of the magnetosheath plasma to 5×10^6 K [*Hargreaves*, 1992].

Polar Cusp

The polar Cusp is a near-Earth deep minimum in the total magnetic field in the magnetosphere. The Cusp is typically situated at high latitudes on the dayside magnetosphere, as

shown in Figure 1.5. The Cusp is a transition region in the magnetosphere, between an open and closed field line configuration. Geomagnetic field lines originating from lower latitudes than the Cusp are closed, while those originating at higher latitudes than the Cusp are generally open [*Hargreaves*, 1992]. At the Cusp, the geomagnetic field lines diverge as a function of radial distance from the Earth, and the magnetopause extends down towards the surface of the Earth. In Figure 1.4, the Cusp region is bounded by field lines 1 and 2 (1 and $2'$ in the southern hemisphere). The Cusp is also illustrated in Figure 1.5. Both the northern and southern hemispheres have a Cusp region. The near absence of the magnetosphere at the Cusp allows for solar wind plasma, decelerated in the magnetosheath, to stream directly down to the upper atmosphere of the Earth, along the geomagnetic field lines [*Russell*, 2000].

1.2.3 Particle motion and magnetospheric current systems

An important condition placed on all plasmas is that of current closure:

$$\nabla \cdot \mathbf{J} = 0. \tag{1.9}$$

As illustrated in Figure 1.5, there are many current sources in the magnetosphere. Some are a result of its geometry, others are due to the interaction between the magnetosphere and solar wind. Nonetheless, since there are current generators there must be current closure. In the magnetosphere-ionosphere (MI) system, the ionosphere acts to facilitate current closure. In some circumstances, the ionosphere may act as a load, while the magnetosphere acts as a generator, a coupling that is analogous to an electrical circuit. The magnetic field lines act as the wires, and allow the current to flow between the generators (in the magnetosphere) and the load (the ionosphere).

General particle drifts

The geometry of the dipole geomagnetic field and its distortions due to its interaction with the solar wind are responsible for the many complex particle drift and current systems in the magnetosphere. The motion of the particles comprising the collisionless magnetospheric plasma can be described by the guiding centre drift of a charged particle in a magnetic field.

It is assumed that the gyrofrequency of the charged particle is much greater than the rate of change any other dynamic process in the system (e.g., the time variation of the ambient magnetic field). Thus, only the geometric centre of the gyromotion about the magnetic field line needs to be considered. This is referred to as the *guiding centre approximation* [*Kelley*, 2009; *Baumjohann and Treumann*, 1997]. Using this approximation, the general force guiding centre drift is:

$$\mathbf{v}_F = \frac{1}{\omega_g}\left(\frac{\mathbf{F}}{m} \times \frac{\mathbf{B}}{B}\right), \tag{1.10}$$

where $\mathbf{v}_F$ is the guiding centre drift of the charged particle, $\omega_g = qB/m$ is the gyrofrequency of the particle, q is the charge of the particle, m is the mass of the particle, $\mathbf{B}$ is the ambient magnetic field, and $\mathbf{F}$ is the force acting on the charged particle [*Baumjohann and Treumann*, 1997].

To give an example of Equation 1.10, consider a charged particle moving in a spatially varying magnetic field. The particle will experience a force $\mathbf{F}_\nabla = -\mu\nabla B$, where μ is the magnetic moment of the particle. This force results in the gradient drift: $\mathbf{v}_\nabla = (mv_\perp^2/2qB^3)(\mathbf{B} \times \nabla B)$ where $v_\perp$ is the perpendicular velocity of the particle with respect to the magnetic field. As the sign of the drift depends on the charge of the particle, q, the gradient drift can result in currents, and is in fact partially responsible for the *ring current* (shown in Figure 1.5). This current system is established in the magnetotail by plasma moving toward the Earth, in the x-direction due to plasma pressure gradients. As it travels closer to the Earth, the plasma encounters the positive magnetic field gradient of the geomagnetic dipole field, establishing a gradient drift. Here, the electrons are directed eastward towards the dawnside of the Earth, while the ions are directed westward towards the duskside of the Earth. The gradient drift combines with other particle drifts, not discussed here, to produce the full ring current.

Field-Aligned Currents – Regions 1 and 2

Field aligned currents are another important component of the MI system. In the magnetosheath, the solar wind decelerates due to its interaction with the magnetosphere. The deceleration is equivalent to a force density directed towards the Sun – in the x–direction. The force density is in the form of $\rho d\mathbf{v}/dt = \mathbf{J} \times \mathbf{B}$, where $\mathbf{J}$ is an induced current density,

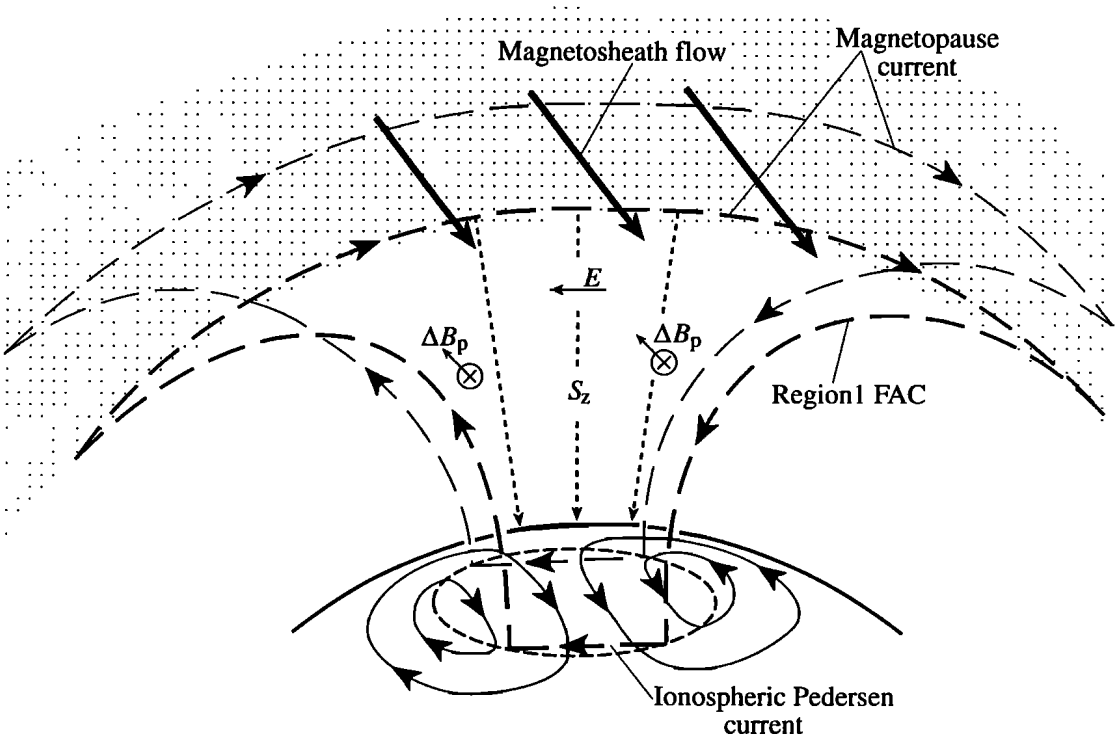

Figure 1.6: A depiction of the Region 1 current system, from [*Cowley*, 2000]. In this image duskside of the Earth is on the left and the dawnside is on the right. The position of the dusk-to-dawn current flow is depicted above the x-z GSM plane here. $\mathbf{S}_z$ is the downward Poynting flux due to the current system, and ΔB_p is the magnetic field perturbation due to the field-aligned currents (neither are discussed in the text).

directed from dusk-to-dawn, the negative y–direction [*Kelley*, 2009]; $\mathbf{v}$ is the velocity of the decelerated plasma; and $\mathbf{B}$ is the geomagnetic field. In this situation, we neglect any other factors such as gravity and pressure gradients, since they are negligible compare to the $\mathbf{J} \times \mathbf{B}$ force. The induced current density is labelled as a magnetopause current in Figure 1.6. The generation of this current is also shown in Figure 1.7, from the perspective of the x-z GSM plane. A magnetic field line that has recently merged with the IMF is shown in red. When the incoming solar wind plasma in the newly merged flux tube enters into the magnetosheath region it undergoes a deceleration (vector is shown in blue) while the rest of the flux tube outside of the magnetosphere is carried along by the solar wind, $\mathbf{v}$. This creates a kink in the flux tube in Figure 1.7. The deceleration is associated with the $\mathbf{J} \times \mathbf{B}$ force, and is associated with the current density, $\mathbf{J}$, directed into the page in Figure 1.7.

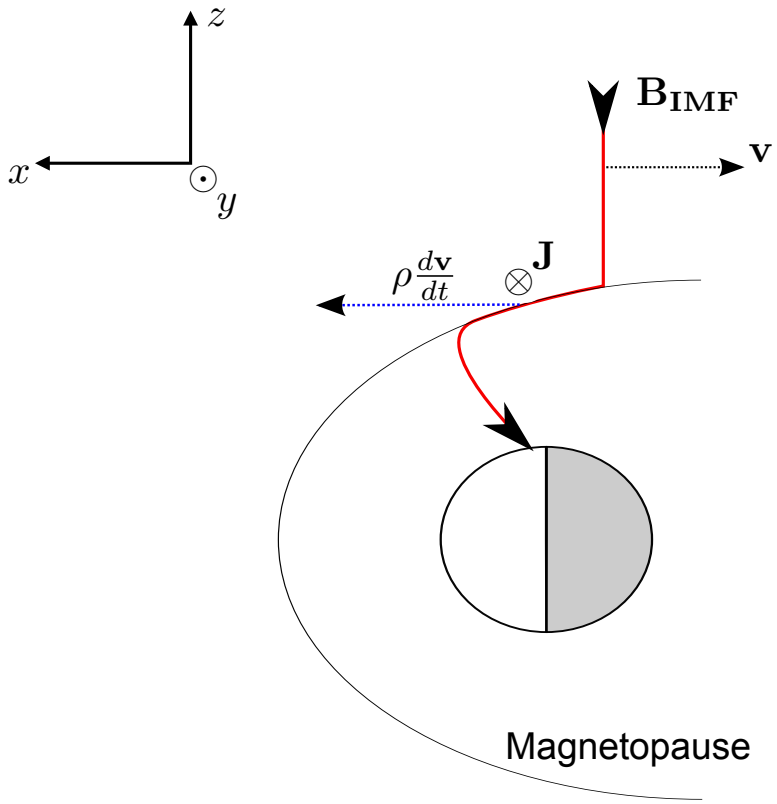

Figure 1.7: A side view of the magnetopause current and Region 1 generation mechanism, as seen in the x-z GSM plane. The magnetosheath is the location in which the incident solar wind becomes decelerated by its interaction with the magnetosphere. A flux tube connected between the solar wind and geomagnetic field is shown in red. The acceleration (blue dotted line), velocity (black dotted line), current density and geomagnetic field vectors on a portion of the flux tube in the magnetosheath are indicated.

Current closure (Equation 1.9) must be maintained throughout the plasma. Therefore, if a current is present and it is directed perpendicular to the magnetic field, a current parallel to the magnetic field must also be present in order to satisfy Equation 1.9. In the magnetosheath, this parallel current is a field-aligned current. As illustrated in Figure 1.6, field-aligned current is directed parallel to the magnetic field on the dawn side of the Earth and anti-parallel on the dusk side of the Earth. The current is completed through the ionosphere, in the form of a Pedersen current which will be introduced in a later section. This current system is referred to as the *Region 1* current system. In the magnetosphere, an electric field is produced in the

non-rotating frame of reference of the Earth; it is known as the dawn-to-dusk electric field, $\mathbf{E}_{DD}$, and is directed opposite to $\mathbf{J}$. The product of the two is $\mathbf{J} \cdot \mathbf{E}_{DD} < 0$; the interaction of the MI system at the magnetopause is a current generator. In the ionospheric portion of the current system, $\mathbf{J} \cdot \mathbf{E}_{DD} > 0$, in which case the ionosphere acts as a load.

Whereas the magnetosphere current drives the Region 1 current system, a space charge build up due to the *partial ring current* in the magnetosphere is responsible for the *Region 2* current system. The ring current is established by the gradient drift of plasma being directed in the x-direction – towards the Earth – by a dawn-to-dusk electric field in the magnetotail. A steep radial gradient (directed from the Earth) in magnetospheric plasma temperature can establish a charge build-up, with positive charges accumulating at the duskward edge of the gradient, and negative charges near dawnward edge [*Cowley*, 2000; *Lotko*, 2007]. Plasmas dissipate space charge build-up quickly; a field-aligned current with a downward current into the ionosphere on the duskside of the Earth, and an upward current out of the ionosphere on the dawnside, will be created to dissipate the charge build-up. Since the ring current is interrupted, a partial ring current forms. This is illustrated in Figure 1.8. Like the Region 1 currents, the Region 2 currents are closed by Pedersen currents in the ionosphere, and here $\mathbf{J}_{RC} \cdot \mathbf{E} > 0$ as well. The Region 2 current system is situated at lower geographic latitude than the Region 1 current system.

An important implication of the Region 1 and 2 current systems, for this work, is that they conspire to impart an $\mathbf{E} \times \mathbf{B}$ drift on the plasma comprising the ionosphere. The current systems generate plasma circulation, throughout the high latitude and polar region. This topic is discussed in more detail shortly.

1.3 The Ionosphere

The density of the terrestrial neutral atmosphere decays exponentially with increasing altitude. For a single species gas in hydrostatic equilibrium the vertical pressure gradient force and the force of gravity on the gas are balanced. The density of the gas is:

$$n\left(z\right) = n_0 \exp\left[-\frac{z - z_0}{H}\right], \tag{1.11}$$

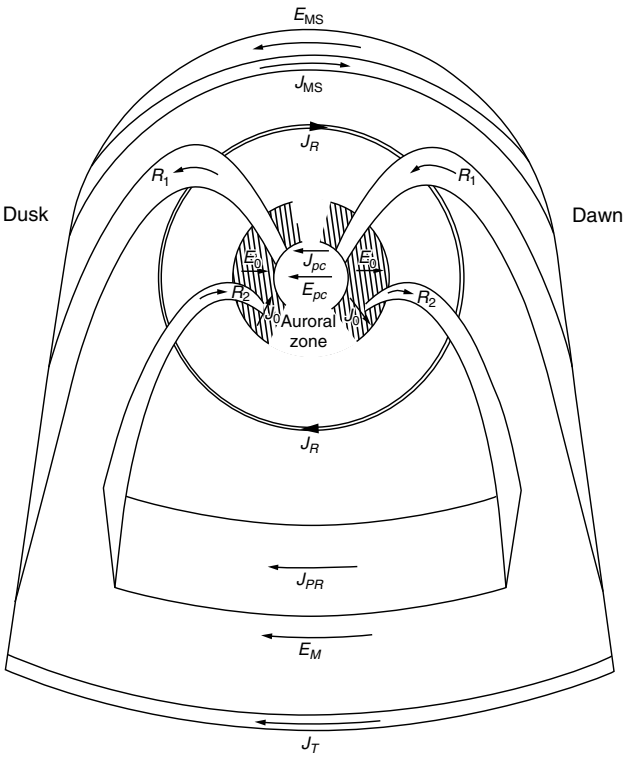

Figure 1.8: A depiction of the Region 1, $\mathbf{R}_1$, and 2, $\mathbf{R}_2$, current systems, from *Kelley* [2009]. Here, $\mathbf{E}_{MS}$ is the magnetosheath electric field; $\mathbf{E}_M$ is the dawn-to-dusk electric field; $\mathbf{J}_{MS}$ is the magnetosheath current; $\mathbf{J}_T$ is the tail current; $\mathbf{J}_R$ is the ring current; $\mathbf{J}_{PR}$ is the partial ring current; $\mathbf{J}_{PC}$ and $\mathbf{J}_0$ are the ionospheric portions Region 1 and 2 current systems, respectively; and, $\mathbf{E}_{PC}$ and $\mathbf{E}_0$ are the ionospheric electric field established by the Region 1 and 2 current systems, respectively.

in which z is the altitude and z_0 is a reference altitude; n_0 is an initial density; $H = k_b T/mg$ is the scale height, the e–folding height of the neutral density of the gas. H is a function of thermal energy, $k_b T$, and the force of gravity, mg, in which m is the mass of a gas particle and g is the acceleration due to gravity, k_b is Boltzmann's constant and T is temperature. A vertical profile of the main constituents of the neutral atmosphere: N_2, He, O_2, O and Ar, between 50 and 1200 km altitude is shown in Figure 1.9.

1.3.1 Plasma production

At an altitude, z, above the surface of the Earth the solar flux, Φ, as a function of wavelength, λ, and solar zenith angle, χ, can be described as [*Tohmatsu and Ogawa*, 1990]:

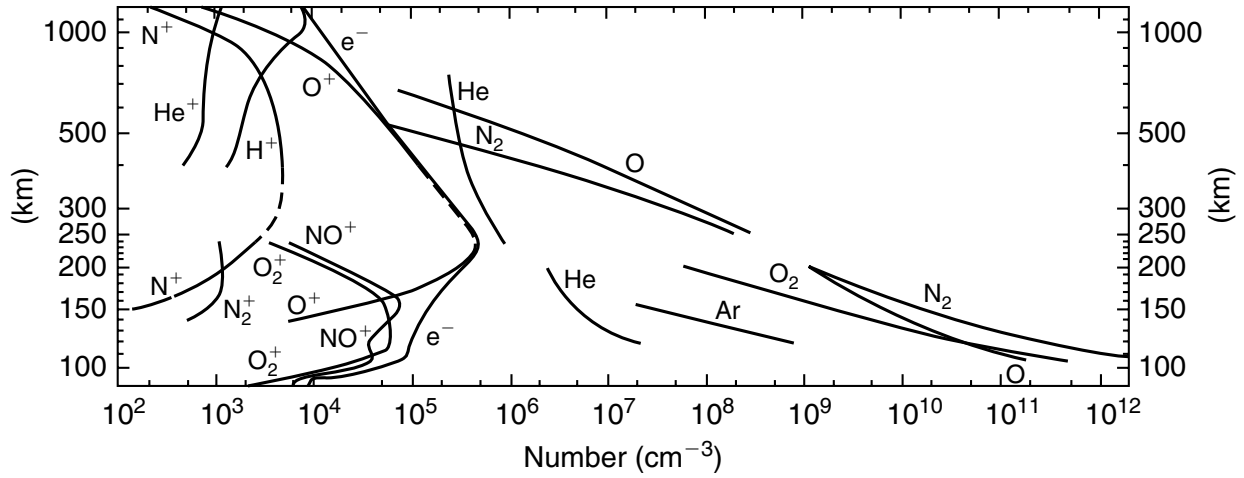

Figure 1.9: The vertical density profiles of the neutral atmosphere and the ionosphere, between an altitude of 50 and 1200 km, in units of cm^{-3} [*Johnson*, 1969].

$$\Phi(\lambda, z, \chi) = \Phi(\lambda, \infty) \exp[-\tau(\lambda, z, \chi)], \tag{1.12}$$

where $\Phi(\lambda, \infty)$ is the incoming solar flux at the top of the atmosphere. τ is the optical depth of the atmosphere, a measure of its opacity:

$$\tau(\lambda, z, \chi) = \sec\chi \sum_X \sigma(X, \lambda) \int_z^\infty n(X, z')\, dz'. \tag{1.13}$$

Here X denotes a atmospheric species and σ is its absorption cross-section and n is the number density of a neutral gas. The amount of energy density, q_T, deposited into the atmosphere by the solar flux is:

$$q_T(z, \chi) = \epsilon(z) \int_0^\infty \Phi(\lambda, z, \chi)\, \sigma(X, \lambda)\, n(X, z)\, d\lambda, \tag{1.14}$$

where ϵ is the heating efficiency that describes how well the incoming solar flux transforms into thermal energy. At the altitude where τ is a maximum, z_{max}, the incoming solar flux is decreased by a factor of $1/e$. It is also at this altitude that the amount of thermal energy deposited by the solar flux is maximized, $q_{T_{max}}$. A plot of where this occurs as a function of λ for incoming solar flux is given in Figure 1.10. Taking this into consideration for a single species we get:

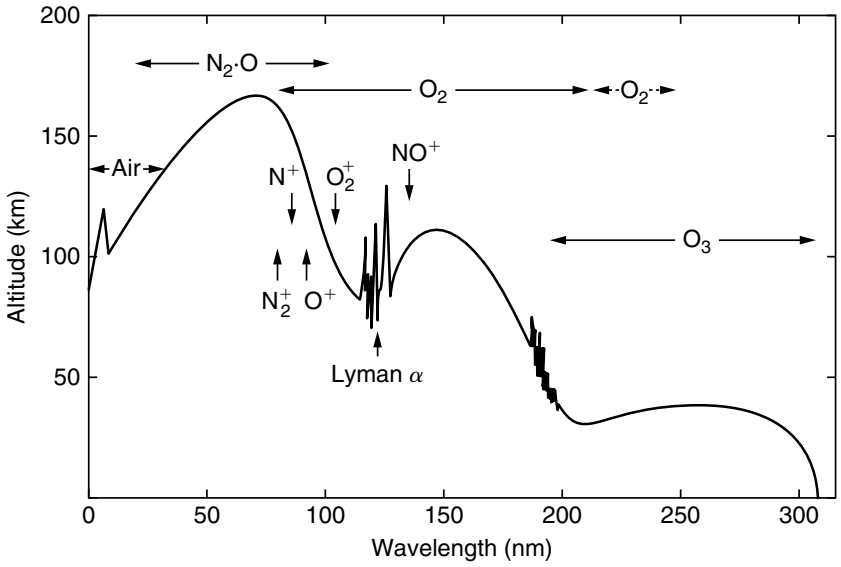

Figure 1.10: A profile of the altitude at which the incoming solar radiation decreases by $1/e$ [*Kelley*, 2009; *Smith and Gottlieb*, 1974]. The ions indicate where their cross section is at a peak, and the neutral molecules indicate the principal absorbers.

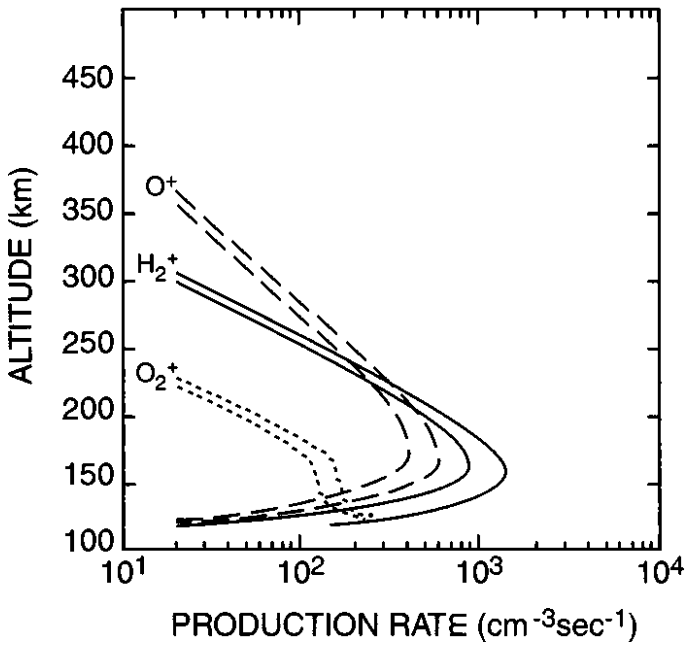

Figure 1.11: Two calculated production rates for each of O_2^+, H_2^+ and O^+, as a function of altitude [*Schunk and Nagy*, 2000]. The lesser production rate is by photoionization, while the larger rate is the total production rate by photoionization and photoelectrons.

$$Ch\left(z,\chi\right)=\frac{q_T\left(z,\chi\right)}{q_{T_{max}}}=\exp\left\{1-\frac{z-z_{max}}{H}-\sec\chi\exp\left[-\frac{z-z_{max}}{H}\right]\right\}. \tag{1.15}$$

Equation 1.15 is known at the *Chapman production function*, $Ch\left(z\right)$. A plot of Equation 1.15 is given in Figure 1.12 for a case in which $\chi = 0$ (the Sun is directly overhead). The Chapman function provides an accurate description of the thermal energy deposition in the neutral atmosphere, by the incoming solar radiation. A Chapman production function is modelled in Figure 1.11. One process by which the thermal energy is deposited into the neutral gas is through photoionization. Above 60 km altitude, the neutral atmosphere is tenuous enough that the production of charged particles by photoionization cannot be completely neutralized by chemistry. This results in a weakly ionized plasma and the region above 60 km which is referred to as the *ionosphere*. A vertical profile of the ionosphere is given in Figure 1.9, showing the profiles of its main ion constituents.

1.3.2 The F region

The ionosphere is vertically stratified, and classified into three regions: the D region, located between 60 and 90 km altitude; the E region, located between 90 and 150 km altitude; and the F region, located between 150 and 1000 km altitude [*Hargreaves*, 1992]. The main focus of this work is on processes occurring in the F region.

In the F region, O^+ is the main ion constituent, produced via photoionization:

$$O + h\nu \rightarrow O^+ + e, \tag{1.16}$$

where $h\nu$ is solar extreme ultraviolet (EUV) radiation. Subsequently, O^+ can be produced by collisions between the photoelectron in Equation 1.16 and atomic Oxygen, if the photoelectron has sufficient ionization energy [*Tohmatsu and Ogawa*, 1990]. According to Figures 1.10 and 1.11 the EUV absorption by atomic oxygen peaks at 150 km altitude, and thus the production of O^+ peaks there as well. Yet, Figure 1.9 places the peak O^+ density at 250 km altitude. This apparent discrepancy can be resolved if one considers the main O^+ sinks:

$$O^+ + O_2 \rightarrow O_2^+ + O, \tag{1.17}$$

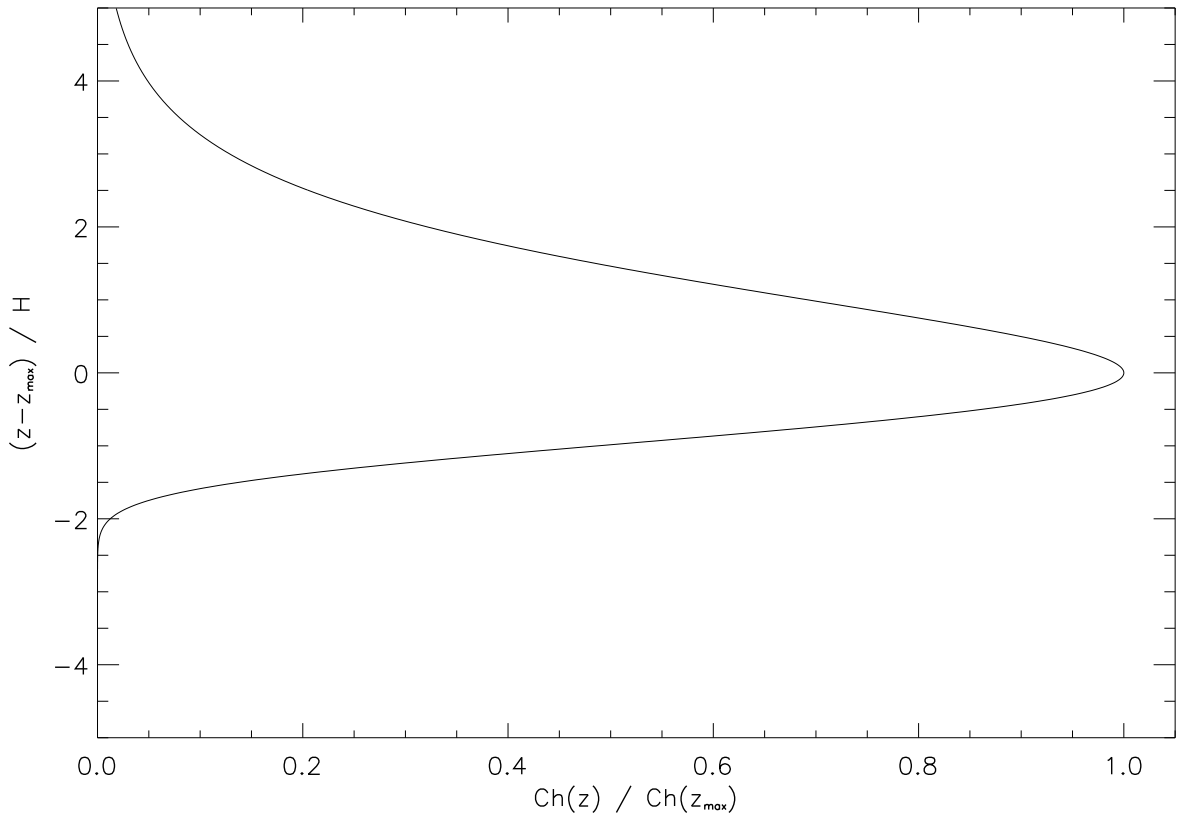

Figure 1.12: A plot of Equation 1.15, the Chapman function.

and

$$O^+ + N_2 \rightarrow NO^+ + N. \tag{1.18}$$

In terms of photochemistry,

$$\left[O^+\right] = \frac{Ch(z)_{[O]}}{k_1\left[O_2\right] + k_2\left[N_2\right]}, \tag{1.19}$$

in which $Ch(z)_{[O]}$ is the production of O^+ by photoionization, and k_1 and k_2 are the recombination rates for Equations 1.17 and 1.18, respectively. As shown by Figure 1.9, $[N_2] > [O] > [O_2]$, between 150 and 250 km altitude. At 250 km, $[N_2] \simeq [O] > [O_2]$, and above that $[O] > [N_2] > [O_2]$. It turns out that in the F region, up to 250 km altitude, $d[O^+]/dz > 0$. The photoproduction of O^+ decreases with increasing altitude above 150 km

(Figure 1.11), but the concentrations of its main sinks, N_2 and O_2, decreases with altitude more quickly. Above 250 km, ambipolar diffusion along the magnetic field line becomes important [*Hargreaves*, 1992; *Schunk and Nagy*, 2000]. The scale height of the plasma becomes much larger than that of the neutrals and the plasma density profiles turns around starting at 250 km, as shown in Figure 1.9.

In general, the F region has the highest plasma density in the ionosphere. There are two important points in the F-region plasma density profile, the F_1 ledge and the F_2 peak, at approximately 175 and 250 km altitude, respectively. Due to photochemistry, the F_1 ledge is only present when the ionosphere is sunlit. On average the F_1 ledge has a plasma density of the order of 10^{11} m^{-3}. The magnitude of the F_2 density peak is the largest in the ionosphere and can be of the order of 10^{12} m^{-3} [*Tohmatsu and Ogawa*, 1990].

1.3.3 The E region

The E region is below the F region, between 90 and 150 km altitude. The main ion constituent in the F region is an atomic ion, O^+, which is only produced directly via photoionization. The molecular ions NO^+ and O_2^+ are dominant in the E region. The former is produced by a number of reactions [*Tohmatsu and Ogawa*, 1990]:

$$O^+ + N_2 \rightarrow NO^+ + N, \tag{1.20}$$

$$N_2^+ + O \rightarrow NO^+ + N, \tag{1.21}$$

$$O_2^+ + NO \rightarrow NO^+ + O, \tag{1.22}$$

and

$$NO + h\nu \rightarrow NO^+ + e. \tag{1.23}$$

Photoionization is responsible for the production of N_2^+ and O_2^+. The first two equations are the main contributors to NO^+ production in the E region; the other two equations contribute

very little since there is not much NO at E-region altitudes. The E-region plasma density reaches a peak of 10^{11} m^{-3}, at approximately 110 km altitude.

NO^+ is only removed via:

$$NO^+ + e \rightarrow N + O, \tag{1.24}$$

a reaction which has the quickest reaction rate of any E or F region chemistry. O_2^+ is removed with a similar reaction, but at a slower rate. As a result, the E-region ionosphere recombines quickly once photoionization ceases after sundown, becoming significantly depleted on a time-scale of 100 s [*Tohmatsu and Ogawa*, 1990].

1.3.4 Ionosphere electrodynamics

Ionospheric Currents

In the ionosphere, the motion of the ions and electrons have two components: the *Pedersen* drift, which is along a transverse electric field with respect to the geomagnetic field, and the *Hall* drift, an $\mathbf{E} \times \mathbf{B}$ drift where $\mathbf{E}$ is a transverse electric field and $\mathbf{B}$ is the geomagnetic field. The magnitude of each drift depends on the mobility of the plasma, which itself depends on the collision properties of the plasma. In general [*Baumjohann and Treumann*, 1997]:

$$\mathbf{j} = \overline{\overline{\boldsymbol{\sigma}}} \cdot \mathbf{E}, \tag{1.25}$$

where $\overline{\overline{\boldsymbol{\sigma}}}$ is the conductivity tensor. In the ionosphere,

$$\overline{\overline{\boldsymbol{\sigma}}} = \begin{pmatrix} \sigma_P & \sigma_H & 0 \\ -\sigma_H & \sigma_P & 0 \\ 0 & 0 & \sigma_\parallel \end{pmatrix}, \tag{1.26}$$

where $\sigma_\parallel$ is the plasma conductivity and is sometimes labelled σ_0; σ_P is the Perdersen conductivity; and σ_H is the Hall conductivity. More precisely [*Kivelson and Russell*, 1995],

$$\sigma_P = \left(\frac{\nu_{en}}{\nu_{en}^2 + \omega_{ge}^2} + \frac{m_e}{m_i} \frac{\nu_{in}}{\nu_{in}^2 + \omega_{gi}^2} \right) \frac{n_e e^2}{m_e}, \tag{1.27}$$

$$\sigma_H = \left(\frac{\omega_{ge}}{\nu_{en}^2 + \omega_{ge}^2} - \frac{m_e}{m_i} \frac{\omega_{gi}}{\nu_{in}^2 + \omega_{gi}^2} \right) \frac{n_e e^2}{m_e}, \tag{1.28}$$

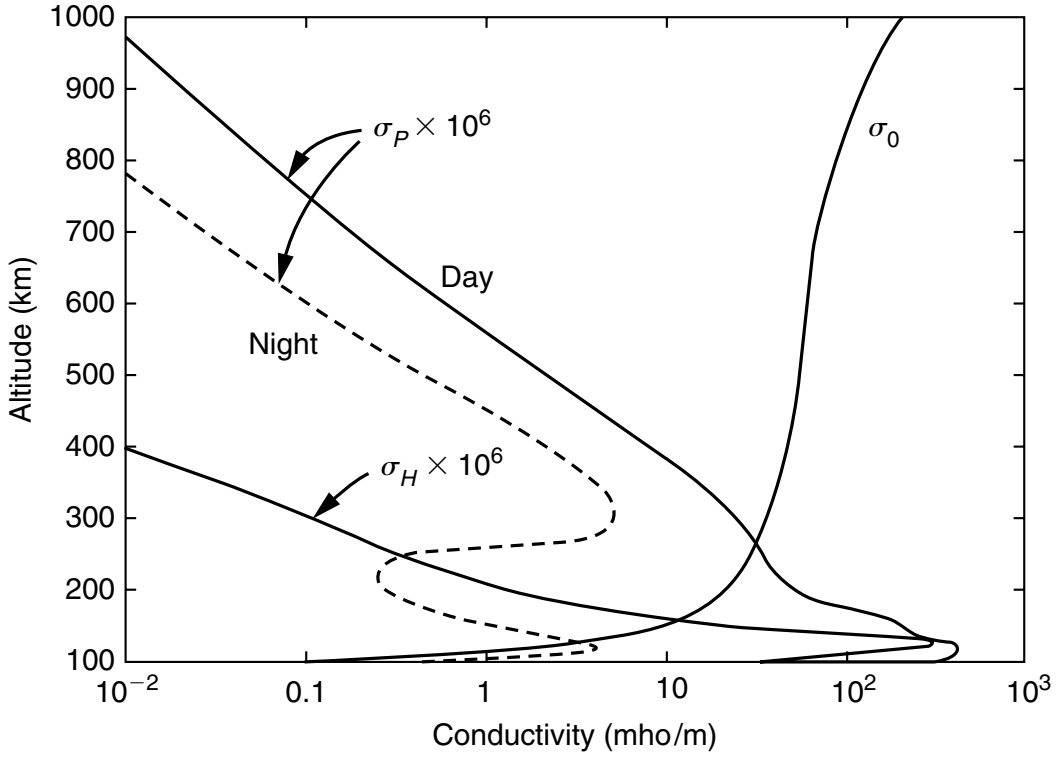

Figure 1.13: The vertical profiles of the plasma, Pedersen and Hall conductivities, as a function of altitude. The Pedersen and Hall conductivities have been multiplied by 10^6 [*Kelley*, 2009].

and

$$\sigma_{\parallel} = \left(\frac{1}{\nu_{en}} + \frac{m_e}{m_i} \frac{1}{\nu_{in}} \right) \frac{n_e e^2}{m_e}, \tag{1.29}$$

where ν_{en} is the electron-neutral collision frequency, ω_{ge} is the electron gyrofrequency, m_e is the electron mass, m_i is the ion mass, ν_{in} is the ion-neutral collision frequency, ω_{gi} is the ion gyrofrequency, n_e is the electron number density, and e is the fundamental charge. A plot of the ionospheric conductivities is given in Figure 1.13.

Equation 1.25 can be re-written as:

$$\mathbf{j} = \sigma_{\parallel} \mathbf{E}_{\parallel} + \sigma_P \mathbf{E}_{\perp} - \sigma_H \left(\frac{\mathbf{E} \times \mathbf{B}}{B} \right), \tag{1.30}$$

in which $\mathbf{E}_{\parallel}$ is the electric field parallel to the magnetic field; and $\mathbf{E}_{\perp}$ is the electric field, transverse to the magnetic field. The second term in Equation 1.30 is the Pedersen current,

and the third term in the Hall current.

An alternate form of Equation 1.30 can be derived from $\mathbf{j} = n_i q_i(\mathbf{v}_{in_\perp} - \mathbf{v}_{en_\perp})$, in which $\mathbf{v}_{in}$ and $\mathbf{v}_{en}$ are the ion-neutral and electron-neutral differential velocities, respectively. The momentum equation for an ion in the ionosphere can be written as [J.P. St. Maurice, personal communication, 2007]:

$$m\frac{\partial \mathbf{v}_{i_\perp}}{\partial t} = q_i\mathbf{E}_\perp + q_i\mathbf{v}_{i_\perp} \times \mathbf{B} - m\nu_{in}\left(\mathbf{v}_{i_\perp} - \mathbf{v}_{n_\perp}\right), \tag{1.31}$$

in which, '$\cdot_\perp$', signifies a vector perpendicular to $\mathbf{B}$, ν_{in} is the ion-neutral collision frequency. Defining $\mathbf{v}_{in_\perp} = \mathbf{v}_{i_\perp} - \mathbf{v}_{n_\perp}$, the ion-neutral differential velocity, a modified electric field vector, $\mathbf{E}'_\perp = \mathbf{E}_\perp + \mathbf{v}_{n_\perp} \times \mathbf{B}$, is introduced such that we transform into the frame of reference of the neutrals. Re-arranging Equation 1.31 and assuming steady-state conditions:

$$\nu_{in}\mathbf{v}_{in_\perp} = \frac{\omega_{gi}\mathbf{E}'_\perp}{B} + \mathbf{v}_{i_\perp} \times \boldsymbol{\omega}_{gi}, \tag{1.32}$$

in which

$$\mathbf{v}_{in_\perp} \times \boldsymbol{\omega}_{gi} = \frac{q_i\mathbf{E}'_\perp \times \boldsymbol{\omega}_{gi}}{m_i\nu_{in}} - \mathbf{v}_{i_\perp}\frac{\omega_{gi}^2}{\nu_{in}}. \tag{1.33}$$

Finally, introducing $\alpha_i = \nu_{in}/\omega_{gi}$:

$$\mathbf{v}_{in_\perp} = \frac{1}{1+\alpha_i^2}\left[\alpha_i\frac{\mathbf{E}'_\perp}{B} + \frac{\mathbf{E}'_\perp \times \mathbf{B}}{B^2}\right] \tag{1.34}$$

Recall that $\mathbf{j} = n_i q_i(\mathbf{v}_{in} - \mathbf{v}_{en})$. Above approximately 80 km altitude, $\omega_{ge} \gg \nu_{en}$ ($\alpha_e \ll 1$) [*Schunk and Nagy*, 2000; *Tohmatsu and Ogawa*, 1990], thus, the electrons always $\mathbf{v}_{en} = \mathbf{E}'_\perp \times \mathbf{B}$ drift above that altitude. Therefore,

$$\mathbf{j}_\perp = n_i q_i\left[\frac{\alpha_i}{1+\alpha_i^2}\frac{\mathbf{E}'_\perp}{B} - \frac{\alpha_i^2}{1+\alpha_i^2}\frac{\mathbf{E}'_\perp \times \mathbf{B}}{B^2}\right] \tag{1.35}$$

In this form:

$$\sigma_H = -n_i q_i \alpha_i^2\left(\frac{1+\alpha_i^2}{B}\right), \tag{1.36}$$

and

$$\sigma_P = n_i q_i \alpha_i \frac{1}{(1+\alpha_i^2)\, B}. \tag{1.37}$$

Equation 1.35 is a convenient way of interpreting how ionospheric currents vary as a function of altitude. In the F region, both the Hall and Pedersen conductivities are low compared to the plasma conductivity; current densities are low. This is due to the fact that at F-region altitude the neutral atmosphere is tenuous; the gyrofrequency is much larger than the collision frequency, $\omega_{gi} > \nu_{in}$ ($\alpha_i < 1$). In the E region, however, the neutral atmosphere is more dense, and accordingly $\omega_{gi} < \nu_{in}$ ($\alpha_i > 1$). As a result, currents in the E region are high; the bulk of the current is carried by the electrons. As can be seen in Figure 1.13, the peak conductivities are found in the E region

High-Latitude plasma convection

Electric fields generated by the interaction of the solar wind and the geomagnetic field, and the Region 1 and Region 2 currents system establish an $\mathbf{E} \times \mathbf{B}$ plasma circulation flow in the high geographic latitudes. Since the F-region plasma is highly conducting (although its conductivity is considerably less than that of the solar wind) and magnetic field lines are essentially perfect conductors (i.e., $\sigma_{\parallel} = \infty$ is a good approximation) the plasma flow is equivalent to the transport of magnetic flux, confined within magnetic flux tubes, flowing along equipotential lines. That is to say, in the high-latitude F-region, plasma $\mathbf{E} \times \mathbf{B}$ drifts along equipotential lines. The plasma circulation is also referred to as *convection*, a term which will be used throughout the rest of this work.

The convection at high latitudes illustrated in Figure 1.14 in which the $\mathbf{E}_{DD}$ (labelled as $\mathbf{E}_{pc}$) and $\mathbf{E}_a$ are the electric fields associated with the Region 1 and 2 current systems, respectively. The convection pattern illustrated in Figure 1.14 is for an ideal situation in the northern hemisphere, under southward IMF conditions. It is plotted in a magnetic local time (MLT) coordinate system, in which the geomagnetic lines of longitudes are divided into 24 hours – each hour representing 15° of geomagnetic longitude. The MLT coordinate system is stationary, and the geocentric coordinate system of the Earth (i.e., the geographic lines of latitude and longitude) rotates eastward with respect to the MLT coordinate system. 12 MLT corresponds to noon, 06 MLT is dawn, 18 MLT is dusk and 24 MLT is midnight.

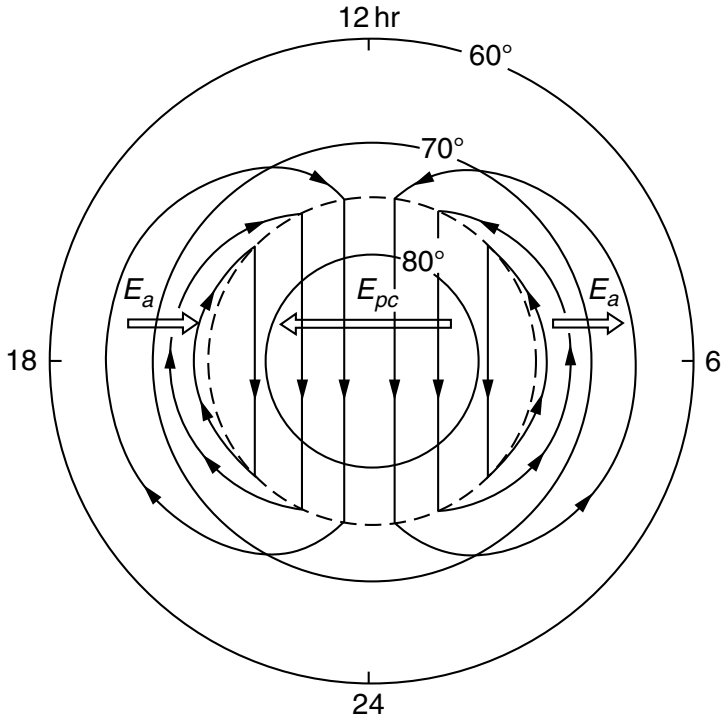

Figure 1.14: A schematic of the electric field regions and plasma convection lines in the high-latitude ionosphere in the northern hemisphere, plotted in the MLT coordinate system, from *Kelley* [2009]. The geomagnetic field, driving electric field and convection flows are all orthogonal to one another. The lines of geomagnetic latitude are labelled. The dashed lines indicates the polar-cap boundary. $\mathbf{E}_{pc}$ and $\mathbf{E}_a$ are associated with the Region 1 and 2 current systems, respectively.

The geomagnetic latitudes are indicated; the polar cap is indicated by a dashed line. The polar-cap boundary (also termed the *open-close field line boundary*) is defined as the locus at which the plasma convection lines transition between sunward and anti-sunward flow, and vice versa. In other words, the magnetic field lines in the polar cap are open field lines, and those outside the polar cap, convecting sunward, are closed field lines. Despite this formal definition, the region above 75° latitude is generally referred to as the polar cap, or the polar region.

For "southward" IMF, the z–component of the IMF, $\mathbf{B}_z$, is negative. Open magnetic field lines and F-region plasma move in an anti-sunward direction (negative x–direction), across the polar cap. This motion establishes the $\mathbf{E}_{DD}$ (labelled as $\mathbf{E}_{pc}$ in Figure 1.14). On the flanks of the high-latitude region, the plasma flows in the positive x–direction. This flux is

established by closed magnetic field lines being driven in the sunward direction. The flows are driven by a poleward electric field on the duskside of the convection flow, and an equatorward electric field on the dawnside (labelled as $\mathbf{E}_a$ in Figure 1.14).

IMF $\mathbf{B}_y$ also has an influence on the convection at high latitudes. The high-latitude convection pattern varies depending on the orientation of the IMF that is incident on the magnetosphere. Different contours of equipotential are formed and therefore different convection patterns are generated for various IMF orientations. Depending on its strength and orientation $\mathbf{B}_y$ will skew the convection patterns either towards the dawn (positive IMF $\mathbf{B}_y$) or dusk (negative $\mathbf{B}_y$). This is shown in the equipotential structure associated orientation of the IMF, depicted in Figure 1.15. The influence of IMF $\mathbf{B}_y$ has important implications for the entry of F-region plasma into the polar cap. If $\mathbf{B}_y > 0$ and $\mathbf{B}_z < 0$, then plasma from the dawnside ionosphere can be convected into the polar cap. Under these conditions, the Cusp, the entry point for plasma into the polar region, shown as the convergence of equipotential contours on the dayside in Figure 1.15, is shifted towards dawn. Plasma for the duskside enters the polar cap when $\mathbf{B}_y < 0$ and $\mathbf{B}_z < 0$. Often, dawnside F-region plasma is less dense than duskside plasma. This is because the duskside upper atmosphere has been exposed to solar EUV radiation for a longer period of time than the dawnside upper atmosphere. Therefore, IMF $\mathbf{B}_y$ can act as a regulator for F-region plasma density in the polar cap. This effect will be mentioned again, shortly.

For "northward" IMF conditions $\mathbf{B}_z$ is positive. The average $\mathbf{E}_{DD}$ is significantly reduced, and the plasma flows in the high-latitude ionosphere are severely altered and highly-structured, as shown in Figure 1.15. The reason for this is that under southward IMF conditions magnetic reconnection occurs upstream allowing for magnetic flux to enter the magnetosphere. The increase in magnetic flux into the magnetosphere produces an effect similar to Lenz's Law: currents and electric fields (i.e., Region 1 and 2 currents) are induced to counteract the increase in magnetic flux in the magnetosphere [*Cowley and Lockwood*, 1992]. However, under northward conditions, magnetic reconnection is significantly reduced; very little magnetic flux enters the magnetosphere. The electric fields and currents that are induced for southward conditions are markedly reduced for northward conditions, resulting in reduced average plasma flows as illustrated in Figure 1.15

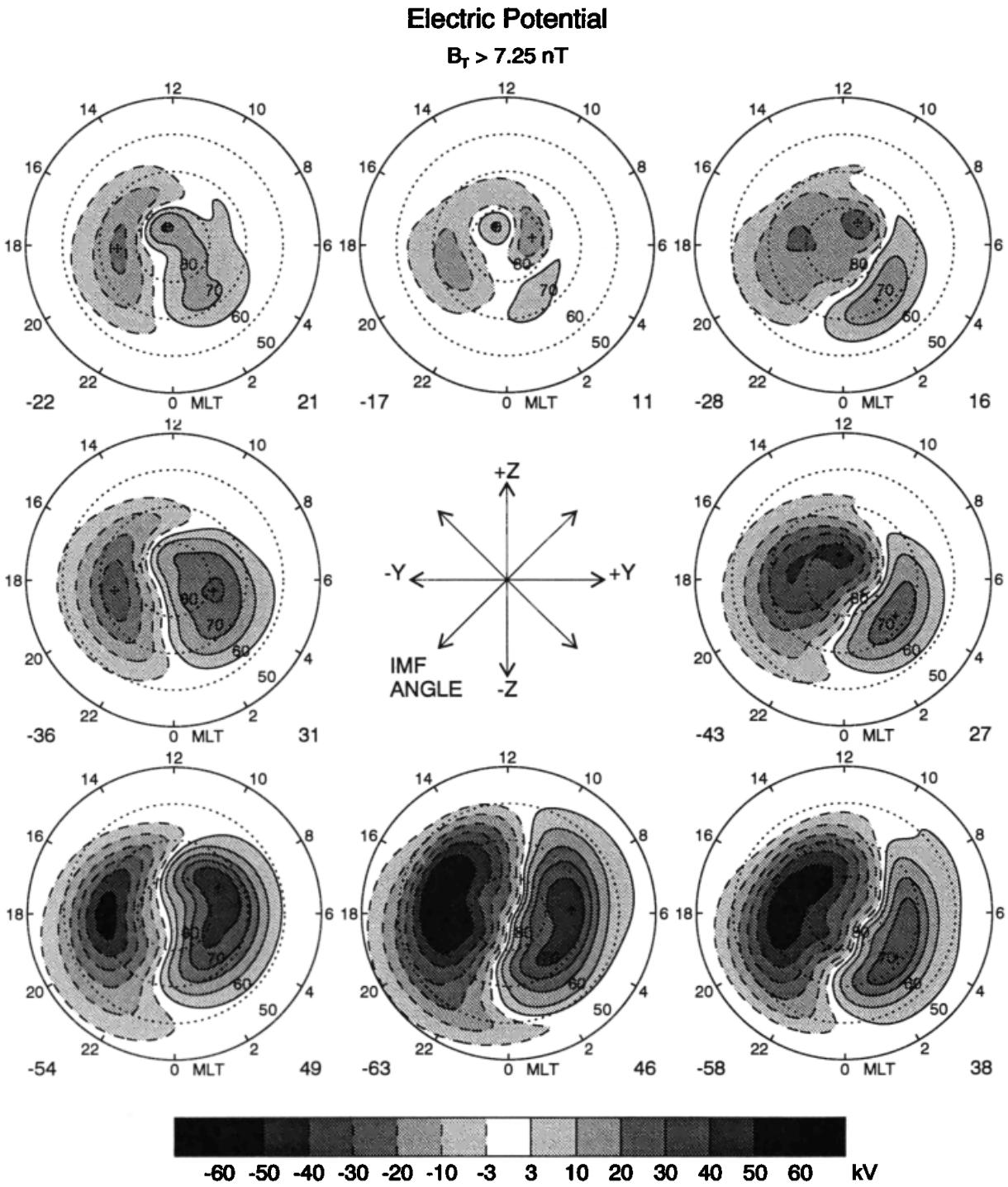

Figure 1.15: A variety of equipotential contours, sorted by IMF orientation, for an IMF magnitude greater than 7.25 nT, from *Weimer* [1995].

Other parameters of the solar wind and IMF can also have a significant effect on the convection patterns at high latitude. The velocity of the plasma flows and the overall convection pattern are intrinsically linked to the velocity of the solar wind. Both are more enhanced for high solar wind velocities, and subdued for lower velocities. This follows from the fact that $\mathbf{E}_{DD}$ is a product of the solar wind velocity. The convection patterns and plasma flows show a similar correlation with the magnitude of the IMF [e.g., *Milan et al.*, 2012, and references therein].

1.4 F-Region plasma density perturbations

At high and polar latitudes (which will be referred to generically as the polar region, from this point forward), perturbations in the F-region plasma density – both enhancements and depletions – can be produced by a variety of electrodynamic processes. The perturbations can then act as fertile ground for subsequent irregularities over a large spectrum of wavelengths [*Kelley et al.*, 1982; *Keskinen and Ossakow*, 1983; *Tsunoda*, 1988; *Moen et al.*, 2012]. In this work, we focus on large scale perturbations – those with scale sizes of the order of 10 to 1000 km. To provide some guidance when studying these density perturbations, consider the continuity equation [*Schunk and Nagy*, 2000]:

$$\frac{\partial n_i}{\partial t} + n_i \nabla \cdot \mathbf{v}_i + \mathbf{v}_i \cdot \nabla n_i = P_i - L_i, \tag{1.38}$$

where n_i is the number density for a plasma species, $\mathbf{v}_i$ is the drift velocity of the plasma, and $P_i - L_i$ are chemical production, P_i, and loss, L_i, terms, respectively.

Any chemical process involving the production of plasma is described by the first term on the right hand side in Equation 1.38, P_i. One major contributor to the production of F-region plasma is photoionization, e.g., Equation 1.16. In the F region, above 200 km altitude, it is reasonable to approximate $n_i \approx [O^+]$, where $[O^+]$ is the concentration of O^+. The chemical loss of O^+, L_i, is described by Equations 1.17 and 1.18. The associated reaction rates are both altitude and temperature dependent. In the F region, below 500 km altitude, the ambient temperature of the neutral atmosphere and plasma is of the order of 1000 K [*Kelley*, 2009], and any large variation in temperature, of the order of 50%, is atypical. Below

250 km altitude the reaction rates are large; a fully ionized F-region can be depleted within an hour via Equations 1.17 and 1.18. Above 250 km the reaction rates are considerably less; the time scale of the depletion is of the order of several hours.

Another contributor to the production of O^+ in the F region is from impact ionization by electrons with energies in the range of 100 – 300 eV. Charged particles can travel along magnetic field lines and collide with the neutral atmosphere, in a process termed *particle precipitation*. A visual byproduct of particle precipitation is the aurora. Precipitation provides a positive perturbation to the plasma density in the F region, namely, a localized plasma density enhancement. Notwithstanding photoionization, precipitation is the only mechanism by which O^+ can be produced in any quantity of significance. In the polar regions, precipitation and its corresponding density enhancements are spatially and temporally sporadic, and cannot compete with photoionization, in terms of plasma production.

If the energy of the precipitating particle is below 1 keV it is "soft" precipitation; above 1 keV it is "hard" precipitation. On closed field lines the source of precipitation is the magnetosphere; on open field lines the source is the solar wind. The energy of soft precipitation is well above a typical energy of thermalized F-region plasma (approximately 0.1 eV). The minimum ionization energy for O^+ is 13.62 eV [*Tohmatsu and Ogawa*, 1990]. Several O^+ ions may be produced from a single precipitating particle during a soft precipitation event. For hard precipitation, the energetic particles penetrate into the E region, depositing most of their energy there and do not significantly contribute to the ionization at F-region altitudes. During the daytime both photoionization and particle precipitation occur simultaneously. During the night time, or during winter, impact ionization due to precipitation has a more important role since photoionization is absent.

The F-region ionosphere is assumed to be incompressible; namely, $n_i \nabla \cdot \mathbf{v}_i = 0$ (the left hand side of Equation 1.38) [*Rishbeth and Hanson*, 1974]. As noted by *Kelley* [2009], this assumption is true in most cases, though it should be verified in each case (a good example of verifying incompressibility can be found in *Perry et al.* [2013]). Assuming incompressibility, all that remains of the left hand side of Equation 1.38 is the convective derivative:

$$\frac{Dn_i}{Dt} = \frac{\partial n_i}{\partial t} + \mathbf{v}_i \cdot \nabla n_i = P_i - L_i. \tag{1.39}$$

Equation 1.39 has important implications in the absence of chemistry, or in a situation where plasma production is counterbalanced by loss, and their rates are much less than $\mathbf{v}_i \cdot \nabla n_i$; Equation 1.39 reduces to: $\partial n_i/\partial t = -\mathbf{v}_i \cdot \nabla n_i$. This case stipulates that the change in plasma density of a volume of plasma at a fixed point in space is the product of the spatial plasma density gradient and the velocity of the plasma. More specifically, if n_i is being measured at a specific point in the ionosphere, $\partial n_i/\partial t \neq 0$ is only true if there is a spatial gradient in the plasma density, ∇n_i, and it is moving through the point of measurement, with a velocity $\mathbf{v}_i$, with respect to the point being measured.

F-region plasma transport was investigated using computer simulations by *Robinson et al.* [1985]. In that work, a parcel of plasma entrained within the polar $\mathbf{E} \times \mathbf{B}$ convection flow was simulated, assuming incompressible flow and no chemistry – i.e., $Dn_i/Dt = 0$. Their results, summarized in Figure 1.16, posit that a parcel of plasma in the F-region will become severely distorted after being displaced along convection streamlines for several hours. This is a direct result of the incompressibility condition. If we consider the same scenario – one in which the blob is a plasma density enhancement (or a depletion) – and are in the frame of reference of the moving blob, $Dn_i/Dt = 0$ holds since the flow is still incompressible. If we place an instrument that measures plasma density, at point A, as shown in Figure 1.16, and measure the plasma density, from the stationary frame of reference of that point, then $\partial n_i/\partial t = 0$ remains true up until $\mathbf{v}_i \cdot \nabla n_i \neq 0$. This would occur 1-hour into the simulation shown in Figure 1.16. At this point $\partial n_i/\partial t = -\mathbf{v}_i \cdot \nabla n_i$, since the instrument at point A would measure the ∇n_i passing by with a velocity $\mathbf{v}_i$.

The results from *Robinson et al.* [1985] have important implications for this work when considering plasma density perturbations in the F-region ionosphere. Most pertinent is the notion that in the absence of chemistry a plasma density perturbation will be transported through the ionosphere indefinitely, in a similar fashion to what is shown in Figure 1.16. Moreover, in a frame of reference outside of that of a moving plasma parcel, e.g in the co-rotation frame of the Earth, at point A in Figure 1.16, any case in which $\partial n_i/\partial t \neq 0$ can only be due to the transport of a plasma density perturbation, in the absence of chemistry. Evidently this is an idealized case since we know photoionization is an important plasma production mechanism, and so chemistry would be constantly present during the day. How-

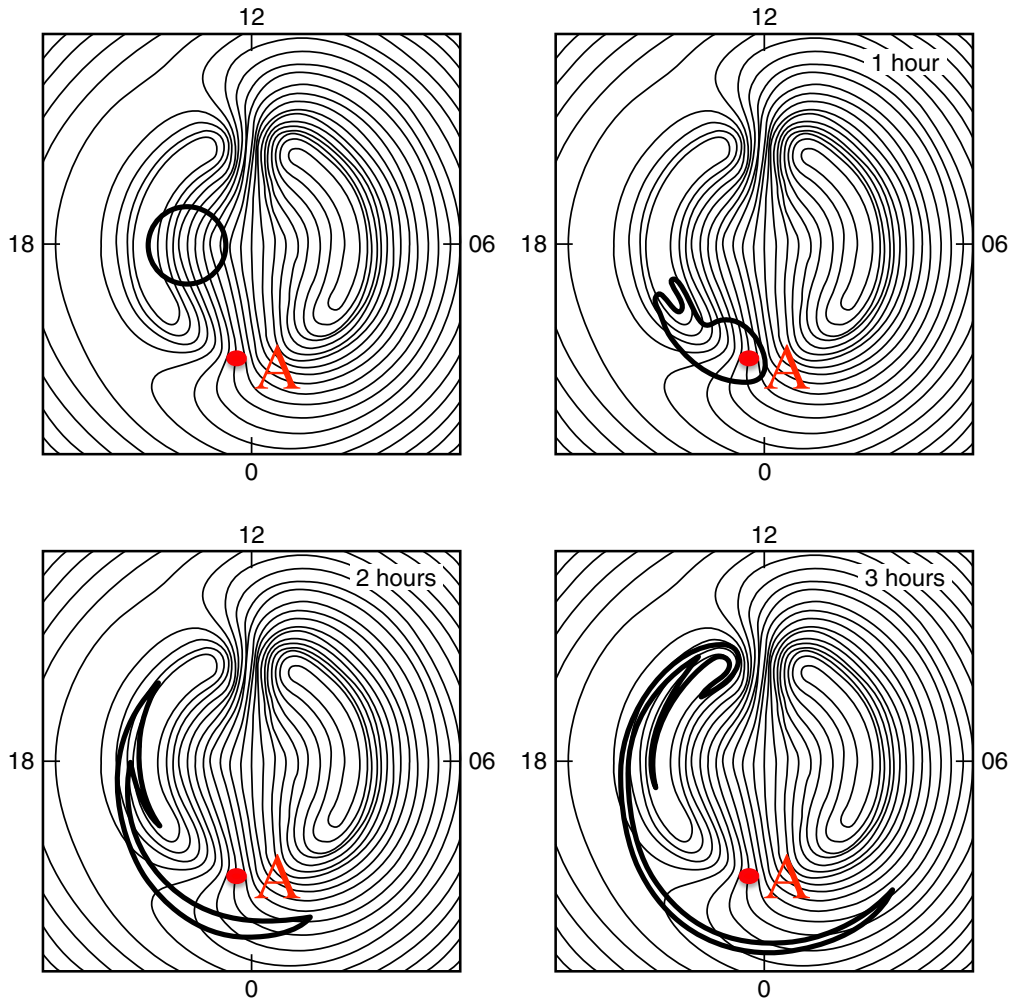

Figure 1.16: The results from a simulation showing the evolution of a blob of plasma entrained in the $\mathbf{E} \times \mathbf{B}$ convection flow, from *Robinson et al.* [1985]; *Kelley* [2009]. The magnetic local times are indicated as well. In this simulation, the ionosphere plasma is assumed to be incompressible.

ever, it is an accurate description for the F-region under some conditions, such as those in northern polar latitudes during nighttime or winter.

Since photoionization has a diurnal variation and is a large contributor to plasma production, and chemical recombination is the main sink, a diurnal variation in the F-region plasma density is expected. This is observed at low- and mid-latitudes, but the diurnal trend is subject to a great deal of variability [*Roble*, 1975; *Hargreaves*, 1992; *Rishbeth and Mendillo*, 2001]. The variability at these latitudes is attributed to other factors that are not discussed in this thesis, such as solar conditions, geomagnetic storms and dynamic coupling between

the ionosphere and the neutral atmosphere [*Kazimirovsky and Kokourov*, 1991; *Forbes et al.*, 2000]. A diurnal variation is not always observed in the F region in the polar regions either. In one study, *Moen et al.* [2008] reported a regular, semi-diurnal variation in the F-region plasma density at polar latitudes. In Figure 1.17 the peak F-region plasma density, labelled N_mF_2, and the height of the peak, h_mF_2, are plotted as a function of Universal Time (UT). The traces labelled "ESR" (EISCAT Svalbard Radar) are a median of 19-days of measurements in February, 2001 (panels a and b), and 28-days of measurements in October, 2002 (panels c and d), made by the incoherent scatter radar (a type of radar which will be introduced later) located at polar latitudes, in Norway, at (78.15° $N, 16.03^\circ$ E) in geographic coordinates. Also plotted is a model of the N_mF_2 and h_mF_2 provided by the International Reference Ionosphere (IRI) model [*Bilitza*, 2001].

It is clear that for N_mF_2, the model and measurements do not agree for all times. The IRI model describes a diurnal variation, with a peak near 12 UT, while the measurements show a semi-diurnal variation, with peaks near 12 UT and 21 UT. This trend is consistent for both panels a and c. The h_mF_2 measurements agree with the IRI model in panel b, but not as well in panel d. The reasoning behind the latter are not discussed here; its implications do not affect the results shown in panels a and c.

At the location where the measurements were taken, geographic noon is 11 UT, coincident with the IRI peak and the first measured N_mF_2 peak. These peaks are due to plasma production by photoionization, which has also been supplemented by soft precipitation as the field-of-view of the ESR passed through the Cusp [*Moen et al.*, 2008]. On the other hand, the second measured N_mF_2 peak cannot be explained by photoionization. In this season, at 21 UT, plasma production by solar radiation incident on the atmosphere at or below F-region altitudes is nearly negligible. Furthermore, all measurements were taken within the Arctic Circle during the northern fall and winter seasons. Thus the atmosphere would have not been exposed to solar radiation for an extended period of time. Chemical recombination would have dissipated any remaining plasma. The additional peak cannot be accounted for entirely by particle precipitation since the presence of the peaks are a regular feature. The traces in Figure 1.17 are a median of several weeks of measurements and would indicate a consistent and relatively fixed region of precipitation to produce the peak in the F-region, such as the

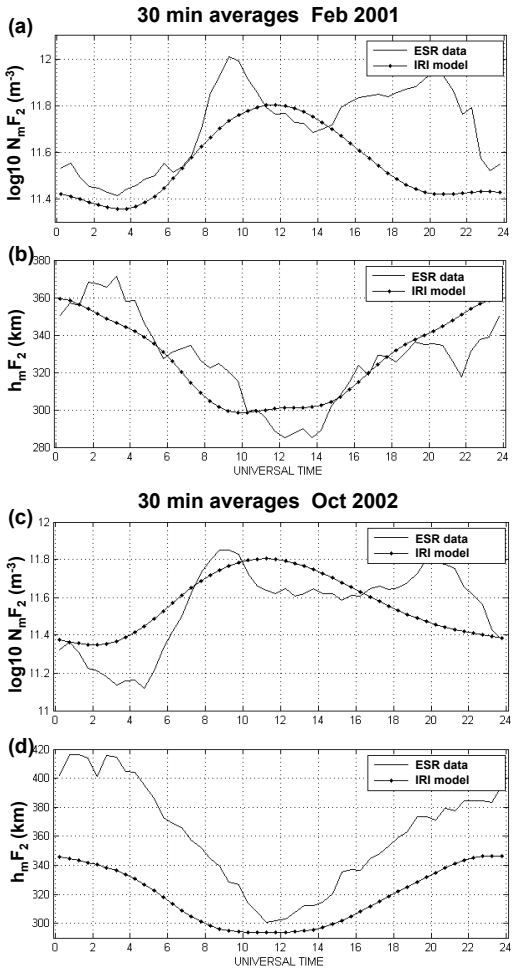

Figure 1.17: A plot from *Moen et al.* [2008] comparing the mean magnitude of the F-region plasma peak, N_mF_2 (a, c), the height of the F-region peak, h_mF_2 (b, d), to a model of the same quantities by IRI, as a function of time. The data in (a, b) and (c, d) were derived from 19 and 28 days of measurements, respectively.

Cusp. Soft precipitation is a characteristic of the Cusp, but atypically high fluxes would be required to produce the amount of plasma measured in the second peak. Most importantly, the Cusp is located on the dayside of the magnetosphere, and its ionospheric footprint is there as well. The peak in question is located in the night side ionosphere. It would have been highly unusual to have a consistent Cusp signature in the night side ionosphere [*Haerendel et al.*, 1978]. Thus, the conditions during which the data in Figure 1.17 were measured are described by Equation 1.39 in which the terms on the right hand side are negligible; the local chemistry is negligible and advection dominates. The ESR radar is fixed in position and, as

the observations of *Moen et al.* [2008] show, rotates into two regions of enhanced F-region plasma density, over a 24-hour period. The only explanation for the results in Figure 1.17 is advection – i.e., $\mathbf{v}_{ESR} \cdot \nabla n_i \neq 0$, where $\mathbf{v}_{ESR}$ is the co-rotation velocity of the ESR. The ESR encounters each region approximately every 12-hours, meaning that the regions are on opposite sides of the northern pole from one another; one is located near local noon, the other near local midnight. It turns out that the transport of volumes of photoionized F-region plasma density across the polar cap, from the dayside to the night side, by the high-latitude $\mathbf{E} \times \mathbf{B}$ convection streams was the culprit in this case study [*Moen et al.*, 2008]. These volumes of F-region plasma are known as "patches", and will now be discussed in detail.

1.4.1 F-Region ionization patches

F-region ionization patches are a class of large scale plasma density perturbations in the polar ionosphere. A patch is defined as a volume of plasma with a plasma density that is at least twice that of the ambient ionosphere, and spatial dimensions of the order of 50 – 1000 km [*Crowley*, 1996].

Instead of being smooth and continuous, the plasma that is transported by the convection flows in the polar ionosphere can be highly structured by patches. Their presence is indicative of the many complex plasma processes that occur in the polar ionosphere. Patches are believed to be a major contributor to the horizontal transport of plasma in the polar ionosphere, and from one serendipitous observation, may even be a significant contributor to vertical plasma transport into the near Earth geospace [e.g., *Semeter et al.*, 2003]. Observed under all geomagnetic conditions, patches can be studied optically and with radio instruments, i.e., radars. Their effects on radio wave propagation and Global Positioning System (GPS) signals can be significant, even during periods of subdued geomagnetic activity [*Moen et al.*, 2013].

Previous patch research

"Moving clouds of ionization" (i.e., patches) in the polar region, at F-region altitudes, were first reported by *Meek* [1949], who used radio instruments to detect them. *Hill* [1963] was the first to identify patches as large volumes of F-region ionization that are displaced through

the high latitudes by $\mathbf{E} \times \mathbf{B}$ convection drifts. *Hill* [1963] also demonstrated that the sunlit, dayside ionosphere, is a source of patches (see Figure 2 in that work).

As noted by *Crowley* [1996], it is generally accepted that there are multiple mechanisms for patch production, although not all are well understood. Of the mechanisms, those involving the transport of a patch from its distant sunlit source into the polar region have received the most attention, as opposed to those involving in-situ production. A strong correlation between the occurrence of patches and the polarity of the B_z component of the IMF was established by *Buchau et al.* [1983]. They found that the polar F region is heavily populated with patches under southward IMF conditions. This was later modified by *Coley and Heelis* [1998] who reported that patches are observed under all IMF conditions, in both hemispheres; however, patch occurrence is greatest in the northern hemisphere under southward IMF conditions. Southward IMF drives anti-sunward convection in the polar ionosphere, from the dayside to the nightside ionosphere, which implies that patches are related to the injection of photoionized plasma into the polar ionosphere from lower latitudes. Southward IMF enables plasma to flow into the polar-cap region from lower latitudes, whereas northward IMF conditions do not, as inferred in Figure 1.15. Observations by *Hill* [1963]; *Knudsen* [1974]; *Foster* [1984, 1993]; and *Foster et al.* [2005] detailed how the $\mathbf{E} \times \mathbf{B}$ convection streams are able to move dense, photoionized plasma from lower to higher latitudes and into the polar regions. *Buchau et al.* [1985] and *Moen et al.* [2008] demonstrated that the densities of measured patches were equivalent to those expected from photoionization, and were not a result of precipitation (recall Section 1.4 in this work), pointing to the sunlit ionosphere as their source. Plenty of compelling evidence exists supporting sunlit F-region plasma as a dominant source of patches.

Despite the fact that particle precipitation provides a secondary contribution to overall plasma production in the F-region ionosphere, its role in patch production should not be ignored. *Oksavik et al.* [2006] reported observations of the formation of a polar-cap patch, under northward IMF conditions. The patch was located in a high latitude region during the winter season, eliminating photoionization as a explanation for its production. Furthermore, since the IMF was northward at the time the patch could not have convected in from lower, sunlit latitudes. It was concluded that the patch was created in-situ, by particle precipitation.

Another case study, by *Walker et al.* [1999] gave an example of a patch being locally produced by precipitation in the polar Cusp under southward IMF conditions.

Another facet of patch generation mechanisms focuses on the partitioning of the plasma into patches as it is injected into the high latitude and polar ionosphere. *Knudsen* [1974] described the plasma being injected into the polar region as a "tongue of ionization" – a large, continuous, plume of plasma with a scale size of several thousand kilometres. Some mechanisms must exist to discretize the injected plasma into the patches that are observed. One way this could be done involves geographically narrow and extended channels of enhanced plasma temperatures. Increased plasma temperatures can be created via Joule or frictional heating, when intense electric fields are present, or when the differential velocity between the plasma and neutral atmosphere is significant [*St.-Maurice and Hanson*, 1982]. The enhanced temperatures increase the reaction rates of the F-region chemistry relating to the depletion of O^+ plasma, i.e., Equations 1.17 and 1.18. Thus, a large plume of plasma can be subdivided by regions of large density depletion, created by enhanced plasma temperature channels. This mechanism for patch generation was put forward by *Valladares et al.* [1994] and *Rodger et al.* [1994], who supported it with multiple observations of patch production in the polar region.

Milan et al. [2002] proposed that varying IMF conditions alter the source region of plasma entering the polar region. Under positive IMF B_y conditions, plasma is more likely to be drawn in from less dense plasma being circulated from the dawn sector (see Figure 1.15), while under negative B_y conditions, the plasma is drawn from the more dense afternoon sector. If the IMF B_y polarity switches with some regularity it would have the effect of injecting plasma of alternating densities into the polar region, appearing as patches. Using computer simulations, *Sojka et al.* [1993] reinforced the notion that variations in the IMF and the resulting structure in the polar-cap electric potential have a significant effect on the injection of plasma material into the polar region, and its discretization into patches.

Lockwood and Carlson [1992] developed the idea that *flux transfer events* (FTE) may be a major source of patches. FTEs are a result of the magnetic reconnection process, where a solar wind flux tube merges with the magnetosphere. The effect of an FTE on the high-latitude ionosphere is an expanded convection pattern with enhanced convection velocities.

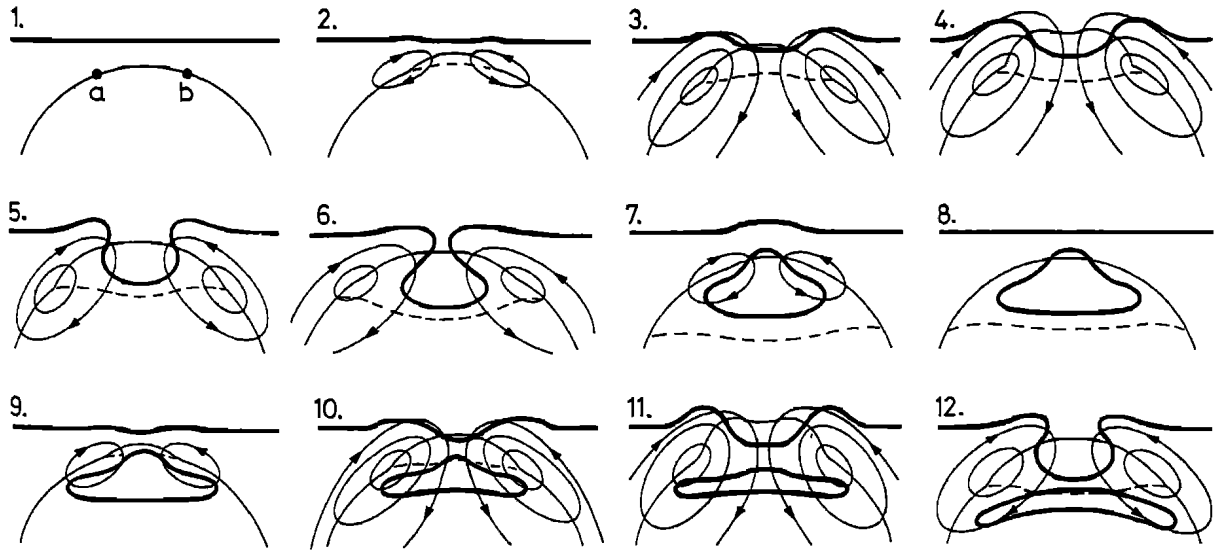

Figure 1.18: A sequence showing the evolution of a FTE, from *Lockwood and Carlson* [1992]. In step 1, a close solar wind flux tube approached the closed field lines of the magnetosphere. Steps 2 through 11 illustrate an expanded convection flow with enhanced flow velocities. The solid line in steps 9 through 12 border a region of enhanced plasma density – a patch – that is subsequently convected anti-sunward.

The equatorward movement of the enhanced polar convection pattern entrains segments of dense, sunlit F-region plasma (i.e., patches) into the enhanced anti-sunward convention flows. This process is illustrated in Figure 1.18. Subsequent observations by *Carlson et al.* [2006] provided strong support for the FTE mechanism and also confirmed it as an important patch generator. More recently, *Hosokawa et al.* [2013c] provided optical evidence of patches with almost identical shape and size to those depicted in Figure 1.18.

The displacement of a patch is influenced by the large scale electric potential pattern in the ionosphere. *Hosokawa et al.* [2009b] determined that the magnitude of $-B_z$ is well correlated with the velocity of a patch travelling through the high-latitude and polar region, and the B_y component is well correlated with the dawn-to-dusk component of the velocity. The time constant of the chemistry that depletes the patch plasma above 250 km altitude is of the order of several hours [*Pedersen et al.*, 2000]. The speed of the convection streams is typically 300 – 500 m/s, allowing for patches to be transported entirely across the polar cap, before being depleted by chemical recombination. With the right electrodynamic conditions, the circumnavigation of the high-latitude convection region by a patch is feasible, and was

recently verified by *Zhang et al.* [2013]. This result was indirectly postulated by *Robinson et al.* [1985], in Figure 1.16. That work did not account for a polar region with a highly structured convection flow field, however.

Once inside the polar region, patches are subjected to further influences that can distort their shape, and even break them apart. A spatially and temporally structured electric field produces variations in the flow, such as shears. These can partition and subdivide patches into smaller patches, a process that was observed optically by *Hosokawa et al.* [2010]. *Oksavik et al.* [2010] further demonstrated the influence of a structured polar-cap electric field on the motion of a patch, by providing evidence that patches undergo significant rotation during their transit through the polar region. In one case, the rotation was substantial enough that the leading edge of a patch quickly became the trailing edge of a patch during its transit.

A vast amount of focus has been placed on the generation mechanisms for patches, and how they enter the polar-cap region. However, the processes surrounding the exit of patches from the polar-cap region is not very well understood. Observations by *Zhang et al.* [2013] and simulations by *Sojka et al.* [1993] demonstrate that patches do exit the polar-cap region, after transiting through it. Once outside of the polar region, patches return to the dayside ionosphere, along the low latitude convection return flows. Tail reconnection, merging between open and closed IMF field lines in the magnetotail (step 6 in Figure 1.4), appears to play a major role in the exodus of patches from the polar region. It was noted by *Zhang et al.* [2013] that without tail reconnection the *open-closed field line boundary* (OCB) is "adiaroic", meaning that no plasma can flow across it. The same deduction was made by *Lorentzen et al.* [2004], who provided optical observations of patches crossing the OCB. In that work, the OCB appeared to expand poleward to entrap the patch, in a sequence of events that was, visually, very similar to descriptions of patch injection by a FTE on the dayside ionosphere. This has led others, such as *Lyons et al.* [2011], to postulate that patches may be associated with other processes occurring in the tail of the magnetosphere, such as the infamous substorm onset mechanism(s) [*Akasofu*, 1964]. Despite the scarcity of research pertaining to patches exiting the polar-cap region, that which does exist describes the processes as very similar to patches entering the polar region on the dayside. Although there is even less knowledge about patches during their trip back towards the dayside ionosphere, it is likely that the patches

are subject to further distortions and perturbations, from convection shears or precipitation, similar to what they experience as they travel through the polar region.

1.4.2 F-Region ionization depletions

Within the scope of investigating a variety of plasma density perturbations in the polar ionosphere, we now briefly turn to the topic of F-region ionization depletions. Since the plasma in the F-region is incompressible, in general, any significant depletion can propagate throughout the F-region. The physics governing the transport of plasma depletions throughout the ionosphere is identical to that governing the transport of patches – unless a depletion encounters a source of ionization, it will remain unchanged if transported along plasma convection flows. As noted by *Crowley et al.* [1993], unlike patches, depletions have historically received little attention, despite their common occurrence in the polar ionospheres.

As mentioned earlier, O^+ plasma is depleted via chemical recombination, described by Equations 1.17 and 1.18. The reaction rates and neutral concentrations at 250 km altitude are such that a plasma parcel with a density of approximately 1.0×10^{11} m^{-3} can be depleted in an hour. Therefore, the longer a parcel of plasma does not encounter a source of ionization, such as photoionization or precipitation, the more depleted it will become. In the high-latitude F-region, $\mathbf{E} \times \mathbf{B}$ and the co-rotation electric field can conspire in such a way as to entrap and stagnate the displacement of plasma in certain regions, preventing the plasma from encountering any source of ionization for several hours.

At polar latitudes, the motion of the plasma is driven by electric fields associated with interactions between the magnetosphere and the solar wind. At lower latitudes, a *co-rotation electric field* becomes more prominent and drives the plasma eastward, such that the plasma co-rotates with the Earth [*Kelley*, 2009, and references therein]. The co-rotation electric field is a function of geographic latitude; it peaks at the equator, while its minimum is at the geographic poles. Referring to Figure 1.15, one can see that in the 18 to 24 MLT sector, the motion of the plasma due to the co-rotation electric field is opposite to that of the convection electric field. This can establish regions in which the plasma flow stagnates, with respect to MLT coordinate system. Where this occurs the plasma can remain entrapped in the nighttime ionosphere, without any source of ionization, slowly depleting due to chemistry.

This region has been named the *sub-auroral trough*, since it is located equatorward of the auroral oval. This region of depletion is also referred to as the *main trough*, and was first reported by *Muldrew* [1965] who used a topside sounder aboard the Alouette 1 satellite to identify it as well as other large scale plasma density depletions in the mid- and high-latitude ionosphere.

Poleward of the auroral region, plasma convecting in an eastward direction in the 00 to 06 MLT sector can be devoid of a source of ionization for lengthy periods of time. This is especially the case during the northern winter, at geographic latitudes above 70°. Here, there is very little photoionization due to its geographic location. Secondly, there are very few sources of particle precipitation; the region is poleward of a large region of precipitation – the aurora oval. If the plasma convection velocities are low, plasma in this region will spend more time in the region, away from ionization sources, allowing more time for the plasma to deplete. This region has been identified with a variety of instruments and is referred to as the *polar hole* [*Brinton et al.*, 1978; *Sojka et al.*, 1981]. The position of the sub-auroral trough and the polar hole in the high-latitude region is given in Figure 1.19.

Another mechanism for creating significant plasma depletion in the polar ionosphere was put forward by *Sojka et al.* [1981]. In the vicinity of the magnetic pole, in the midnight sector, the anti-sunward $\mathbf{E} \times \mathbf{B}$ convection has a non-negligible downward component. Accordingly, the plasma is driven vertically downward into the neutral atmosphere and encounters an exponentially increasing neutral atmosphere density. For slow convection flows, the downward component is very low and the effect on the plasma is nearly negligible. However, if anti-sunward plasma flow is enhanced the downward flows can become significant – of the order of 100 m/s [*Sojka et al.*, 1981]. In this case, the descending plasma recombines quicker than plasma that is not descending, since it encounters larger neutral densities. As a result, the region where the downward component of the $\mathbf{E} \times \mathbf{B}$ drift is significant becomes appreciably more depleted than the surrounding region – a different type of polar-hole.

Arguably the most frequently cited mechanism for plasma depletion in the ionosphere is frictional heating between the ion and neutral gases. Both the electrons and ions $\mathbf{E} \times \mathbf{B}$ drift in the F-region, while the neutral atmosphere does not. A differential velocity between the ions and neutral atmosphere can become significant enough to increase the temperature of

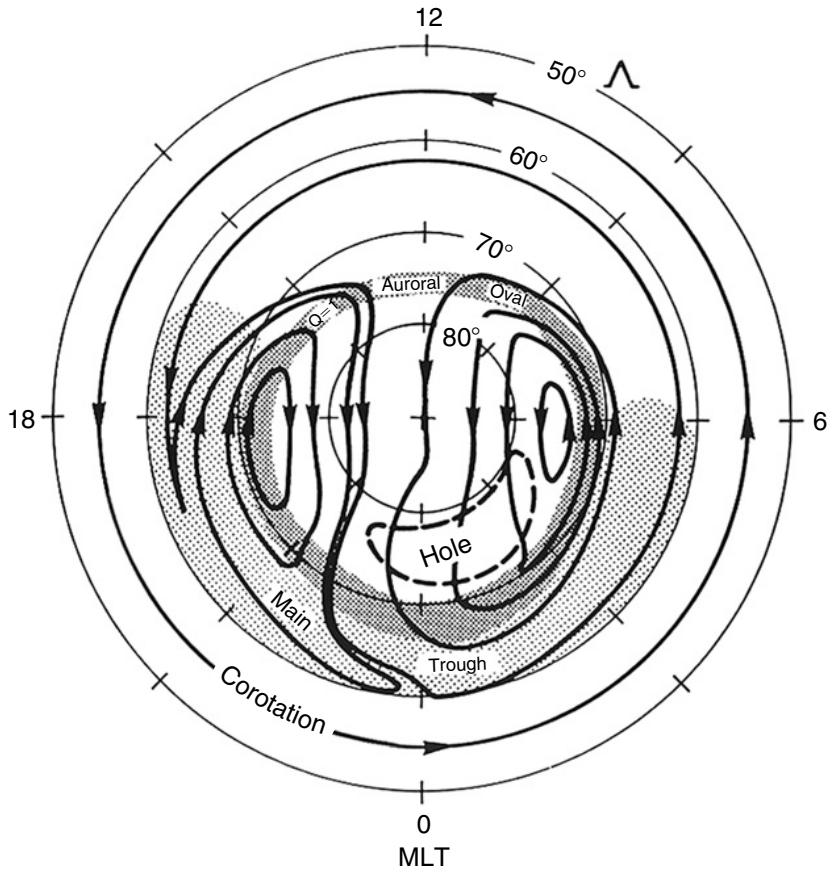

Figure 1.19: A plot showing the average location of the polar hole, sub-auroral trough and the auroral oval, in MLT coordinates [*Brinton et al.*, 1978; *Kelley*, 2009]. The plasma flows of the high-latitude convection, along with the lower latitude co-rotation plasma flows are indicated.

the ion gas, due to frictional heating; namely [*St.-Maurice and Hanson*, 1982]:

$$\psi_{in} 3 k_b \left(T_i - T_n\right) \simeq \left(\mathbf{V}_i - \mathbf{V}_n\right)^2 \phi_{in}, \tag{1.40}$$

where ψ_{in} and ϕ_{in} are coefficients describing the heat transfers between ions and neutrals, and are approximately 1; T_i and T_n are the ion and neutral temperatures, respectively; $\mathbf{V}_i$ and $\mathbf{V}_n$ are the velocities of the ion and neutral gases, respectively, and k_b is Boltzmann's constant.

Equation 1.40 outlines the relationship between the ion and neutral gas in the F-region; the temperature of the ion plasma can be increased if it has a significant enough relative

velocity with respect to the neutral gas (assuming that the collisions are non-negligible). An increased ion temperature will enhanced the reaction rates for Equations 1.17 and 1.18. If the enhanced reaction rates persist, the plasma can become significantly depleted. Frictional heating is a significant contributor to the energy budget in the polar ionosphere, and is commonplace in the literature regarding the high-latitude and polar ionosphere [e.g., *St.-Maurice and Hanson*, 1982; *Maeda et al.*, 2009; *Goodwin*, 2013]. In fact, frictional heating is invoked for some of the ionization patch creation mechanisms mentioned earlier in Section 1.4.1.

1.4.3 F-Region ionization depletions and enhancements

A method by which plasma density depletions and enhancements can be created together is through the gradient-drift instability (GDI). Up until this point, the plasma density depletions discussed were a byproduct of chemistry. The GDI does not use chemical recombination to create plasma density depletions. Instead, the GDI redistributes the plasma with respect to plasma density gradients that may be present. The GDI is reintroduced in more detail shortly, but for now, the GDI and its effect on plasma density can be explained via a classic Rayleigh-Taylor instability analogy involving two liquids of different density, for example, water and oil. If one places water and oil into a container (in a laboratory on Earth), both substances will separate and stratify as the system reaches equilibrium. The oil will rest on top of the water since the density of oil is less than that of water; a density gradient will exist, parallel to the gravitational field. In this configuration the system is stable. If the system is suddenly inverted, the density gradient becomes anti-parallel with respect to the gravitational field of the Earth. In this configuration, the system is unstable. When unstable, any perturbation along the interface between the two liquids will grow as an instability. The less dense oil will migrate vertically into the layer of water in "finger" like structures, creating density depletions within the water. An example of a Rayleigh-Taylor instability is given in Figure 1.20, which depicts the time progression of the instability as a more dense liquid, in blue, migrates into a less dense liquid, in yellow. The GDI instability produces very similar results in ionospheric plasma; however, in the F-region ionosphere, the $\mathbf{E} \times \mathbf{B}$ drift takes the place of the gravitational field. Its orientation with respect to the density gradients in the system governs the systems stability.

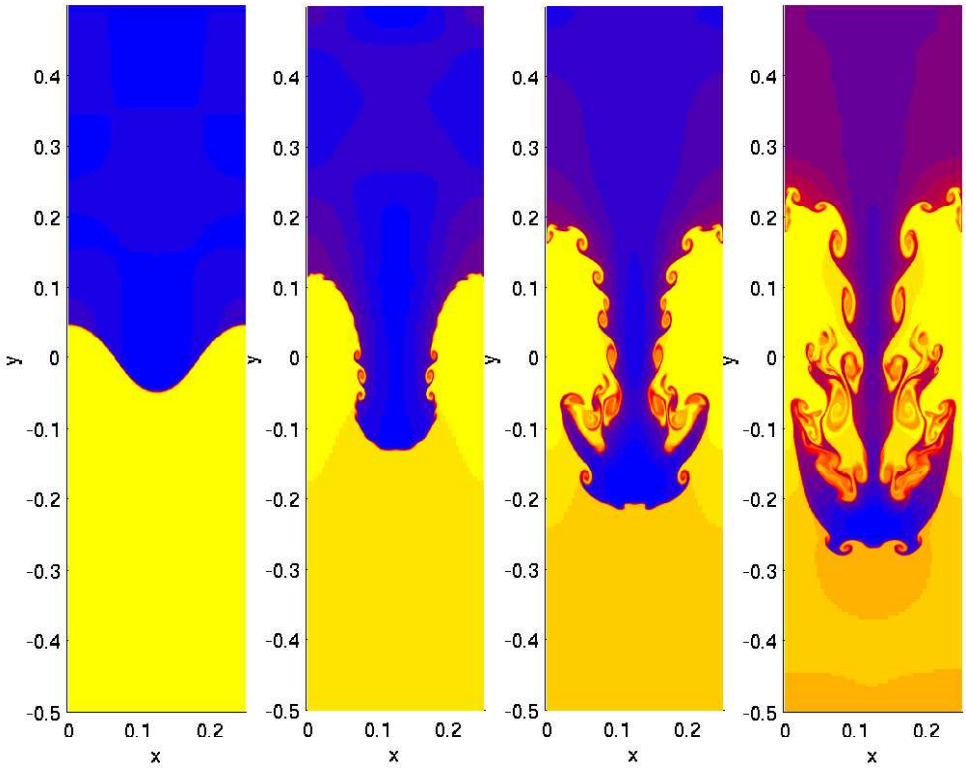

Figure 1.20: An illustration of the Rayleigh-Taylor instability, for a more dense liquid (blue) migrating into a less dense liquid (yellow) [*Li and Hui*, 2006]. The Rayleigh-Taylor instability is analogous to the GDI which operates in the ionosphere. Both produce density depletions without the use of chemical recombination.

1.5 Motivation for research

Interest in F-region ionization patches and depletions has waxed and waned since they were first studied over 50 years ago. It is apparent that increased research efforts have been well correlated with the introduction of new instruments and experimental techniques. With each evolution comes new questions. Patches were first detected and studied with radio and optical instruments, and interest in them grew as instruments were installed deeper into the polar regions. In the last quarter of the 20th century the development of more sophisticated radio, rocket and satellite borne instrumentation reinvigorated interest in patches. This was bolstered with the introduction of sophisticated computer modelling and simulations which provided a deeper understanding of the physics behind the perturbations. Most recently, the scientific infrastructure in the high-latitude and polar region has undergone further develop-

ment [e.g., *Hosokawa et al.*, 2006; *Chisham et al.*, 2007; *Nicolls et al.*, 2007; *Bahcivan et al.*, 2010]. In the northern hemisphere, above 40° geographic latitude, a significant portion of the sky is now covered by a comprehensive network of radio and/or optical instruments. The instruments have become more sensitive and sophisticated. Their geographic distribution in the polar region enables common volume measurements with multiple radio and optical instruments, opening up new opportunities to gain new insight into polar ionospheric system.

This thesis is motivated by the new questions emerging from the refocused attention on the polar ionosphere. Using existing and recently deployed instruments in the polar region the aim of this research is to advance our understanding of large scale plasma density perturbations in the polar ionosphere, their generation mechanisms, transport properties and signatures at optical and radio wavelengths. This will be carried out by directly addressing a selection of some of the many outstanding questions pertaining to these features, including:

- Is there a link between the optical signature of F-region ionization patches and their motion in the ionosphere?

- Using radar, can our existing capabilities in identifying and characterizing F-region ionizations patches be improved?

- How strong is the interconnection between the occurrence of high frequency (HF) radar echoes from the polar-ionosphere and the presence of F-region ionization patches there?

- Are patches a dynamic or stagnant feature of the ionosphere? Is there any evidence of internal morphology?

- What geophysical phenomena are related to the frictional heating events producing plasma density depletions in the polar ionosphere?

- What is the time scale of generating plasma density depletions in the polar-ionosphere via a frictional heating mechanism?

1.6 Thesis outline

This dissertation is written in the traditional thesis format. Chapters 3 through 6 each focus on one or two of the aforementioned questions regarding F-region ionization enhancements and depletions. Chapter 2 provides a thorough description of instruments used to detect and investigate the polar F-region ionosphere. Particular attention is given to the instruments supporting the research in Chapters 3 to 6, including: optical imagers, HF radar, and incoherent scatter radar (ISR).

Chapter 3 discuses the interconnection between the optical signatures of an F-region ionization patch and its motion through the polar region. A case study showing that the optical intensity of a patch is highly correlated with the velocity of a patch is discussed in detail, using the support of both an optical imager and an HF radar. The results of this case study and a model developed from it are tested in another patch event, using the same two instruments with the addition of an ISR system.

Chapter 4 details the work conducted to improve methods of detecting patches and depletions. Using the formal definition of a patch – an F-region plasma density enhancement that is twice as dense as the surrounding ionosphere [*Crowley*, 1996] – an algorithm is developed to detect ionization patches, with an ISR located in the polar cap. Currently, there is no reliable technique to detect patches or depletions using HF radar systems. The link between the occurrence of patches and depletions detected by the ISR, and HF radar signatures originating from the same geographic region is also investigated.

In Chapter 5, a case study of an individual ionization patch detected with an ISR, HF radar and optical imager is presented. Close inspection of the plasma density properties suggest a quickly evolving plasma density profile, according to the ISR system. The results indicate that the patches are not necessarily stagnant features of the F-region ionosphere, and that they may be home to significant plasma redistribution processes. An alternate theory to account for the plasma signatures is also outlined. It proposes that the detected patch could be a grouping of several patches that cannot be resolved by the ISR system. The signature of several small patches may be represented as the dynamic plasma density properties measured.

Chapter 6 focuses on an event featuring a sun-aligned arc – a longitudinally extended line of particle precipitation – and an associated plasma density depletion that is also longitudinally extended and adjacent to the arc. Using an optical imager, an HF radar and ISR system, the plasma density properties of the depletion and arc are probed in detail. A field-aligned current system associated with the arc is inferred using estimates from the ISR.

In Chapter 7 a summary of the results from Chapters 3 through 6 is given in the context of the questions posed in Section 1.5. Suggestions for future research avenues concerning plasma density enhancements and depletions are also discussed.

Chapter 2

Instrumentation

In this chapter instruments and measurement techniques used to probe and investigate F-region ionization patches and depletions are discussed. Three instruments of particular interest to this work are the Resolute Bay Incoherent Scatter Radar – North (RISR-N), the Super Dual Auroral Radar Network (SuperDARN), and the Optical Mesosphere and Thermosphere Imagers (OMTI). The capabilities and techniques for each instrument are outlined in some detail.

2.1 Incoherent Scatter Radar

Incoherent scatter radar (ISR) data is featured prominently in the analysis throughout this research. An ISR system transmits radio waves into the ionospheric plasma, which are then backscattered via the incoherent scattering process. From this, many important plasma parameters can be obtained including plasma density, ion and electron temperature and the line-of-sight velocity of the plasma.

To understand the incoherent scattering process we must first consider the radar equation for the setup in which the transmitter and receiver are at the same location [*Skolnik*, 2003]:

$$P_r = \frac{P_t G_t}{4\pi R^2} \frac{\sigma}{4\pi R^2} A_e \tag{2.1}$$

where P_t and P_r are the power transmitted and received by the transceiver of the radar, respectively; A_e is the effective aperture area of the transceiver; σ is the radar cross-section of the radar target, in our case plasma density fluctuations in the ionosphere; $G_t = 4\pi A_e/\lambda^2$ is the antenna gain in which λ is the radar wavelength; and R is the range to the radar target. Except for σ, each of the terms in Equation 2.1 can be obtained with relative ease. In

most cases with radar, σ is well defined, discrete, and considered a "hard target"; a coherent object with a cross-section well within the scattering volume defined by the beam width of the radar e.g., a plane, satellite, car, etc. In general, the ionosphere is not a hard target and is considered a "soft target". Ionospheric plasma is composed of equal numbers of ions and electrons (i.e., the quasineutral condition) in thermal equilibrium and fill up the entire scattering volume. Both the ions and electrons are in constant motion. The ions have much more inertia than the electrons, and are often assumed to be stationary [*Chen*, 2010]. Thus, the electrons oscillate about the ions at the plasma frequency, ω_p:

$$\omega_p = \sqrt{\frac{n_e q_e^2}{\epsilon_0 m_e}}. \tag{2.2}$$

In a plasma, an electrostatic potential is "shielded-out" beyond a distance, λ_D, the *Debye length*:

$$\lambda_D = \sqrt{\frac{\epsilon_0 k_b T_e}{n_e q_e^2}}. \tag{2.3}$$

In the above equations, n_e is the number density of the plasma; ϵ_0 is the permittivity of free space; q_e is the fundamental charge; m_e is the mass of the electron; k_b is Boltzmann's constant; and T_e is the electron temperature. The plasma comprising σ is a collection of charged particles, with a given velocity distribution (typically a Maxwellian distribution).

The incoherent scatter process is sometimes referred to as the *Thomson scattering* process, in reference to the notion that the received power at an ISR receiver is a sum of the radiated power of all of the plasma particles in the ionospheric scattering volume. The name also implies that the incident radio waves scatter off each and every particle in the plasma, which is not necessarily the case. For radar wavelengths that are larger that the λ_D of the plasma, the incident radar waves undergo coherent backscatter analogous to Bragg scattering. The backscattering is due to low amplitude plasma density fluctuations ever-present in the plasma. When the first ISR systems were brought online, it became quickly evident that σ for the ionosphere was largely determined by the electrons, and not the ions [*Gordon*, 1958; *Bowles*, 1958]. The electrons have much less inertia and therefore are more easily accelerated by the applied electric field (i.e., an incident radar wave). The opposite is true for the ions,

due to their large inertia. In order to undergo genuine incoherent scattering, the incident radar signal must be at a wavelength that is less than the λ_D. Despite the mislabelling, the incoherent scatter moniker remains – any radio wave scattering measured by an ISR is termed incoherent scattering, despite the proper definitions.

Guided by *Sheffield* [1975] and *Alcaydé* [2001] the interconnection between P_r, σ_e and n_e, T_e, ion temperature T_i, and the line-of-sight plasma velocity, v_{los} is now considered. The product of an incident electric field, E_i, scattering off of an electron in a volume, V, can be expressed as:

$$E_s = E_i \exp\left(i\omega_0 t - i\mathbf{k}_i \cdot \mathbf{r}_p(t)\right) \frac{\sigma_e \sin\chi}{|\mathbf{R}|} \exp\left(-i\mathbf{k}_s \cdot \mathbf{R}\right) \exp\left(i\mathbf{k}_s \cdot \mathbf{r}_p(t)\right), \tag{2.4}$$

in which E_s is the scattered electric field with wave vector, $\mathbf{k}_s$; ω_0 is the angular frequency of the incident electric field; $\mathbf{k}_i$ is the wave vector of E_i; $\mathbf{r_p}(t)$ is the position of the electron as a function of time, with respect to the origin; $|\mathbf{R}|$ is the magnitude of the vector between the observer (radio receiver) and the origin, $\mathbf{R}$; χ is the angle between $\mathbf{k}_i$ and $\mathbf{R}$; c is the speed of light; and

$$\sigma_e = \frac{q_e^2}{4\pi\epsilon_0} \frac{1}{m_e c^2}, \tag{2.5}$$

is the classical radius of the electron. The geometry of Equation 2.4 is shown in Figure 2.1.

For direct backscatter, $\mathbf{k}_i = -\mathbf{k}_s$. Now, taking the number of electrons, p, within the volume, V, each contributing a scattered electric field, Equation 2.4 becomes:

$$E_r = \frac{E_i \sigma_e \sin\chi}{R} \exp\left\{i(\,\omega_0 t - \frac{\omega_0}{c} R\,)\right\} \sum_p \exp\left(-2i\mathbf{k}_i \cdot \mathbf{r}_p(t)\right). \tag{2.6}$$

Now, the density of the electrons in the volume, V, can be expressed as:

$$n\left(\mathbf{r}, t\right) = \frac{1}{V} \sum_p \delta\left\{\mathbf{r} - \mathbf{r}_p(t)\right\}, \tag{2.7}$$

and taking a Fourier transform of both sides:

$$V \int n\left(\mathbf{r}, t\right) \exp\left(-i\mathbf{k} \cdot \mathbf{r}\right) d\mathbf{r} = \sum_p \int \delta\left\{\mathbf{r} - \mathbf{r}_p(t)\right\} \exp\left(-i\mathbf{k} \cdot \mathbf{r}\right) d\mathbf{r} \tag{2.8}$$

produces:

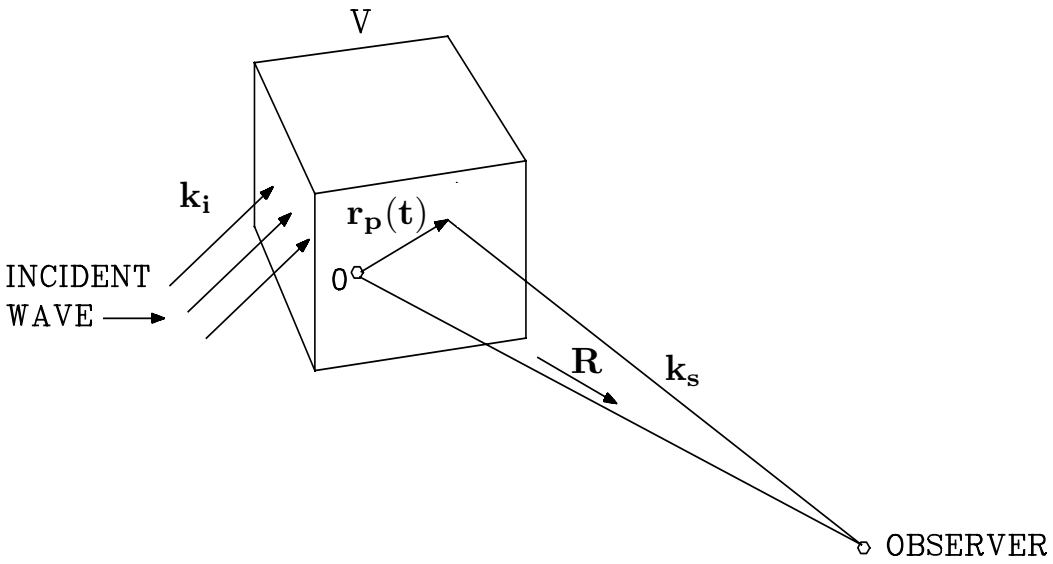

Figure 2.1: The scattering geometry of an incident electric field and electron inside a volume, V, reproduced from *Alcaydé* [2001].

$$Vn\left(\mathbf{k},t\right)=\sum_{p}\exp\left(-i\mathbf{k}\cdot\mathbf{r}_{p}\left(t\right)\right). \tag{2.9}$$

Since we are dealing with Bragg scattering, $\mathbf{k}=2\mathbf{k}_i$. Equation 2.9 can be inserted into Equation 2.6, producing:

$$E_r=n\left(\mathbf{k},t\right)\frac{E_i\sigma_e\sin\chi}{R}V\exp\left\{i\left(\omega_0 t-\frac{\omega_0}{c}R\right)\right\}. \tag{2.10}$$

The ISR (or any radar) receiver receives Equation 2.10, a modulated signal centered about the carrier frequency of the radar, ω_0, with an arbitrary phase shift added to it. However, notice that the density information is encoded in the amplitude; namely:

$$A_r\left(t\right)=n\left(\mathbf{k},t\right)\frac{E_i\sigma_e\sin\chi}{R}V. \tag{2.11}$$

In order to obtain any useful information from the received signal, such as range to the scattering volume, Doppler shift or phase of the signal, it must be compared to the original transmitted signal. This is performed via the autocorrelation function (ACF):

$$P_r(t)=\int A_r\left(t\right)\cdot A_t\left(t+\tau\right)dt. \tag{2.12}$$

in which A_t is the original, transmitted signal. Via the Wiener-Khinchin theorem, the Fourier transform of the above ACF is the power spectrum of the received signal:

$$P_r(\omega) = n_e P_e \phi(\mathbf{k}, \omega). \tag{2.13}$$

where n_e is the total number of electrons in the scattering volume, V; $P_e = \left(E_i^2 \sigma_e^2 \sin^2 \chi V^2\right)/R^2$ is the power received from the scatter from a single electron; and $\phi(\mathbf{k}, \omega)$ is the power spectrum of the electron density fluctuations in the scattering volume, as a function of the Doppler shift of the received signal, $\omega = \omega_0 - \omega_r$, in which ω_r is the received carrier frequency.

An important property of Equation 2.13 is that the received power, P_r, is directly proportional to the number of electrons in the scattering volume. Thus, by measuring the received power, ISR systems provide information about the plasma density within scattering volume, V. It should be noted that this is an extremely difficult measurement to make. The ISR scatter is very weak compared to the transmitted power of the ISR system. It is not unusual for P_r be 20 orders of magnitude less than P_t [P. J. Erickson, personal communication, 2014]. This excludes many radar systems from being able to measure P_r (including the SuperDARN system, which will be discussed shortly) since they simply do not have a sufficient power-aperture product to measured the weak scattering process [*Kelley*, 2013].

The other important feature of Equation 2.13 is the ISR spectrum, $\phi(\mathbf{k}, \omega)$. If we assume the collision frequency of the plasma is sufficiently small and of a single species composition then:

$$\phi(\mathbf{k}, \omega) = \frac{2\pi}{k}\left|1 - \frac{G_e\left(\frac{\omega}{k}\right)}{\epsilon\left(\frac{\omega}{k}\right)}\right|^2 f_{e0}\left(\frac{\omega}{k}\right) + \frac{2\pi}{k}\left|\frac{G_e\left(\frac{\omega}{k}\right)}{\epsilon\left(\frac{\omega}{k}\right)}\right|^2 f_{i0}\left(\frac{\omega}{k}\right), \tag{2.14}$$

where ϵ is the permittivity of the plasma; f_{i0} and f_{e0} are the velocity distribution of the ions and electrons, respectively. In this formula we are assuming that both exhibit a Maxwellian distribution. $G_e\left(\frac{\omega}{k}\right)$ and $G_i\left(\frac{\omega}{k}\right)$ are the electric susceptibility of the plasma for the ions and electrons such that $\epsilon\left(\frac{\omega}{k}\right) = 1 + G_e\left(\frac{\omega}{k}\right) + G_i\left(\frac{\omega}{k}\right)$. Since we are assuming that both the ions and electrons exhibit a Maxwellian velocity distribution, Equation 2.14 is recast to:

$$\phi(\mathbf{k}, \omega) = \frac{2\sqrt{\pi}}{ka}\left[\frac{\Gamma_e}{|\epsilon|^2} + \frac{\Gamma_i}{|\epsilon|^2}\right], \tag{2.15}$$

where:

$$\Gamma_e = \exp\left(-x_e^2\right)\left[\left(1+\alpha^2\frac{T_e}{T_i}\Re\{Z\left(x_i\right)\}\right)^2+\left(\alpha^2\frac{T_e}{T_i}\Im\{Z\left(x_i\right)\}\right)^2\right] \tag{2.16}$$

and

$$\Gamma_i = \sqrt{\left(\frac{m_i T_e}{m_e T_i}\right)}\exp\left(-x_i^2\right)\left[\left(\alpha^2\Re\{Z\left(x_e\right)\}\right)^2+\left(\alpha^2\Im\{Z\left(x_e\right)\}\right)^2\right]. \tag{2.17}$$

Furthermore, $|\epsilon|^2$ in the denominator is given by:

$$|\epsilon|^2 = \left[1+\alpha^2\left(\Re\{Z\left(x_e\right)\}+\frac{T_e}{T_i}\Re\{Z\left(x_i\right)\}\right)\right]^2+\left[\alpha^2\left(\Im\{Z\left(x_e\right)\}+\frac{T_e}{T_i}\Im\{Z\left(x_i\right)\}\right)\right]^2 \tag{2.18}$$

Here, $Z\left(x_e\right)$ and $Z\left(x_i\right)$ are the plasma dispersion functions for the ions and electrons, respectively, and [*Fried and Conte*, 1961]:

$$Z\left(x\right) = x\exp\left(-x^2\right)\left(i\sqrt{\pi}-2\int_0^x \exp\left(x'^2\right)dx'\right). \tag{2.19}$$

In Equations 2.16 and 2.17, $\alpha = 1/k\lambda_D$; x_i and x_e are the ratios of transmitted angular frequency, ω, and the thermal velocity of the ions and electrons:

$$x_i = \frac{\omega}{k}\sqrt{\frac{m_i}{2k_b T_i}}, \tag{2.20}$$

and

$$x_e = \frac{\omega}{k}\sqrt{\frac{m_e}{2k_b T_e}}. \tag{2.21}$$

There are some important features of the previous equations 2.14 which help provide a qualitative description of the ISR spectrum. Firstly, notice that for the $\alpha \ll 1$ case, $\Gamma_e \to \exp\left(-x^2\right)$, $|\epsilon|^2 \to 1$, and $\Gamma_i \to 0$. This is a high-frequency case; the probing wavelength of the radar, $\lambda \ll \lambda_D$. At this scale, the plasma does not undergo any collective motion. The electrons mimic a free electron gas. For $\lambda \gg \lambda_D$ the electrons provide the Debye shielding for the ions, and therefore their motion through the plasma is heavily influenced by the ions. The plasma displays collective motion. The ISR spectrum is different for each case.

In a high-frequency case the spectrum takes on a Gaussian shape with a broadening that is governed by the thermal properties of the plasma.

For cases in which $\alpha \gtrsim 1$ the contributions from the ions become more important. When $x_i > 1$ but small, the Γ_i term dominates in Equation 2.15. This is simply due to the fact that $x_i^2 \sim 1836 x_e^2$ – the mass ratio of a proton and electron (for a plasma in which $T_i = T_e$; for the O^+ dominated plasma in the F region, this ratio would be 16 times higher). A resonance peak occurs as $x_i \to x_{ac}$, the ion-acoustic peak; $|\epsilon|^2$ reaches a minimum at this point. The resonance peak is centered near the ion-acoustic velocity in the plasma. Ion-acoustic waves are analogous to sound waves in a neutral gas, and have a phase speed [*Chen*, 2010]:

$$v_s = \sqrt{\frac{k_b T_e + \gamma_i k_b T_i}{m_e + m_i}}, \tag{2.22}$$

in which $\gamma_i = 3$. This resonance peak is referred to as the "ion line" or the "ion-acoustic line". The amplitude of the resonance peak is determined by the ratios of the ion and electron mass, and ion and electron temperature in the plasma.

Lastly, for large values of x_e, $\Gamma_e \to \exp(-x_e^2)$, and $\Gamma_i \to 0$. However, unlike the scatter case described earlier, $|\epsilon|^2 \to 1 + \alpha^2 \Re\{Z(x_e)\}^2$. It can be shown that $1 + \alpha^2 \Re\{Z(x_e)\}^2$ is minimized when

$$\omega^2 \simeq \omega_p^2 + \frac{3}{2} k^2 v_{th_e}^2 \tag{2.23}$$

– the Bohm-Gross plasma dispersion relation, in which v_{th_e} is the thermal velocity of the electrons [*Chen*, 2010]. Thus, an additional notable feature of Equation 2.15 is the "plasma line", also known as the "electron line" – a peak at a Doppler frequency that is the sum of the plasma frequency, ω_p, and the Doppler frequency of the thermal electrons.

Equation 2.15 is plotted in both Figures 2.2 and 2.3, for an F-region plasma (O^+ is the main ion constituent) with $n_e = 1 \times 10^{11}$ m^{-3}, $T_i = 1000$ K, $T_e = 2000$ K (a range of T_e is plotted in Figure 2.3), for an ISR at a wavelength of 443 MHz. In the first, a log of the $\phi(\mathbf{k}, \omega)$ is given. This is done in order to show the relative positioning and magnitudes of the ion and electron lines (the spectrum is symmetric about $\omega = 0$). The ion line is centered at ~ 5700 Hz, a $v \simeq 1930$ m/s, which is the fluid ion-acoustic speed of $v_s = 1610$ m/s (according to Equation 2.22).

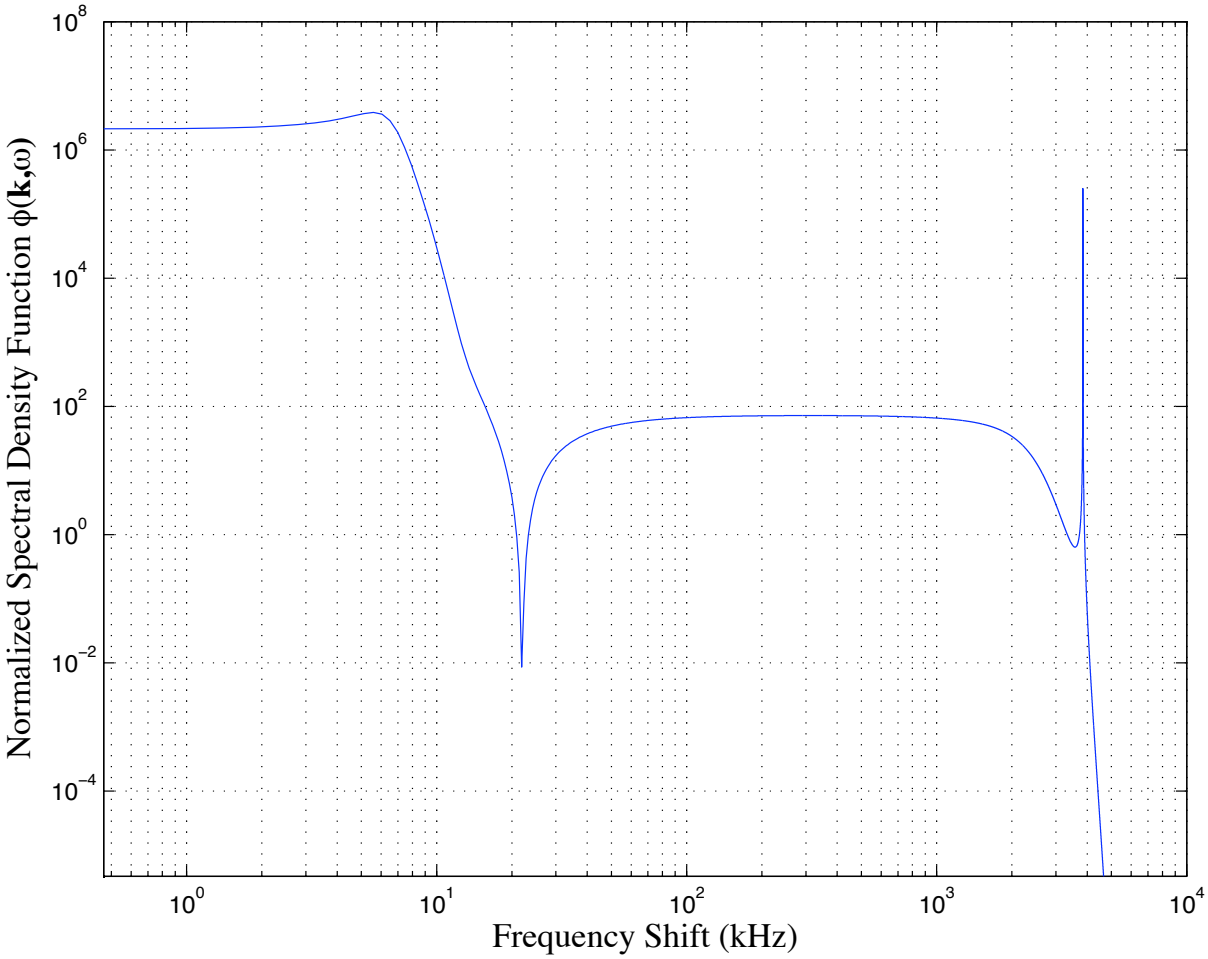

Figure 2.2: A log plot of $\phi(\mathbf{k}, \omega)$ for an ISR operating at 443 MHz, probing an O^+ plasma with $n_e = 1 \times 10^{11}$ m^{-3}, $T_i = 1000$ K, $T_e = 2000$ K. Code courtesy of P. Perron.

In Figure 2.3, the plot range is narrowed to focus on the ion lines – the "double-hump" spectrum. In practice, this feature is of most interest. For one, this spectrum provides a variety of information about the plasma being probed, e.g., plasma density and temperature. The electron lines are extremely difficult to detect in normal ISR operation, due to other complications not discussed here. They also only provide plasma density information, and not plasma temperature information. When the plasma lines cannot be measured an absolute plasma density measurement is unavailable. To obtain a density measurement without the plasma line, the ISR spectrum must be calibrated against another instrument which can provide plasma density information. A nearby ionosonde is typically used. In Figure 2.3,

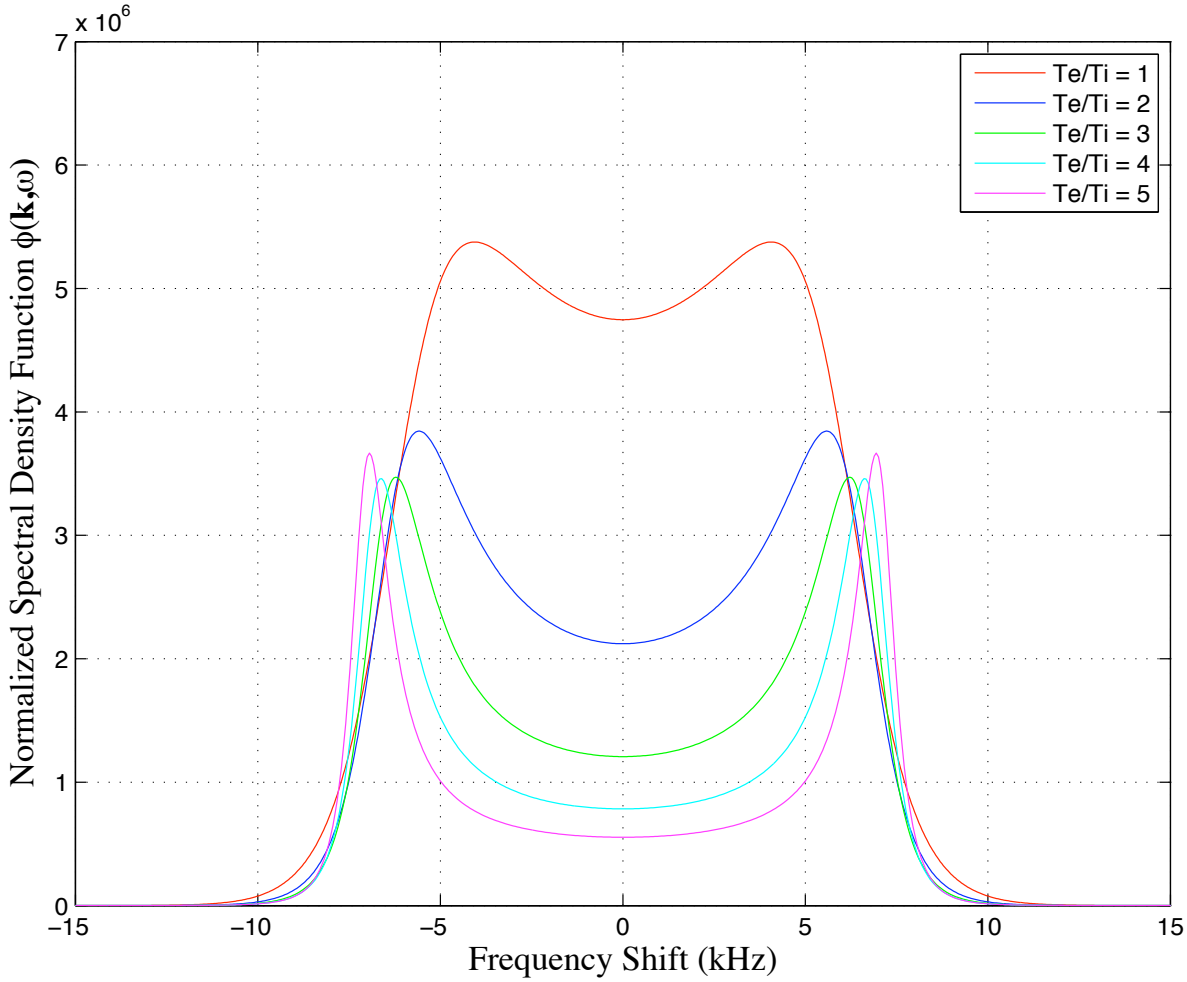

Figure 2.3: The ion lines of $\phi(\mathbf{k}, \omega)$ for an ISR operating at 443 MHz, probing an O^+ plasma with $n_e = 1 \times 10^{11}$ m^{-3}, $T_i = 1000$ K, $T_e = 1000,\ 2000,\ 3000,\ 4000$ and 5000 K. Code courtesy of P. Perron.

several profiles are plotted to show the variation of the ionic spectrum as a function of the ion and electron temperatures. The spectrum plotted in Figure 2.2 is plotted as $T_e/T_i = 2$ in Figure 2.3. As one can see, the valley in between the two ion line peaks becomes deeper as T_e/T_i increases. Other variations in the spectrum due to varying ion compositions and other effects also occur, but are not shown here.

Once a measurement of the double-hump spectrum, Figure 2.3, is obtained, calculating n_e via Equation 2.13 is relatively straightforward since n_e is a density proportional to the area under the curve in Figure 2.3. However, T_i and T_e factor into this estimate. Their influence

on the spectral shape is ascertained using fitting techniques – fitting the measured spectrum to a model of an expected ISR spectrum [M. J. Nicolls, personal communication, 2010]. An additional instrument, an ionosonde, is typically used to calibrate the ISR n_e measurements. v_{los}, the bulk plasma flow, is simply a measure of the offset of the spectrum from the centre frequency.

2.1.1 The Resolute Bay Incoherent Scatter Radar – North

The RISR–N system is an example of an Advanced Modular Incoherent Scatter Radar (AMISR) system [*Bahcivan et al.*, 2010]. There are currently two AMISR systems operational in the world. The first is located at Resolute Bay, Canada (74.7° N, 265.1° E, in geographic coordinates). A second AMISR system, RISR-Canada (RISR-C), is located at the same location in Resolute Bay, and was scheduled to begin operations in summer, 2014. The second operational AMISR system, the Poker Flat Incoherent Scatter Radar (PFISR) is located at Poker Flat, Alaska, in the United States (65.13° N, 212.53° E, geographic) [*Nicolls et al.*, 2007].

The RISR–N radar transmits ultra high frequency (UHF) radio waves, at 441.9 MHz, into the polar ionosphere. The system uses an ingenious method of electronic beam steering in order to obtain an "image" of the ionosphere. The first generation of ISRs feature large, fixed or steerable antenna dish with a single beam look direction. For these systems, it is time consuming to change the look direction of the radar, which may not be desirable for certain experiments. This can produce unwanted spatiotemporal ambiguities when processes in the ionosphere are changing more quickly than the steering rate of the radar dish. The AMISR class of radar systems overcome this by employing electronic beam steering techniques. Instead of a single radar dish, an AMISR system is composed of several thousand, stationary, double-dipole antennas, on a stationary face, as shown in Figures 2.4 and 2.5. The transmitted radar signal can be phased differently for each section of beams, allowing for the look direction of the radar to be changed rapidly, from radar pulse to radar pulse. This is known as electronic beam steering. As a result, the entire AMISR field-of-view can be sampled much more quickly than that of a single, steerable dish system, and on a time-scale that is of the order of the temporal characteristics of the ionosphere. A RISR-N mode with

Figure 2.4: The RISR-N system at Resolute Bay, Canada. Photo courtesy of C. Heinselman.

Figure 2.5: A closer view of the RISR-N face, showing some of the many thousands of antennas. Photo courtesy of C. Heinselman.

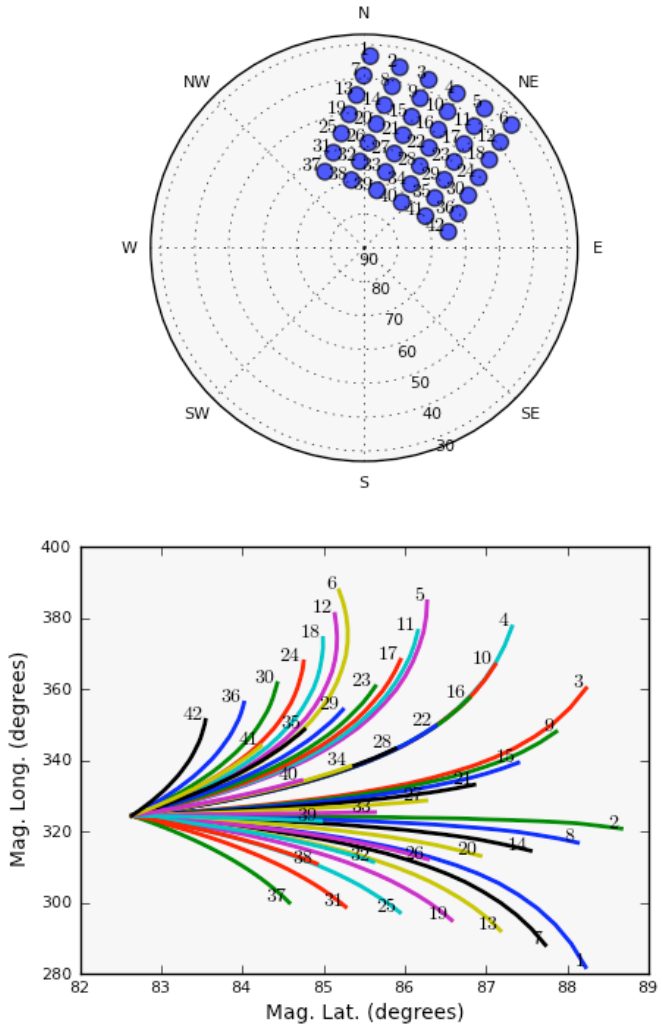

Figure 2.6: A plot of a 42-beam RISR-N mode (top), with the projections of the 42 look directions plotted in a geomagnetic coordinate system (bottom), courtesy of SRI International.

42 beams, configured in a rectangular, 6×7 grid, is plotted in Figure 2.6 with the geographic coordinate direction. Concentric circles indicate elevation contours from the zenith. In the bottom-half of Figure 2.6 the look directions of the beams are plotted with respect to a geomagnetic coordinate system.

2.2 Coherent Scatter Radar

HF radar signals transmitted into the ionosphere may undergo coherent backscatter in both the E and F region. Like an ISR scattering process, an HF transmitted signal backscatters off of plasma density irregularities with spatial scales that satisfy the Bragg scattering condition. The main difference between the ISR and coherent backscattering is the amplitude of the density irregularities and therefore the amplitude of the backscatter signal is much larger in the latter. Whereas the ISR cross section is linked to small amplitude irregularities due to the thermal fluctuations in the plasma, the HF cross section is established by large amplitude field-aligned irregularities attributed to plasma instability mechanisms, such as the gradient-drift instability (GDI). Overall, in order to receive backscattered HF signal, or "echo", two conditions must be met: plasma density irregularities must be present in the radar beam and the HF radar signal must undergo sufficient refraction to backscatter off field-aligned irregularities. This is a result of the nature of the irregularities in the F-region ionosphere, of which the GDI is regarded as the primary source. This will be discussed in detail shortly.

2.2.1 HF propagation

For a plasma immersed in a magnetic field, such as the E- and F-region ionosphere, the index of refraction, n, is described by the *Appleton-Hartree equation* [*Hargreaves*, 1992; *Appleton and Builder*, 1933; *Hartree*, 1929]:

$$n^2 = 1 - \frac{X}{1 - iZ - \left[\frac{Y^2 sin^2\theta}{2(1-X-iZ)}\right] \pm \sqrt{\left[\frac{Y^4 sin^4\theta}{4(1-X-iZ)^2} + Y^2 cos^2\theta\right]}}, \tag{2.24}$$

in which $X = \omega_p^2/\omega_0^2$, where ω_0 and ω_p are the probing and plasma frequencies, respectively; $Y = \omega_B/\omega_0$, where ω_B is the gyrofrequency of the electron; θ the angle of incidence of an HF ray with respect to the magnetic field; and $Z = \nu/\omega_0$, where ν is the electron collision frequency.

For the HF radio band, 3 MHz $\leq \omega_0/2\pi \leq$ 30 MHz, and in the ionosphere, $\omega_0 \gg \omega_B$, thus Equation 2.24 can be reduced to that of an unmagnetized and collisionless plasma; namely, $\nu \ll \omega_B$ above 100 km altitude:

$$n^2 \simeq 1 - \frac{\omega_p^2}{\omega_0^2} \simeq 1 - \frac{f_p^2}{f_0^2}. \tag{2.25}$$

As mentioned in Section 1.4, ω_p^2 undergoes a diurnal variation in the F-region. Other variations may occur due to enhanced geomagnetic conditions or localized, particle precipitation. To first order, in the polar F-region, 4 MHz $\leq f_p \leq$ 8 MHz [*Moen et al.*, 2008]. If the HF signal probing the ionosphere has a frequency $f_p = 10$ MHz, then $0.60 \leq n \leq 0.92$, in general.

Equation 2.25 has significant consequences for HF radio waves propagating through the ionosphere. Taking *Snell's Law* into consideration, HF propagation – and more specifically – HF refraction play a vital role in HF coherent backscatter [e.g., *Gillies et al.*, 2009; *Gillies et al.*, 2012, and references therein]. In essence, the ionosphere acts as a stratified medium in which the plasma density, and therefore n varies in altitude. An incident HF radio wave will propagate and refract through the ionosphere, according to Snell's Law. This is illustrated Figure 2.7. Here, a 2-D trace in altitude and latitude of the propagation of several HF radar beams transmitted at $f = 12.0$ MHz is shown, with several different incident angles from a single point (on the left side of the figure), into a model of the terrestrial ionosphere, with an index of refraction, n, that varies with altitude. The interface between the neutral atmosphere ($n_{air} \simeq 1$) and the ionosphere is just below 100 km altitude. Since, $n_{air} \geq n$ at the interface, the incident HF radio wave is refracted away from the normal, in accordance with Snell's Law; the HF beam becomes more horizontal. Some rays refract towards the vertical. This is a result of the stratification of the ionosphere and the fact that the ray is transmitting into a layer of the ionosphere with a larger index of refraction at those points, unlike the transition from n_{air} to n at the bottom of the ionosphere.

With the appropriate ionospheric conditions, the phase front of an HF radio wave may turn downward in the ionosphere, be refracted, and propagate back towards the surface of the Earth as shown in Figure 2.7. The refracted HF wave may then reflect from the surface of the Earth, and re-enter the ionosphere. This is an important property of HF propagation, and is a distinct advantage of HF radar systems. Essentially, an HF radar can "hop" its radio waves over large geographic regions, extending its field-of-view beyond the line-of-sight range. This also provides a more subtle advantage to using HF radio waves for studying the ionosphere. The plasma density irregularities comprising the HF radar backscatter cross-

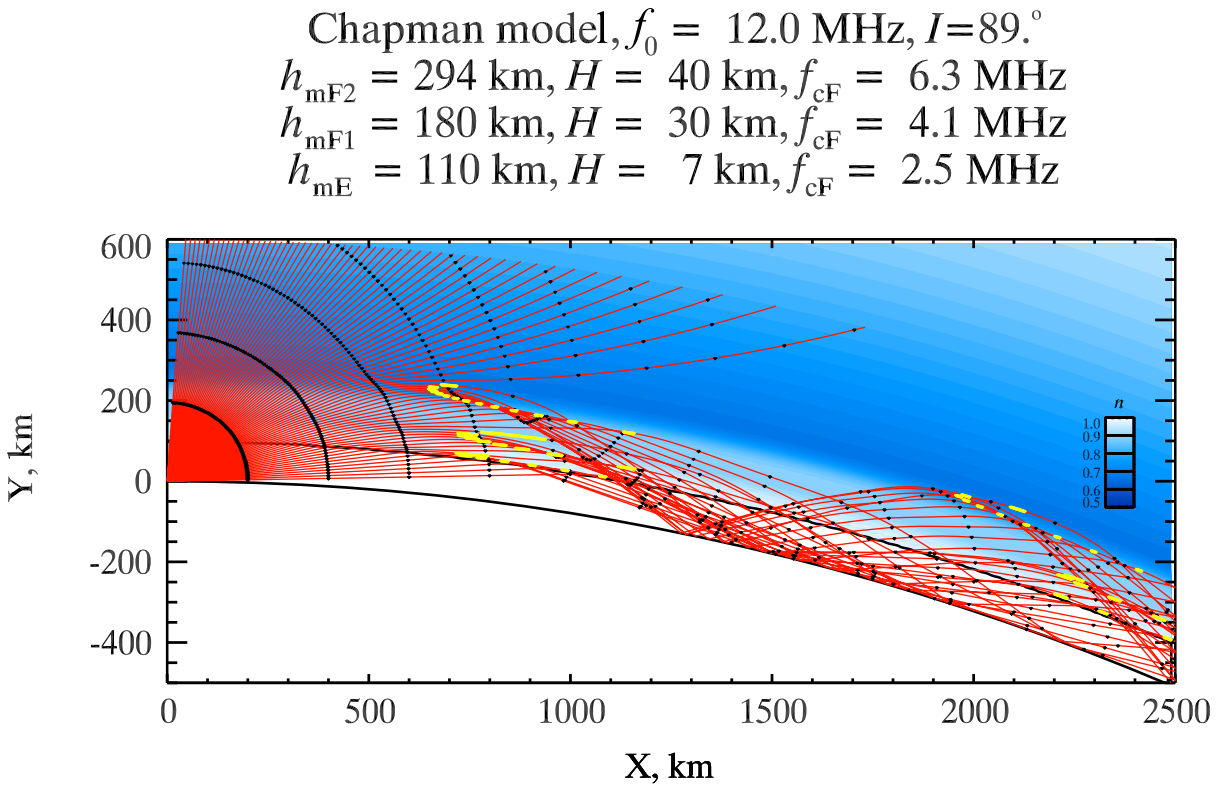

Figure 2.7: From *Bahcivan et al.* [2013], a plot of an HF ray trace model for a modelled ionosphere. Ray tracing model courtesy of P. Ponomarenko.

section are strongly field-aligned; that is, their growth is perpendicular to the geomagnetic field lines (described in more detail shortly). To satisfy the Bragg scattering condition, the incident HF radio wave must have a nearly negligible angle of incidence with respect to the geomagnetic field lines. In the polar region, the geomagnetic field lines are nearly vertical with respect to the surface of the Earth. Since HF radio wave undergo a significant amount of refraction as they propagate through the ionosphere, they are able to satisfy the Bragg condition at several locations along the propagation path – extending the coverage for studying HF coherent backscatter, beyond the line-of-sight regime. In Figure 2.7, points along the HF ray path in which the incident ray satisfies the aspect angle condition are marked in yellow.

2.2.2 The Gradient-Drift Instability

Focus is now placed on the mechanism behind the processes responsible for the decametre (HF band) plasma density irregularities in the F-region ionosphere. The theoretical underpinning of the HF, coherent scattering process is not as well developed as that of the ISR scattering process. Nonetheless, it is generally believed that the gradient-drift instability (GDI) is the main mechanism behind backscattering at HF frequencies [*Simon*, 1963; *Cerisier et al.*, 1985].

The GDI occurs due to naturally occurring plasma density gradients. Consider a plasma that has a density gradient, ∇N, immersed in an electric and magnetic field, $\mathbf{E}_0$ and $\mathbf{B}$ which impart an $\mathbf{E}_0 \times \mathbf{B}$ drift velocity field in the direction of x, as illustrated in Figure 2.8. If a plasma perturbation develops, plasma protruding into a region of higher density plasma will develop a polarization electric field, $\mathbf{E}_p$, in the direction of the ambient electric field, $\mathbf{E}_0$, along y, while plasma moving into a less dense region will develop a polarization electric field in the opposite direction, along $-y$. When the ions encounter a perturbation introducing a less dense plasma with a lower conductivity the ion drift will decrease, creating a charge build-up. The opposite occurs when the ions encounter a denser plasma with a higher conductivity as illustrated in Figure 2.8. A result of the polarization field is a $\mathbf{E}_p \times \mathbf{B}$ drift that will develop either in the $+x$ or $-x$ direction. The drift will push less (more) dense plasma into a region of higher (lower) density. A positive feedback instability ensues. In the case of a large density enhancement moving in the $-x$ direction, it is pushed further along due to diffusion and pressure gradients. The perturbation is amplified due to the larger density gradients (between the invading plasma and the ambient plasma), thereby increasing conductivity gradients and increasing the polarization electric field, pushing the protrusion even farther in the $-x$ direction, etc..

A very thorough quantitative description of the GDI operating in the F-region ionosphere is given by *Keskinen and Ossakow* [1982], which is also applicable to the polar ionosphere. In it, the GDI is described by the dispersion relation $\tilde{\omega} = \omega_r - i\gamma$, in which the growth rate, γ, for a plasma density perturbation with a wavevector $\mathbf{k} = k_x\hat{\mathbf{x}} + k_y\hat{\mathbf{y}} + k_z\hat{\mathbf{z}}$ is given by:

$$\gamma = \cos\alpha \frac{\frac{\nu_{ei}}{\Omega_e}\frac{1}{L}\left(\frac{\nu_{in}}{\Omega_i}\frac{E_0}{B}\cos(\alpha-\beta) + \theta V_d\right)}{\theta^2 + \frac{\nu_{in}}{\Omega_i}\frac{\nu_{ei}}{\Omega_e}} - D_\perp k_y^2 - D_\parallel k_z^2 \tag{2.26}$$

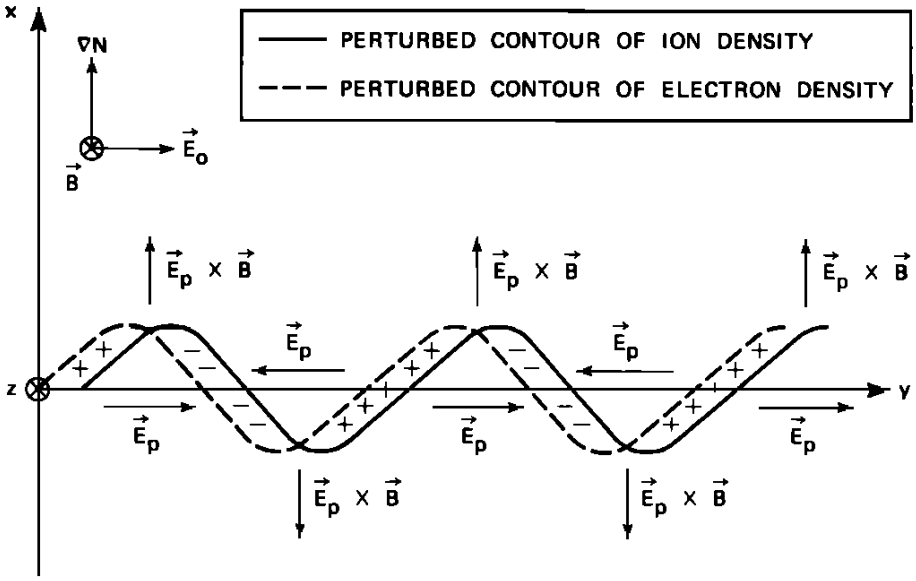

Figure 2.8: From *Tsunoda* [1988], an illustration of the GDI, in which $\gamma > 0$, the system is unstable. If $\mathbf{E}_0$ is reversed, $\gamma < 0$ and the system becomes stable.

with respect to the geometry presented in Figure 2.8. In Equation 2.26, $\mathbf{E}_0 = E_0 \sin\beta\hat{\mathbf{x}} + E_0 \cos\beta\hat{\mathbf{y}}$; $\hat{\mathbf{k}}_\perp = \sin\alpha\hat{\mathbf{k}}_x + \cos\alpha\hat{\mathbf{k}}_y$; $\theta = k_z/k_y$; $\mathbf{V}_d = (v_0 - V_0)\hat{\mathbf{z}}$ is the differential velocity of the ions and electrons along the magnetic field line; ν_{in} and ν_{ei} are the ion-neutral and electron-ion collision frequencies, respectively; Ω_i and Ω_e are the ion and electron gyrofrequencies, respectively; $1/L = (1/n_0)(\partial n_0/\partial y)$ is the plasma density scale length; B is the magnitude of the magnetic field; and, $D_\perp$ and $D_\parallel$ are the perpendicular and parallel diffusion coefficients with respect to the magnetic field.

Plasma irregularities, i.e., the GDI protrusions, grow when $\gamma > 0$; however, this is strongly dependent on the orientation of the plasma density perturbations and the ambient electric field with respect to the density gradients. For a situation in which $\beta = 0$ and $\alpha = 0$ or 180° (i.e., Figure 2.8) *Keskinen and Ossakow* [1982] analyzed the maximum growth rate for γ in terms of θ; namely, $\partial\gamma/\partial\theta|_{\theta=\theta_m} = 0$ for

$$\theta_m = \frac{\nu_{in}}{\Omega_i}\frac{E_{0y}}{BV_d} \pm \sqrt{\left(\frac{E_{0y}}{BV_d}\right)^2\left(\frac{\nu_{in}}{\Omega_i}\right)^2 + \left(\frac{\nu_{ei}\nu_{in}}{\Omega_e\Omega_i}\right)}, \tag{2.27}$$

in which $E_{0y} = E_0\hat{\mathbf{y}}$ is the magnitude of the ambient electric field. They used numbers which are applicable to the polar-ionosphere: $\nu_{in}/\Omega_i \simeq 10^{-4}$, $\nu_{ei}/\Omega_e \simeq 10^{-4}$, $E_{0y} \simeq 10$ mV/m,

$j_\parallel = n_0 e V_d \simeq 1\ \mu\text{A/m}^2$, $B = 0.5 \times 10^{-4}$ T, $n_0 \simeq 10^{11}$ m^{-3}, which gave $\theta_m = 10^{-4}$, meaning that the growth rate γ is maximized in a direction that is perpendicular the magnetic field – the GDI is strongly field-aligned. Consequently, the following approximation is commonly used:

$$\gamma|_{\theta=0} = \frac{E_0}{BL} = \mathbf{v} \cdot \nabla \ln n_0, \tag{2.28}$$

in which $\mathbf{v}$ is the plasma drift velocity. The plasma is unstable, $\gamma > 0$, in regions where the $\mathbf{v} \cdot \nabla N > 0$, and stabilized, $\gamma < 0$, in regions in which $\mathbf{v} \cdot \nabla N < 0$. The first case is one which was described previously and illustrated in Figure 2.8. One can construct the opposite case, in which $\mathbf{v} \cdot \nabla N < 0$ and $\gamma < 0$, by switching the direction of the plasma drift in Figure 2.8, from the $+y$ to $-y$ direction. As a result, the directions of $\mathbf{E}_p$ will be flipped as well. The initial protrusion of less dense plasma along the $+x$ direction will be halted and reversed by the $\mathbf{E}_p \times \mathbf{B}$–drift; the same will occur for the denser plasma protrusion.

An important property to note is that, on average, the irregularities produced by the GDI will move at the same speed as the ambient plasma flow in the F region. This was verified experimentally by *Ruohoniemi et al.* [1987]. It is also important to note that the theory described by Equations 2.26 and 2.27 is a first order, linear theory. Other non-linear theories exist which account for the subtler properties of E- and F-region plasma density irregularities observed [e.g., *Fejer et al.*, 1975; *Kelley*, 2009, and references therein]. Nonetheless, the linear theory is sufficient for studying the irregularities encountered in this work, including F-region ionization patches in the polar ionosphere [e.g., *Tsunoda*, 1988; *Hosokawa et al.*, 2013b].

2.2.3 SuperDARN

SuperDARN [*Chisham et al.*, 2007; *Greenwald et al.*, 1995] is a network of HF coherent scatter radars located at mid-, auroral-, and polar-latitudes, in both the northern and southern hemispheres. A map of the current operational SuperDARN radar sites with their nominal fields-of-view is given in Figures 2.9 and 2.10, respectively. Tables 2.1 and 2.2 give a brief description of each operational radar in the northern and southern hemispheres. Subsets of the SuperDARN carry their own moniker, for example, the SuperDARN radars at Inuvik,

Rankin Inlet and Clyde River are collectively referred to as the Polar Dual Auroral Radar Network (PolarDARN).

Each individual SuperDARN radar measures HF backscatter from the E- and F-region ionosphere over a vast geographic region. This is accomplished by using the ability of HF radio waves to propagate beyond the line-of-sight range (see Section 2.2.1) to provide an extended FOV radially, combined with the electronic beam steering capability of each radar to expand the field-of-view azimuthally. The result is a triangle shaped field-of-view coverage, as shown in Figures 2.9 and 2.10. Each radar site also has a secondary, passive array of antennas that provides interferometric information providing an angle-of-arrival measurement of the received radar echo.

An individual SuperDARN system implements similar radar techniques to those of an ISR, to provide information about the plasma in the scattering volume; that is, an ACF is constructed by transmitting and receiving HF radio waves into the ionosphere (e.g., Equation 2.12). The line-of-sight Doppler shift of the plasma is estimated from the rate of change of the phase of the received radar signal with respect to time. However, unlike an ISR system, which can provide information about the state parameters of the ionosphere, the only information that can be retrieved from the SuperDARN ACF is the backscatter power of the received echo (the square of the amplitude of the ACF), a function of the amplitude reflection coefficient of the plasma [G. J. Sofko, personal communication, 2012]; and, the spectral width, which is linked to the turbulence of the plasma [*Villain et al.*, 1996], and measured as the decorrelation time of the ACF.

Beyond a certain range from the radar site the HF beams penetrate into the F region; it is assumed that the radar echoes received originate from the F region, and are due to coherent backscatter from field-aligned irregularities drifting at the $\mathbf{E} \times \mathbf{B}$ velocity [*Ruohoniemi et al.*, 1987]. In Figure 2.7, this occurs as close as 600 km downrange from the radar. The yellow markings indicate that the aspect angle condition for coherent backscatter is satisfied at these ranges – the k-vector of the radar wave is perpendicular to the geomagnetic field line. If one wants to make sure that echoes being investigated are only from the F region, the typical practice is to simply only consider echoes from beyond 750 km range. For this work we are only concerned with F-region echoes since they only drift at the $\mathbf{E} \times \mathbf{B}$. At lower altitudes,

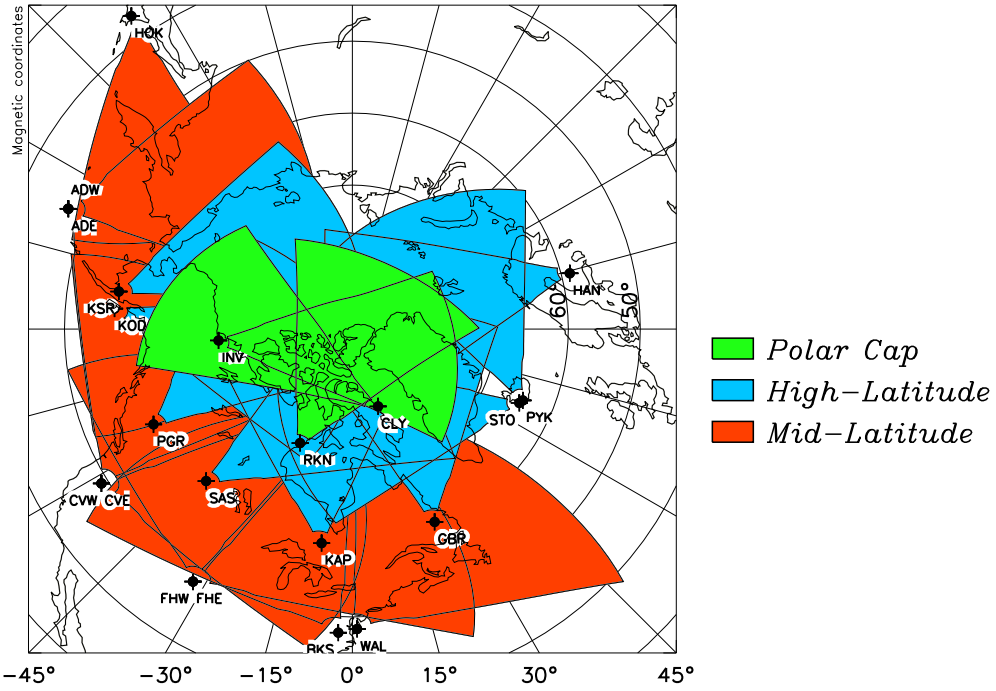

Figure 2.9: The individual fields-of-view of the radar sites comprising the SuperDARN in the northern hemisphere, in geomagnetic polar coordinates. Plot courtesy of Virginia Tech SuperDARN.

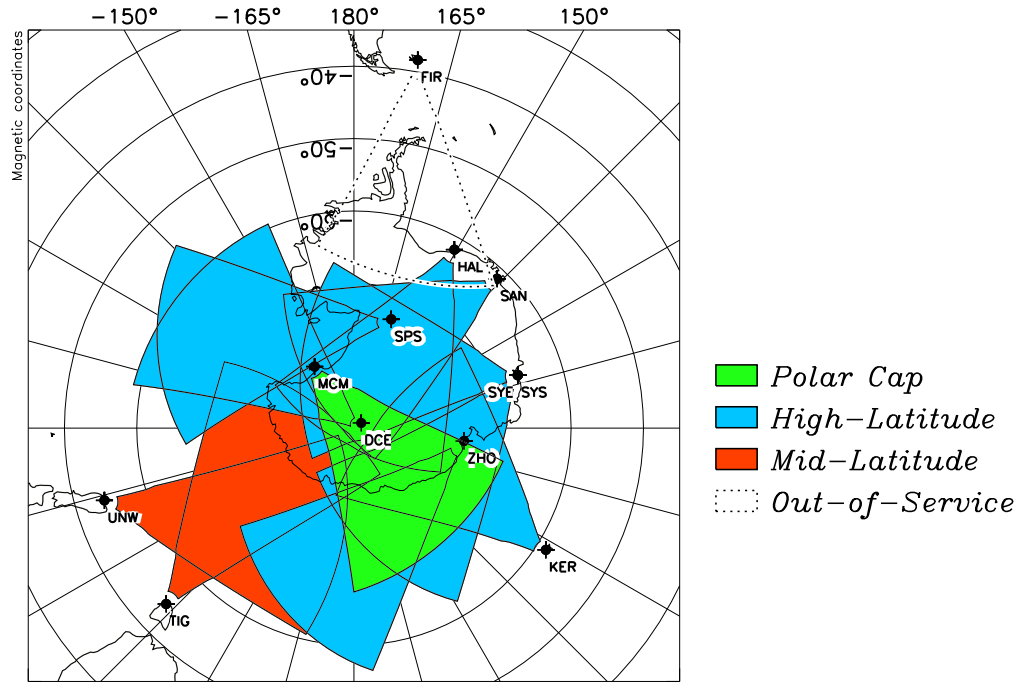

Figure 2.10: The individual fields-of-view of the radar sites comprising the SuperDARN in the southern hemisphere, in geomagnetic polar coordinates. Plot courtesy of Virginia Tech SuperDARN.

Radar Name	Code	Latitude	Longitude	Boresite
Adak Island East	ADE	51.88°	-176.62°	31.60°
Adak Island West	ADW	51.88°	-176.62°	-34.20°
Blackstone	BKS	37.10°	-77.95°	-41.50°
Christmas Valley East	CVE	43.27°	47.66°	40.2°
Christmas Valley West	CVW	43.27°	47.66°	-31.20°
Clyde River	CLY	70.49°	-68.50°	-42.50°
Fort Hays East	FHE	38.86°	-99.39°	41.30°
Fort Hays West	FHW	38.86°	-99.39°	-32.30°
Goose Bay	GBR	53.32°	-60.46°	11.00°
Hankasalmi	HAN	62.32°	-26.61°	1.50°
Hokkaido	HOK	43.53°	143.61°	23.90°
Inuvik	INV	68.42°	-133.50°	4.40°
Kapuskasing	KAP	49.39°	-82.32°	15.30°
King Salmon	KSR	58.68°	-156.65°	-31.30°
Kodiak	KOD	57.62°	-152.19°	11.9°
Pykkvibaer	PYK	67.77°	-20.54°	40.20°
Prince George	PGR	53.98°	-122.59°	-16.20°
Rankin Inlet	RKN	62.82°	-93.11°	1.80°
Saskatoon	SAS	-52.16°	-106.53°	16.90
Stokkseyri	STO	63.86°	-22.02°	-33.00°
Wallops Island	WAL	37.93°	-75.47°	46.70°

Table 2.1: A table of the geographic locations of the SuperDARN radars in the northern hemisphere. The boresite is the pointing direction of the radar at the midpoint of its FOV. Table information courtesy of Virginia Tech SuperDARN.

Radar Name	Code	Latitude	Longitude	Boresite
Dome C	DCE	-75.09°	123.35°	-105.5°
Halley	HAL	-75.52°	-26.63°	174.10°
Kerguelen	KER	-49.22°	70.14°	-163.00°
McMurdo	MCM	-77.88°	166.73°	-148.20°
Sanae	SAN	-71.68°	-2.85°	-162.40°
South Pole Station	SPS	-89.995°	118.29°	-20.30°
Syowa East	SYE	-69.00°	39.58°	143.00°
Syowa South	SYS	-69.00°	39.58°	-157.70°
Tiger	TIG	-43.40°	147.20°	169.40°
Unwin	UNW	-46.51°	168.38°	-152.20°
Zhongshan	ZHO	-69.38°	76.38°	123.50°

Table 2.2: A table of the geographic locations of the SuperDARN radars in the southern hemisphere. The boresite is the pointing direction of the radar at the midpoint of its FOV. Table information courtesy of Virginia Tech SuperDARN.

in the E region, those irregularities do not necessarily have the same drift properties. In Figure 2.7, one can see that there are some yellow markings over a wide range of altitudes, indicating that SuperDARN radar receives scatter from both the E and F region, at distances where only the latter is expected. There is some experimental evidence to support this notion, [e.g., *Bahcivan et al.*, 2013, and references therein], but it is beyond the scope of this work.

Some echoes received by SuperDARN are considered "ground scatter", a product of the HF beam refracting and backscattering off of the surface of the Earth (see Figure 2.7). These echoes have a distinct spectral width that is very small since the scattering target which they are backscattering from – the ground – has a very large decorrelation time. Ground scatter echoes also have very low Doppler velocity magnitudes, since the ground is not moving. These two properties allow for ground scatter echoes to be easily identified and segregated from other SuperDARN coherent echoes from the ionosphere. Ground scatter echoes can

be used to infer other ionospheric phenomena [e.g., *Ponomarenko et al.*, 2005, 2010, and references therein].

Arguably the most important measurement a SuperDARN system provides (notwithstanding an echo itself) is the line-of-sight Doppler velocity measurement. *Villain et al.* [1985]; *Ruohoniemi et al.* [1987] showed that the phase velocity of F-region irregularities measured by an HF coherent radar travel at the bulk flow velocity of the F-region plasma; namely, the Doppler shift of the coherent backscatter signal is equivalent to the $\mathbf{E} \times \mathbf{B}$ drift. This property has very important implications for SuperDARN and measuring the high-latitude plasma convection flows. The irregularities, for example those produced by the GDI, act as tracers for the plasma flows. If the phase velocity of the irregularity can be measured, then the electric field driving the $\mathbf{E} \times \mathbf{B}$ plasma flows can be measured as well. Next, the method of obtaining accurate velocity information is discussed.

SuperDARN merge technique

SuperDARN offers a real advantage for studying the F-region ionosphere when the Doppler velocity measurements from multiple radars with overlapping fields-of-view (as see in Figures 2.9 and 2.10) are considered. A single SuperDARN radar can only provide line-of-sight Doppler velocity information. By adding a second radar with a field-of-view that overlaps with the first, information from both radars can construct a horizontal plasma flow vector; hence, the "Dual" in SuperDARN. This is illustrated in Figure 2.11, which shows how the horizontal flow vector, $\mathbf{v}$, is constructed. With two line-of-sight velocity measurements, $\mathbf{v_1} = \mathbf{v} \cdot \hat{\mathbf{k}_1}$ and $\mathbf{v_2} = \mathbf{v} \cdot \hat{\mathbf{k}_2}$, with unit wave vectors $\hat{\mathbf{k_1}}$ and $\hat{\mathbf{k_2}}$, respectively, measured by two SuperDARN radars, the horizontal flow vector $\mathbf{v}$ can be solved by recognizing that [*Cerisier and Senior*, 1994; *Chisham et al.*, 2002; *Fiori*, 2011]:

$$\mathbf{v} = a\hat{\mathbf{k}_1} + b\hat{\mathbf{k}_2}, \tag{2.29}$$

in which a and b are coefficients. They can be calculated by solving the following system of equations:

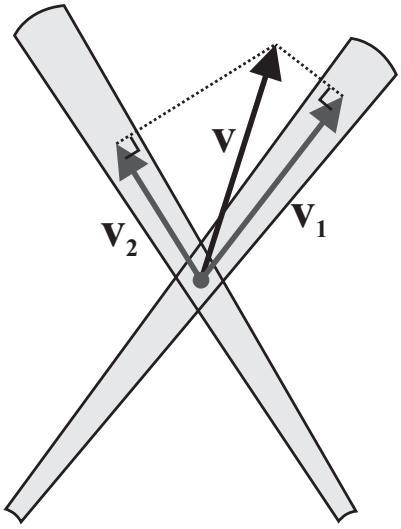

Figure 2.11: From *Fiori* [2011], a depiction of merging two line-of-sight velocity measurements from two SuperDARN radars, into a merged velocity vector.

$$v_1 = a + b\left(\hat{\mathbf{k}_2} \cdot \hat{\mathbf{k}_1}\right)$$
$$v_2 = a\left(\hat{\mathbf{k}_1} \cdot \hat{\mathbf{k}_2}\right) + b,$$

giving:

$$\mathbf{v} = \frac{\left[v_1 - v_2\left(\hat{\mathbf{k_1}} \cdot \hat{\mathbf{k_2}}\right)\right]\hat{\mathbf{k_1}} + \left[v_2 - v_1\left(\hat{\mathbf{k_1}} \cdot \hat{\mathbf{k_2}}\right)\right]\hat{\mathbf{k_2}}}{1 - \left(\hat{\mathbf{k_1}} \cdot \hat{\mathbf{k_2}}\right)^2}. \tag{2.30}$$

The process of combining dual velocity measurements in this way is referred to as the SuperDARN "merge technique". The technique is a robust method of determining the F-region plasma flow in a localized region. However, it can only be used in regions where data from two SuperDARN radars overlaps, which is less common. To rectify this, and to obtain velocity measurements on a global scale the velocity information from many more SuperDARN radars – such as all of those shown in Figures 2.9 or 2.10 – must be used. A more sophisticated technique is required.

SuperDARN FIT technique

In an effort to study the global convection patterns in each hemisphere, *Ruohoniemi and Baker* [1998] introduced the SuperDARN "FIT' technique. All SuperDARN line-of-sight velocity measurements in a hemisphere are placed onto a grid, projected onto a spherical geometry of the Earth within the boundaries of latitude poleward of the auroral oval. The problem of turning the gridded line-of-sight velocity measurements into a global map of plasma flow vectors is one of solving Laplace's equation in spherical coordinates [*Ruohoniemi and Baker*, 1998; *Fiori*, 2011]:

$$\nabla^2 \Phi = 0, \tag{2.31}$$

in which Φ is the electrostatic potential, and related to the electric field:

$$\mathbf{E} = -\nabla \Phi, \tag{2.32}$$

which is of course related to the $\mathbf{E} \times \mathbf{B}$ convection velocity, $\mathbf{v}$:

$$\mathbf{v} = \frac{-\nabla \Phi \times \mathbf{B}}{B^2}. \tag{2.33}$$

A solution to Equation 2.31 in spherical coordinates may be expressed as:

$$\Phi(\theta, \phi) = \sum_{k=0}^{k_{max}} \sum_{m=0}^{k} \left[A_{km} \cos(m\phi) + B_{km} \sin(m\phi) \right] P_k^m (\cos(\theta)), \tag{2.34}$$

in which P_k^m are the associated Legendre polynomials of degree k and order m; k_{max} is the maximum degree of the Legendre polynomial, θ and ϕ are the geomagnetic colatitude and longitude, respectively. A_{km} and B_{km} are coefficients solved for a given set of boundary conditions by minimizing [*Ruohoniemi and Baker*, 1998; *Fiori*, 2011]:

$$\chi^2 = \sum_{i=1}^{N} \frac{1}{\sigma_i^2} \left(\mathbf{v}_i \cdot \hat{\mathbf{k}}_i - v_{los_i} \right)^2, \tag{2.35}$$

which is the familiar χ^2 expression for N line-of-sight velocity measurements, $\mathbf{v}_{los_i}$, which have a variance σ_i. $\mathbf{v}_i$ is a fitted velocity vector projected onto the line-of-sight of a radar via $\mathbf{v}_i \cdot \hat{\mathbf{k}}_i$. In essence, SuperDARN $\mathbf{v}_{los}$ measurements are used to constrain the solutions to

Equation 2.31. The solution is an electrostatic potential for the auroral and polar-latitude regions. For areas that do not contain any SuperDARN line-of-sight velocity measurements, artificially gridded velocity vectors derived from historic SuperDARN data sets and other instruments are used as constraints [e.g., *Ruohoniemi and Greenwald*, 1996; *Shepherd and Ruohoniemi*, 2000; *Ruohoniemi and Greenwald*, 2005].

The product of the SuperDARN fitting technique is a global convection map, which provides a snapshot in time of the global $\mathbf{E} \times \mathbf{B}$ convection pattern, in both the northern and southern hemispheres. Convection maps may be generated on a time scale as quick as 1-minute. A plot of a convection map in the northern hemisphere, in polar geomagnetic coordinates, from October 2, 2013 is given in Figure 2.12. The derived velocity vectors are a straight line with a point denoting the base of the vector. The merged velocity measurements from each radar are shown in Figure 2.13 to illustrate the advantage of using the fit technique over the merged velocity vector technique, to infer global convection field. Both plots were generated using data from some of the radars in the northern hemisphere, shown in Figure 2.9, i.e., those that were in operation at the time the data was collected.

In Figures 2.12 and 2.13, information regarding the orientation of the IMF is given, along with other quantities (which are not discussed in this work) including: the polar cap potential, Φ_{pc}; the "Heppner and Maynard Boundary", Λ_{HM} [*Shepherd and Ruohoniemi*, 2000; *Heppner and Maynard*, 1987], which is plotted as a black and green line equatorward of the data; the number of radars used to produce the map N_{rads}; and the number of velocity vectors plotted in the map, N_{VC}. The convection equipotential contours derived from the SuperDARN fit technique are shown in both plots. By comparing the two plots, it is clear that the merge technique is unable to produce velocity flow vectors that show the large scale structure of the auroral and high-latitude convection flows. This is simply due to the fact that there was not enough overlap of SuperDARN echoes in much of the northern hemisphere for the merge technique to be very effective. However, since the fit technique does not require overlap between echoes, it is able to provide a more detailed estimate of the convection flows in the high-latitude and polar-cap regions. The structuring in these convection flows is very important to study as they relate to plasma structuring and dynamics in the near-Earth geospace, since electric fields map along magnetic field lines.

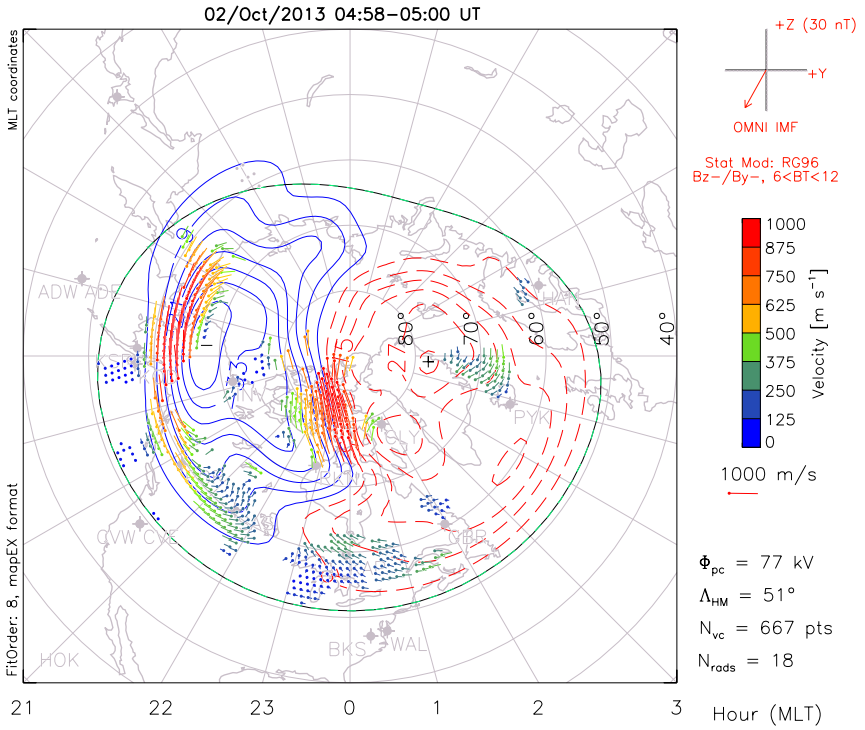

Figure 2.12: A convection plot of the northern hemisphere for 5:00 UT, Ocotber 2, 2013, generated using the SuperDARN fit technique. Plot courtesy of Virginia Tech SuperDARN.

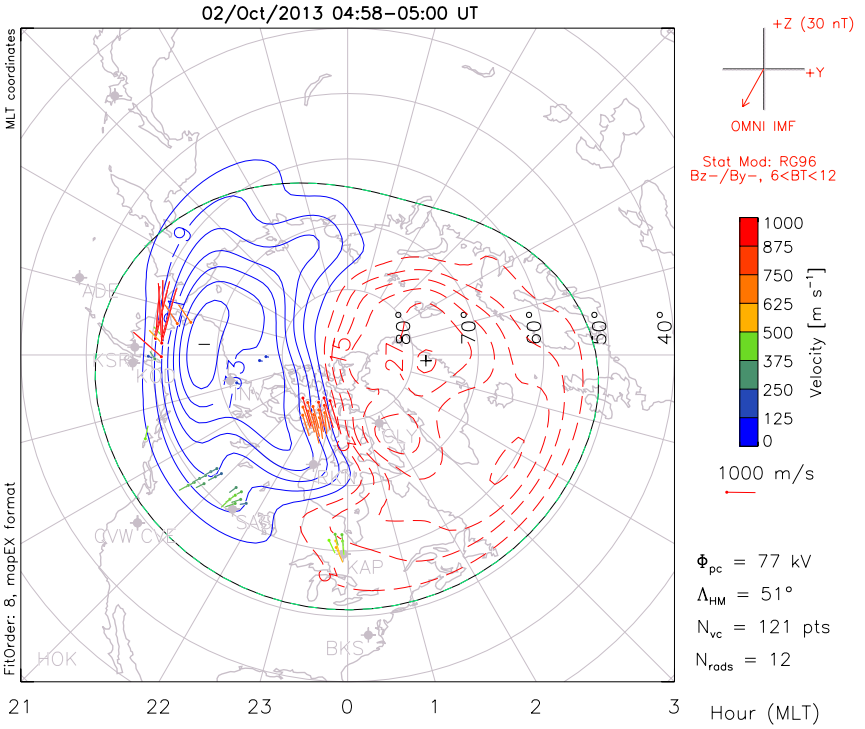

Figure 2.13: A plot of the northern hemisphere for 5:00 UT, Ocotber 2, 2013, generated using the SuperDARN merge velocity technique. Plot courtesy of Virginia Tech SuperDARN.

More recently, other data assimilation techniques for obtaining an accurate picture of the auroral and high-latitude convection have been developed [e.g., *Cousins and Shepherd*, 2010; *Fiori et al.*, 2010]. Although they are not discussed here in any detail it is important to acknowledge as deriving convection maps from SuperDARN line-of-sight velocity measurements is not a resolved problem, and efforts to improve the accuracy of these analysis techniques are ongoing.

2.3 Optical imagers and OMTI

Undoubtedly, optical imagers have been the backbone of experimental space physics since the inception of the field. The application of an optical imager is simple: use a camera to study the optical emissions of the aurora, or airglow, using filters specific to the optical wavelength of those phenomena. The sensitivity and sophistication of the imagers used has improved steadily with camera technology. Today, the newest optical imagers feature electron-multiplying charged coupled device technology (EMCCD), [e.g., *Taguchi et al.*, 2012], and are capable of detecting optical features below 100 R in brightness, over a short integration time.

In this thesis work, all of the optical data was derived from an Optical Mesosphere Thermosphere Imager (OMTI) all-sky instrument installed at Resolute Bay, Canada (74.73° N, 265.07° E, geographic) [*Shiokawa et al.*, 1999]. A second OMTI imager operates at Athabasca, Canada (54.7° N, 246.7° E, geographic); however, this station is situated for auroral observations. The OMTI imager at Resolute Bay has a field-of-view that is nearly horizon-to-horizon. Its coverage in the northern polar region, mapped to 250 km altitude, is shown in Figure 2.14. The optical filters, bandwidth, exposure time and sensitivity of the imager are outlined in Table 2.3.

The optical wavelengths of 557.7 and 630 nm are of particular interest for observations in ionospheric physics. Both wavelengths correspond to optical emissions from energetically excited atomic oxygen. The former emission corresponds to the forbidden atomic transition between an excited singlet S and an excited singlet D orbital. More specifically, ${}^1S_0 \leftrightarrow {}^1D_2$. We are using the LS Coupling notation: ${}^{2S+1}L_{L+S}$ where S is the spin multiplicity of the elec-

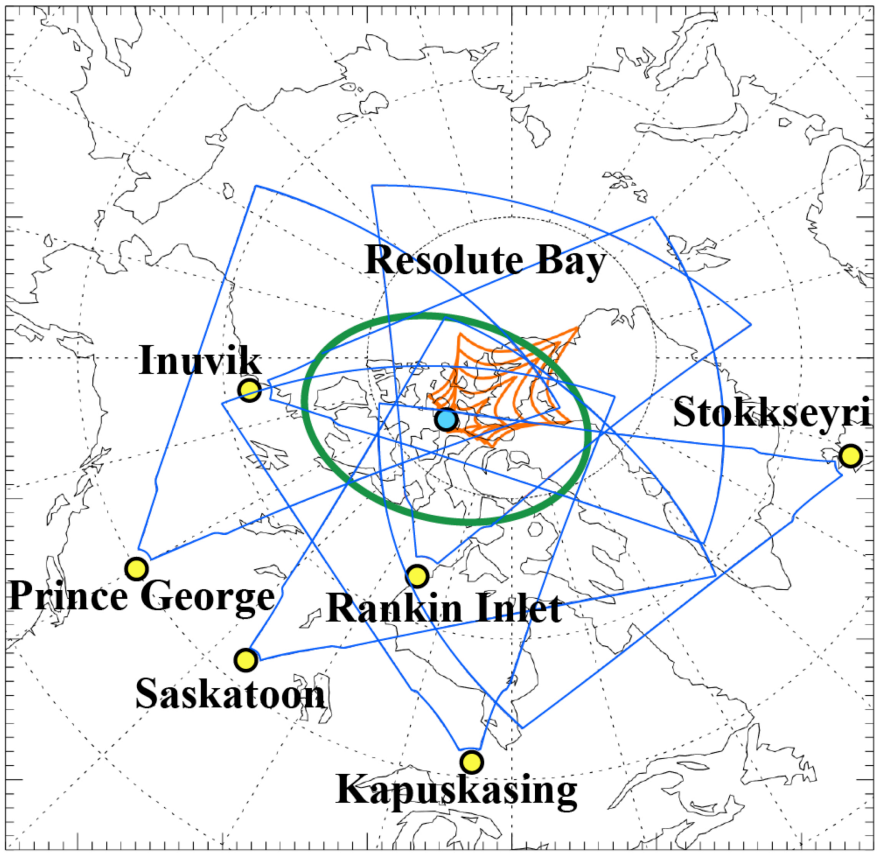

Figure 2.14: The OMTI field-of-view (green) mapped to 250 km altitude, and the fields-of-view of RISR-N (orange) and several SuperDARN sites (blue).

tronic state, and L is the quantum number of the total orbital angular momentum [*Tohmatsu and Ogawa*, 1990]. The transition produces an emission at 557.7 nm, and is referred to as the "green-line emission". Although this emission can occur due to chemistry, its most intense emissions are caused by auroral precipitation. These auroral emissions are associated with 1 keV precipitation energies, in which incoming electrons penetrate down to the 100 – 120 km altitude. The mean lifetime of the excited state is on the order of 1 s, and therefore monitoring the green-line emissions serves as a good proxy for particle precipitation location and flux.

The 630 nm emission is dubbed the "red-line emission", and corresponds to another forbidden transition: ${}^1D_2 \leftrightarrow {}^3P_2$ [*Tohmatsu and Ogawa*, 1990]. This transition may be excited by either auroral excitation or chemical recombination. Both are important for polar-region observations. The auroral excitation of the red-line emission is a signature of soft precipi-

Emission	Wavelength (nm)	Bandwidth (nm)	Exposure (s)	Sensitivity (count/R/s)
OI	557.7	1.76	105	0.029
OI	630.0	1.90	165	0.038
OH^*	720 – 910	190	15	–
Na	589.3	1.83	105	0.032
background	572.5	1.75	105	0.031

Table 2.3: The bandwidths, exposure time and sensitivity of the optical filters of the OMTI all-sky imager at Resolute Bay. Reproduced from *Shiokawa et al.* [1999].

tation, and occurs at F-region altitudes. Emissions related to chemical recombination arise from the following set of reactions, starting with Equation 1.17:

$$O^+ + O_2 \rightarrow O_2^+ + O$$

which is followed by:

$$O_2^+ + e \rightarrow O^* + O, \tag{2.36}$$

in which O^* is the excited state referred to earlier. The mean lifetime of the red-line emission is on the order of 100 s.

The lifetimes of both the red- and green-line emissions have important implications for altitudes below 250 km. The electronic transitions involved are considered forbidden; they are vulnerable to collisional deactivation, a process known as "quenching". However, since the neutral atmosphere is tenuous at E- and F-region altitudes the forbidden transitions are able to occur since collisions are so infrequent at higher altitudes. Below approximately 95 km altitude, the green-line emission is heavily quenched; below approximately 250 km, the red-line emissions is heavily quenched [*Jones*, 1974]. Below those altitudes, for each respective emission, quenching increases with the collision frequencies – exponentially with decreasing altitude. The green-line emission is predominately excited at E-region altitudes, at which

the red-line emission is quenched; the two emissions can be used to monitor processes in the E and F regions, respectively.

2.4 Summary

In this work, data from RISR-N, SuperDARN and OMTI are predominately used to investigate mesoscale plasma density perturbations in the F-region polar ionosphere. Data sets from multiple instruments can be combined to increase the level and quality of research. To help illustrate this point, consider the optical properties of a patch. We are able to optically detect it via the red-line emission described in Equation 2.36. From Equation 1.17, the neutral density also plays a role in the red-line emissions; the altitude of the patch is an important consideration. If a patch is at an altitude in which the neutral atmosphere is sparse, its red-line emissions may be undetectable using optical techniques. The lack of optical emissions does not negate the presence of the patch; it may be detected using radar techniques, i.e., with the ISR, or from coherent backscatter (i.e., SuperDARN) from the edge of a patch that is unstable. Therefore, utilizing other instruments offers a distinct advantage for studying the polar ionosphere.

It is important to note that many other instruments in the polar region are able to provide insight into the processes investigated, including: satellites using optical imagers, and radio instruments for providing total electron content (TEC) measurements; ionosondes; and ground based GPS receivers which measure radio scintillations. Notwithstanding their value, the analysis presented in the proceeding chapters does not include data from any other instrument except for RISR-N, SuperDARN and OMTI.

Chapter 3

The luminosity of F-region ionization patches

3.1 Introduction

This chapter focuses on the optical properties of F-region ionization patches and their value as diagnostic tools for the F-region ionosphere. By monitoring their luminosity (the brightness), patches may be used as a "tracer" for $\mathbf{E} \times \mathbf{B}$ convection flows in high-latitude and polar ionosphere, since the optical emissions move in conjunction with the patch plasma, which itself is $\mathbf{E} \times \mathbf{B}$ drifting. Also, the optical emissions of a patch are product of chemical recombination between the patch plasma and surrounding thermosphere. Therefore, the luminosity of the patch can be used to study the local ionospheric and thermospheric chemistry in the vicinity of the patch. Both of these concepts are touched-upon in this chapter. The optical properties of a pair of F-region ionization patches detected over Resolute Bay are linked to the $\mathbf{E} \times \mathbf{B}$ motion of the patches and local F-region chemistry. It is shown that variations in the polar-cap electric field strength can actually also lead to detectable modulations in the luminosity of the patches through the vertical component of their $\mathbf{E} \times \mathbf{B}$ motion. As we show, this relates to observed temporary increases in luminosity that are not related to a source of ionization like soft particle precipitation. Results from this chapter have been published for the most part in *Perry et al.* [2013].

3.2 Background

The brightness of F-region patches has its root in the reaction

$$O_2^+ + e \rightarrow O + O^*. \tag{3.1}$$

The excited O emits the red line 630 nm emission that is used to monitor the motion of the patches [e.g., *Weber et al.*, 1984; *Weber et al.*, 1986; *Hosokawa et al.*, 2006]. The other recombination reaction of interest in the F-region comes from the dissociative recombination of NO^+ ions. However, NO^+ recombination does not produce excited atomic oxygen, but rather excited atomic nitrogen, which therefore does not lead to 630 nm emissions [e.g., *Wayne*, 1985, section 6.4].

Polar cap patches are large volumes of F-region plasma that convect over the polar regions (see *Crowley* [1996] for a review). One idea about patches is that F-region ionization increases while the plasma circulates on the day-side and passes through the cusp, where further ionization can be triggered by soft particle precipitation. The plasma then continues its circulation over the polar cap. However, temporal and spatial variations in the electric field magnitude and direction break the plasma into "patches" of ionization as it moves into the polar cap. *Cowley and Lockwood* [1992] proposed that pulsed magnetic reconnection in both the dayside and nighttime magnetosphere would modulate the polar cap electric field, thereby inducing chaotic plasma flows throughout the region. The impact on the plasma of a changing electric field in time and space was further explored by *Sojka et al.* [1993, 1994] through model calculations that showed that patches would form and evolve while circulating over the polar regions during winter. Subsequent observations by *Moen et al.* [1995] and *Lorentzen et al.* [2004] reinforced the notion that pulsed reconnection events were associated with a dynamic polar region – the latter providing a link to the evolution of patches.

In the next section a quantitative description of the evolution of the density inside a patch is presented, based on the ion continuity equation and associated chemistry. From that an equation describing the variations in the luminosity of a patch in association with a change in the convection speed is developed.

3.3 Basic quantitative description

While polar cap patches circulate through the polar regions, the plasma also slowly undergoes recombination. In the process, faint light is emitted by the reaction described by Equation 3.1, which allows observers to monitor the passage of the patches [*Weber et al.*, 1984]. This can

be described by the continuity equation of a particular species with number density n_i is given by [*Schunk and Nagy*, 2000]

$$\frac{Dn_i}{Dt} = \frac{\partial n_i}{\partial t} + \mathbf{v}_i \cdot \nabla n_i = P_i - L_i - n_i \nabla \cdot \mathbf{v}_i, \tag{3.2}$$

where D/Dt is often referred to as the "convective derivative", P_i and L_i are the chemical production and loss rates, respectively, while $\mathbf{v}_i$ is the ion drift. We are dealing here with a situation for which there is no sunlight and no particle precipitation; therefore, $P_i \approx 0$. We also assume that the F-region is made mostly of O^+ ions. This is a well-known fact and is based on the notion that, above 200 km, it takes far longer to convert an O^+ ion into a molecular ion than it does to recombine a molecular ion once it has been created. The slow conversion of O^+ ions into molecular ions is due to the scarcity of molecular neutrals. Specifically, the reactions that turn O^+ into "fast" recombining molecular ions in the F-region are

$$O^+ + O_2 \rightarrow O_2^+ + O \tag{3.3}$$

and

$$O^+ + N_2 \rightarrow NO^+ + N. \tag{3.4}$$

3.3.1 Derivation of a leading order description

In order to obtain a basic description of the fluctuations in patch density and luminosity, it is necessary to first study the relative role played by each of the terms in Equation 3.2. First, for patches on scale sizes of a few hundred kilometers, the term $\mathbf{v}_i \cdot \nabla n_i$ is greater than all the terms on the right-hand-side (RHS) of Equation 3.2. This is simply due to the fact that patches are large plasma density perturbations, enhancements, and therefore by definition they have large density gradients on their edges. Furthermore, the recombination term L_i should normally have a much larger magnitude than $n_i \nabla \cdot \mathbf{v}_i$, since $n_i \nabla \cdot (\mathbf{E} \times \mathbf{B}/B^2) = 0$ in the electrostatic case [*Rishbeth and Hanson*, 1974]. Finally, as stated above, we assume that there is no ion production over the night-time polar cap, i.e., $P_i \rightarrow 0$. We obtain this hierarchy of terms from a calculation of their various contributions. The recombination rate at 250 km is of the order of $6 \times 10^{-4} n_i$. By comparison, even with a drift as small as 100 m/s and a gradient scale as large as 100 km, the convective derivative is of the order of $10^{-3} n_i$ and therefore, even

then, greater than a typical loss rate associated with L_i. Finally, even with a 50 mV/m polar cap electric field, which is exceptionally large for the polar-ionosphere, we obtain, for a 1000 km scale in the change of said field, $n_i \nabla \cdot \mathbf{v}_i = n_i(\nu_i/\Omega_i)\nabla \cdot \mathbf{E}/B \approx n_i 10^{-2} 1000/10^6 = 10^{-5} n_i$, meaning that the divergence of the velocity field is clearly smaller than the chemical recombination term. These numbers refer to a horizontal drift; however, the ordering is equivalent for vertical drifts as well. Our equation becomes:

$$\frac{Dn_0}{Dt} = -L(n_0). \tag{3.5}$$

The description provided by Equation 3.5 is that of a patch moving at $\mathbf{v}_i$, namely at the $\mathbf{E} \times \mathbf{B}$ drift, while slowly decaying at a loss rate determined by local chemistry.

3.4 Temporal evolution of a patch and its luminosity

We can now apply Equation 3.5 to the dominant O^+ F-region ion population to obtain

$$\frac{D[O^+]}{Dt} = -[O^+]\left(k_1[O_2] + k_2[N_2]\right), \tag{3.6}$$

where k_1 and k_2 are the reaction rates associated with Equations 3.3 and 3.4, respectively. The square brackets are used to denote chemical concentration.

The $[O_2]$ and $[N_2]$ are not constant since the altitude of a patch changes as a function of time. Normally, the $\mathbf{E} \times \mathbf{B}$ velocity of a patch is assumed to be horizontal in the polar region since the geomagnetic field in nearly vertical and the polar-cap electric field is nearly horizontal and in a dawn-to-dusk direction. However, here we refrain from making this approximation for reasons that will become clear shortly. From the reference frame of the patch, at a starting altitude z_0 at $t = 0$, we have

$$\begin{aligned}[O_2] &= [O_2]_0 \exp\left[-\frac{(z(t) - z_0)}{H_{O_2}}\right] \\ &= [O_2](z_0) \exp\left[\frac{-v_z t}{H_{O_2}}\right],\end{aligned} \tag{3.7}$$

and similarly for $[N_2]$. In Equation 3.7, the oxygen is assumed to be in diffusive equilibrium, and $H_{O_2} = k_b T/m_{O_2} g$ is the scale height of O_2 in which k_b is Boltzmann's constant, T is the

temperature of the neutral gas, m_{O_2} is the mass of molecular Oxygen and g is the acceleration due to gravity. Note that we are particularly interested here in negative values of v_z, i.e., in the effects of descending motion on the ion concentration and ultimately on luminosity.

According to Equation 3.1, the 630 nm emission rate is proportional to the rate at which O_2^+ recombines, i.e.,

$$J = A\alpha[O_2^+][O^+] \tag{3.8}$$

where $A \sim 0.8$ and is a product of the quantum yield of the recombination reaction and the total transition coefficient [*Gudadze et al.*, 2008], and α is the recombination rate for O_2^+, which is in principle a function of the electron temperature (assumed here to be constant in time). In this expression, we have also used $n_e \approx [O^+]$, which is a very good approximation for the F-region.

The O_2^+ concentration in Equation 3.8 is in turn given by equating production with loss for that ion. Using k_1 for the reaction rate associated with Equation 3.3, we obtain

$$\alpha[O_2^+][O^+] = k_1[O^+][O_2]. \tag{3.9}$$

We must also consider the effect of quenching in Equation 3.9; that is, the de-activation of Equation 3.1 due to collisions with the neutral atmosphere. Guided by *Gudadze et al.* [2008], Equation 3.9 is modified using Equation 3.8 to give the volume emissions rate, and is referred to as the luminosity, J,

$$J = \frac{Ak_1\,[O^+]\,[O_2]}{1 + d_{N_2}\,[N_2] + d_{O_2}\,[O_2] + d_O\,[O]}, \tag{3.10}$$

where d_{N_2}, d_{O_2} and d_O are the quenching coefficients due to collisions with the molecular nitrogen, molecular oxygen and atomic oxygen, respectively.

After some straightforward manipulations, we obtain the rate of change in the luminosity

$$\frac{D\ln J}{Dt} = \frac{D\ln[O^+]}{Dt} + \frac{D\ln[O_2]}{Dt} - \frac{D}{Dt}\ln(1 + d_{N_2}[N_2] + d_{O_2}[O_2] + d_O[O]) \tag{3.11}$$

Solving for the luminosity, J:

$$\begin{aligned} J = \exp\left\{\int_0^t Dt'\left(\frac{1}{[O^+]}\frac{D\,[O^+]}{Dt'} + \frac{1}{[O_2]}\frac{D\,[O_2]}{Dt'}\right)\right\} \\ \cdot \int_0^t Dt'\left[\frac{D}{Dt'}\left(\frac{1}{1 + d_{O_2}\,[O_2] + d_{N_2}\,[N_2] + d_O\,[O]}\right)\right]. \end{aligned} \tag{3.12}$$

In this derivation, we consider v_z (e.g., Equation 3.7) to be constant in time. Evaluating the above gives:

$$J = J_0 \exp\left\{-\frac{v_z t}{H_{O_2}} + \frac{k_1[O_2](z_0)H_{O_2}}{v_z}\left(e^{\frac{-v_z t}{H_{O_2}}} - 1\right) + \frac{k_2[N_2](z_0)H_{N_2}}{v_z}\left(e^{\frac{-v_z t}{H_{N_2}}} - 1\right)\right\} \cdot Q, \tag{3.13}$$

in which J_0 is the initial luminosity of the patch, Equation 3.13 with $t = 0$, and Q is the quenching factor:

$$Q = \frac{1 + d_{N_2}[N_2](z_0) + d_{O_2}[O_2](z_0) + d_O[O](z_0)}{1 + d_{N_2}[N_2](z_0)e^{\frac{-v_z t}{H_{N_2}}} + d_{O_2}[O_2](z_0)e^{\frac{-v_z t}{H_{O_2}}} + d_O[O](z_0)e^{\frac{-v_z t}{H_O}}}.$$

For $t > 0$, the last two terms inside the exponential in Equation 3.13 are always negative and account for the decrease in ion density owing to steady recombination. At the same time, the first term in the exponential is positive in the case of downward motion (v_z is negative). The intensity can increase while the overall ion density decreases, provided the downward speed is large enough. Therefore, as a patch moves downward the 630 nm emission tends to increase in response to an increase in $[O_2]$. However, at the same time the $[O^+]$ density also decreases. We therefore have to combine the two processes in order to assess whether or not the intensity of a patch will increase as a result of its downward motion. Equation 3.13 describes the competition between these two processes.

3.4.1 Numbers

The reaction rates for Equations 3.3 and 3.4 depend on the ion temperature. We have assumed here that the ion temperature was comparable to the neutral temperature, i.e., that the polar cap electric fields are typically too weak to generate large ion temperatures through frictional heating. We have used the chemical reaction rates published by *St.-Maurice and Torr* [1978] which are based on cross-sections obtained by *McFarland et al.* [1973]. We therefore chose our reaction rates to be $k_1 = 1.5 \times 10^{-11}$ cm^3 s^{-1} and $k_2 = 6.5 \times 10^{-13}$ cm^3 s^{-1}. The initial altitude of the descending patches was chosen to be 250 km. Guided by the Mass Spectrometry and Incoherent Scatter (MSIS) model [*Hedin*, 1991] for the event presented in this paper, we picked a neutral temperature of 850 K, and neutral densities at 250 km equal to 3.7×10^7 cm^{-3} for O_2 and 4.0×10^8 cm^{-3} for N_2.

The initial altitude of the patch is an important parameter for the results that will be discussed shortly. Most patch studies suggest that the altitude of patches should be near and above 275 km and perhaps higher than 300 km [*Rodger et al.*, 1994; *Pedersen et al.*, 1998, 2000; *Moen et al.*, 2008; *Hosokawa et al.*, 2011]. *Lorentzen et al.* [2004] used triangulation with two imagers to determine the altitude of two patches to be 320 km (± 25 km) and 310 km (± 25 km), respectively. The patches investigated in those studies were situated deep within the night-time polar-cap, and had spent several hours circulating through the polar ionosphere. Their patch densities would have been significantly depleted from their long lifetime in the polar ionosphere, especially at altitudes below 300 km. The two patches studied in this case study were observed in the afternoon sector, and would have not spent as much time in the night-time polar-cap. Hence, their plasma densities below 300 km would not have been as depleted which is why patch altitudes in the region of 250 to 275 km are considered here.

Results from our calculations for constant velocities are shown in Figure 3.1 for downward vertical velocities $v_z = -40$ m/s and -60 m/s. For our choice of parameters, the luminosity in the first case goes up by nearly 30%, reaching its maximum value after about 8 minutes. However, after another 8 minutes the luminosity rapidly goes to values much less than the initial value. At first, the luminosity increases as the O_2^+ ion production increases, as the layer decreases in altitude. However, in the long run, the very processes that increase the luminosity are those responsible for the decrease in the ion density through the reduction of O^+ ions.

With a faster downward speed of -60 m/s, Figure 3.1 shows that the evolution is obviously faster than in the -40 m/s case. However, the brightening becomes quite large even though the phenomenon is shorter-lived. The maximum increase in luminosity is now more than a factor of 1.6. An important point to notice is that the time taken for the intensity to return to the initial value is actually longer with the -40 m/s case. In the long run, at least for this comparison, the patch that goes through the brightest phase is also the one that becomes less luminous, more quickly. Clearly, this is because the ion density rapidly decreases in the -60 m/s case.

As shown in the next section, optical observations can provide information on the lumi-

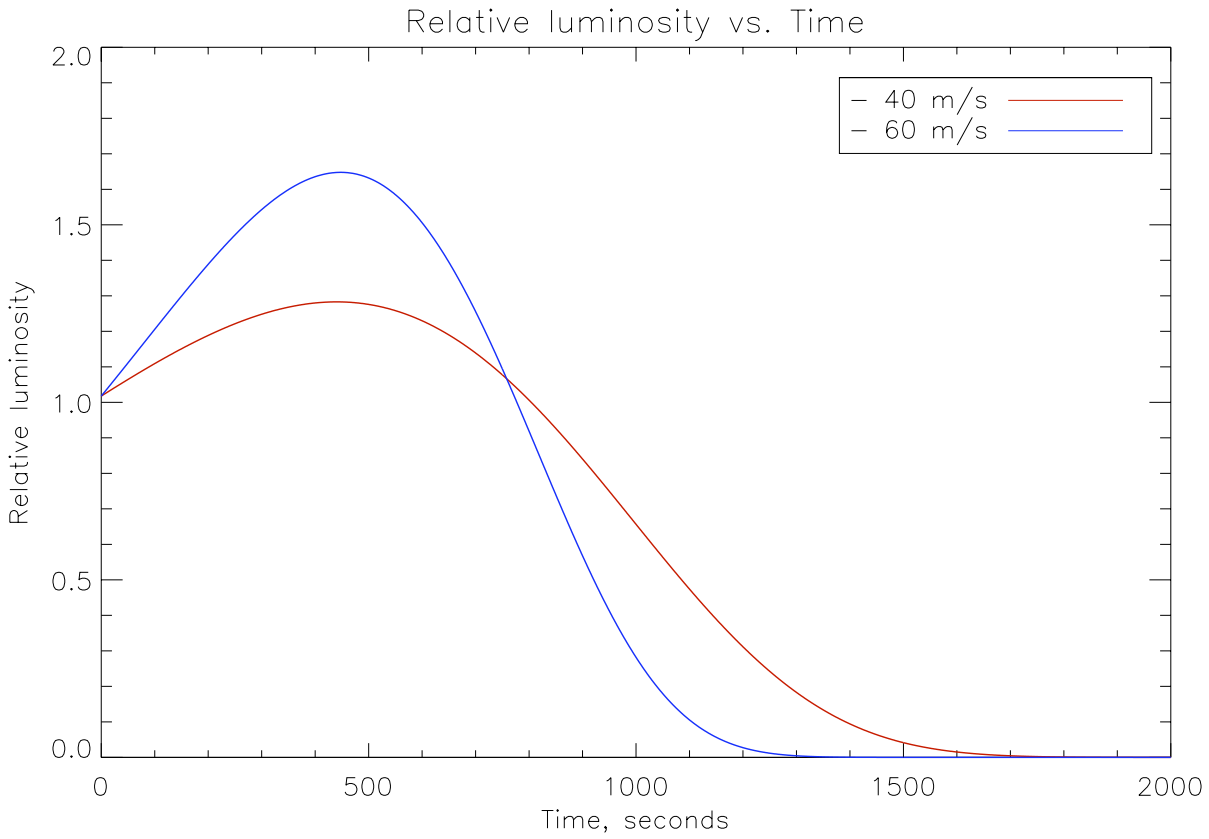

Figure 3.1: Calculated luminosity change as a function of time for $v_z = -40$ m/s (red trace with the lower maximum amplitude) and for $v_z = -60$ m/s (blue trace). The velocities were applied at $t = 0$. The parameters were chosen to be appropriate for at 250 km starting altitude in the winter night-time polar cap.

nosity gain when a patch starts moving down, and also on how long it takes for the patch to go down to a certain luminosity level. As just shown above, one parameter that clearly controls this evolution is the vertical drift. Another parameter is the starting values for the neutral densities, which is equivalent to choosing a different starting altitude for a patch. We have run a series of cases where we varied the starting neutral densities and the constant vertical drift. We held the neutral temperature fixed at 850 K. We recorded the maximum intensity and the time interval it took for the intensity to fall back to 60% of its initial value. The results were compiled in the form of a chart, which is presented in Figure 3.2. On the vertical axis we have posted the ratio of the starting neutral density to the "standard" value that was used in Figure 1 (a 250 km altitude). On the horizontal axis we have posted the

value of the drift. We only used negative values with magnitudes in excess of 10 m/s because for slower downward drifts the luminosity always decreases monotonically, without peaking (though it of course decreases more slowly, the less negative or more positive the drift is). We have posted two sets of curves in the chart. One set, posted in blue is the time it would take, in seconds, for the intensity to fall back to 60% of its initial value. The numbers associated with these contours are typically of the order of 1000 to 2000 s. Contours posted in red represent the ratio of the maximum intensity to the starting intensity and are of order 1. With allowances for uncertainties in the relaxation time and in the peak intensity, the chart could be used to identify the kinds of densities and vertical velocities that would be involved in a brightening event. The chart can also be used, of course, to simply assess the relaxation time and the amount of increase in the brightness that can be found for particular conditions.

3.5 Comparison with OMTI observations

An Optical Mesosphere Thermosphere Imagers (OMTI) [*Shiokawa et al.*, 1999] all-sky airglow imager has been in use at Resolute Bay (74.73° N, 265.07° E; AACGM latitude 82.9°) since January, 2005. The data of interest here were obtained with a 630 nm filter to capture the red line emission produced by patches through Equation 3.1 [*Hosokawa et al.*, 2006, 2009a, 2010]. Images were obtained every 2 minutes with an exposure time of 30 s. Background continuum emission from the sky was sampled every 20 minutes at a wavelength of 572.5 nm and used to derive the absolute intensity of the airglow lines [*Shiokawa et al.*, 2000, 2009]. On December 20, 2006, shortly after 22:25 UT, a patch that had been temporarily devoid of horizontal motion broke into two separate patches that started to move towards lower latitudes at different speeds. The faster horizontally moving patch, referred to as patch B1 in *Hosokawa et al.* [2010], had a larger increase in its intensity than the slower moving one – patch B2. To obtain the relative intensity, contributions from the van Rhijn effect [*Tohmatsu and Ogawa*, 1990] had to be removed and the atmospheric extinction was taken out using the procedure proposed by *Kubota et al.* [2001]. More details about the data set can be found in *Hosokawa et al.* [2010].

What we wish to focus on here is the temporal evolution of the intensity (more specifically,

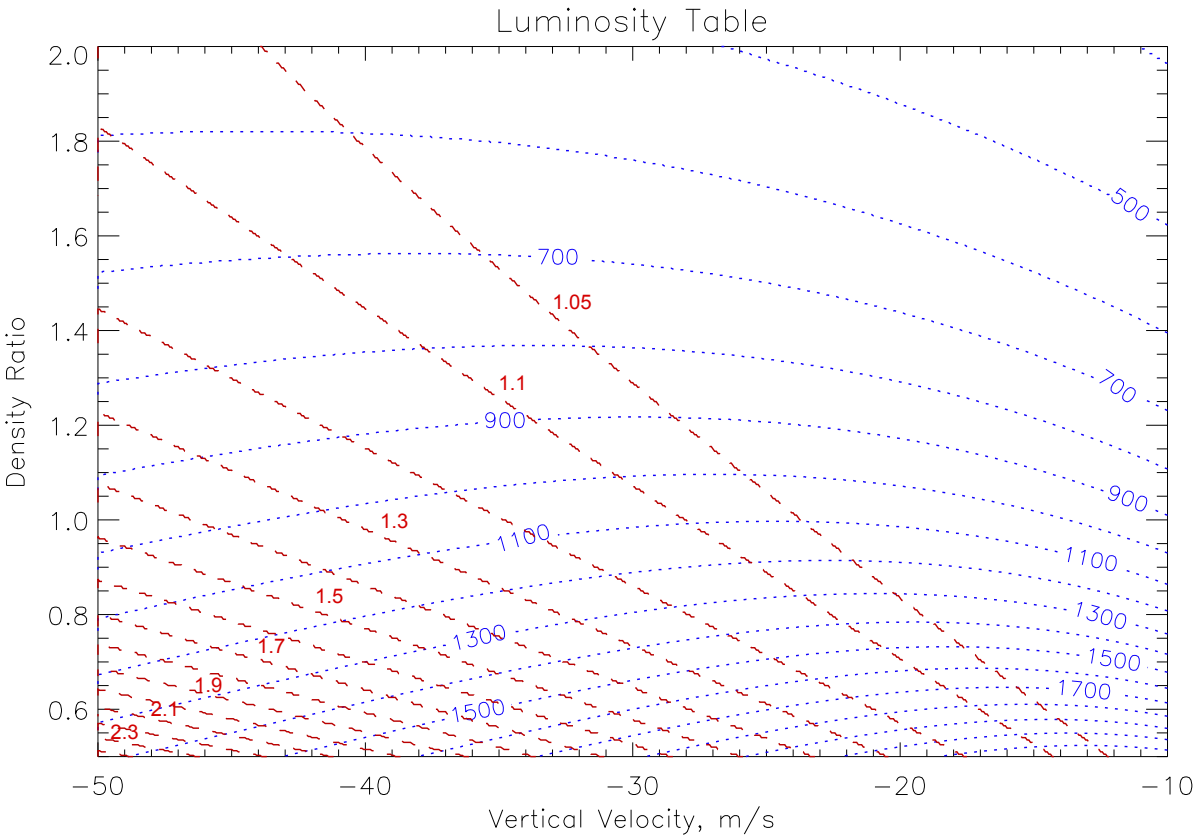

Figure 3.2: Chart of the time, in s, taken to go down to 60% of the initial luminosity (blue contours) and of the ratio of the maximum luminosity to the starting luminosity (red contours) as a function of vertical drift (horizontal axis) and of the ratio of the starting density to the density used in Figure 3.1 (vertical axis).

the relative intensity) of the two patches. Figure 3.3 shows the evolution of patch B1 and Figure 3.4 that of patch B2. The increase in relative luminosity for the horizontally faster moving patch reached a maximum 15% higher than its initial value, while the time needed for the patch luminosity to fall back to 60% of its initial value was of the order of 1700 to 1800 s. For the slower patch, the time taken to fall back to 60% of the initial luminosity was about 5 minutes shorter, of the order of 1400 to 1500 s while the peak intensity was about 5% greater than its initial value. According to the chart in Figure 3.2 these numbers are fairly consistent with the model used in Figure 3.1, though they suggest a density 60 to 65% of what we used there. The inference is that the vertical drift of the faster patch was of the order of −17 m/s and an altitude somewhat higher than the nominal 250 km that we have selected as our starting point. Figure 3.3 shows how good a fit we can get, using a drift of

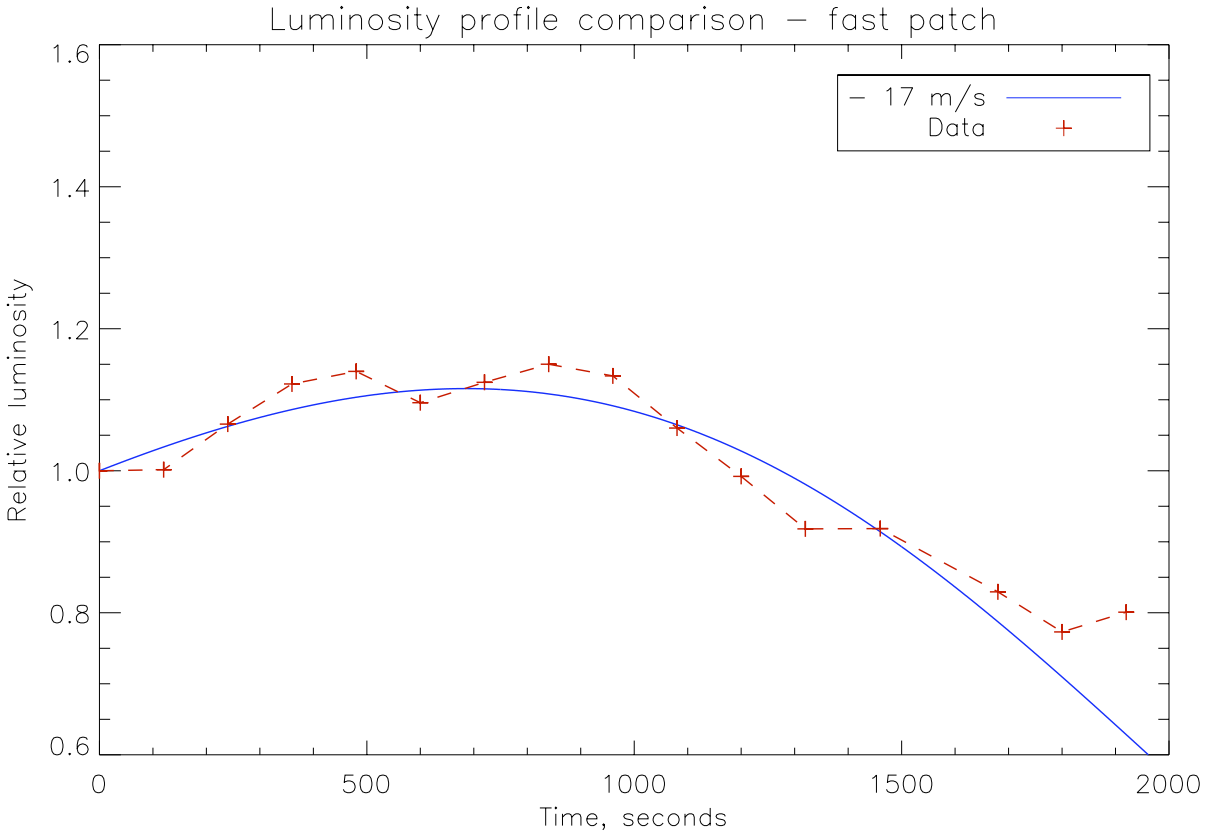

Figure 3.3: Observations of patch B1 in *Hosokawa et al.* [2010] (the fast moving patch) obtained at 630.0 nm on Dec 20, 2006 with the OMTI all-sky imager at Resolute Bay (crosses connected with red dashed line). The two patches emanated from a single broader feature divided into two parts, starting at 22:30 UT (roughly the 300 s mark in this figure). The blue solid line was obtained with constant vertical drifts of -17 m/s, starting from an altitude of 265 km. See text for details.

-17 m/s and a starting density that is 65% of the value at a 250 km altitude (approximately 265 km altitude), recommended by MSIS. The observations in Figure 3.3 agree quite well with the theoretical calculations up until the 1800 s mark, when the theoretical calculations begin to underestimate the luminosity of the patch. The underestimation may be due to the simplified model, which only describes the luminosity from a peak altitude of 250 km, and not the optical contributions from the descending patch volume above and below the peak altitude. Furthermore, the velocity of the patch may have changed during the period of observation. Since our theoretical prediction assumes a constant velocity, it would not account for any additional brightening or dimming of the patch caused by sudden changes in

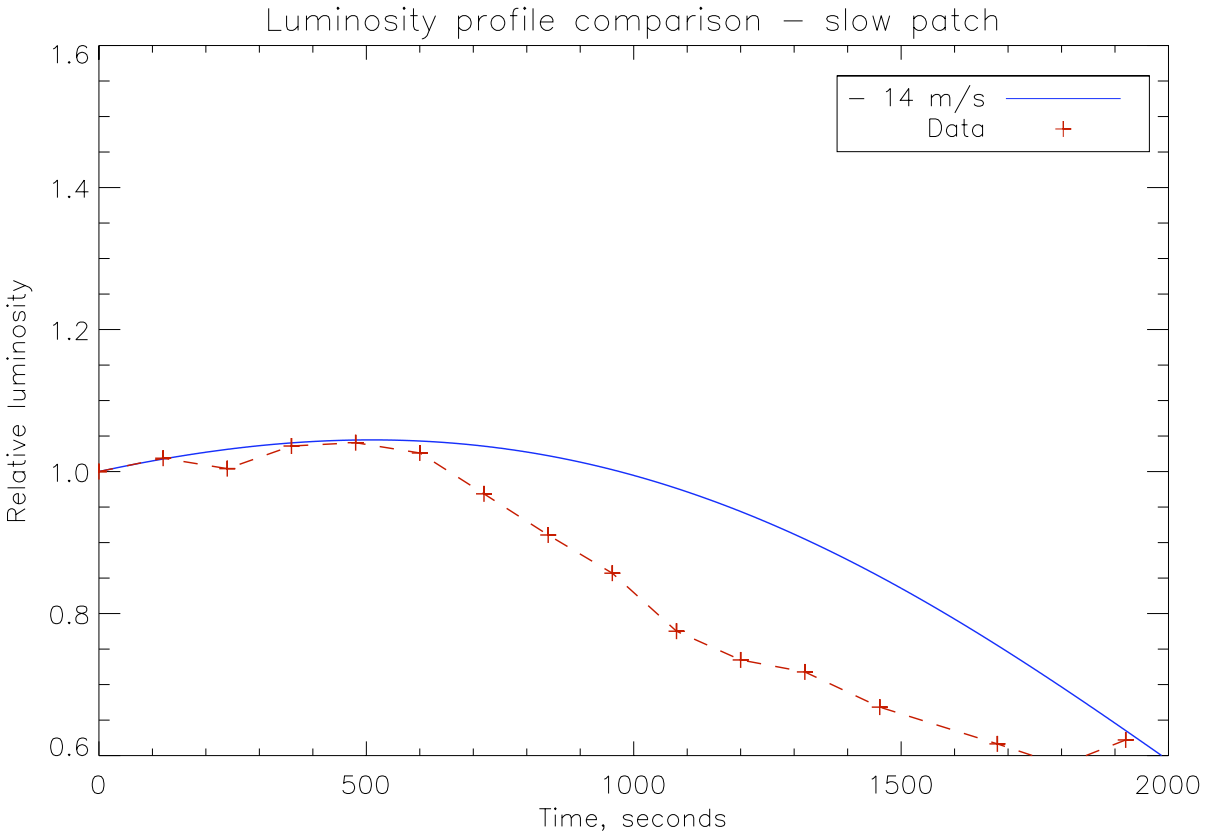

Figure 3.4: Observations of patch B2 in *Hosokawa et al.* [2010] (the slow moving patch) obtained at 630.0 nm on Dec 20, 2006 with the OMTI all-sky imager at Resolute Bay (crosses connected with red dashed line). The two patches emanated from a single broader feature divided into two parts, starting at 22:30 UT (roughly the 300 s mark in this figure). The blue solid line was obtained with constant vertical drifts of − 14 m/s, starting from an altitude of 265 km. See text for details.

its velocity which may occur due to varrying geomagnetic conditions. Both of these points are discussed in more detail shortly.

For the profile in Figure 3.4 we have used the same starting altitude as Figure 3.3, that is, 65% of the value the densities would have at 250 km, according to MSIS. This choice is consistent with the fact that the patches were observed to be initially two parts of an original elongated patch [*Hosokawa et al.*, 2010]. However, as can be seen from Figure 3.4, we had to use a slower downward drift to fit these observations, since the observed increase in luminosity was smaller than the patch in Figure 3.3. As shown by the red dashed line, we could fit the first 600 s well with a steady −14 m/s downward drift. However, for times exceeding 600 s,

our theoretical curve ended up systematically overestimating the observations.

We should note that the velocities of the patches, as determined by PolarDARN data, were approximately 320 m/s for the faster moving patch and 240 m/s for the slower one [*Hosokawa et al.*, 2010] (The Polar Dual Auroral Radar Network consists of the SuperDARN radars at Rankin Inlet, Inuvik and Clyde River. At the time of these observation, only the first two were operational.). The ratio of these two speeds is very similar to the ratio 17/14 obtained from the fit to the intensity curves during the first 10 minutes (note that after the first 10 minutes of observations, radar echoes were not available anyway, as they disappeared from the patches). This agreement in the ratios suggests that the vertical component of the $\mathbf{E} \times \mathbf{B}$ drift was indeed responsible for the changes in luminosity. This stated, the dip angle near Resolute Bay is rather large, of the order of 87.2° according to the International Geomagnetic Reference Field (IGRF) model. There is an uncertainty here due to the meandering of the pole and the presence of iron ore in the area. Taken at face value, a 17 m/s downward drift (of the faster patch, in Figure 3.3) would require of the order of 350 m/s for the speed of the patch, i.e., a drift 9% greater than reported from the PolarDARN observations. However, the PolarDARN speeds do not include a correction for a non-unity index of refraction. Applying this correction means that the speed produced by the SuperDARN data inversion algorithm could be of the order of 10% smaller than the actual speed [*Drayton et al.*, 2005; *Gillies et al.*, 2009; *Ponomarenko et al.*, 2009; *Gillies et al.*, 2012]. We conclude from these considerations that the vertical speeds inferred by the theoretical fits to the luminosity curves are consistent with the radar observations of the cross-cap $\mathbf{E} \times \mathbf{B}$ drift.

3.6 Effects associated with plasma drift variations

We have concentrated our study thus far on a situation where a patch begins to descend from a given altitude and keeps a fixed speed thereafter. However, the data set that we have used makes the case that the plasma drift can change with time. While the patches started nearly at rest prior to acquiring their equatorward motion, the latter occurred at a fairly constant (but not exactly constant) speed. Indeed, for the slower of the two patches there was a need to introduce a change in speed after the first 10 minutes of observations. In fact,

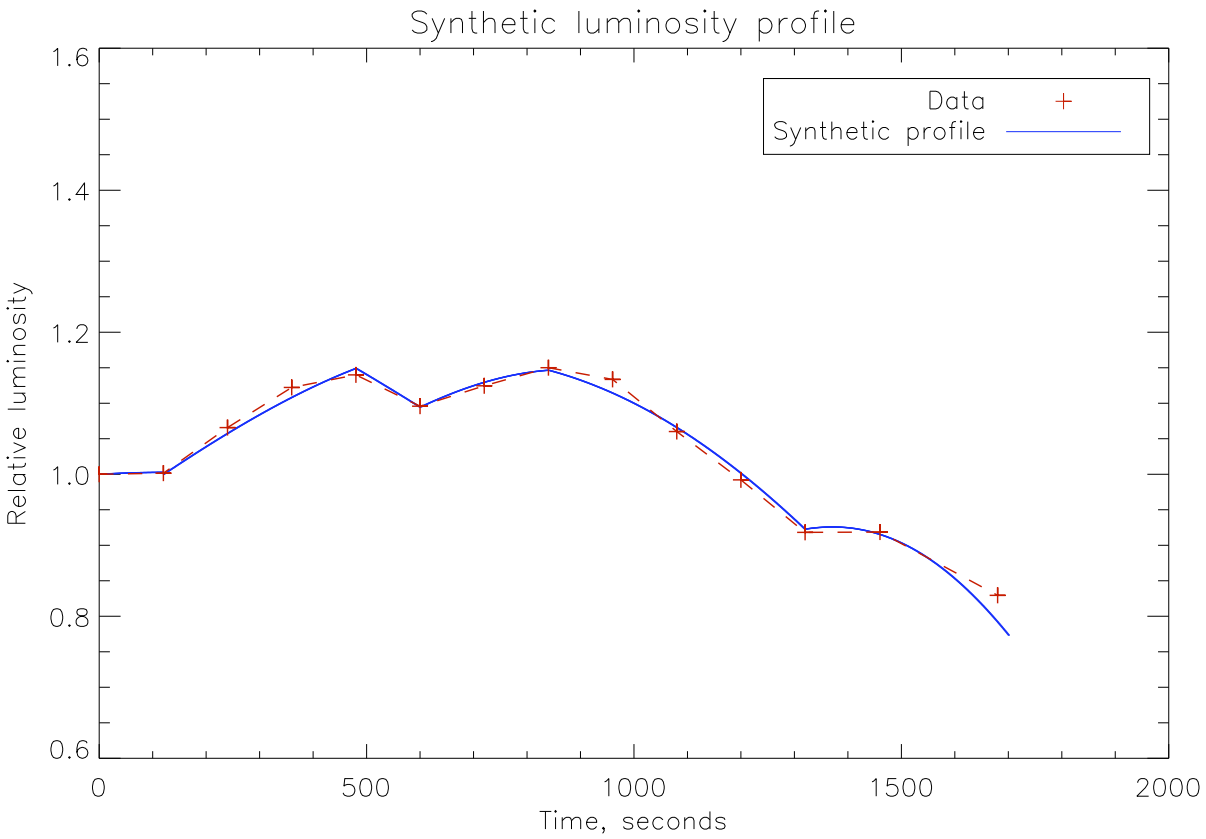

Figure 3.5: Synthetic luminosity curve obtained by changing v_z at various times during the evolution of a patch. The patch descent initiated at an altitude of 265 km. See text for details about the changes that were used.

just a change in the distance of a patch to the pole and subtle changes in the direction of the convection can introduce changes in the vertical velocity associated with an otherwise constant looking convective motion. For all these reasons, we should at least briefly consider how changes in the vertical velocity can affect the results.

One easy way to assess how a changing velocity can affect the evolution in the luminosity is to consider a succession of constant velocity steps instead of the formal solution given by Equation 3.13. Going through a succession of velocity steps is simply a matter of making repeated use of Equation 3.13 with different v_z values. If we follow this procedure, we simply have to replace z_0 and J_0 in Equation 3.13 by the altitude and intensity reached by the patch at the end of the previous v_z step.

By altering the v_z values, we can reproduce the various sudden changes in the luminosity of patches (which, of course, could just be noise anyway). This is illustrated with Figure 3.5,

which shows the results of an attempt to mimic the various jumps in observed luminosity shown in Figure 3.3. In particular, we sought to reproduce the two maxima, with a minimum in the middle. The profile in Figure 3.5 was constructed with a starting altitude of 265 km (i.e., the density correction used in Figure 3.3), plus the following evolution for the downward drift: $v_z = -13$ m/s for the first 120 s, $v_z = -24$ m/s for the next 360 s, $v_z = -10$ m/s for the next 120 s, $v_z = -27$ m/s for the next 240 s, $v_z = -21$ m/s for the next 480 s, and $v_z = -38$ m/s for the rest of the time. Clearly, by playing with v_z over the desired time intervals we could get quite close to the changes seen in the observations.

The separation in time between the two maxima in the measured patch luminosity, located at 480 s and 840 s, is equivalent to the separation between two critical points at which the patch speeds peaked [*Hosokawa et al.*, 2010]. This provides additional support to the notion that sudden changes in the luminosity profile in Figure 3.3 may be due to sudden changes in the velocity of the patch. The horizontal convection speed data was not directly measured but inferred past the 840 s mark, causing any additional comparison to be unreliable [*Hosokawa et al.*, 2010]. We reemphasize that the jumps in the intensity may well just be the result of uncertainties in their extraction, i.e., just noise artefacts. Our point here is simply that plausible fluctuations in v_z can also generate changing features that are similar to the observations.

3.7 Line-of-sight integration

Up until this point, we have only considered the luminosity of a single emitting plasma layer; that is, we have only investigated the luminosity of a patch with an infinitesimal thickness, or a "delta-layer". To account for the finite thickness of a patch we now consider the line-of-sight integration through a plasma patch and its contribution to the luminosity profile. Effects introduced due to the positioning of a patch within the field-of-view of an all-sky imager, which include the Van Rhijn effect, atmospheric extinction and imager sensitivity as a function of the angle of the patch with respect to the zenith, are corrected for in the OMTI data in a procedure described in *Kubota et al.* [2001]. Therefore, we only need to consider the line-of-sight integration along the vertical profile of a plasma patch.

3.7.1 Line-of-sight integration methodology

A variety of patch density profiles have been investigated for their effects on the line-of-sight integration results. We used a modified Chapman profile (recall Equation 1.15),

$$\left[O^+\right] = \left[O^+\right](z_0) \exp\left[1 - \frac{z - z_0}{H} - \exp\left(-\frac{z - z_0}{H}\right)\right], \tag{3.14}$$

with a different scale height, H, above and below the plasma density peak. Here, z is the altitude and z_0 is the altitude of the peak density.

It is well known that the plasma profiles of plasma patches have smaller e-folding distances below the plasma peak than above the peak. This is due to the increased reaction rates at lower altitudes [*Smith et al.*, 2000]. Above the peak plasma density of the patch (*top-side*), scale heights ranging from 100 to 250 km were investigated, and we considered scale heights ranging from 10 to 100 km below the peak (*bottom-side*). Hereafter, the term "scale height" will be used when referring to the e-folding distance of a patch plasma profile. An example of a patch profile is shown in Figure 3.6. The patch profile is normalized to a peak height, z_0, of 250 km, with a top-side scale height of 250 km and bottom-side scale height of 25 km.

The procedure for performing a line-of-sight integration along the vertical profile of the patch is as follows: the initial luminosity $J(t = 0)$ is calculated for a given altitude using Equation 3.10, J is then calculated for $t > 0$ using Equation 3.13, producing a delta-layer luminosity profile. This process is repeated for each discrete altitude along the vertical profile of the patch. The luminosity profiles of each delta-layer, composing the patch profile, are then summed to complete the integration process.

The line-of-sight integration of two, and three delta-layers is demonstrated in Figure 3.7. Here, the relative luminosity profile of a delta-layer patch at a 265 km altitude is compared to the integrated profile of two delta-layer patches at 250 and 265 km, and three delta-layer patches each at 240, 250 and 265 km. All the layers are descending at 17 m/s. It is evident that the relative luminosity profile becomes more diminished as additional discrete layers are accounted for. This is a counterintuitive result. The addition of discrete layers to the descending patch broadens the relative luminosity profile of the patch. Recall from Figure 3.2 that the magnitudes of the relative luminosity peak and the point in time in which the peak

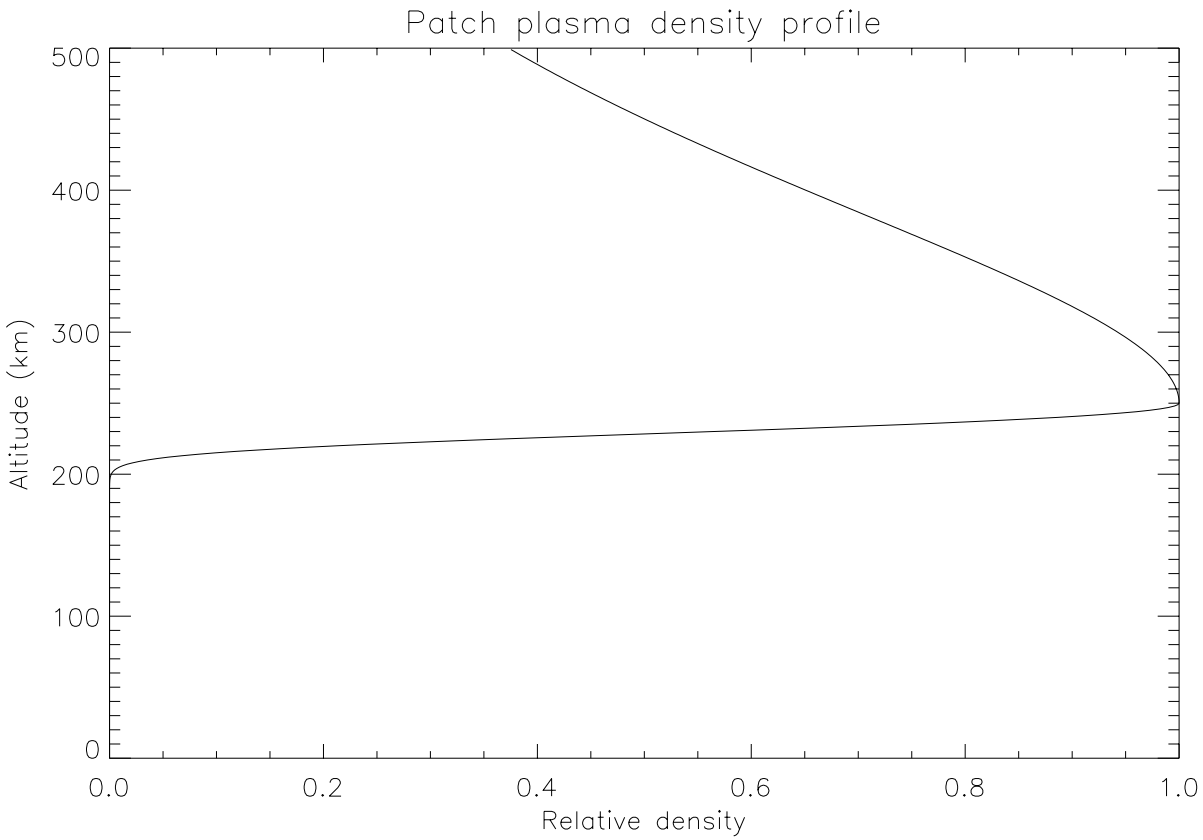

Figure 3.6: The plasma profile of a polar cap patch with a peak density at 250 km in altitude. Above the peak (*top-side*) the patch has a density scale height of 250 km and below the peak (*bottom-side*) the density scale height is 25 km.

will be reached, will be different for each discrete layer in the patch profile. Discrete patch layers that start at lower (higher) altitudes will have luminosity profiles that peak more quickly (slowly), with lower (higher) magnitudes. It must be stressed that integrating over the discrete layers produces an overall subdued relative luminosity profile compared to the delta-layer profile; however, the luminosity magnitude of the patch (the brightness of the patch) will be higher since there will be more O^+ and O_2^+ by virtue of adding in discrete patch layers.

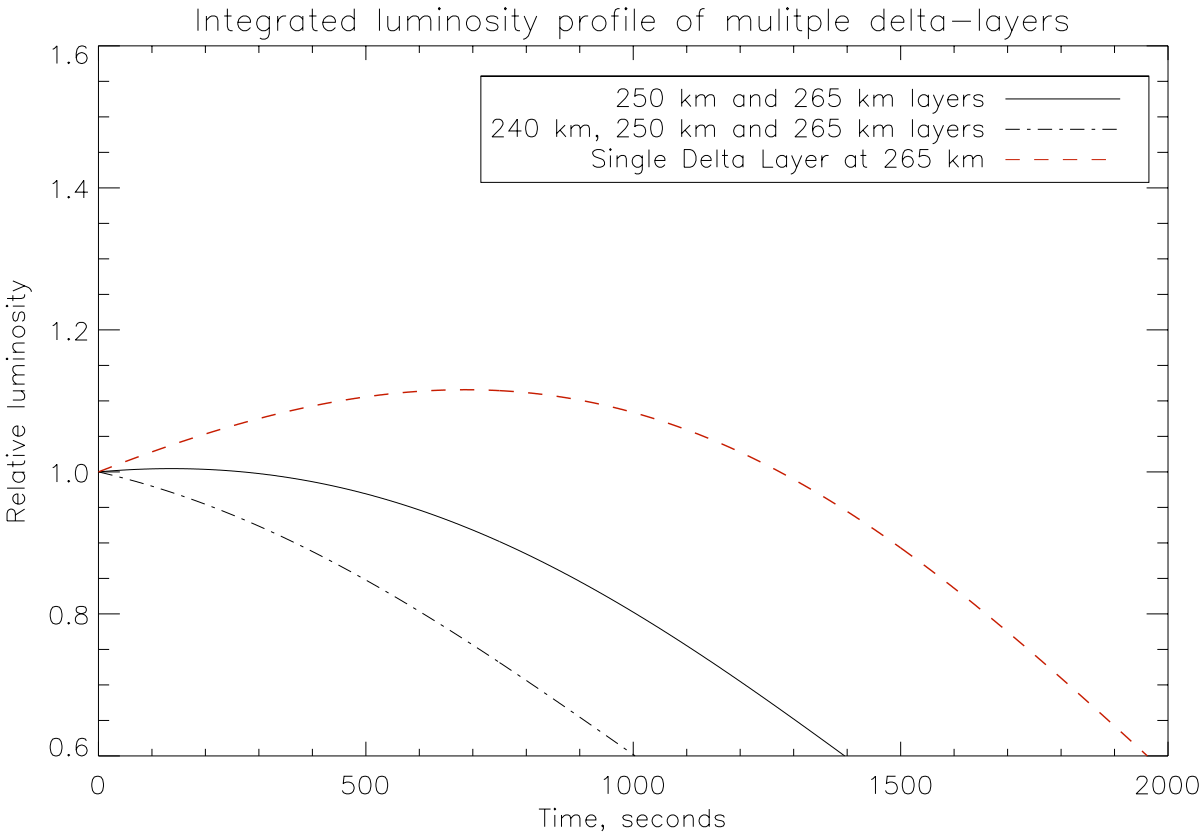

Figure 3.7: Comparison between single delta-layer luminosity curved (red) and the result of integrated multiple delta-layers together. The downward velocity of the patches is 17 m/s.

3.7.2 Line-of-sight integration results

An investigation into the luminosity characteristics of a descending plasma patch was performed for a variety of patch profiles. The profiles differ in top-side and bottom-side density scale heights, though all have a plasma density peak at 265 km in altitude. Patch density profiles and their resulting initial luminosity profiles are plotted in Figure 3.8. The initial luminosity, $J\,(t=0)$, is plotted using Equation 3.10. Each plasma patch plotted in Figure 3.8 has a top-side density scale height of 100 km, although the bottom-side density scale height is varied.

A feature of note in Figure 3.8 is the increased distance between the peak patch density and the peak initial, relative luminosity $J\,(t=0)$. As the bottom-side density scale height increases, the peak altitude of $J\,(t=0)$ for the associated patch decreases. One might expect

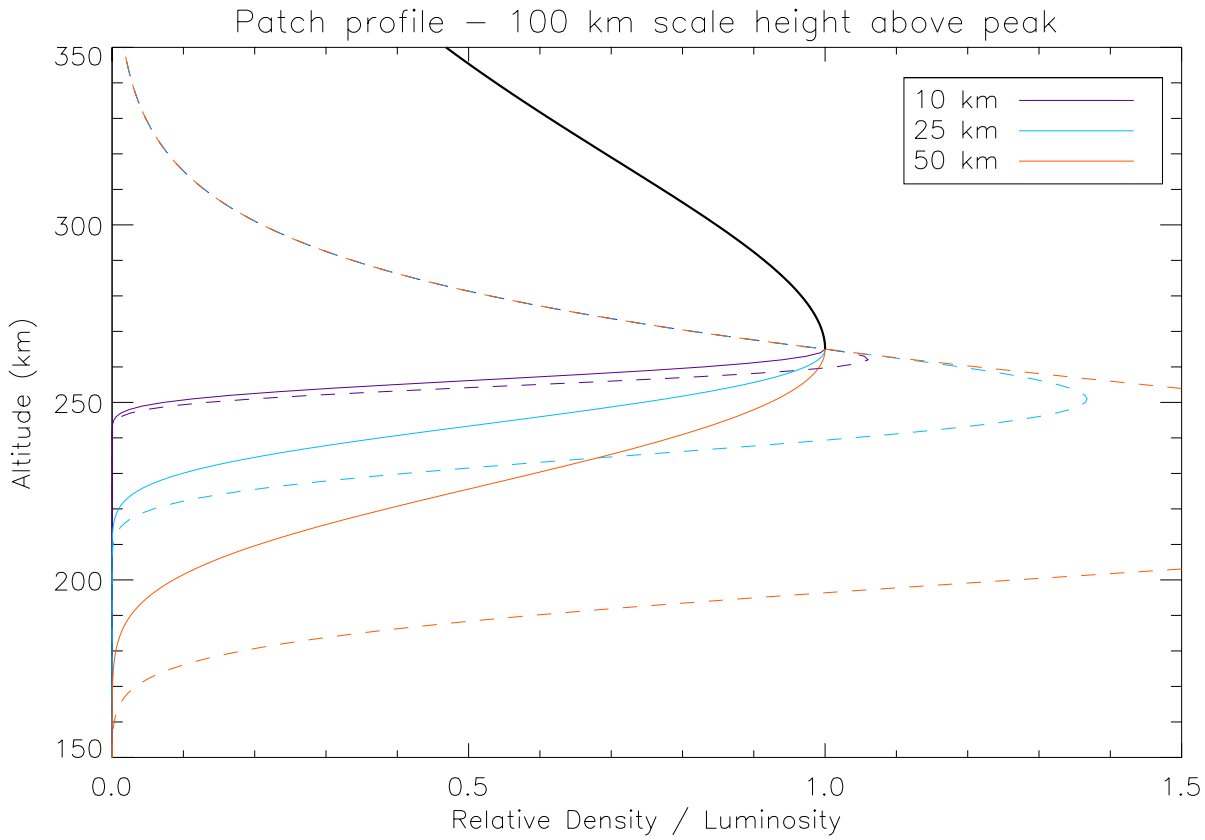

Figure 3.8: The vertical profile of plasma patch models used. The patch plasma density (solid) and initial luminosity (dashed) profiles are plotted. The patch plasma profiles here have a top-side density scale height of 100 km. The top-side density profile is colored black. Bottom-side density scale heights are distinguished by color. All profiles are plotted relative to a 265 km altitude.

the peak in $J\,(t=0)$ to coincide with the peak patch plasma luminosity, indicating a strong coupling between the luminosity and $[O^+]$; however, Figure 3.8 shows that $J\,(t=0)$ is most dependent on $[N_2]$ and $[O_2]$. The increased bottom-side initial luminosity profiles are a result of reaction rates for the patch-associated chemical reactions described by Equation 3.1 – increasing with a decreasing altitude.

The integrated luminosity profiles for a variety of patch profiles descending at 23 m/s are plotted in Figure 3.9. Also plotted is the luminosity profile for a single delta-layer patch descending at 17 m/s and the data from *Hosokawa et al.* [2010]. Each integrated luminosity profile in Figure 3.9 is for a patch with a top-side density scale height of 250 km, centered at 265 km in altitude. Bottom-side density scale heights of 10, 20, 25 and 50 km are plotted

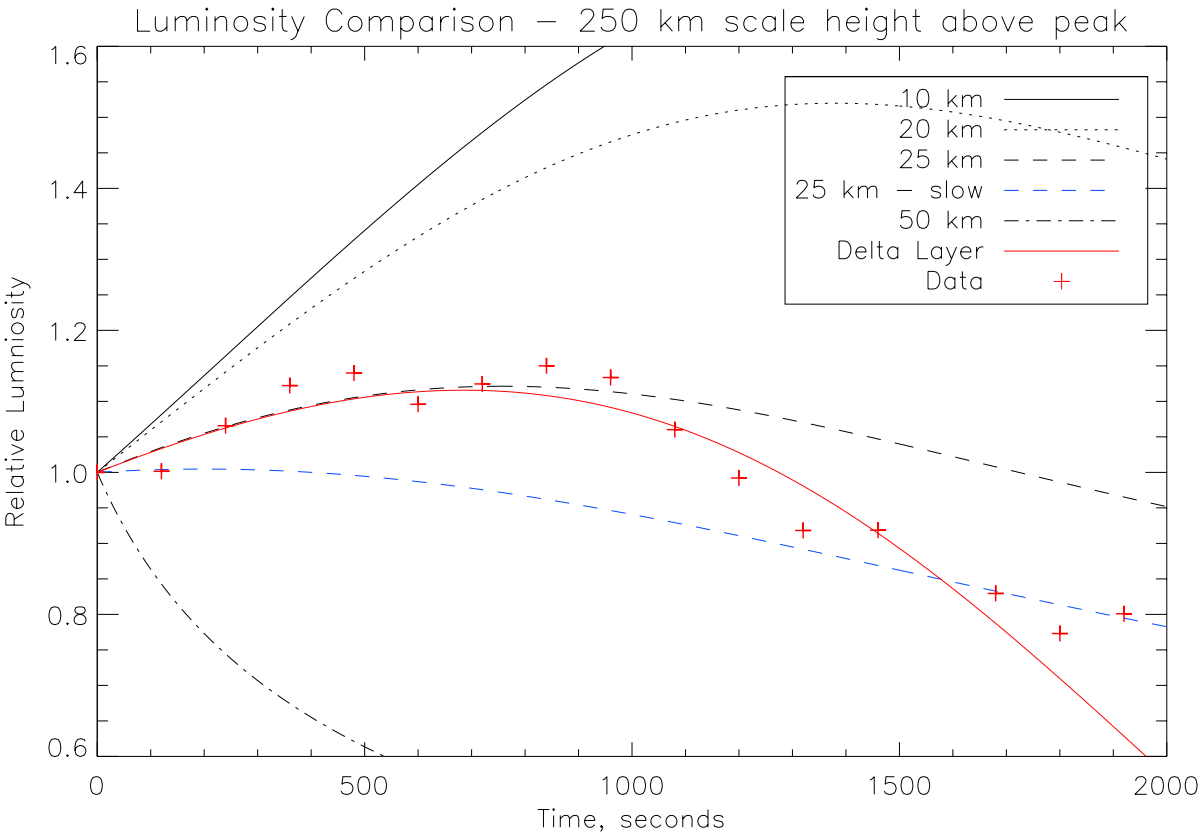

Figure 3.9: Luminosity profiles for the delta-layer case (red), descending at 17 m/s, and integrated profile case (black) are plotted along side patch data from *Hosokawa et al.* [2010]. The profiles in black are descending at 23 m/s. The blue profile corresponds to a speed of 17 m/s for an integrated profile. Each patch has a top-side density scale height of 250 km and a peak density at 250 km.

to demonstrate the effect of the bottom-side patch density scale height on the integrated luminosity curve. Also, an integrated luminosity profile for a patch descending at 17 m/s with a bottom-side scale height of 25 km is plotted in blue. Comparing this profile to that of the profiles descending at 23 m/s highlights the effect of the line-of-sight integration. Of the integrated profiles, the luminosity profile with a bottom-side scale height of 25 km, descending at 23 m/s, appears to have the best agreement with the *Hosokawa et al.* [2010] data in Figure 3.9.

The effect of changing the top-side plasma density scale height for a plasma patch on the luminosity profile is noticeable, but not as significant as changing the bottom-side density scale height. This is consistent with Figure 3.8 which suggests that the majority of the

luminosity from a patch is generated below the density peak, due to the higher O_2 and N_2 densities there. In Figure 3.9, the integrated profile for a patch with a bottom-side scale height of 25 km agrees well with the luminosity data and the delta-layer profile, for the first 1000 s. After this time, integrated profile over-estimates the luminosity of the patch. The need to increase the speed (and therefore luminosity) of the integrated profile is consistent with the diminished luminosity profiles seen in Figure 3.7; the thickening of the patch diminishes the relative luminosity profiles. The integrated and delta-layer luminosity profiles begin to diverge from each other when their luminosities both peak at 1000 s. The integrated profile takes longer to decrease, which is due to the contribution of the luminosity from the additional patch plasma above the density peak reacting with the neutral atmosphere. This sustains the relative magnitude of the patch luminosity.

In an effort to match the integrated profiles in Figure 3.9 to the *Hosokawa et al.* [2010] data, the top-side patch density scale height was lowered to 100 km and is plotted in Figure 3.10. The luminosity profile in Figure 3.10, corresponding to a patch with a bottom-side scale height of 25 km provides the best agreement with the *Hosokawa et al.* [2010] data, compared to any of the other integrated profiles investigated. The most accurate integrated luminosity profile in Figure 3.9 is in good agreement with the *Hosokawa et al.* [2010] data up until the 1300 s mark, when the theoretical luminosity curve begins to overestimate the patch luminosity. The integrated luminosity profile in Figure 3.10 remains in good agreement with the *Hosokawa et al.* [2010] data throughout the duration of the observations. We can therefore conclude that the inclusion of contributions from to the line-of-sight integration along the vertical density profile of the patch also agree with the *Hosokawa et al.* [2010] data.

Even though the integrated luminosity profiles appear to agree well with the imager data, some inconsistencies still need to be addressed. In Figure 3.10, the delta-layer profile model is for a patch descending at 17 m/s, while the integrated profiles are for patches descending at 23 m/s. A larger speed was required to account for the dimmer relative luminosity curves of the patches with finite thickness. The increased vertical speed equates to an $\mathbf{E} \times \mathbf{B}$ speed of 470 m/s – 47% higher than the speed determined from the PolarDARN data. As mentioned earlier, one must consider radio wave propagation conditions when dealing with the PolarDARN velocity data; however, it is unlikely these conditions could account for such

a large discrepancy in speed. In *Hosokawa et al.* [2010], the horizontal speed of the patch is also estimated from the optical data. Starting at 22:30 UT (the 300 s mark in Figure 3.3), the horizontal speed of the patch increases from 225 to 425 m/s (only 11% higher than the model) in 420 s, and then suddenly drops back down to 325 m/s in the next 120 s. The integrated model (as well as the delta-layer model) assumes a constant speed, and therefore the luminosity profile discrepancy may be an acceleration affect (the result of speed variation on the delta-layer model was discussed in Section 3.6). This would also support the larger patch speeds suggested by the integrated luminosity model. There are many factors which can affect the precision of the luminosity profile and the patch velocities it suggests including: a varying patch velocity, instrumental effects or even inaccurate information about the neutrals. It is therefore important to re-iterate the purpose of this work: to provide a model that can qualitatively explain the relative luminosity profiles observed over Resolute Bay.

It is interesting that the delta-layer model appears to agree well with the imager data, since it is a first order approximation. In an effort to determine the robustness of the delta-layer model, the luminosity profile of patch B2 – the slower of the two patches in the *Hosokawa et al.* [2010] data – was considered. In Figure 3.4, it is evident that the delta-layer model deviates from the data quite significantly. Using the line-of-sight integration method, a plasma patch with similar characteristics (a peak at 265 km, similar velocity and plasma density scale heights) can not account for the luminosity profile of patch B2. If the starting altitude of the patch is lowered to approximately 250 km and the line-of-sight integration technique is used once again, a better agreement with the luminosity data in Figure 3.4 is achieved. This is shown in Figure 3.11, where the relative luminosity profile for patches descending at 22 m/s is plotted along with the patch B1 and B2 data. This case demonstrates the superiority of the integrated luminosity technique since it provides a better agreement with the patch B2 data than the delta-layer case.

Figure 3.11 raises another question, however. It suggests that patches B1 and B2 may be at different altitudes. *Hosokawa et al.* [2010] reported that patches B1 and B2 result from a larger patch being sheared apart, suggesting the patches should be at the same altitude. In the *Hosokawa et al.* [2010] data, the luminosity of patch B2 is well defined several minutes before that of patch B1 and the luminosity of B2 subsides before that of B1. This is an indication

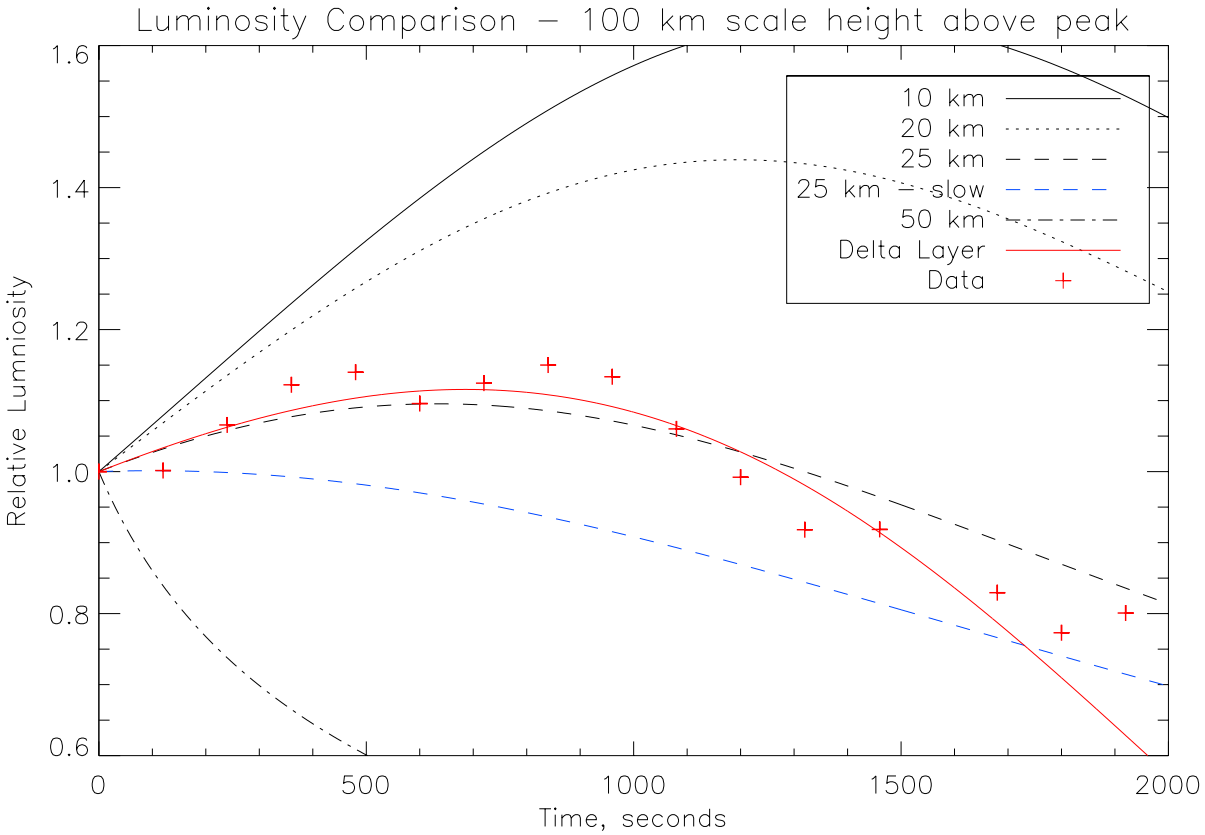

Figure 3.10: Luminosity profiles for the delta-layer case (red), descending at 17 m/s, and integrated profile case (black) are plotted along side patch data from *Hosokawa et al.* [2010]. Each patch has a top-side density scale height of 100 km and a peak density at 265 km.

that the plasma in B2 was reacting with a larger concentration of neutral atmosphere, perhaps at lower altitudes. The imager data only offers a two-dimensional projection of the sky, and so with a combination of the diffuse patch emissions and a parallax effect it is difficult to determine whether patch B1 and B2 both originated from a larger patch or were located at the same altitude. The results also suggest that the downward velocity of the patches are approximately equivalent, which seemingly contradicts the PolarDARN data.

Although the agreement between the integrated profile and the data is not ideal, it is important to remember that the luminosity profile is sensitive to variations of many parameters. We have shown that the luminosity profile is sensitive to both a starting altitude change, as well as any variation in the downward velocity of the patch. The values for $[N_2]$ and $[O_2]$

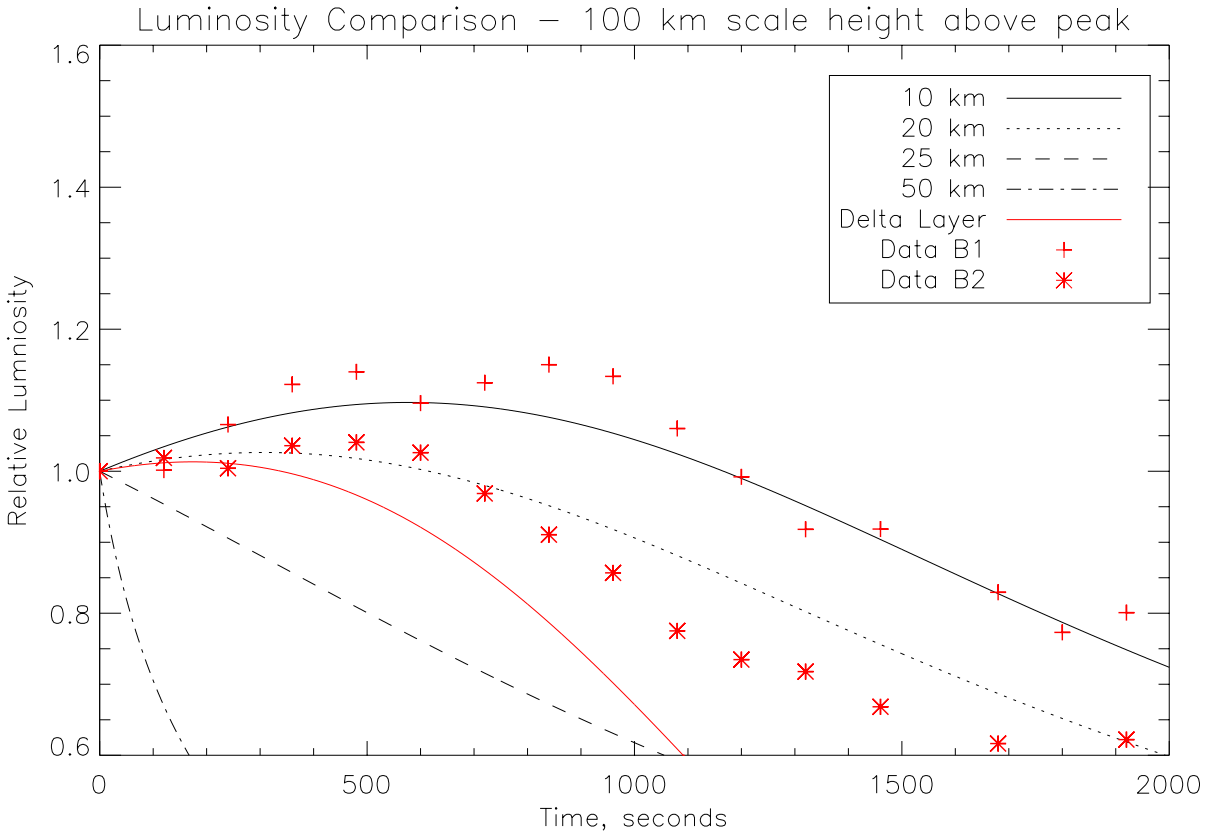

Figure 3.11: Luminosity profiles for the delta-layer case (red) and integrated profile case (black) are plotted along side patch data from *Hosokawa et al.* [2010] for patch B1 and B2. All patches are descending at 22 m/s. Each patch has a top-side density scale height of 100 km and a peak density at 250 km.

are provided by the MSIS model and not by any direct measurement. Any under-/over-estimation in the values of $[N_2]$ and $[O_2]$ by the MSIS model, may account for the difference between the profile and data in Figures 3.10 and 3.11. The velocity of the descending patch is assumed to be constant and although it was not done here, we are confident that creating a synthetic luminosity curve using techniques discussed in Section 3.6 would establish better agreement between the integrated profile and the *Hosokawa et al.* [2010] data.

3.8 Conclusion

We have shown that the very fact that polar cap F-region patches can be used to track the plasma drift motion means that their chemical evolution can be described to first order just

by knowing their mean altitude and characteristic density scale lengths. Given that once the patches are injected into the polar cap, there is typically no production from photoionization or particle precipitation, a change in altitude amounts to a change in the recombination rate. We have shown that under winter nighttime conditions, for patches starting near and above 250 km in altitude, a descending motion in excess of 10 m/s, starting from rest, introduces an initial increase in the intensity of the 630.0 nm patch emissions. The increase can be as large as a factor of 2 for a 50 m/s downward drift. The increase is related to the accelerated conversion of O^+ ions into O_2^+ ions which then recombine to produce the observed red line emission. However, after the initial increase the intensity goes down relatively fast (20 minutes time scale) owing to the resulting decrease in the O^+, i.e., in the net patch density, precisely because of the accelerated recombination rate. We have shown that the theory provides an excellent explanation for red line patch observations made over Resolute Bay at the end of December, 2006. On that day we found a clear instance of patches that started near rest as a result of changes in the interplanetary magnetic field. Following the halt in convection, the patches moved equatorward. The vertical component of the $\mathbf{E} \times \mathbf{B}$ was downward in this case and of the order of the 10 to 20 m/s needed to explain the change in brightness that was observed in two adjacent patches over time. We showed that even small modulations in the intensity of the patches could be explained through plausible variations in the plasma motion.

The present work opens up the possibility of using changes in patches intensity to monitor the vertical motions of patches and possibly even their vertical position (through the determination of neutral densities required to determine the time evolution of their brightness). As far as the motion of the patches is concerned we note in particular that the magnitude and direction of the plasma $\mathbf{E} \times \mathbf{B}$ drift control the vertical drift in the plasma. Changes in the intensity could be used to constrain other pieces of information related to plasma drift. For instance, the motion of patches is determined by monitoring the position of the patches with time. However, as the patches deform over time, this determination is not always as easy to perform as it looks. Similarly, under favorable conditions, one can use coherent radar data to determine the Doppler shift of the irregularities carried out within the patches. From this one can monitor the plasma drift, although, in principle, only along the line-of-sight of the radar.

The intensity modulations are related to the equatorward motion of the plasma and could, in this context, be used as additional information to constrain the motion of the patches. We have for instance shown that for the December 20, 2006 event that we discussed, the vertical motion inferred from changes in the intensity would have been more consistent with drifts measurably greater than reported by the PolarDARN Rankin Inlet HF radar data. Recent work [e.g., *Gillies et al.*, 2009; *Ponomarenko et al.*, 2009; *Gillies et al.*, 2012, and references therein] has demonstrated, however, that such an underestimation of the plasma drift is entirely possible once one takes into account the fact that the index of refraction is not unity, but could be as small as 0.7 to 0.8 for HF radars. In addition to this, the neutral densities provided by MSIS may be over-estimated. In this context, the inferred vertical motion of the patches can be used to constrain the index of refraction of the medium so as to have agreement between the vertical drift and the horizontal component of the plasma motion.

We also notice that the present work offers a possible explanation for the disappearance of HF radar echoes, starting 10 minutes after the onset of the cross-cap plasma drift. In particular, the calculation of the changes in the patch density associated with the changes in the luminosity reveals that the patch density had gone down by a factor of 2 after about 800 s and by a factor of 10 after about 1800 s in the case of the fast moving patch (Figure 3.3). The accompanying reduction in the patch density gradients would surely mean a reduction in the production of irregularities through the gradient-drift mechanism, the overall plasma density having become more uniform.

3.9 Summary and future work

In this chapter, the optical properties of F-region ionization patches was investigated through a case study involving two patches observed over Resolute Bay. It was concluded that the vertical motion of a patch can have a drastic effect on the luminosity and chemistry of the patch, establishing a connection between the polar-cap convection electric field and the luminosity of F-region ionization patches.

At the time of the observations, the RISR-N radar was not yet operational, preventing plasma density measurements which could constrain the model developed in this work. It

would be extremely beneficial to incorporate measurements from the RISR-N and soon to be operational RISR-C radars, to test the luminosity model introduced in this chapter. In this chapter only the relative luminosity was considered since the plasma density characteristics were not known. With RISR-N/-C, one could link the magnitude of 630 nm emissions to the neutral dynamics, plasma properties and electrodynamics of the region.

Chapter 4

An algorithm to detect F-region ionization patches

In this chapter, an algorithm to detect F-region ionization patches in RISR-N data is introduced. The output of the patch detection algorithm is compared to OMTI data to verify its ability to detect patches passing through the RISR-N FOV. The algorithm is then used to investigate the relationship between SuperDARN radar echo occurrence and the presence of patches in its FOV during March and December, 2010. The comparison between the presence of patches and SuperDARN echoes is done in an effort to clarify the interconnection between patches and SuperDARN echoes in the polar ionosphere. A survey of the patches detected in March and December, 2010, in terms of the standard ISR parameters, n_e, T_i, and T_e is also conducted.

4.1 Motivation

The vast majority of previous patch research is in the form of a case study in which an individual or a group of patches were probed with an ISR and another radio instrument [e.g., *Buchau et al.*, 1983; *Dahlgren et al.*, 2012a; *Dahlgren et al.*, 2012b, and references therein], or monitored with an all sky imager [e.g., *Hosokawa et al.*, 2011; *Perry et al.*, 2013; *Hosokawa et al.*, 2013b, c]. These studies are beneficial for gaining insight into patch generation mechanisms, [e.g., *Valladares et al.*, 1994; *Walker et al.*, 1999; *Oksavik et al.*, 2010], or the morphology or evolution of a singular patch or group of patches, as they transit through the ionosphere [e.g., *Lorentzen et al.*, 2004; *Zhang et al.*, 2013]. One of the interesting characteristics of patches is their persistent presence in the nighttime polar ionosphere, under southward IMF conditions

(recall Section 1.3.4). *Carlson* [2012] reasoned that patches are the distinctive feature of the polar ionosphere in a southward IMF state. Therefore, patches should not be investigated as an evanescent feature of the polar ionosphere, but as a fundamental component of the polar ionosphere. Patch research should include studies incorporating large data sets populated with numerous patch events spanning over long periods of time. With such studies, comparisons can be made between patch characteristics, such as their absolute density or their occurrence, to other long term trends such as solar wind conditions and variations in the IMF.

ISRs are a very effective tool for investigating F-region ionization patches. Their ability to provide accurate and precise diagnostic measurements of the ionosphere, namely, their ability to detect a patch, an F-region plasma volume with a density that is twice that of the background ionosphere [*Crowley*, 1996], is fundamental to patch research. The location of the EISCAT Svalbard Radar (ESR), RISR-N and PFISR radars, in the high- and polar-latitudes is also ideal for observing patches. Despite this, an automated method of detecting patches in ISR has yet to be developed, even though algorithms have been created for other instruments and datasets, which are discussed shortly. The intent of this work is to remedy this by establishing an algorithm that effectively identifies ionization patches within the FOV of the RISR-N.

4.2 Previous work featuring patch detection algorithms

Coley and Heelis [1998] analyzed a patch dataset containing 225 patches detected by the Dynamics Explorer 2 (DE2) satellite. They used an algorithm developed by *Coley and Heelis* [1995], which identified a patch in a multi-step process. First, a candidate patch "edge" was detected if the n_e measured by the retarding potential analyzer (RPA) onboard the spacecraft increased by 40% over a spatial scale of 140 km. If the positive gradient was followed by a second edge with a negative gradient shortly thereafter (as the spacecraft moved through the candidate patch), the candidate patch was selected for further inspection, after which, if the RPA data revealed that the n_e between the patch edges was twice that of the background n_e (their definition of the background ionosphere is discussed in the next section),

then the candidate patch was confirmed as a patch. With this method, only structures of scale size between 100 and 875 km were analyzed. From the dataset, the authors found the distribution of patch occurrence was asymmetric with respect to the orientation of the IMF, with the most patches occurring during negative B_z and B_y IMF conditions. The distribution of patch occurrence during northward IMF conditions was found to be reduced and nearly symmetric about IMF $B_y = 0$ [*Coley and Heelis*, 1998]. The authors also reported on the structuring of patch edges and the velocity of the patches.

Separate, alternative methods for patch detection were introduced by *Noja et al.* [2013] and *Burston et al.* [2014], who reported on datasets containing several thousand and 71 patches, respectively (a precise number was not given in the former). In both methods, patches were identified via a satellite-based total electron content (TEC) measurement. TEC is an estimate of the total number of electrons along the path length, in this case, between a GPS receiver and transmitter. With a high precision timing signal, such as one provided by GPS, the ionospheric n_e along a GPS patch length can be estimated by measuring the dispersion of the GPS signal as a function of its carrier frequency [*Garner et al.*, 1996]. With the large dataset in *Noja et al.* [2013], a thorough comparative analysis of the spatial and seasonal distribution of patches with respect to solar and IMF conditions was performed, in both the northern and southern hemisphere. This was accomplished for patches of at least 75 km in scale size. In *Burston et al.* [2014], an assimilative computer model using TEC measurements as an input, was able to not only detect patches but track their motion through the ionosphere as well. However, this method was only effective for patches with a scale size of at least 500 km.

Hosokawa et al. [2006] developed an algorithm which tracked the motion of 19 patches detected by the OMTI imager at Resolute Bay. The tracking method involved the cross-correlation of sequential 630 nm OMTI images in time. Patches were identified as enhancements in 630 nm emissions which did not have a corresponding increase in the 557.7 nm emissions, distinguishing patches from other optical phenomena such as aurora. The magnitude of the emissions was required to be 30 R above a baseline emission intensity which was estimated for a 12-minute "search window". Whereas *Hosokawa et al.* [2006] tracked patches that were manually identified from the data, *Hosokawa et al.* [2009b] were able to

track the motion of patches that were automatically detected. It should be pointed out that the *Crowley* [1996] definition of a patch is specific to n_e, and not optical emission intensity. As it stands, a working definition of an optical patch does not yet exist since emissions at 630 nm are a function of the altitude of the patch, as well as the vertical velocity of the patch [e.g., *Perry et al.*, 2013, and Chapter 3 of this work]. Nonetheless, the definition put forward by *Hosokawa et al.* [2009b] was shown to be effective at capturing the optical signature of patches. This allowed for the optical database of patches observed by OMTI to be significantly augmented to include 561 patches. Analysis on the larger dataset revealed a strong correlation between the magnitude of southward IMF B_z and the speed of the patch. Also, a strong correlation between the velocity and the IMF B_y component, in which the velocity of the patch is directed in the dawn-to-dusk (dusk-to-dawn) direction for positive (negative) IMF B_y, was also reported.

4.3 RISR-N patch detection algorithm

4.3.1 The "background" ionosphere

The patch detection algorithm developed for the RISR-N system, hereafter referred to as the "RISR-N algorithm", which will be introduced shortly, is based on the *Crowley* [1996] definition of an F-region ionization patch; that is, a volume of plasma with a n_e that is greater than twice that of the background ionosphere. Despite the simplicity of the definition, there is a caveat: what constitutes the "background" ionosphere? As it turns out, a concise definition does not exist. A working definition of "background" was discussed in each of the communications featuring patch detection algorithms reviewed earlier.

In *Coley and Heelis* [1995], the n_e data was filtered to eliminate any n_e features outside of the 100 to 875 km scale size along the trajectory of the DE2 spacecraft. Any features outside of the desired scale size were considered as the background. *Burston et al.* [2014] used a mean of all of the TEC measurements above 50° geographic latitude, over a time-frame of 15 minutes as a measurement for background. As was mentioned previously, *Hosokawa et al.* [2009b] used a 1 hour mean of the 630 nm emissions, excluding patches, as an estimate for

the background. *Noja et al.* [2013] chose a different tact; spatial and temporal smoothing was not used. In that work the next-to-lowest n_e measurements in the vicinity of a peak in TEC (bounded by a positive and negative slope in TEC) as a proxy for the background ionosphere. A more coarse definition of a patch was used by *Moen et al.* [2008], who labelled any measurement of $n_e > 1 \times 10^{12}$ m^{-3} as a patch, thereby designating any measurement below 0.5×10^{12} m^{-3} as the background ionosphere.

In this work an estimate of the background ionospheric density is based on n_e measurements obtained within the RISR-N FOV. RISR-N offers a distinct advantage in providing a background estimate; it is able to provide a multipoint volumetric measurement of the ionospheric n_e upon which a patch detection will be based. An alternative to this would be to use a model such as the International Reference Ionosphere (IRI) [*Bilitza*, 2001; *Bilitza and Reinisch*, 2008] as an estimate for the background ionosphere. However, as the results from *Moen et al.* [2008] and *Gillies et al.* [2012] show, the IRI does not sufficiently describe the F-region polar regions to justify its use there.

A plot of the F-region n_e measured by RISR-N as function of altitude along RISR-N Beam 23 for the entire day of March 11, 2010 is plotted in Figure 4.1. A plot of a shorter time segment on the same beam during the same day is given in Figure 4.2. The IRI model output is also plotted in both figures. In Figure 4.1 error bars are not plotted with the data, to avoid cluttering the figure; however, error bars are plotted with the data in Figure 4.2 as dashed lines. A plot of the RISR-N beam geometry for this date is shown in Figure 4.3. The goal of these plots is to demonstrate the amount of fluctuation the n_e profile can undergo in the polar ionosphere. The variability of the n_e profile in both Figures 4.1 and 4.2 is substantial. Throughout the day, the n_e varies by over an order of magnitude. In Figure 4.1, there are several examples of disagreement between the IRI profile and the RISR-N measured profile. For example, at 03:00 UT, the IRI model (triangle symbols) suggests a n_e peaking near 1×10^{11} m^{-3}, while the RISR-N n_e peaks are about twice that amount during that time frame. As it turns out, the variability of the RISR-N measurements at this time was a signature of patches moving through the FOV. At 15:00 UT, the IRI model (square symbols) systematically underestimates the measured RISR-N vertical profile. On closer inspection of Figure 4.2, it is clear that the large changes transpire on a time-scale of minutes. Some

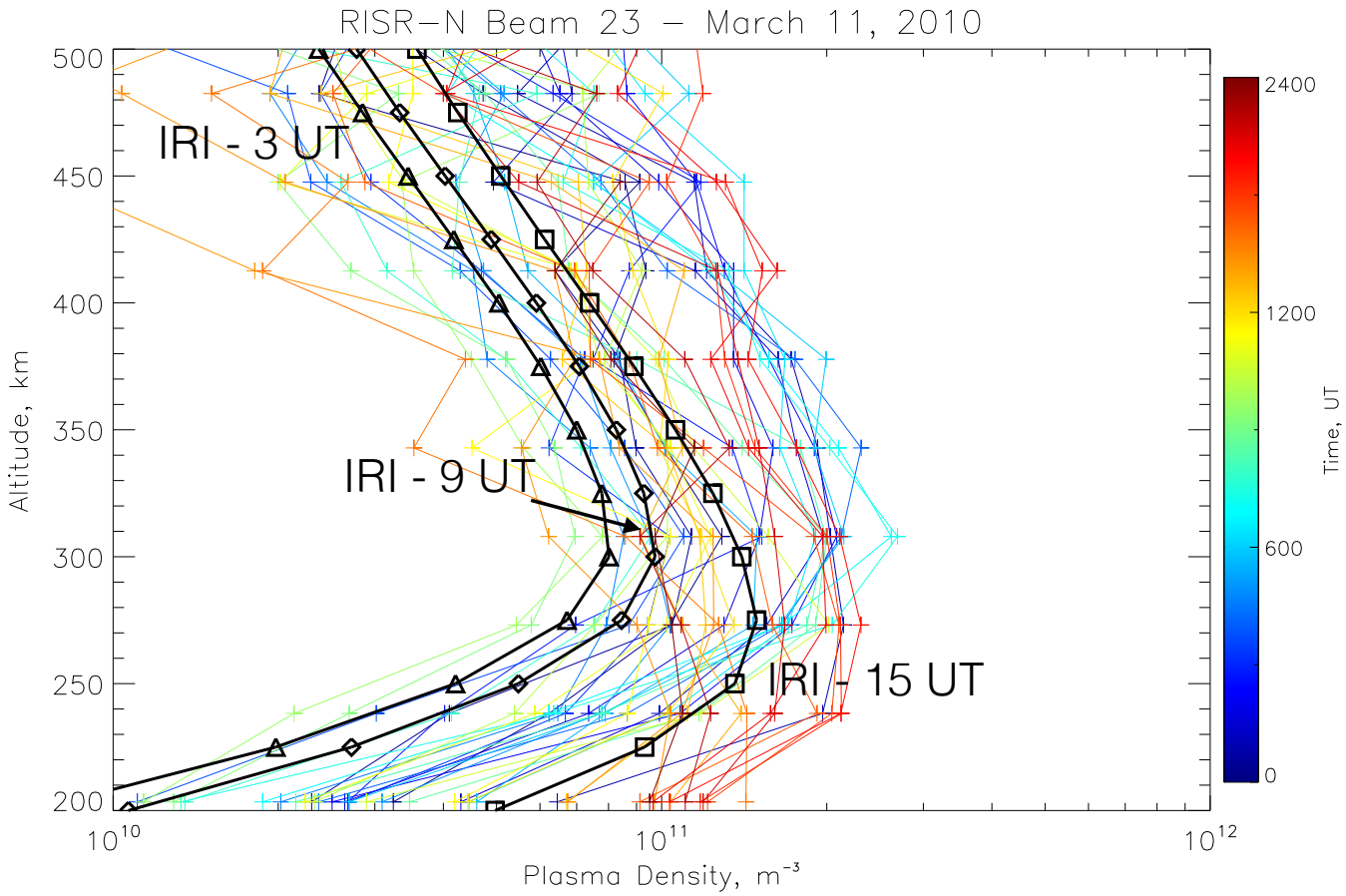

Figure 4.1: A plot of the n_e as function of altitude along RISR-N Beam 23, for the entire day on March 11, 2010. Profiles from the IRI model for 03:00 UT (triangle), 09:00 UT (diamond), and 15:00 UT (square) are also plotted.

of this variability may be attributed to patches passing through the RISR-N FOV between 03:00 and 11:00 UT (see Section 4.3.3). Once again, the IRI model appears to systematically underestimate the RISR-N n_e measurements. Not only does the magnitude of the density vary considerably, but the general shape of the altitude profile as well as the positioning of the peaks show marked fluctuations as well. It is difficult to justify using IRI since it does not accurately model the variability of the polar ionosphere, even though the variability is seemingly due to the presence of patches.

One strategy to obtaining an estimate describing the background polar ionosphere would be to model a vertical n_e profile that would be representative of the region given an input of other parameters, such as solar and IMF conditions. In this case, to detect a patch, one

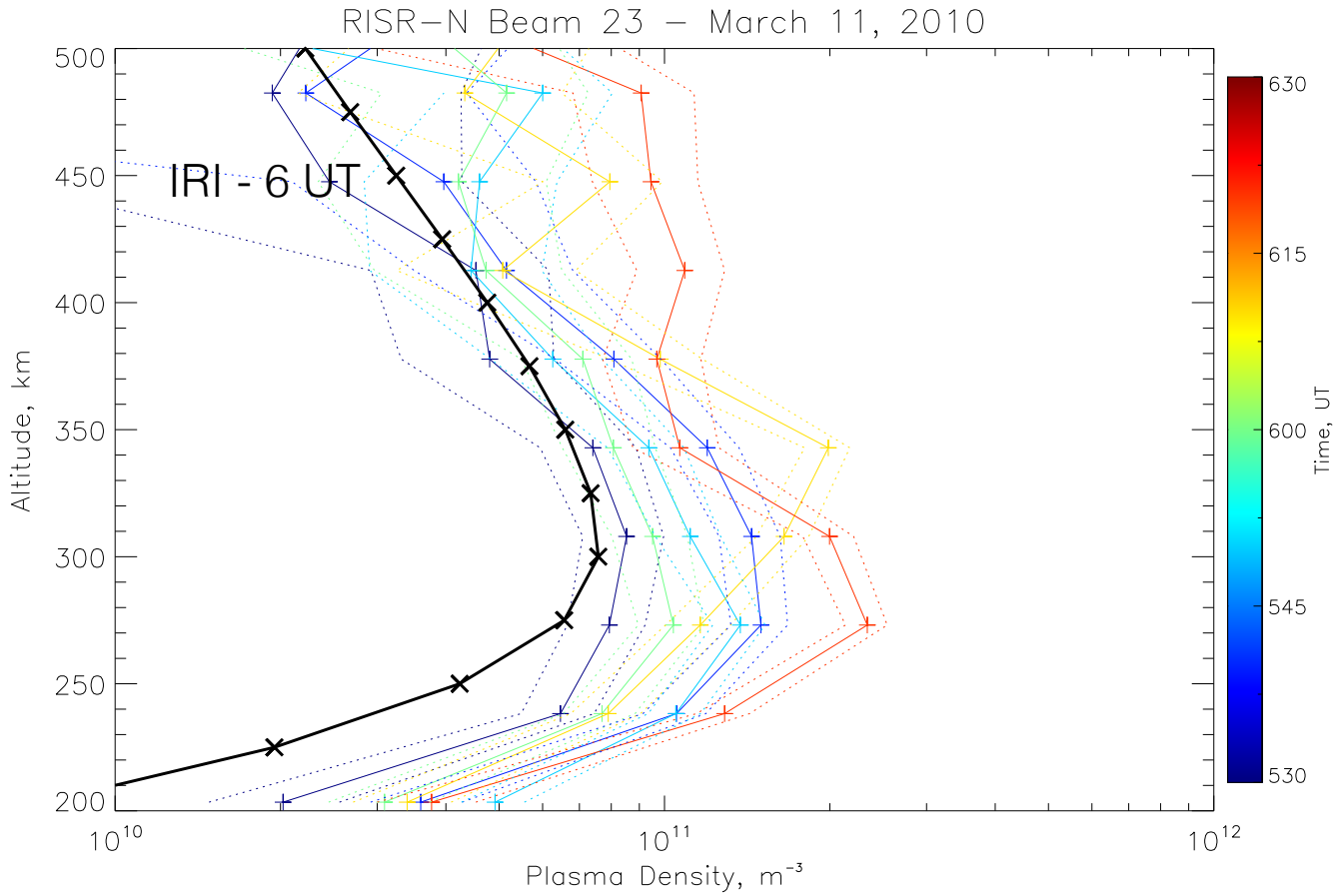

Figure 4.2: A plot of the n_e as function of altitude along RISR-N Beam 23, between 05:30 and 06:30 UT on March 11, 2010. Profiles from the IRI model for 06:00 UT is also plotted.

would need to detect an n_e profile that is at least twice that of the background density profile. This is a difficult task to accomplish not only because of the short time-scale on which the magnitude of the profile changes, but also because of changes in the shape of the profile, as evidenced in Figure 4.2. Also, by comparing measurements to a modelled profile, we would also be introducing a bias into the patch detection method. An estimate of the profile of the background ionosphere would be a product of some filtering, and would invariably resemble a standard F-region n_e profile, i.e., an IRI modelled output. Some patch generation mechanisms may produce vertical plasma profile that may not take on the same shape of the vertical F-region plasma profile, such as patches created by particle precipitation. Even though patches created by this mechanism may satisfy the *Crowley* [1996] criterion, they

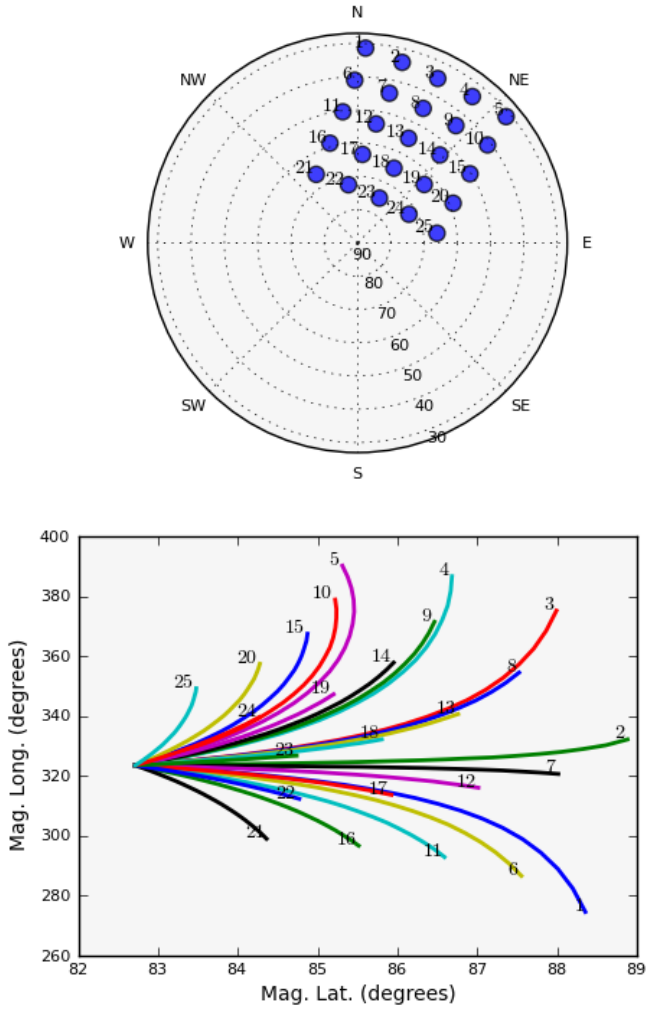

Figure 4.3: A plot of a 25-beam RISR-N mode (top) operating on March 11, 2010, with the projections of the 25 look directions plotted in a geomagnetic coordinate system (bottom), courtesy of SRI International.

would risk being overlooked by a detection algorithm comparing them to a background n_e profile. It is therefore most suitable to create an estimate of the background polar ionosphere which can serve as a threshold over which a candidate plasma density enhancement must surpass in order to be registered as a patch.

In order to obtain a suitable estimate of the background n_e of the polar ionosphere a characteristic time of the ionosphere is needed, a time over which we can assume that the polar ionosphere is static. For the RISR-N algorithm, the characteristic time is considered to be the length of time a patch takes to drift through the RISR-N FOV. The definition

of a patch is relative; identifying a patch requires a comparison to the background ionosphere. It is therefore most appropriate to compare a candidate patch to the ionosphere in which it is immersed. The RISR-N FOV at F-region altitudes spans approximately 500 km meridionally and 600 km zonally. Patches have been observed to drift through the polar ionosphere at speeds ranging from 300 to 1000 m/s. However, the patch speeds are generally below 500 m/s [*MacDougall and Jayachandran*, 2001]. The distribution of patch speeds reported by *Hosokawa et al.* [2009b] is centred at approximately 300 m/s, and the data from *MacDougall and Jayachandran* [2001] showed median velocities nearing 400 m/s. This corresponds to a travel time across the RISR-N FOV of the order of 30 minutes. The time-scale of chemical recombination must be considered here as well. Using Equation 3.6, with the chemical reaction rates cited in Section 3.4.1, at 300 km altitude, it would take of the order of 60 minutes to deplete a n_e of 2×10^{11} m^{-3} (consistent with measurements in Figure 4.2) by 35%. It would take two hours to deplete that amount of plasma by a factor of e, thus the chemical recombination time-constant is approximately 2 hours. This estimate is higher than time-constants inferred by *Pedersen et al.* [1998]. They attributed the steepness of the horizontal gradients of patches to chemical recombination, and therefore inferred the chemical recombination decay time from the horizontal gradients they measured with an ISR. They reported a time-constant of 1 hour. This means that a volume that started out as a patch would not be depleted by chemical recombination during the 30 minutes time-frame. Thus, 30 minutes is an appropriate estimate for a characteristic time for the polar ionosphere within the RISR-N FOV. This has more to do with the sensitivity of RISR-N rather than the formal definition of a patch. A patch and the background ionosphere deplete at an equal rate since they are both immersed in equal neutral densities. However, below a certain plasma density a patch or the background ionosphere may be too tenuous to detect and quantify with RISR-N. We wish to avoid this circumstance while a patch is drifting through the RISR-N FOV.

The diffusion time-scale should also be considered here. In the F region, the diffusion coefficient for ions diffusing perpendicular to the magnetic field, $D_{i\perp} = r_g^2 \nu_{in}$, is a function of the gyroradius of the ion, r_g and the ion-neutral collision frequency, ν_{in} [*Kelley*, 2009]. In the polar F region, at 300 km altitude, $D_{i\perp} \simeq 300^2 \times 0.3 \simeq 27 \times 10^3$ m^{2}s^{-1}. Using a

gradient scale length of 100 km for a patch, consistent with measurements by *Pedersen et al.* [1998], the perpendicular diffusion rate for a patch with a density 2×10^{11} m^{-3} is two orders of magnitude slower than the chemical recombination rate, equating to a time constant of the order of days. According to *Schunk and Nagy* [2000] diffusion along the magnetic field line, ambipolar diffusion, has a diffusion coefficient about an order of magnitude larger than perpendicular diffusion. Thus a patch will recombine long before it is dissipated by diffusion.

Taking the aforementioned into consideration, a 30-minutes running average of the median n_e in the RISR-N FOV, between 200 and 500 km altitude, will be considered the "background" for the RISR-N algorithm.

4.3.2 The RISR-N algorithm

The RISR-N algorithm is relatively straightforward. Focusing on the 200 to 500 km altitude range within the RISR-N FOV:

1. Calculate a 30-minute running average of the median n_e in the RISR-N FOV. Each RISR-N scan (RISR-N scans typically range from 2 - 5 minutes in length, depending on the number of beams in the FOV and the operating mode) is represented by a median of the n_e measured in that scan. This is the "background" estimate.

2. Sample each resolution cell along a RISR-N beam, comparing each n_e measurement to the background estimate.

3. If the measured n_e along three consecutive resolution cells along a beam are twice that of the background estimate, a patch has been detected in that beam.

4. Repeat steps 2 through 3 for each beam in the RISR-N FOV.

The RISR-N algorithm takes advantage of the field-aligned nature of patches, the slant of the RISR-N beams and the acute angle they make with respect to the surface of the Earth and the local geomagnetic field. The geomagnetic field-lines are nearly vertical in the RISR-N FOV. Their dip angle, measured with respect to the surface of the Earth, is approximately 87°. Patches are therefore approximately vertically aligned; they are strongly

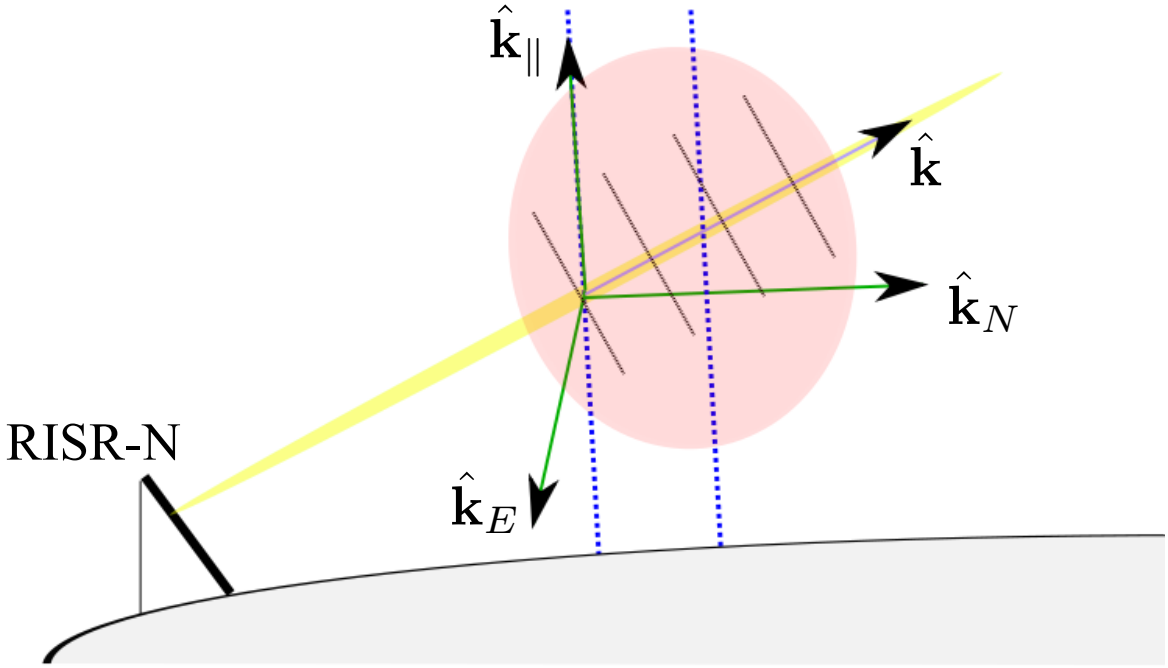

Figure 4.4: The geometry of a single RISR-N beam with unit k-vector, $\hat{\mathbf{k}}$, probing a patch aligned along the local geomagnetic field, shown in blue. The component of the beam parallel to the magnetic field is labelled $\hat{\mathbf{k}}_{\parallel}$. The orthogonal zonal and meridional components are $\hat{\mathbf{k}}_E$ and $\hat{\mathbf{k}}_N$, respectively. Resolution cells along the beam are marked by black lines.

field-aligned as a result of the low diffusion coefficient, $D_{i\perp}$. RISR-N beams have elevation angles which range from 30° to 70°, with respect to the surface of the Earth, and will thus intersect patches at an acute angle with respect to the geomagnetic field line. By requiring three consecutive RISR-N resolution cells along the beam to have a patch n_e that is twice that of the background ionosphere (Step 3, above), satisfying the *Crowley* [1996] criterion, the algorithm identifies volumes of plasma that are approximately the scale size and density of patches, by virtue of the RISR-N beam geometry.

Three resolution cells along a slanted RISR-N beam can have sizeable projection that is normal and parallel to a patch. To help illustrate this point, the geometry of a single RISR-N beam intersecting a patch is shown in Figure 4.4. Here, $\hat{\mathbf{k}}$ is the unit vector of the radar beam; $\hat{\mathbf{k}}_{\parallel}$ is the parallel direction of $\hat{\mathbf{k}}$, with respect to the geomagnetic field; $\hat{\mathbf{k}}_N$ is the northward direction of $\hat{\mathbf{k}}$, with respect to the geomagnetic field; and $\hat{\mathbf{k}}_E$ is the eastward

direction of $\hat{\mathbf{k}}$, with respect to the geomagnetic field. RISR-N beam 23 in Figure 4.3 reaches 308 km altitude at a distance of 318 km along the beam (i.e., downrange). At this point, $\hat{\mathbf{k}}_{\parallel} = 0.96$, $\hat{\mathbf{k}}_E = 0.05$, and $\hat{\mathbf{k}}_N = 0.28$ (information courtesy of SRI International). Starting at 308 km altitude, three consecutive resolution cells span a cumulative distance of 108 km along the beam. With the given beam geometry, the three cells span 104 km in altitude, 5 km zonally and 30 km meridionally. These values vary between beams in the RISR-N FOV, from 55 to 110 km in altitude, 5 to 75 km zonally, and 10 to 90 km meridionally. Therefore, any beam with a patch signature encompasses a non-trivial portion of the ionosphere. Along with the beam geometry, it should be pointed out the beams in Figure 4.3 are separated by approximately 30 km. This spacing governs the spatial resolution of the RISR-N system and RISR-N algorithm. *Crowley* [1996] stipulated that a patch must have a scale size of the order of 100 km, which is larger than some of the scales stated here. Nonetheless we believe the RISR-N algorithm and its associated scale sizes is still suitable. One reason is that the *Crowley* [1996] criterion is rather arbitrary and biased. In the regime above the 10 km scale length, there is no physical justification for placing a lower limit on the scale size of a patch. Moreover, there is enough evidence to suggest that patches can be smaller than the 100 km scale size [e.g., *Kelley et al.*, 1982; *Dahlgren et al.*, 2012a; *Dahlgren et al.*, 2012b]. By arbitrarily placing a lower limit on the scale size of patches at 100 km, we may be underestimating their population and importance in the polar ionosphere.

4.3.3 RISR-N algorithm test

The RISR-N algorithm was tested against an OMTI dataset showing an unambiguous case of patches drifting over Resolute Bay. An OMTI keogram showing 630 nm emissions, from 03:00 to 10:00 UT on March 11, 2010 is plotted in Figure 4.5. The keogram shows the data collected from the North to South meridian within the OMTI FOV. The dim, slanted features showing a North to South displacement are clear signatures of patches over Resolute Bay [cf. *Hosokawa et al.*, 2006; *Hosokawa et al.*, 2013a]. The optical data has not been corrected for atmospheric extinction or the non-uniformity of the viewing geometry, i.e., the van Rhijn effect. Also shown in Figure 4.5 is a plot of the n_e measured by RISR-N in beam 23, as a function of altitude along the beam. The n_e enhancements measured are signatures of patches

passing through the RISR-N beam. In Figure 4.5, it is clear that the optical signatures in the OMTI keogram are concurrent with the n_e enhancements measured in RISR-N beam 23. Similar

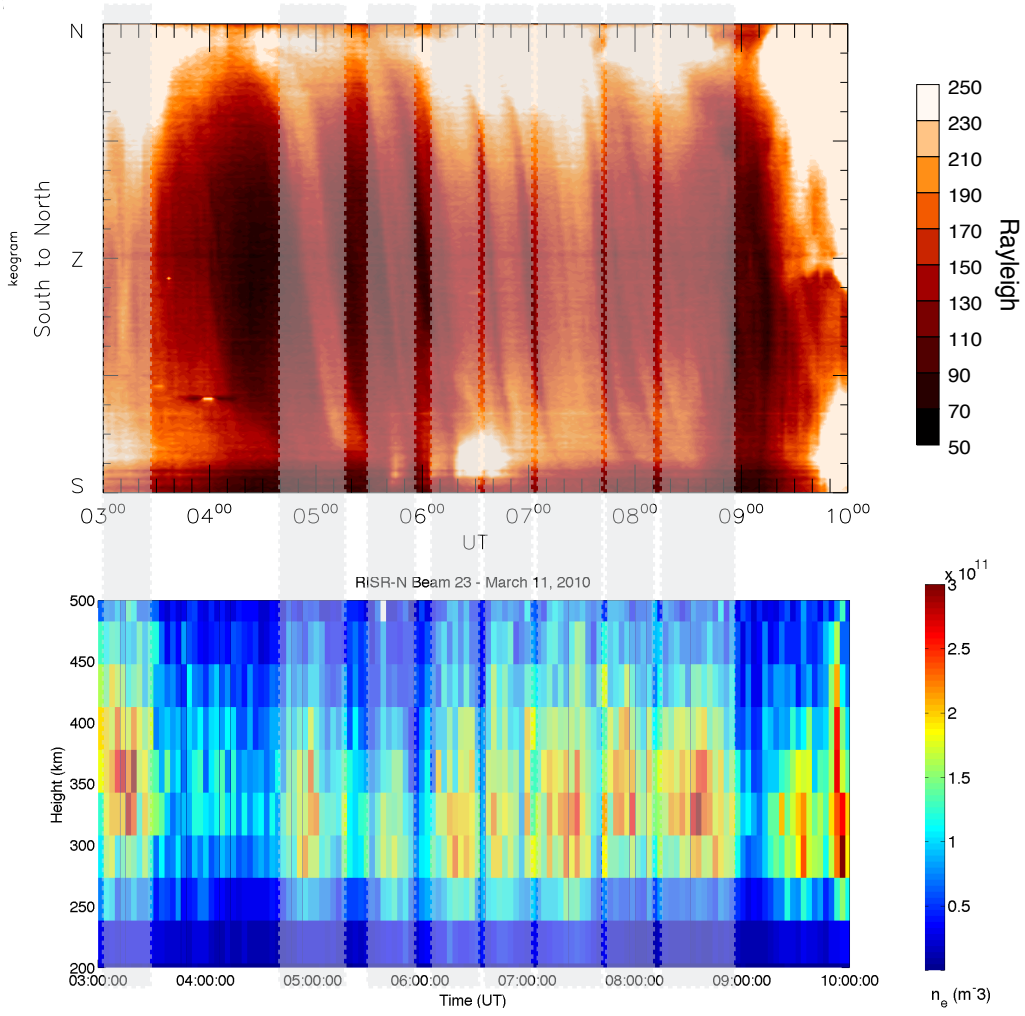

Figure 4.5: An OMTI keogram (top) from March 11, 2010, showing several optical signatures at 630 nm consistent with patches moving in a North to South direction. A plot of the n_e (bottom) measured in RISR-N beam 23, as a function of altitude. The RISR-N density signatures are consistent with patches and concurrent with the patches observed in OMTI, which has been highlighted to guide the eye.

A plot of the output of the RISR-N algorithm output is plotted in Figure 4.6. The patch detection "count" is plotted along with OMTI data, for the same segment of time displayed in Figure 4.5. A patch detection count is registered when a patch has been detected by the RISR-N algorithm. Since RISR-N beams have many resolution cells along the beam in the 200 to 500 km altitude range, multiple counts can be tallied for a single RISR-N beam.

Counts will be converted into a more meaningful quantity, the "patch index", shortly. The OMTI data plotted is from the zenith of the imager, labelled as Z in Figure 4.5. From the collocation of the luminosity and patch Figure 4.6, it is clear that the RISR-N algorithm is capable of detecting density enhancements within the RISR-N FOV that are consistent with patches. For nearly all of the peaks in the OMTI trace, there is a corresponding peak in the patch count output by the RISR-N algorithm. This indicates that bright optical features and n_e signatures, which are both a signature of patches, were passing through the same region of ionosphere at the same time. It is important to note that the OMTI measurements are biased to an altitude of approximately 250 km. Above that altitude, the neutral atmosphere becomes too tenuous to produce significant amount of luminosity at 630 nm, and below that altitude the 630 nm emissions become quenched [*Perry et al.*, 2013]. This may be why the RISR-N algorithm showed a peak at approximately 08:30 UT while the OMTI emissions remained relatively featureless. The emissions of these patches may have been quenched, or the altitude of the patches may been too high to produce any significant luminosity feature.

Non-patch events: identifying "false-positives"

In order to further gauge the effectiveness of the RISR-N algorithm, it was also tested against instances in which other ionospheric phenomena were passing through the RISR-N and OMTI FOV, such as a case of polar aurora, and one of a sun-aligned arc. A four hour segment on December 11, 2009 featuring a brilliant sun-aligned arc event was selected to test the algorithm. A keogram of the event along with a general FOV plot of the OMTI imager from 02:30 UT is given in Figure 4.7. A plot of the plasma density, n_e, ion temperature T_i, and electron temperature, T_e, measured in RISR-N beam 12 for the same segment of time is plotted in Figure 4.8. The results of the patch detection algorithm are plotted in Figure 4.9, and are presented in the same form as Figure 4.6.

In Figure 4.8, the plasma density, n_e in the polar ionosphere was quite low until the arrival of the arc, at approximately 02:30 UT. The RISR-N was not operational after approximately 03:20 UT. In Figure 4.8, the absence of colour is not due to the absence of RISR-N data, but due to $n_e < 1 \times 10^{10}$ m^{-3}, which does not register on the provided colour scale. Since the ionosphere being measured is at polar latitudes and the measurements occurred

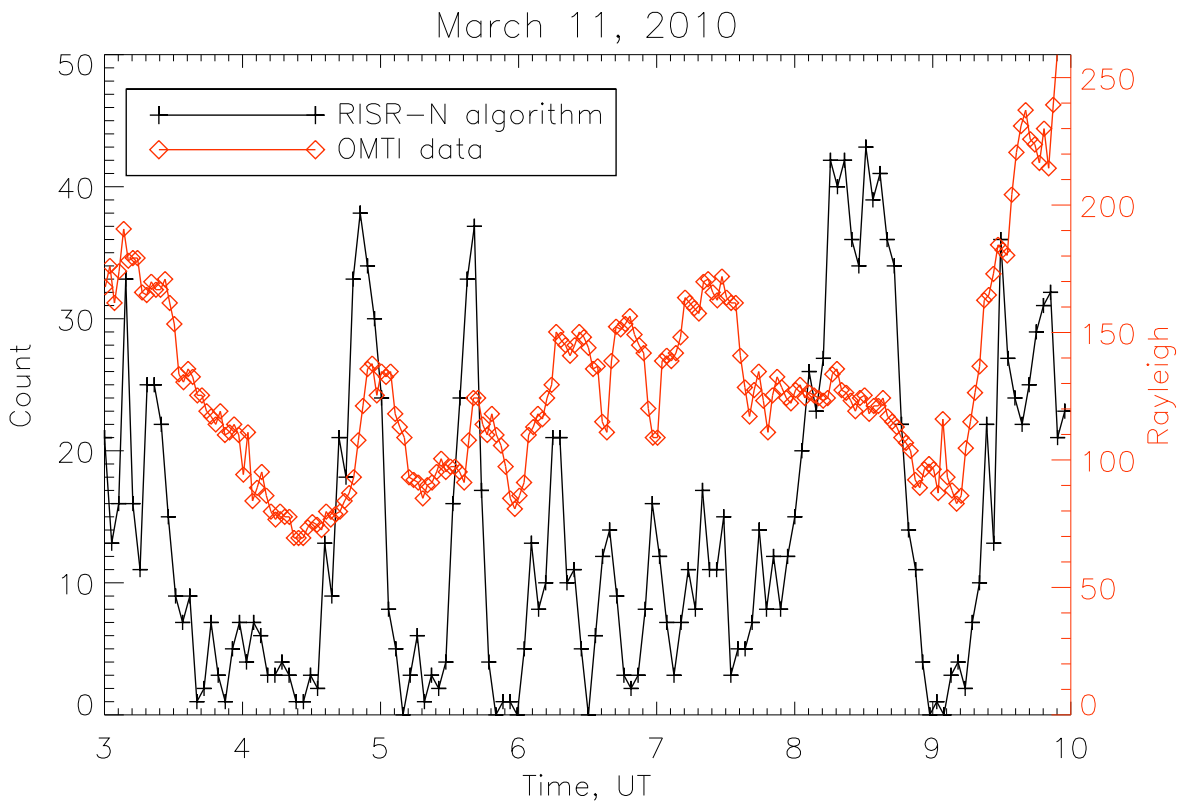

Figure 4.6: The output of the RISR-N algorithm plotted with the optical data from the zenith of the OMTI imager, for the same segment of time plotted in Figure 4.5. A good correlation between the peaks of the RISR-N algorithm and peaks in the OMTI luminosity data is evident.

during the winter, no photoionization would have been taking place. Chemical recombination would have had nearly an entire day to deplete n_e levels in the region. The arrival of the arc is marked in the top panel of Figure 4.8, by a sudden increase in n_e, by an order of magnitude, with a peak near 300 km altitude. Signatures of the arc arrival are also seen as ion temperature, T_i and electron temperature T_e increases. The former being a byproduct of enhanced electric field and frictional heating between the ion and neutral gasses.

Enhanced n_e and T_e are indicative of particle precipitation, and can be attributed to arcs [e.g., *Carlson et al.*, 1984; *Mende et al.*, 1988; *Dahlgren et al.*, 2014]. The main optical body of the arc is due to an upward field-aligned current (FAC), carried by precipitating electrons. However, it is difficult to identify an arc strictly from ISR data, and so optical data is normally used to confirm the presence of an arc. The results of the RISR-N algorithm

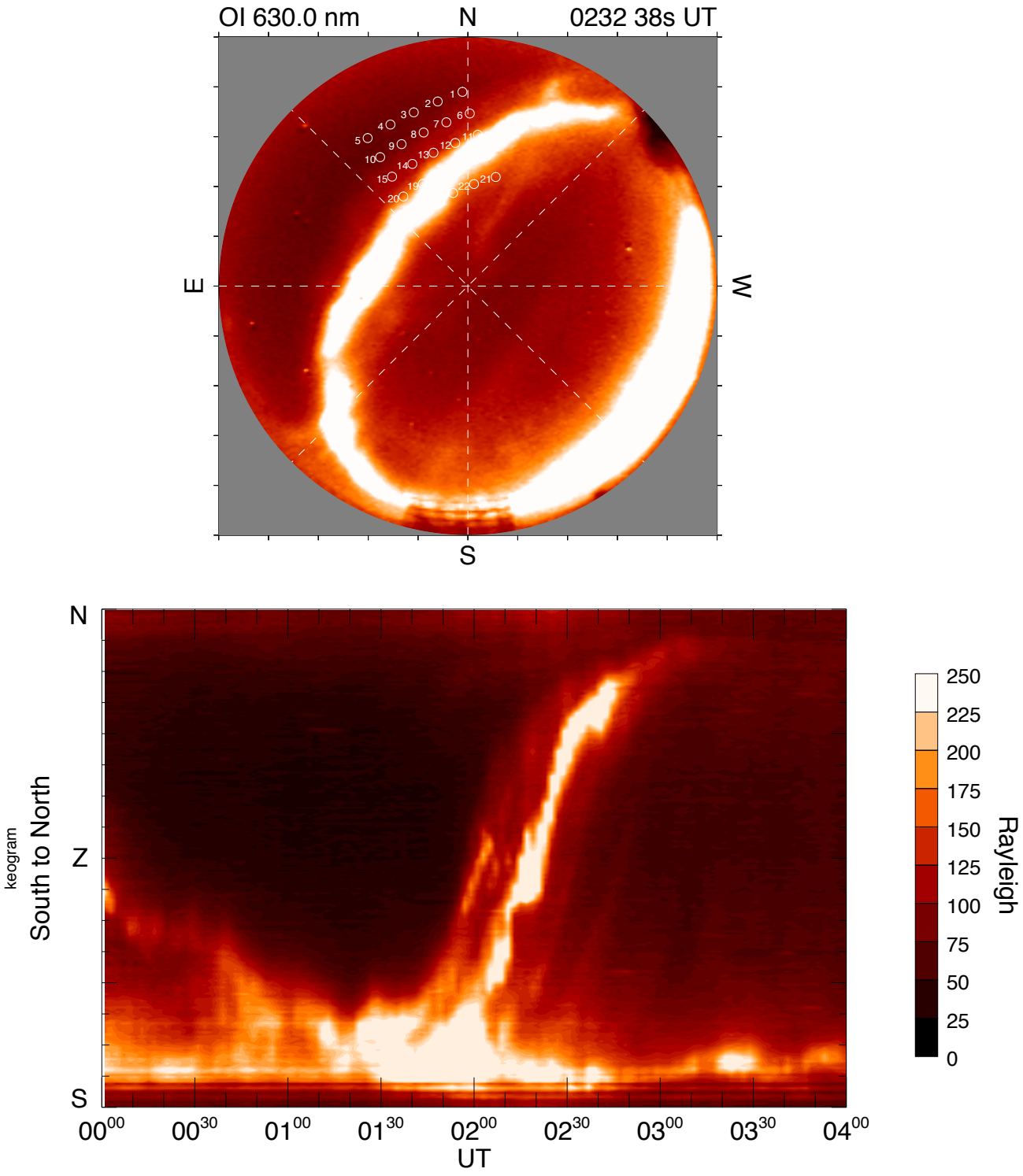

Figure 4.7: An OMTI FOV plot (top) showing an arc event at 02:32 UT on December 11, 2009. RISR-N beams are shown as white circles. A keogram (bottom) of the four hour segment surrounding the arc event. Both plots share the same colour scale.

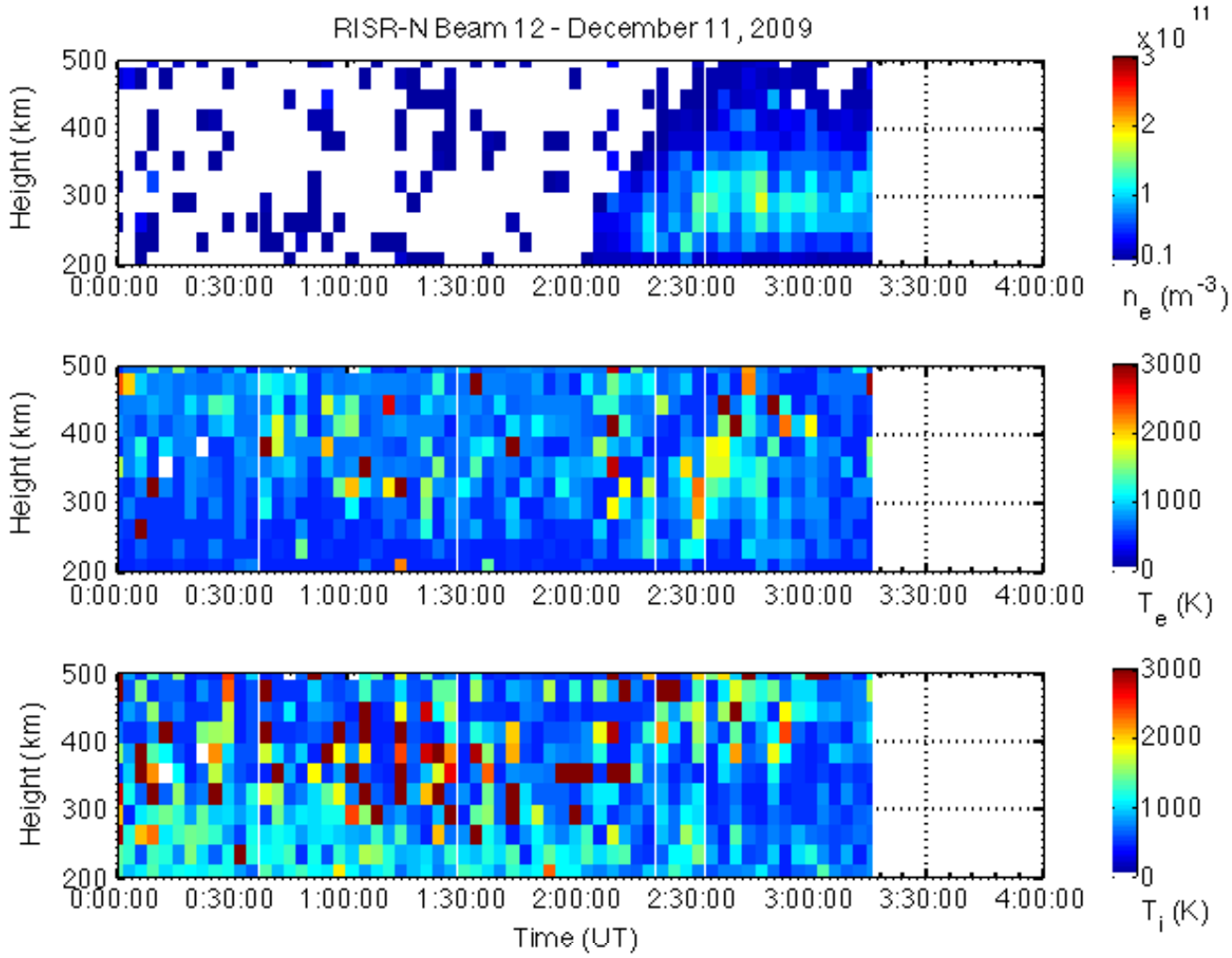

Figure 4.8: A RISR-N parameter plot showing n_e (top panel), T_e (middle panel) and T_i (bottom panel) from RISR-N beam 12 as a function of time and altitude. The signature of the arc shown in Figure 4.7 can be seen starting at approximately 02:30 UT.

in Figure 4.9 show that the arc passing through the RISR-N FOV produces a similar patch count to that of a patch moving through the FOV, as shown in Figure 4.6. This is clearly an undesirable result, since the arc presents a "false-positive" result for the RISR-N algorithm. This notion can be extrapolated to concluding that any phenomena producing aurora, not only arcs, would also result in a false-positive result with the RISR-N algorithm, as long as n_e became enhanced as a result.

One possible solution to this is to incorporate a temperature filter in the RISR-N algorithm. If the RISR-N algorithm detects an n_e enhancement that is consistent with a patch, but the temperature of the plasma is above a level that is more indicative of parti-

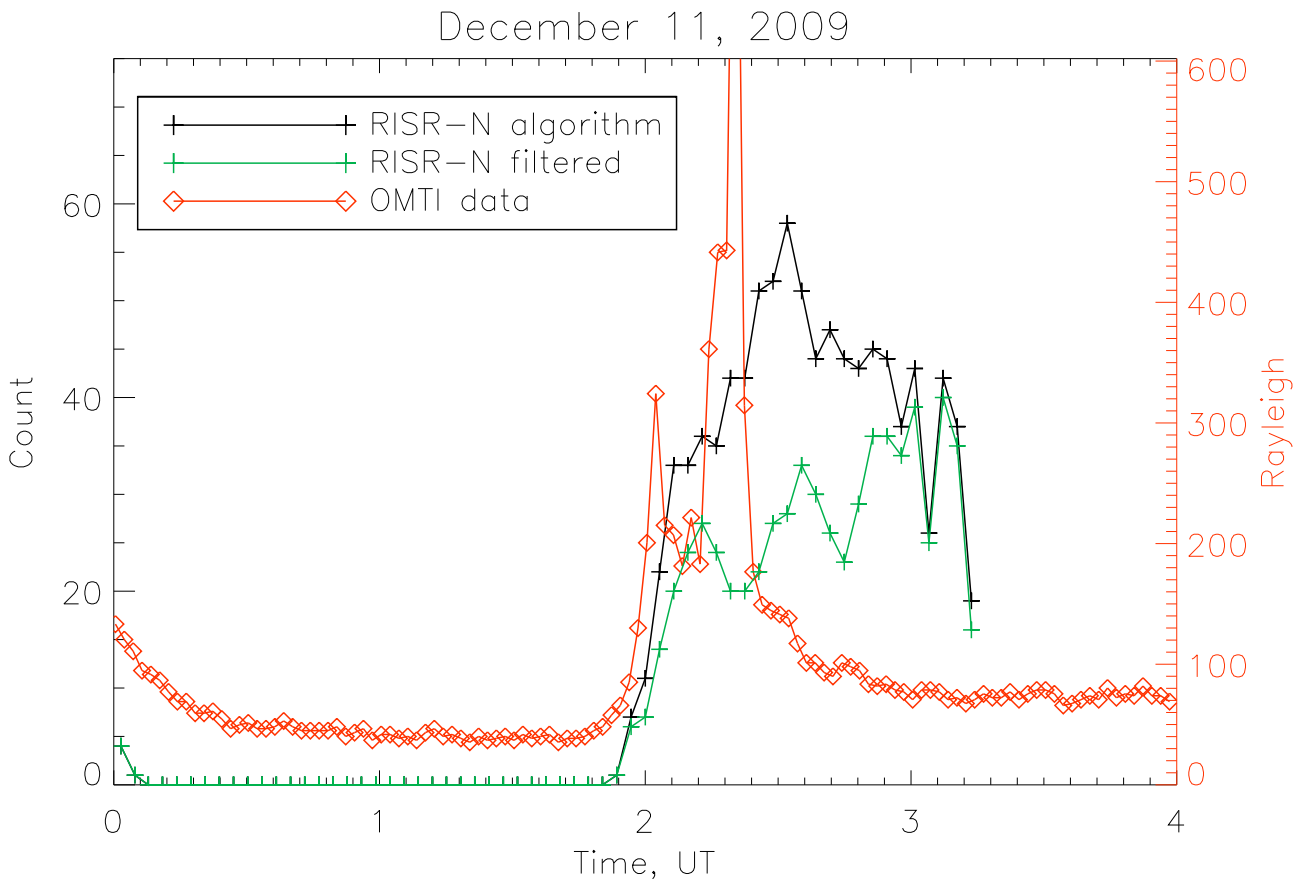

Figure 4.9: A plot of the RISR-N algorithm output (black trace), RISR-N output that has had a temperature filter applied to it (green trace) and OMTI data from the zenith of the imager (red trace) as a function of time between 00:00 and 04:00 UT on December 11, 2009.

cle precipitation, or an arc such as the case studied here, then that patch detection event can be disregarded. Such a filter was implemented with the RISR-N algorithm for the arc event presented here. The filter was set to disregard any patch detections which had T_i or $T_e > 1000$ K. The results of the RISR-N algorithm with the temperature filter are plotted in green in Figure 4.9. Evidently, the filter was successful at reducing the patch count by 50% in some instances, but did not completely eliminate all of the patch counts. It would not be feasible to lower the temperature threshold of the filter any lower than 1000 K. 800 K is approximately the ambient temperature of the thermosphere in altitude range of interest – 200 to 500 km [*Kelley*, 2009].

On the definition of a patch

The results of the temperature filter RISR-N algorithm presented in Figure 4.9 have important implications for patch detection in the polar ionosphere, more so than simply highlighting the inability of the algorithm to identify and disregard aurora. Using optical imagers to identify patches introduces a bias into the detection process itself [J. L. Semeter, personal communication, 2012]. Had it not been for the OMTI data in the arc event presented in Figure 4.7, the n_e enhancements measured by RISR-N in beam 12 would have been identified as patches by the RISR-N algorithm, even with the temperature filter included in the analysis. According to the *Crowley* [1996] criterion patches were created since the n_e created by the arc precipitation measured twice that of the background ionosphere. This underlines a dilemma for patch identification: is an n_e created by an auroral event, i.e., particle precipitation, still a patch? To address this question, we present the following thought experiment. Suppose a patch passes through the RISR-N and OMTI FOV, displaying the "normal" features of a patch, i.e., n_e enhancement that is twice that of the background, red-line luminosity, etc. Now, restrict the possible generation mechanisms for that patch to that of particle precipitation. It cannot be discerned whether the patch was generated by precipitation several hours prior to its passage through the RISR-N and OMTI FOVs, or by a precipitation several minutes prior to its passage through the FOVs. The ion gas has a large heat capacity, and the electron gas will reach thermal equilibrium with the neutral atmosphere within approximately 30 s [*Mantas et al.*, 1981; *Carlson et al.*, 2002] (There is clear evidence of this in Figure 4.8. After the arc passed through the RISR-N beam, at 02:30 UT, the T_i and T_e returned to temperatures below 1000 K almost immediately). Moreover, since the RISR-N algorithm temperature filter proved ineffective against n_e production by precipitation, the only way one could single-out particle precipitation as a generation mechanism for the patch is if an optical imager, such as OMTI, observed the precipitation event. Therefore, since the generation mechanism and the time-history of the patch are irrelevant in the definition of a patch, any n_e enhancement that satisfies the *Crowley* [1996] criterion is a patch even if the n_e enhancement is being actively generated within the RISR-N and/or OMTI FOV in the form of a aurora or an arc.

4.4 A survey of patches over Resolute Bay

With the characteristics of the RISR-N algorithm outlined, it will now be used to survey patches detected over Resolute Bay, during two, five-day datasets. The first dataset consists of RISR-N data from March 10, 14, 16, 18 and 19, 2010. The second dataset consists of RISR-N data from December 8 to 12, 2010. These datasets were chosen for two main reasons. First, the datasets use the same RISR-N beam configuration, a 5 $\times$ 5 "World Day" mode, which is displayed in Figures 4.3 and 4.7. Secondly, each dataset offers a nearly continuous sample of the polar ionosphere under equinox and winter conditions. This provides an opportunity to compare and contrast the polar ionosphere and patches during times with and without extended periods of pronounced photoionization.

4.4.1 Patch survey results: plasma density, n_e

Figures 4.10 and 4.11 show the plasma density, n_e, of the patches detected by the RISR-N algorithm, as a function of time (both UT and MLT at Resolute Bay). The solar zenith angle at the location at which the patch was detected is also provided (the solar zenith angle was provided by SRI International). The solar zenith angle is the angle subtended between the vertical and the geometric centre of the Sun. The zenith angles in Figures 4.10 and 4.11 are mapped down the surface of the Earth such that sunrise/sunset occurs when the solar zenith angle is 90°. The ionosphere is sunlit for solar zenith angles below 90°.

Each day in Figures 4.10 and 4.11 shows significant variability in the n_e of patches. Effects due to photoionization (or lack thereof) can be seen in both figures. In March, 2010, sunrise occurred at approximately 13:30 UT. After this time, less patches were detected, as evidenced by the marked decrease in the number of data points after that time. This trend reversed just before 24:00 UT, the approximate time of sunset. The decrease in the number of patches is expected since plasma production due to photoionization of the neutral atmosphere will increase the n_e of the background ionosphere under sunlit conditions. Since patch detection is subject to ratio of the n_e of the patch and the background ionosphere, of which the latter increases in the presence of photoionization, less n_e enhancements will satisfy the *Crowley* [1996] criterion under sunlit conditions – fewer patches will be detected. This is also why

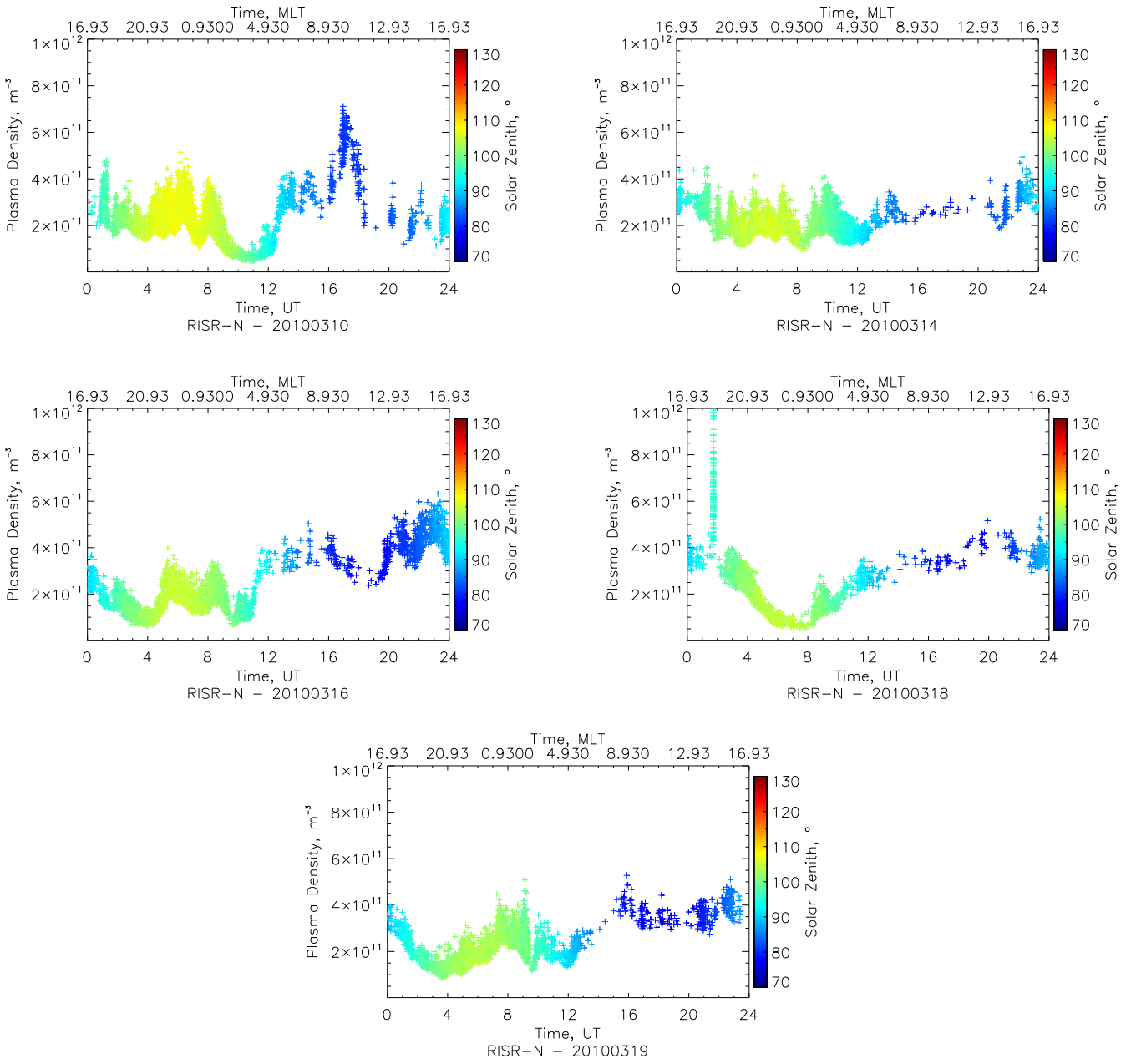

Figure 4.10: A plot of the n_e of the patches detected using the RISR-N algorithm, as a function of time (UT and MLT) for March 10, 14, 16, 18 and 19, 2010. The plot points are coloured according to the modelled solar zenith angle at the location at the time of the patch detection.

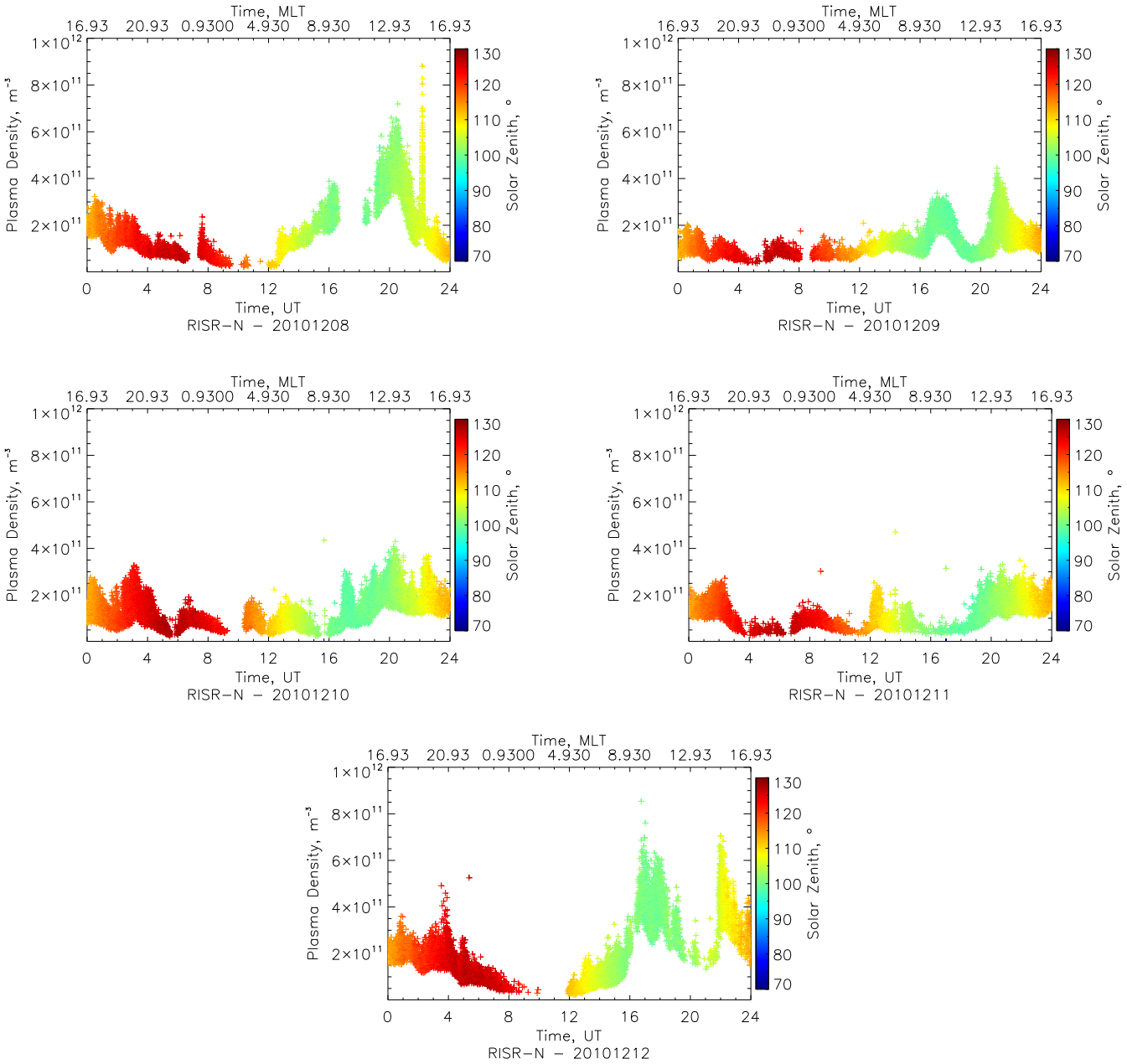

Figure 4.11: A plot of the n_e of the patches detected using the RISR-N algorithm, as a function of time (UT and MLT) for December 8, 9, 10, 11 and 12, 2010. The plot points are coloured according to the modelled solar zenith angle at the location at time of the patch detection.

fewer patches were detected in March than in December, 2010, in general.

During the December, 2010 time period surveyed, the solar zenith angle was never below 100°; the ionosphere over Resolute Bay suffered little photoionization throughout the entirety of these days. Overall, the n_e of the patches detected in December appear to be similar to those detected in March. There is one subtle difference, however. In the 00:00 to 12:00 UT sector (17:00 to 05:00 MLT, see Figure 1.15), the n_e of some of the patches detected in December, 2010 are lower than those detected in March, 2010, in general. This is not an unexpected result. Patches travelling along a trajectory from the sunlit ionosphere to Resolute Bay in March will have been subject to less depletion by chemical recombination than patches travelling the same route in December. This is due to the seasonal variation of the solar EUV exposure at high-latitudes. This will be discussed in more detail shortly.

A n_e distribution for all of the patches displayed in Figures 4.10 and 4.11 is given in Figure 4.12. The patches detected in March and December are sorted by solar zenith angle: patches that were detected at locations at which the solar angle was less than 90°, i.e., sunlit conditions, are plotted in black; all others, i.e., "dark" ionosphere conditions, are plotted in red. These conditions are labelled as dark even though the ionosphere may have been still exposed to sunlight, since the photoionization at altitudes above 200 km it extremely low for high solar zenith angles. Recall that photoionization declines exponentially with increasing solar zenith angle, i.e., Equation 1.14. The bin size of the distributions in Figure 4.12 is 2×10^{10} m^{-3}. The characteristics of the patches displayed in Figures 4.10 and 4.11 are easily identifiable. In Figure 4.12, the March, 2010 distribution shows that the number of patches detected in sunlit conditions is less than the number detected in dark ionosphere conditions. It also shows that significantly fewer patches were detected in March compared to December; the magnitude of the sunlit distribution has been multiplied by a factor of five to make it easier to see. For $n_e > 1.5 \times 10^{11}$ m^{-3} in Figure 4.12, the combined shape of both distributions for March is somewhat similar to the distribution in December (if we neglect the magnitudes of each distribution). The dark ionosphere distribution in March has a peak near $n_e = 1.5 \times 10^{11}$ m^{-3}. In the December, 2010 distribution a "shoulder" feature is centered at approximately the same n_e. Both the sunlit distribution (there is only one) and the dark ionosphere distribution have a relative peak centered at $n_e \simeq 3.5 \times 10^{11}$ m^{-3}.

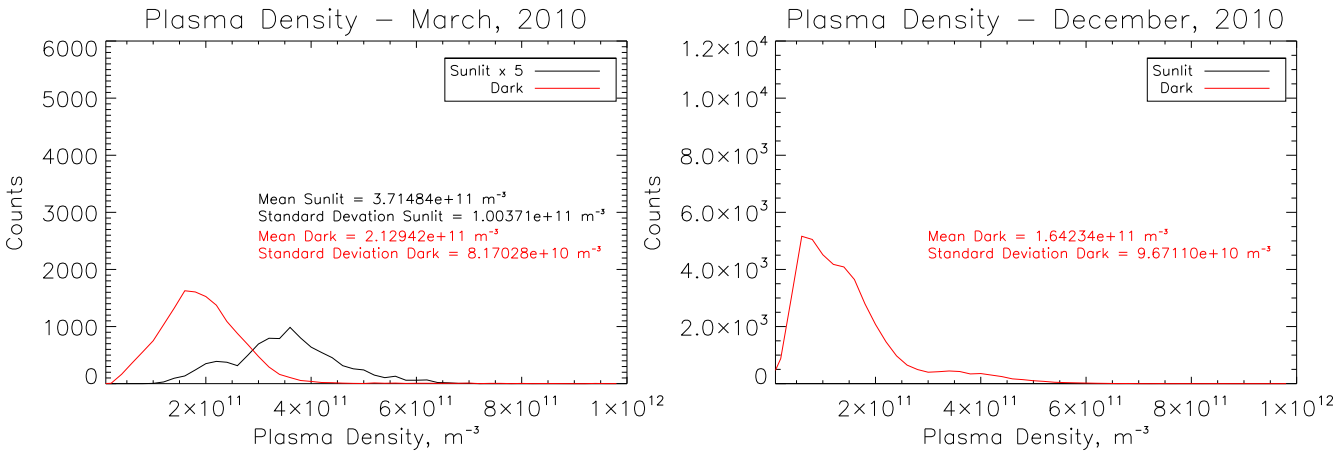

Figure 4.12: A histogram of the n_e of all of the patches detected in the March, 2010 dataset (left) and December, 2010 dataset (right) for sunlit (black trace) and dark ionosphere (red trace) conditions. Note that the vertical scale changes from March to December.

Notwithstanding the magnitudes of each distribution, the only significant difference between the patch n_e distribution for March and December in Figure 4.12 is that in December there is a peak in patch occurrence centered just above $n_e = 0.5 \times 10^{11}$ m^{-3}. In March, there are very few patch detections for $n_e < 1.0 \times 10^{11}$ m^{-3}, relative to patches detected in December, 2010. The low n_e population of patches in December, 2010 was briefly discussed earlier. This population may be patches that have been depleted more by chemical recombination than patches in March. Assuming no other source of n_e production, and no source of n_e depletion besides chemical recombination (i.e., we are considering Equations 3.5 and 3.6), patches measured in December would have been more depleted than those measured in March, since a greater portion of the polar ionosphere is exposed to photoionization (i.e., n_e production) in March. Recall that increased plasma production reduces the patch detection count. The duration of the trip between sunlit ionosphere and Resolute Bay is shorter for the patches in March than it is in December, and therefore chemical recombination has less time to erode the n_e of a patch in March.

For an estimate of the difference in n_e magnitudes for patches in March and December, we consider the following. In Figures 4.10 and 4.11, the value of the solar zenith angle at 16:00 UT is approximately 80° and 100° in March and December, respectively – a difference of 20°. This

difference is equivalent to the latitudinal migration of the boundary between the sunlit and dark ionosphere – the day/night terminator, over those months, with respect to Resolute Bay. In other words, a patch starting from the terminator in March, convecting along a meridian towards Resolute Bay, will have travelled 20° in latitude less than a patch starting from the terminator at the same time and travelling the same path in December. At 300 km altitude, 20° in latitude traces out an arc length of $s = 20 \times (6371 \text{ km} + 300 \text{ km}) \times \pi/180 \simeq 2300$ km. Using the patch velocity of 300 m/s quoted earlier [*Hosokawa et al.*, 2009b] in Section 4.3.1, a patch would take 2 hours to travel this distance. This amount of time is of the order of the time required to deplete the n_e of a patch by a factor of e, a calculation described earlier, in Section 4.3.1. The largest peak in the patch distribution for March in Figure 4.12 is at $n_e \simeq 1.5 \times 10^{11}$ m^{-3}. Dividing that value by a factor of e gives $1.5/e \times 10^{11}$ m^{-3} = 0.55×10^{11} m^{-3}, which is approximately the n_e at which the largest peak in the December patch density distribution is centred at, in Figure 4.12. Thus, it seems plausible that this population of patches only found in the December patch detection data were more depleted by chemical recombination as a result of the seasonal migration of the day/night terminator.

n_e results: comparison the previous studies

To the best of our knowledge, the distributions plotted in Figures 4.10, 4.11 and 4.12 (and other distributions that will be shown in this section) are the first of their kind. Previous studies have not analyzed the state parameters of patches with as many events as presented here. An analogous study was presented by *Moen et al.* [2008], who investigated two datasets of the n_e values measured by the ESR radar. In both months they investigated, unexpectedly large n_e values measured during times which the ionosphere was dark, peaking at approximately 20:00 UT, as illustrated in Figure 1.17. *Moen et al.* [2008] attributed the abnormally large n_e to patches. Assuming that postulate is correct the n_e measurements of the patches displayed in Figure 1.17 were at least as large any patch measured in March or December, 2010 by RISR-N. This discrepancy is likely a signature of the increased solar EUV flux present during the *Moen et al.* [2008] study, which compiled measurements from February, 2001 and October, 2002, in the midst of the peak of Solar Cycle 23.

Solar EUV flux is strongly correlated with the solar cycle; the solar EUV flux is at its

most intense during the peak of a solar cycle. The EUV flux can vary substantially between the maximum and minimum of a solar cycle, by as much as a factor of two or three [*Chen et al.*, 2011]. Since the F-region n_e is strongly coupled to the solar EUV flux, it also has a significant variation over a solar cycle. A standard proxy measurement for solar EUV flux is the F10.7 index, a measure of the solar flux density at the 10.7 cm wavelength [*Schunk and Nagy*, 2000]. The magnitude of the peak F-region n_e, the solar EUV flux and the F10.7 are strongly correlated to one another for F10.7 values below 150 (the units of the F10.7 index are 10^{-22} $\mathrm{Wm^{-2}Hz^{-1}}$) [*Richards*, 2001].

During the months surveyed by *Moen et al.* [2008], February, 2001 and October, 2002, the F10.7 flux was 144 and 166, on average, respectively. During the months surveyed with the RISR-N algorithm, March and December, 2010, the F10.7 flux was 85, on average. Estimates from the IRI model show that this difference in solar EUV flux translates into a nearly five-fold increase in the peak n_e in the F region. Thus, we should expect to see a similar variation in the n_e of the patches measured in both studies. This is not the case, however. The peak n_e of the patches for the *Moen et al.* [2008] survey were approximately 6.3×10^{11} $\mathrm{m^{-3}}$ – nearly three-times as dense as the patches detected with the RISR-N algorithm, not a five-fold increase as suggested by IRI. Nonetheless the increased densities substantiate the notion that since the n_e was higher in February, 2001 and October, 2002, due to the increased EUV flux, then the patches drifting from the dayside to the nightside ionosphere during that time would have been denser than those patches detected in March and December, 2010 with the RISR-N algorithm. It is therefore not unexpected for the n_e of the patches referenced in *Moen et al.* [2008] and plotted in Figure 1.17 to be higher than the n_e of those displayed in Figure 4.12.

4.4.2 Patch survey results: plasma temperature

The ion and electron temperatures, T_i and T_e, of the patches plotted in Figures 4.10 and 4.11 are plotted in Figures 4.13, 4.14, and Figures 4.15 and 4.16, respectively. When comparing T_i and T_e for patches in March and December, a stark contrast emerges: the characteristics of the T_i of the patches remains approximately the same under sunlit and dark ionosphere conditions; however, the characteristic of the T_e of the patches shows significant variation

between sunlit and dark ionosphere conditions.

Distributions of T_i and T_e for the data presented in Figures 4.13, 4.14, 4.15 and 4.16 are plotted in Figures 4.17 and 4.18. Like the previously discussed distribution plots, the black traces correspond to patches detected under sunlit conditions and have been increased by a factor of five for readability. The red traces correspond to patches that were detected when the ionosphere was dark. The bin sizes in both Figures 4.17 and 4.18 is 100 K.

Ion temperatures – T_i

In March, 2010, the mean T_i of the patches detected during sunlit conditions is approximately 855 K, while the T_i of the patches under dark ionosphere conditions is approximately 801 K. By inspection the T_i values of these patches are on par with what has been observed over Resolute Bay at this time of year with RISR-N. These temperatures are in the expected range of T_i for this altitude [*Schunk and Nagy*, 2000], assuming that the ion gas is in thermal equilibrium with the neutral atmosphere.

The mean T_i of the patches detected in December is 769 K. These cooler temperatures are likely a result of a cooler neutral atmosphere in that month. During December, the neutral atmosphere is exposed to less sunlight and is therefore cooler than a month where it is exposed to more sunlight, e.g., March. Since the ion gas is in thermal equilibrium with the neutral atmosphere, it will be cooler as well, producing cooler patch ion temperatures.

Electron temperatures – T_e

The mean T_e of the patches detected by the RISR-N algorithm in March, 2010 in the dark ionosphere is 1185 K, and the mean T_e for the same conditions in December, 2010 is 875 K. Both the March and December, 2010 values of T_e are consistent with a previous study of the region by *Brinton et al.* [1978], who compiled satellite measurements for altitudes near 300 km during the summer season in the northern hemisphere. The results of that study show that the northern high-latitude ionosphere is highly structured in terms of T_e; several latitudinal bands of T_e are present. The coolest bands measured 500 K, and were located in the polar regions. Meanwhile, the hottest bands were associated with the auroral zone and measured 3500 K. The dayside coverage of those measurements was limited, but showed a range of

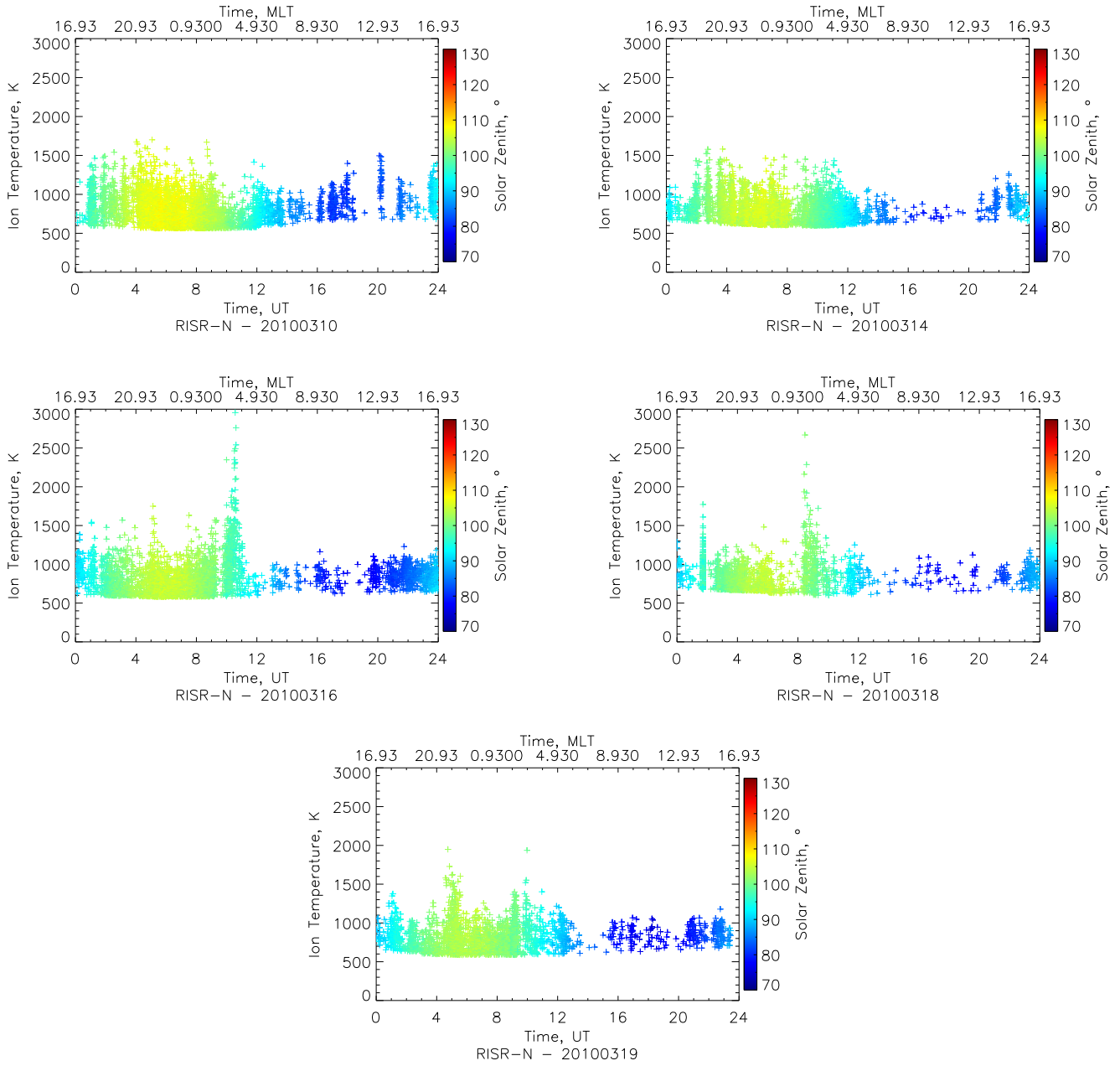

Figure 4.13: A plot of the T_i of the patches detected using the RISR-N algorithm, as a function of time (UT and MLT) for March 10, 14, 16, 18 and 19, 2010. The plot points are coloured according to the modelled solar zenith angle at the location at time of the patch detection.

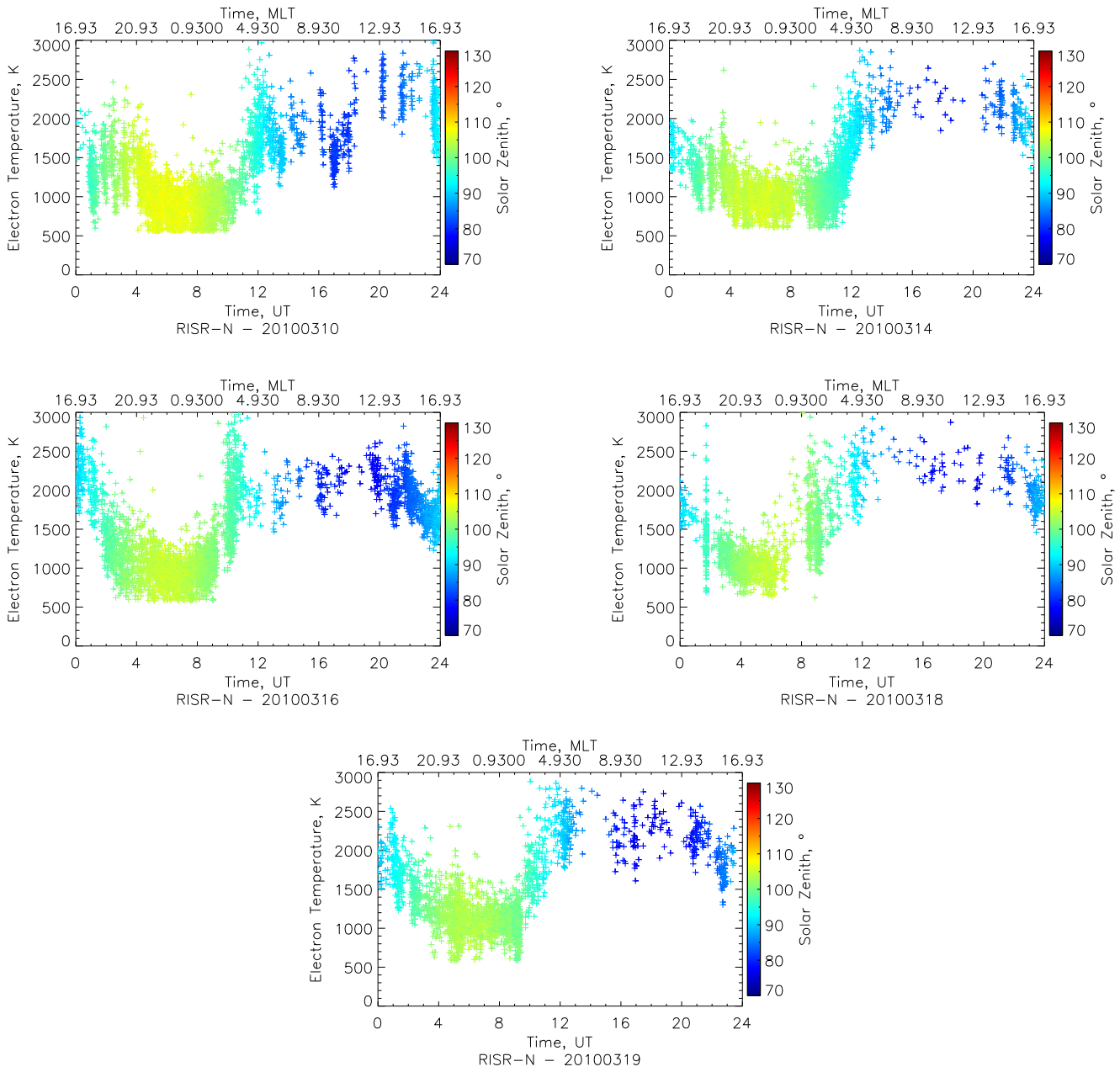

Figure 4.14: A plot of the T_e of the patches detected using the RISR-N algorithm, as a function of time (UT and MLT) for March 10, 14, 16, 18 and 19, 2010. The plot points are coloured according to the modelled solar zenith angle at the location at time of the patch detection.

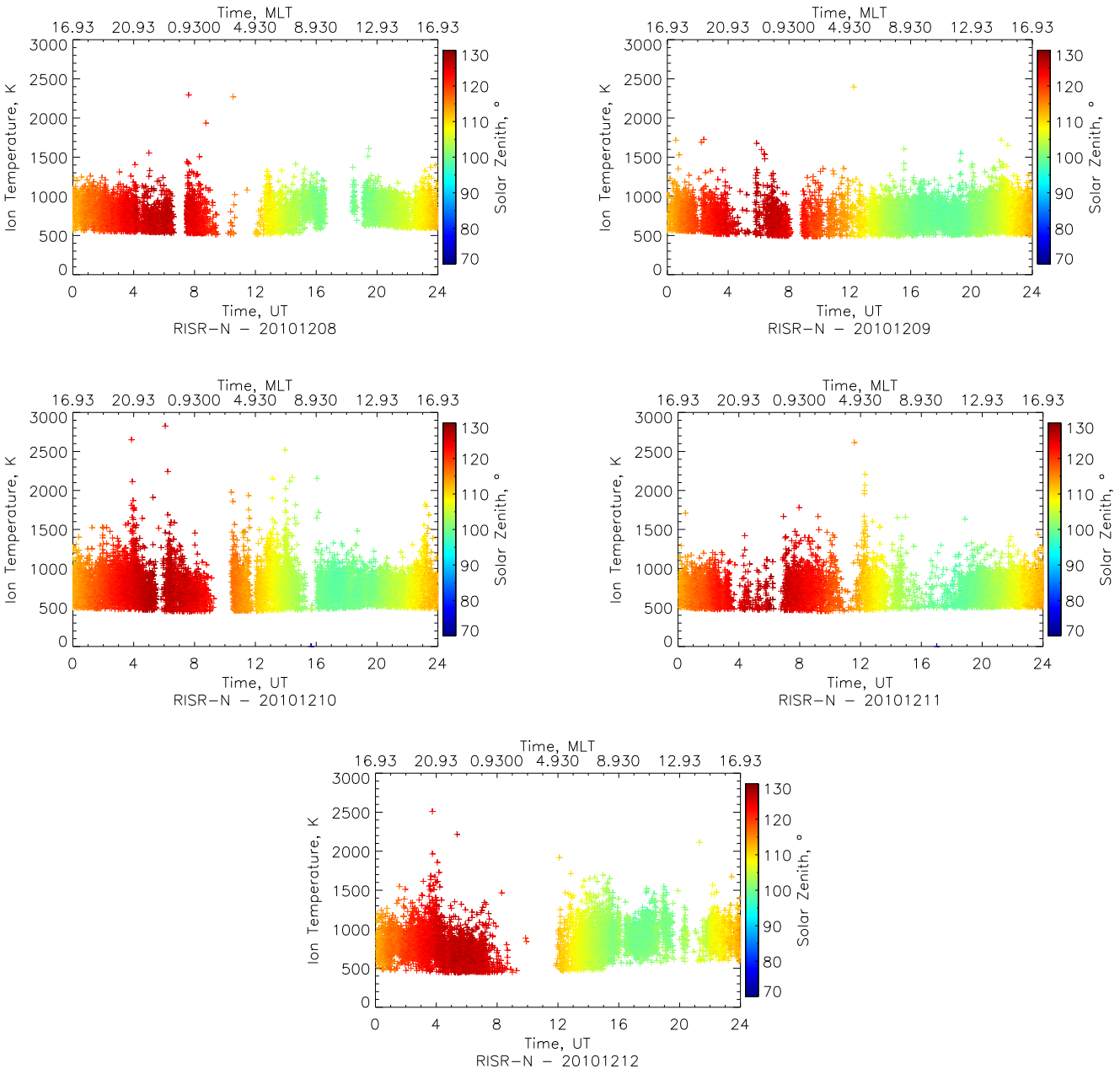

Figure 4.15: A plot of the T_i of the patches detected using the RISR-N algorithm, as a function of time (UT and MLT) for December 8, 9, 10, 11 and 12, 2010. The plot points are coloured according to the modelled solar zenith angle at the location at time of the patch detection.

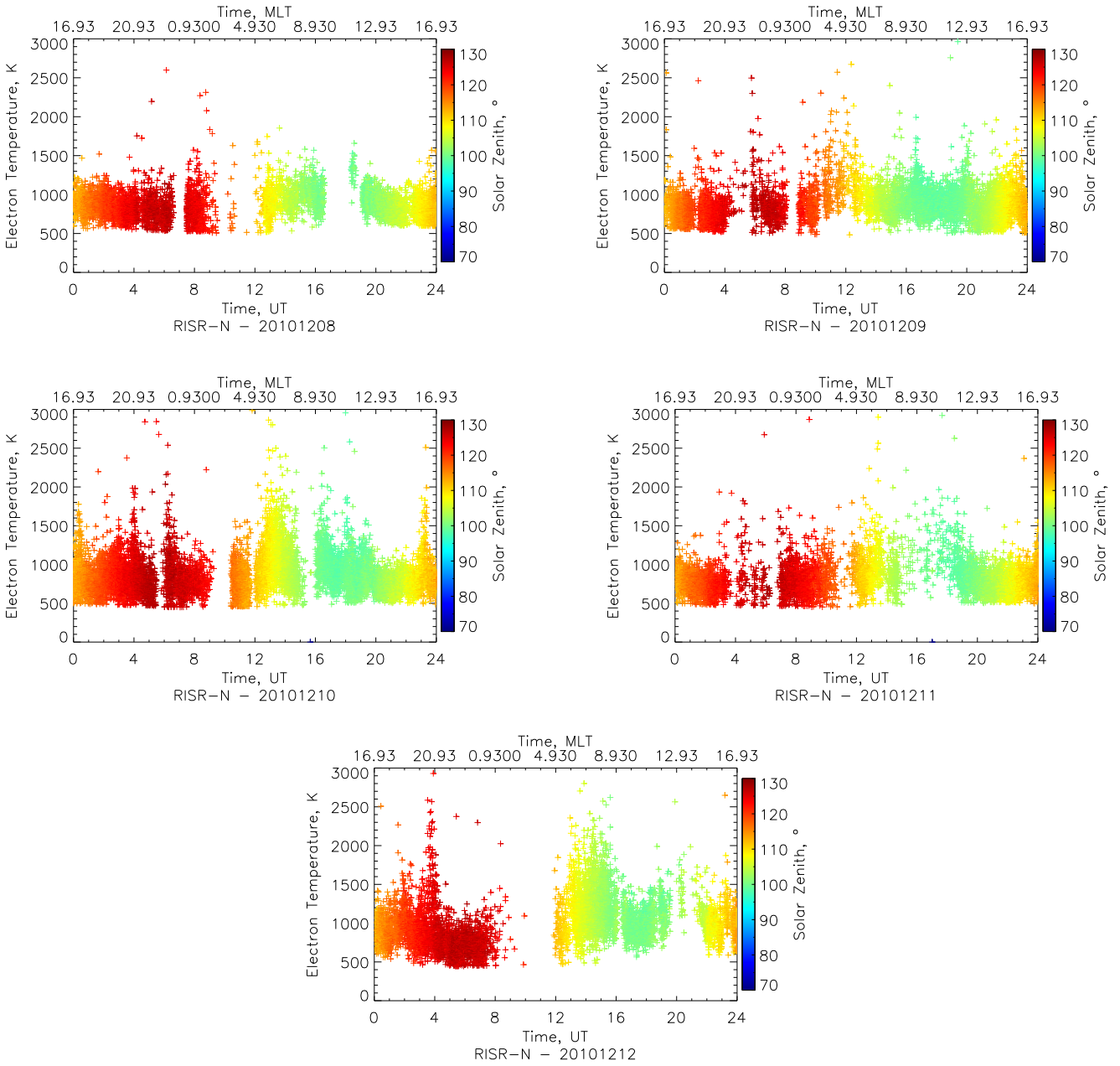

Figure 4.16: A plot of the T_e of the patches detected using the RISR-N algorithm, as a function of time (UT and MLT) for December 8, 9, 10, 11 and 12, 2010. The plot points are coloured according to the modelled solar zenith angle at the location at time of the patch detection.

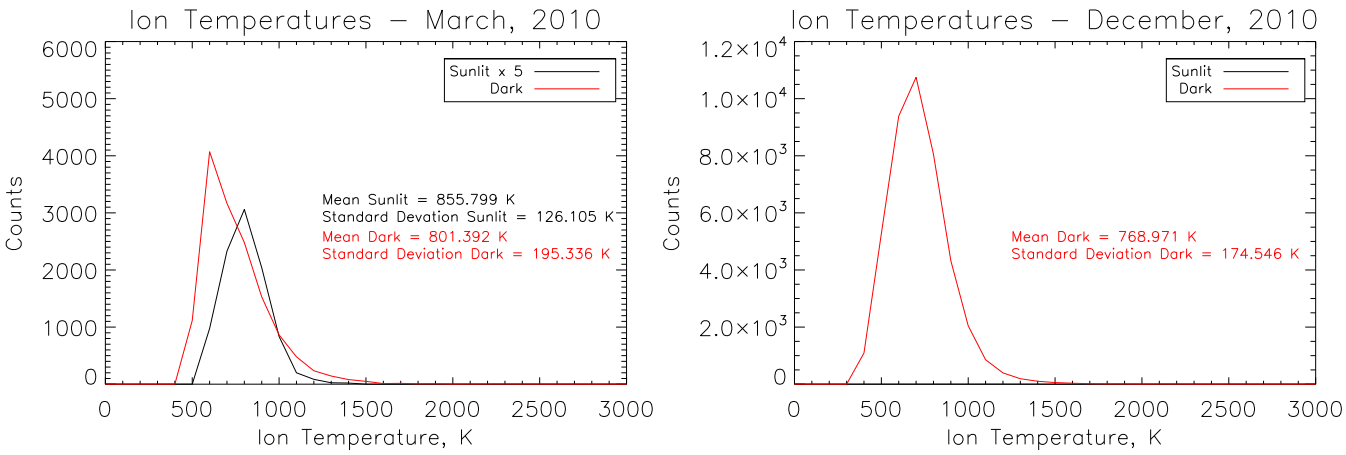

Figure 4.17: A histogram of the T_i of all of the patches detected in the March, 2010 dataset (left) and December, 2010 dataset (right) for sunlit (black trace) and dark ionosphere (red trace) conditions. Note that the scales are different in each plot.

2000 $K \leq T_e \leq 2666$ K, consistent with the sunlit distribution Figure 4.18. The sunlit T_e is governed by the influence of solar radiation, which will be discussed shortly. *Brinton et al.* [1978] attributed the latitudinal variations of T_e to differing particle precipitation energies and intensities. After being exposed to a heat flux, such as particle precipitation, the electron gas will reach thermal equilibrium with the neutral and ion gas on a time scale of approximately 30 s [*Mantas et al.*, 1981; *Carlson et al.*, 2002]. Therefore, signatures of enhanced T_e can be used to identify active particle precipitation – an active heat flux. There are examples of patches with T_e of the order of 3500 K, e.g., March 16, 2010, but these cases were sporadic.

The increase (decrease) in T_e that occurred when the solar zenith angle decreased (increased) through 90° in March, 2010, is a signature of solar heating and an expected result [*Schunk and Nagy*, 2000]. *Kitamura et al.* [2011] studied the T_e in the polar ionosphere using ESR and measurements from the Akebono satellite. They found very similar T_e trends: $T_e \leq 1500$ K under dark ionosphere conditions, with a drastic increase for sunlit conditions in which $T_e \geq 2500$ K. They also noted a strong coupling between the solar zenith angle and T_e. A similar trend between the solar zenith angle and T_e can also be seen in *Varney et al.* [2014] who compared a polar region T_e model to RISR-N data.

It is interesting to note that for dark ionosphere conditions, the T_e distributions in March and December, 2010 are not similar. In March, 2010, the mean T_e is over 300 K hotter

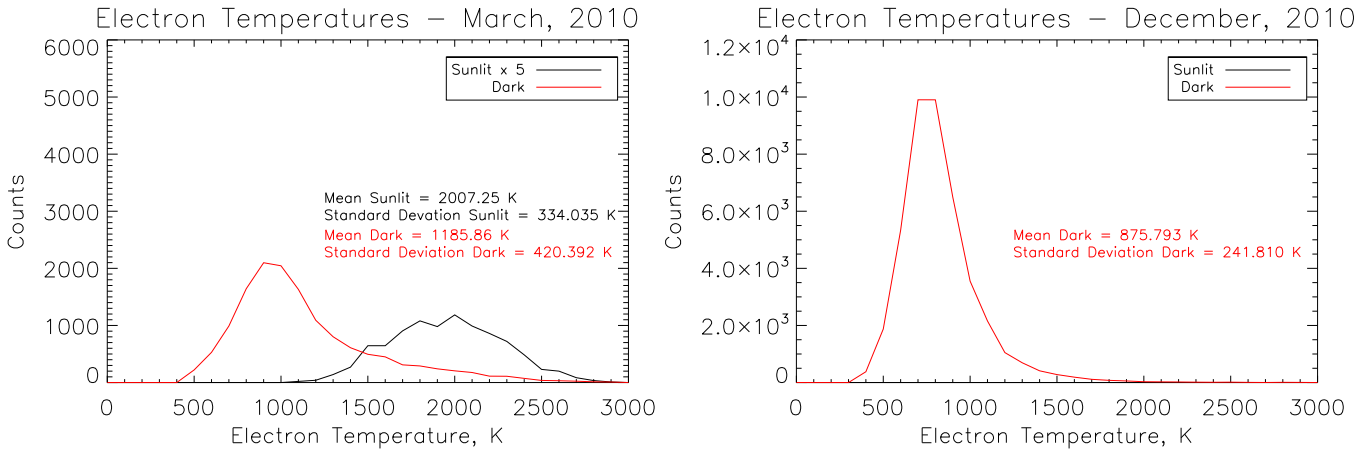

Figure 4.18: A histogram of the T_e of all of the patches detected in the March, 2010 dataset (left) and December, 2010 dataset (right) for sunlit (black trace) and dark ionosphere (red trace) conditions. Note that the scales are different in each plot.

than of the December, 2010 distribution. This is likely a result of the relaxation time of the electron gas. Once the sun sets on the ionosphere, the electron gas cools since its temperature is enhanced above the ion and neutral gas. As mentioned previously, this relaxation time is quick for an event involving precipitation, which is restricted in altitude. In the solar heating case, we must consider heat conduction of the electron gas from higher altitudes which have been heated by solar radiation as well. The relaxation time of T_e is proportional to n_e [*Tohmatsu and Ogawa*, 1990; *Schunk and Nagy*, 2000] and therefore the electron gas at 300 km, for example, will cool much quicker than the electron gas at 1000 km (cf. Figure 1.9). This will create a heat flow from the higher altitude electron gas to the lower altitude electron gas, extending the relaxation time of the electron gas at 300 km from minutes to of the order of an hour [R. H. Varney, personal communication, 2014]. Therefore, the enhanced T_e measured in March, 2010 may simply be patches which had been exposed to solar EUV within the previous hour, and whose electrons have not yet cooled down to the levels measured in December, 2010.

4.5 The Patch Index

Up until now a patch detection with the RISR-N algorithm has been referred to as a "count". In its current state the descriptor does not offer any information. A patch extending over several RISR-N beams produces several patch counts, which cannot be distinguished from one another. That is to say, we cannot distinguish whether patch counts from adjacent RISR-N beams are from a large patch spanning those beams, or two smaller, separate patches intercepted by each beam. The patch count is not a useless quantity, however. Since there is a finite and constant number of RISR-N beams and range gates between 200 and 500 km altitude in the RISR-N FOV, for which a count can be registered, an estimate of how much of the RISR-N FOV contains a patch n_e signature can be calculated. This estimate is termed the "patch index".

4.5.1 Definition of the Patch Index

The RISR-N World Day mode illustrated in Figure 4.3 features 25 beams which have 14 range gates each, between 200 and 500 km altitude – 350 range gates in total. Patch Index, PI, in defined as:

$$PI = \frac{patch\ count}{350} \times 100\%. \tag{4.1}$$

The PI quantifies the amount of the RISR-N FOV that contains a n_e that generates a patch count according to the RISR-N algorithm outlined in Section 4.3.2. It is defined for a single RISR-N integration period, which is typically of the order of two minutes but may vary. It is important to note that the PI does not quantify the number of patches with the RISR-N FOV. A value of $PI = 100\%$ is undefined. The PI may approach 100% but can never achieve that value. As the PI approaches 100% the RISR-N FOV becomes more occupied with patch material which would increase background n_e estimate used by the RISR-N, thereby decreasing the number of patches detected by that algorithm and decreasing the patch count.

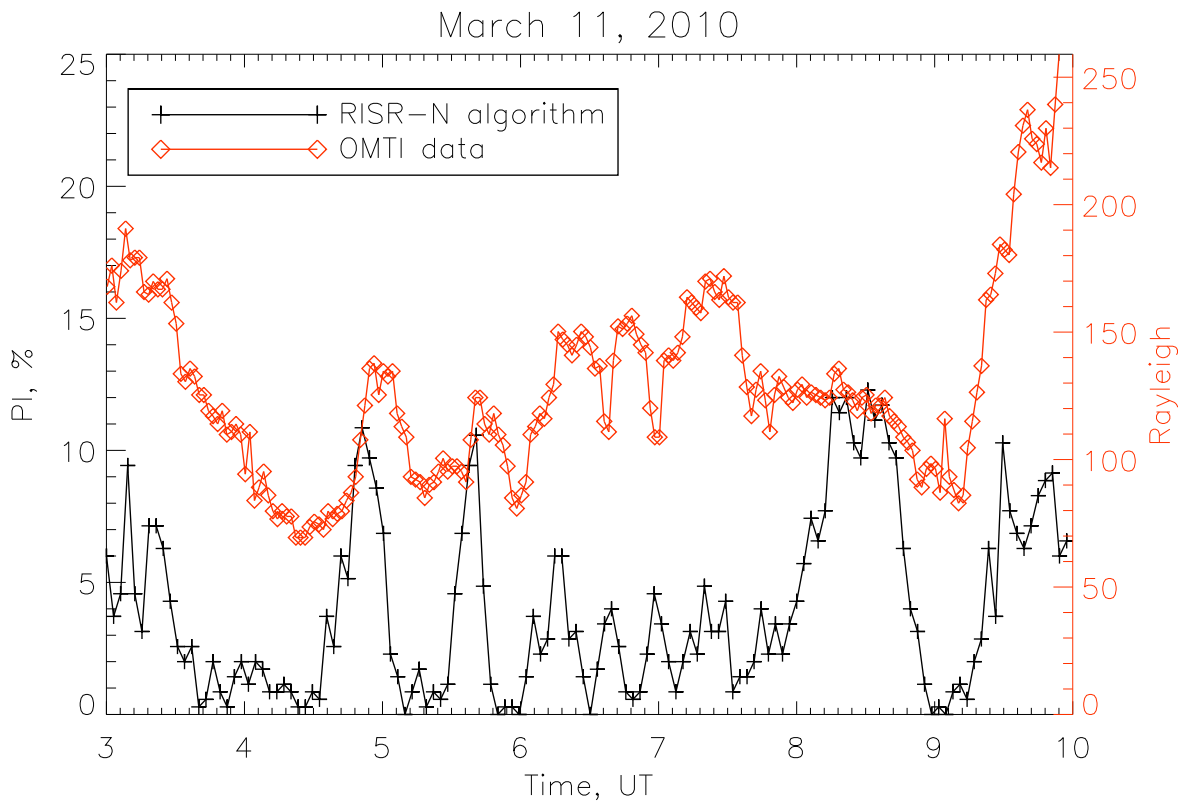

Figure 4.19: The *PI* from the RISR-N algorithm plotted with the optical data from the zenith of the OMTI imager, for the same segment of time plotted in Figure 4.5. A clear agreement between the output of the RISR-N algorithm and OMTI luminosity data exists.

Patch Index: examples

Figure 4.6 is re-created in Figure 4.19 using the *PI* instead of patch count to describe the patch material moving through the RISR-N FOV. For times in which patches were seen moving through the OMTI FOV, the *PI* is increased. There are five peaks in *PI* during the interval displayed which approach 10% in Figure 4.19; each has a corresponding optical peak. It is apparent that there is some correlation between *PI* and the optical emissions measured by OMTI; however, the maxima and minima in the OMTI data do not correspond to the maxima and minima in *PI*. This is an expected result. As described in Chapter 3, the emissions of a patch are not only related to its altitude and concentration, but its vertical motion as well. Furthermore, soft particle precipitation may be responsible for some of the observed enhancements in Figure 4.19, rather then patches. At the present time, it is too

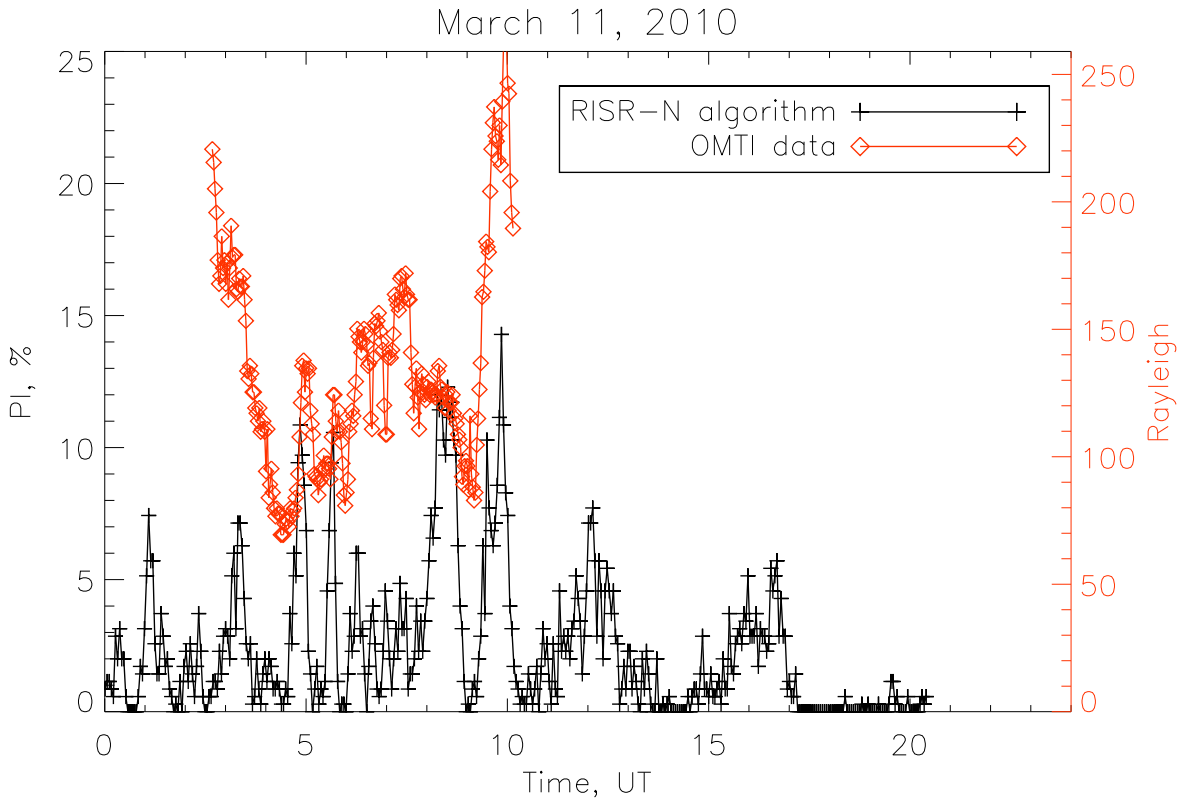

Figure 4.20: The *PI* from the RISR-N algorithm plotted with the optical data from the zenith of the OMTI imager, for the entirety of March 11, 2010. The RISR-N was operational until just after 20:00 UT that day.

difficult to extract any connection between the value magnitude of the *PI* and the optical emissions.

The *PI* for the entirety of March 11, 2010 is plotted in Figure 4.20. On this day, RISR-N was operational from 0:00 to just after 20:00 UT. OMTI was operational between approximately 03:00 and 10:00 UT, presumably while the OMTI FOV was dark enough such that the solar light would not saturate the imager. This day is not among those displayed in Figures 4.10 through 4.18. Nonetheless, many of the trends found in those figures can be seen in Figure 4.20. This includes a somewhat reduced *PI* while the ionosphere was sunlit, after approximately 12:00 UT, as well as an increase in patch occurrence at around 12:00 and 16:00 UT, as evidenced by *PI* values exceeding 5%.

4.6 On the interconnection of SuperDARN radar echoes and patches

Patches have long been recognized as a significant source of HF coherent backscatter at high-latitudes [*Milan et al.*, 2002; *Oksavik et al.*, 2006; *Hosokawa et al.*, 2009a]. A combination of n_e gradients and the $\mathbf{E} \times \mathbf{B}$ drift produce decametre n_e irregularities that permeate throughout a patch [*Cerisier et al.*, 1985; *Gondarenko and Guzdar*, 2004, 2006], and are a large target for HF coherent scatter radars such as SuperDARN. What is not clear is what portion of the HF coherent backscatter echoes from the polar regions are due to patches. It is a common yet unsubstantiated belief that the majority of HF radar echoes from the polar ionosphere originate from patches. In this section we investigate the interdependence between the F-region ionization patches and HF coherent backscatter echoes in the polar ionosphere to provide insight into this commonly held notion, using the newly developed RISR-N algorithm.

The RISR-N, OMTI and SuperDARN FOVs intersect over Resolute Bay. Figure 4.21 shows all of the RISR-N range gates (in the 5×5 RISR-N World Day mode) between 200 and 500 km altitude plotted along with the FOVs of the Rankin Inlet, Inuvik and Clyde River SuperDARN radars, and the OMTI imager. The OMTI FOV cuts out an oval shape from the SuperDARN FOVs.

The common FOVs of the SuperDARN, OMTI and RISR-N systems are ideal for studying the interconnection between SuperDARN echo occurrence and patches. In theory, either of the Rankin Inlet, Inuvik or Clyde River radars may detect SuperDARN echoes, and either the OMTI or RISR-N system can be used to confirm the presence of patches at the location of the SuperDARN echoes. Previous work has focused on patches and SuperDARN echoes on a case-by-case basis [e.g., *Hosokawa et al.*, 2009a]. In this section, we explore the relationship between the SuperDARN echo occurrence and patches on a larger scale by considering all of the SuperDARN echoes and patches that were present within the RISR-N FOV over several days, namely, the 10 days studied in Section 4.4: March 10, 14, 16, 18 and 19, 2010 and December 8, 9, 10, 11, and 12, 2010.

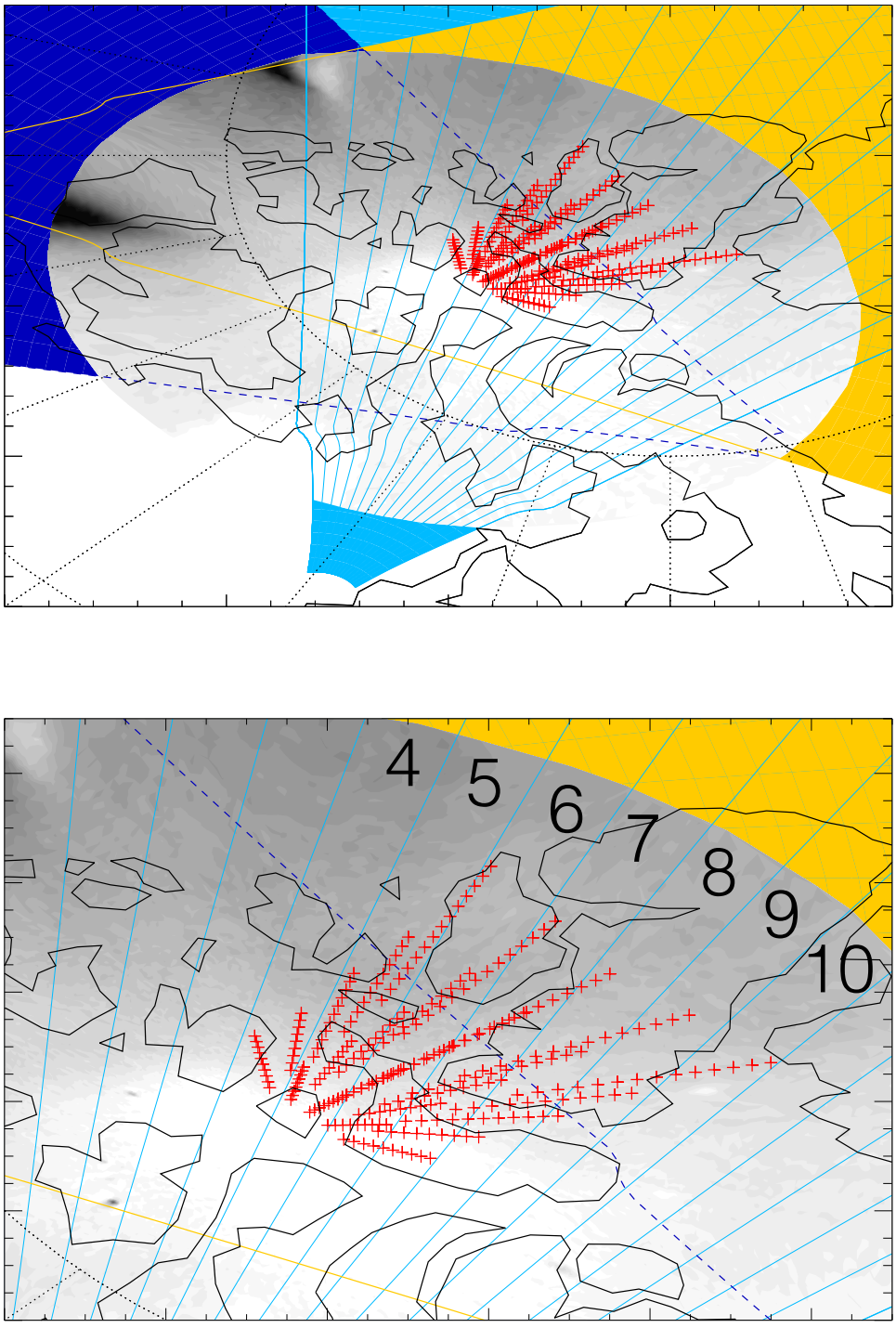

Figure 4.21: (top) A plot of the colour filled FOVs of the Rankin Inlet (light blue), Inuvik (yellow) and Clyde River (violet, dashed line) SuperDARN radars. Each Rankin Inlet beam is also outlined. The Clyde River FOV is dashed since it was not operational in 2010. All of the RISR-N range gates between 200 and 500 km, in the World Day mode configuration, are plotted (red). The OMTI FOV is also shown as an oval shape cut out of the SuperDARN FOVs. (bottom) A closer view in the vicinity of Resolute Bay. The Rankin Inlet SuperDARN beams are numbered.

4.6.1 Instruments

The PI introduced in Section 4.5 is implemented in this study to detect the presence of patches in the RISR-N FOV. There are a few reasons why the PI is used to detect the presence of patches, and not the OMTI imager. First, the presence of 630 nm optical emissions does not guarantee the detection of a patch. The *Crowley* [1996] criterion for a patch is subject to the n_e of a patch and the ionosphere in which it is immersed – not the luminosity of the patch. For example, soft particle precipitation may present an optical signature similar to that of a patch, but not the requisite n_e. Furthermore, OMTI data is ineffective if clouds are present in its FOV, unlike RISR-N. In addition to that, OMTI is only operational after sunset so as to not saturate or damage its optical sensors. This prevents it from detecting patches during sunlit conditions, which we know exist, according to our work in Section 4.4. It is therefore most appropriate to use the RISR-N algorithm and the PI to study the interconnection between SuperDARN radar echoes and the presence of patches, since the RISR-N algorithm is immune to the aforementioned issues.

The RISR-N FOV is situated within the FOV of eight SuperDARN radars, three of which are shown in Figure 4.21: Rankin Inlet, Clyde River, and Inuvik. The Clyde River radar did not begin full operation until 2012 [J.-P. St.-Maurice, personal communication, 2012], and so its data is of no use in this present study. Its role in future studies will be discussed near the end of this section. The Inuvik radar receives backscatter echoes from the region covered by the RISR-N FOV. However, the echo occurrence is only a fraction of that of the Rankin Inlet radar [*Bahcivan et al.*, 2013]. Although these echoes should not be discounted in general, we wish to start this study with a dataset that is most likely to contain radar echoes within the RISR-N FOV. Therefore, backscatter echoes from the Rankin Inlet SuperDARN radar were used in this study.

4.6.2 PI and Rankin Inlet echo occurrence: preliminary results

As shown in Figure 4.21, beams 4 through 10 of the Rankin Inlet radar intersect with the RISR-N FOV and the OMTI imager. Plots of the Rankin Inlet echo occurrence and the PI for the SuperDARN Rankin Inlet beams 5 and 6 for the days in March and December, 2010,

respectively, are given in Figures 4.22 and 4.23. A modified version of the PI, Equation 4.1, in which the denominator is changed to reflect the number of RISR-N rage gates within SuperDARN beams 5 and 6, respectively, is used instead. This alters the meaning of the PI to: the amount of the RISR-N FOV bounded by the SuperDARN beam that contains a n_e signature of a patch (this is responsible for the "discreteness" of the PI in those figures, due to the lower number of RISR-N beams in the PI calculation). Both quantities are binned in three minute intervals, the temporal resolution of the RISR-N scans. A SuperDARN scan is two minutes in length for the period studied. Rankin Inlet beams 5 and 6 were chosen since they had continuous data for the 5 days in each data set. Only RISR-N data taken from within the FOV of Rankin Inlet beam 5, for March, and beam 6, for December, are considered in this survey. In terms of SuperDARN echoes, both Figures 4.22 and 4.23 show a high amount of day-to-day variability. Nevertheless, their occurrence does show good correspondence with PI. At this point in the analysis, the correlation between PI and the echo count has no value; more analysis is needed to investigate the link between the PI to the number of echoes expected. We are only concerned with the presence of SuperDARN echoes, i.e., whether or not there is any echo count and an accompanying, non-trivial PI value.

The SuperDARN echo count scaling is highest for the December, 2010 dataset; more SuperDARN echoes were detected in the December dataset than the March dataset. This is consistent with the earlier described results which showed that more patches were detected by the RISR-N algorithm during December compared to March, and that more patches are detected during dark ionosphere conditions compared to sunlit conditions. Another interesting feature is the drop-off in both SuperDARN echoes and PI at around 05:00 and 12:00 UT in both datasets. In December, there were almost no SuperDARN echoes during those hours. A very similar trend can be seen in the n_e of the patches plotted in Figures 4.10 and 4.11, in which the n_e of the patches detected with the RISR-N algorithm decreased considerably at those times. In the December, 2010 data set, the n_e of the patches was rarely above $n_e = 1 \times 10^{11}$ m^{-3} during the 05:00 to 12:00 UT time segment. Even so, the number of patches during this time segment does not disappear completely, unlike the SuperDARN echoes.

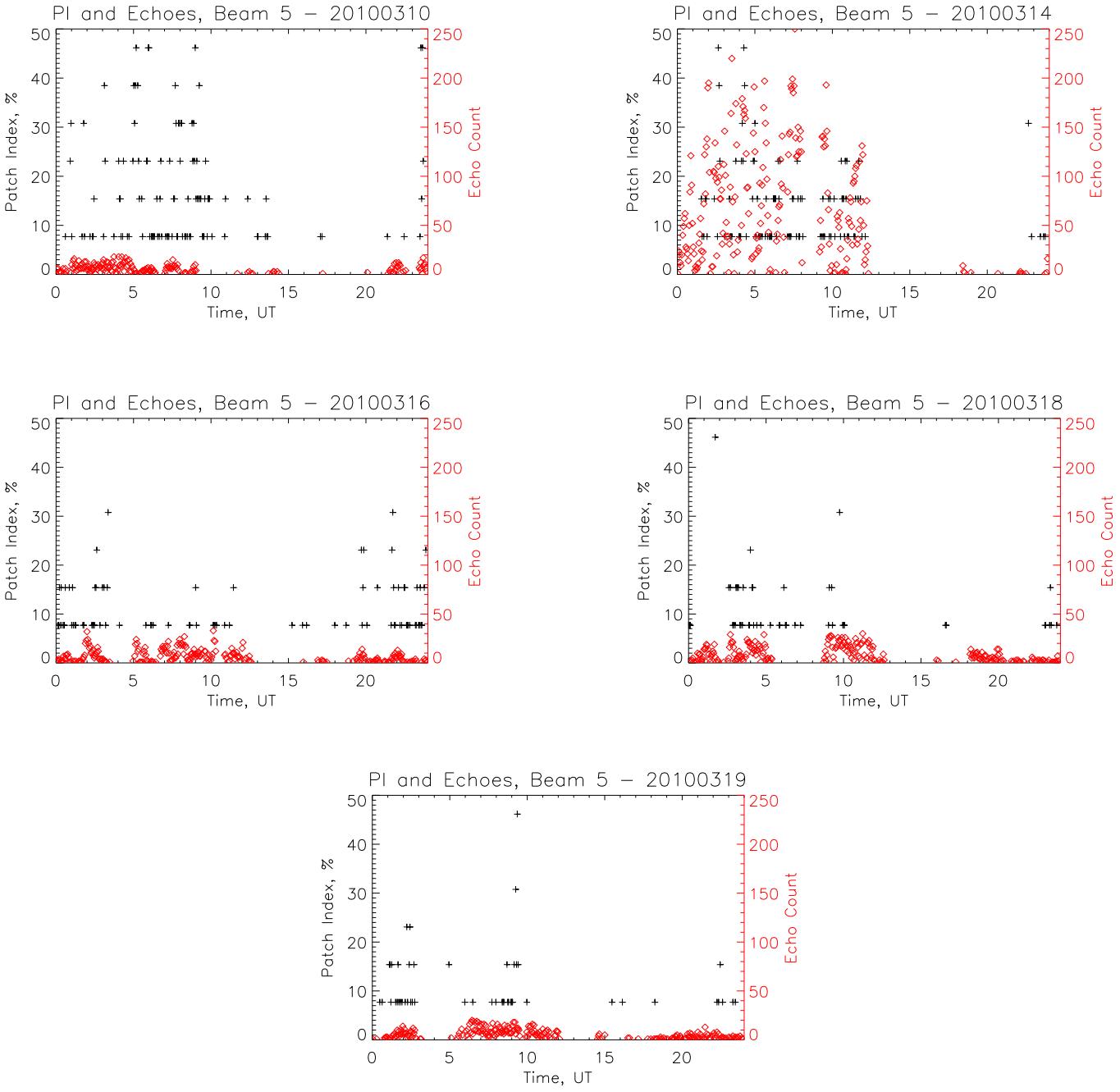

Figure 4.22: A plot comparing the *PI* (black) and the SuperDARN echoes (red) detected in Rankin Inlet beam 5, as a function of time for March 10, 14, 16, 18, and 19, 2010.

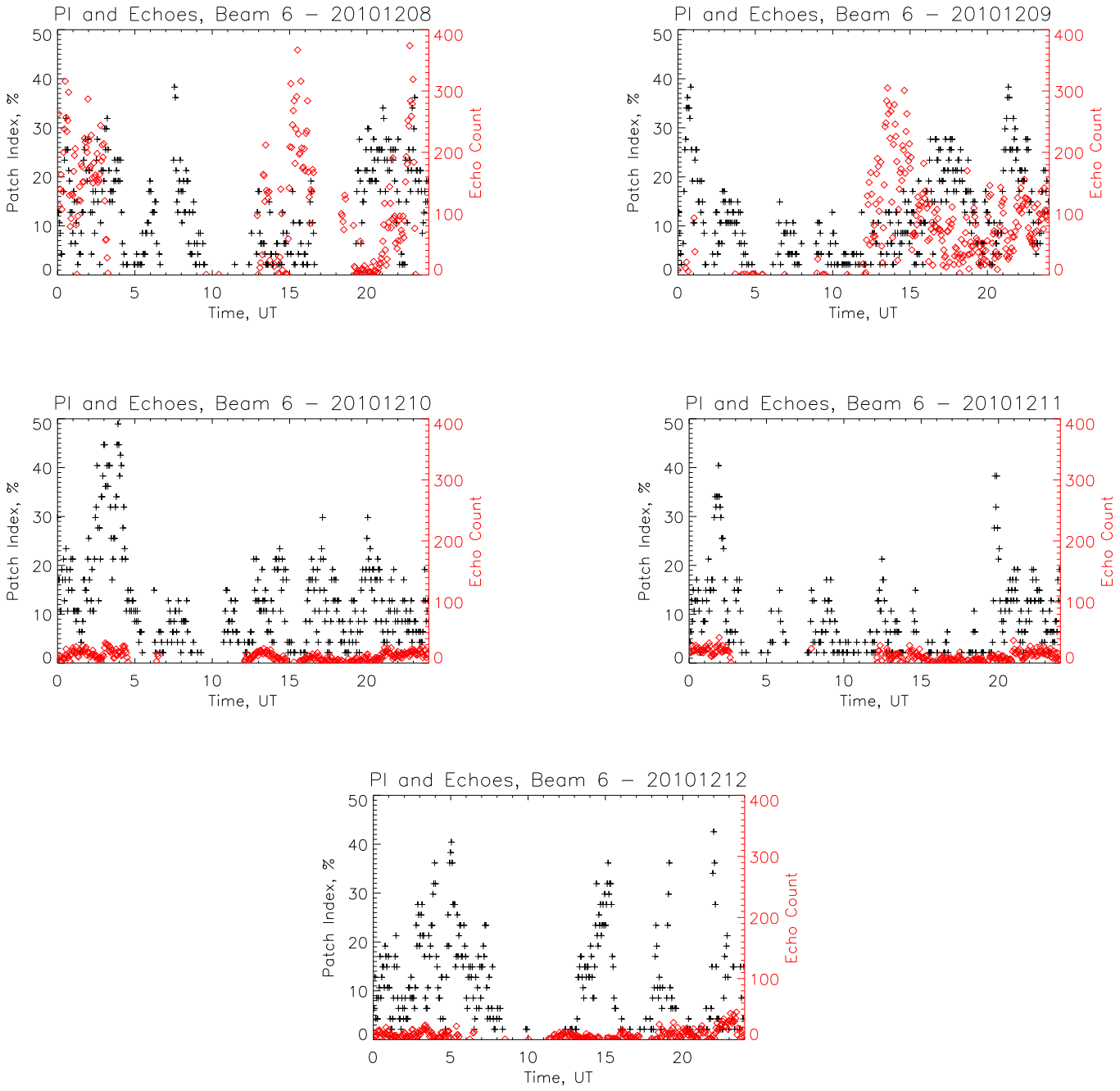

Figure 4.23: A plot comparing the *PI* (black) and the SuperDARN echoes (red) detected in Rankin Inlet beam 6, as a function of time for December 8, 9, 10, 11, and 12, 2010.

The lack of SuperDARN echoes during this time segment, despite the clear presence of patches, may be due to poor HF radio wave propagation. Recall that in order to have a HF coherent backscatter echo two conditions must be met: a target in the form of a FAI must be present in the radar beam; and, the requisite HF propagation conditions that would allow for the HF beam to sufficiently refract and satisfy the aspect angle condition must be present [*Milan et al.*, 2002]. Presumably the former is satisfied since patches are present during this time and are a reliable source of FAIs [*Hosokawa et al.*, 2009a; *Moen et al.*, 2012]. This leaves the HF propagation condition to consider. SuperDARN Rankin Inlet was transmitting at approximately 12.5 MHz for the majority of March 10, 14 and 19, and transmitted at approximately 10.25 MHz for most of March 16 and 18. In December, Rankin Inlet transmitted at approximately 12.5 MHz for each day except for December 12, when it transmitted at 10.25 MHz from 0:00 to 16:00 UT. Recall that according to Equation 2.25 the index of refraction, $n = 1 - f_0^2/f^2$, is related to both the carrier frequency of the radar wave, f, and the plasma frequency, f_0. For March, 2010, $n_e = 2 \times 10^{11}$ m^{-3} is a representative value for the patches during the 05:00 to 12:00 UT (approximately 22:00 to 05:00 MLT) time segment. This means the n_e of the surrounding ionosphere was at least half that value; the RISR-N algorithm only picks out n_e values that are twice that of the background ionosphere. This gives [*Chen*, 2010] $n = 1 - (8980\sqrt{1 \times 10^5})^2/(12.5 \times 10^6)^2 = 0.9$ (notice here that n_e is in units of cm^{-3}) for a SuperDARN operating frequency of 12.5 MHz and $n = 0.92$ for 10.25 MHz. For December, 2010 $n_e = 1 \times 10^{11}$ m^{-3} is a representative value, giving $n = 0.97$ and $n = 0.96$ for 12.5 MHz and 10.25 MHz Rankin Inlet transmitting frequencies, respectively. When the n_e of the patches detected by the RISR-N algorithm was lower, the n_e in the surrounding area was lower as well – half the n_e of the patches, or less, so the HF radar beam transmitted by SuperDARN would not have undergone as much refraction. Therefore, one possibility is that the coincidental decline in the n_e of patches and disappearance in SuperDARN echoes during the 05:00 to 12:00 UT time segment was due to the inability of the HF to achieve enough refraction to satisfy the aspect angle condition.

Admittedly this postulate is somewhat naive since HF ray propagation is a complex process, as shown in Figure 2.7, and has many subtleties and modes [e.g., *Ponomarenko et al.*, 2009, and references therein]. For example, if the difference between sufficient and

insufficient HF propagation is a variation in n as little as 0.05, then we would expect to have seen some variation in the SuperDARN echo count when the Rankin Inlet transmission frequency switched from 10.25 MHz to 12.5 MHz at approximately 16:00 UT on December 12, 2010. But, this is not the case. The HF propagation postulate seems plausible, but it is not conclusive. To proceed further, the intricacies of HF propagation must be taken into account before a conclusion can be drawn for the data sets presented here. More analysis is required, and a novel experiment may be necessary. This is discussed further in Section 4.6.3.

4.6.3 Simultaneity of PI and Rankin Inlet echoes

The parameter, Γ, has been developed to provide a more quantifiable way of describing the simultaneity of patches and SuperDARN echoes in a given SuperDARN beam. For a given time bin (which is three minutes in length, the duration of a RISR-N scan), and SuperDARN beam, three cases are considered: both patches and echoes are present; only echoes are present; or, only patches are present. By definition, Γ is a Boolean-like function, and is defined as:

$$\Gamma = \begin{cases} 0 & RB \cdot SD + \overline{RB} \cdot \overline{SD} \\ 1 & RB \cdot \overline{SD} \\ -1 & \overline{RB} \cdot \ SD \end{cases}, \tag{4.2}$$

in which '+' is the OR operation, '$\cdot$' is the AND operation; '$\overline{*}$' is the negation operation. $RB = 1$ for any patch count value, i.e., for any non-zero PI value, and $SD = 1$ for any SuperDARN echo count value. Equation 4.2 states that at a given time $\Gamma = 0$ in two cases: if a patch and SuperDARN echo are present, or if neither is present. If a patch is present but a SuperDARN echo is not, $\Gamma = 1$. If a patch is not present but a SuperDARN echo is, $\Gamma = -1$.

The premise of Section 4.6 is to explore the interconnection of the patches and SuperDARN echoes in the polar ionosphere. In this context, $\Gamma = -1$ is a crucial case. If the majority of SuperDARN echoes in the polar ionosphere originate from patches then very few cases should exist in which SuperDARN echoes are present but patches are not; namely, very

few occurrences of $\Gamma = -1$ should exist. Those cases indicate that SuperDARN echoes are being generated by some mechanism other than patches and therefore contradict the stated hypothesis that patches are at the origin of most of the SuperDARN echoes in the polar ionosphere.

A plot of Γ for the March and December, 2010 datasets is given in Figures 4.24 and 4.25, respectively. For a majority of the March, 2010 dataset, 60%, $\Gamma = 0$, i.e., the majority of patch and echo cases happened simultaneously. The second most common case was $\Gamma = 1$, a patch was present but without a corresponding SuperDARN echo. This occurred 35% of the time. As discussed in Section 4.6.2, this may be due to HF propagation conditions, but more work is needed to test this hypothesis. The rarest case was $\Gamma = -1$, for which a SuperDARN echo was present, but a patch was not. Of the all cases in the March, 2010 dataset, only 5% were of the $\Gamma = -1$ variety. Therefore, it appears that the majority of echoes in Rankin Inlet beam 5 during March, 2010, originated from FAIs associated with patches.

The day with the most $\Gamma = -1$ cases in the March, 2010 dataset was March 10. On closer inspection, the majority of those cases occurred during the 05:00 to 12:00 UT sector. It is interesting to note that according the Figure 4.10, there was an increase in patch occurrence in this time segment (we must keep in mind that Figure 4.10 shows the patch occurrence for the entire RISR-N FOV, and not just the portion bounded by SuperDARN beam 5). In other words, there were more patches in the RISR-N FOV during this time segment, but there were also more $\Gamma = -1$ cases in which SuperDARN echoes were present but patches were not. This is an unexpected result, but may be another byproduct of HF propagation, which will be discussed shortly. Also, the $\Gamma = -1$ cases may be patches with densities that are just below the *Crowley* [1996] criterion, e.g., a patch with a n_e that is only 1.75 times as dense as the background ionosphere. This patch may generate FAIs, but would be neglected by the RISR-N algorithm.

The March and December, 2010 datasets share one common trend: for the majority of the dataset, 66% in December, $\Gamma = 0$. Once again this indicates that patches are indeed a considerable source of SuperDARN echoes in the polar ionosphere. The major differences between the two datasets can be found with the $\Gamma = 1$ and $\Gamma = -1$ cases. As shown in Figure 4.25, there are very few instances of $\Gamma = 1$ – only 10% for the entire dataset. Thus,

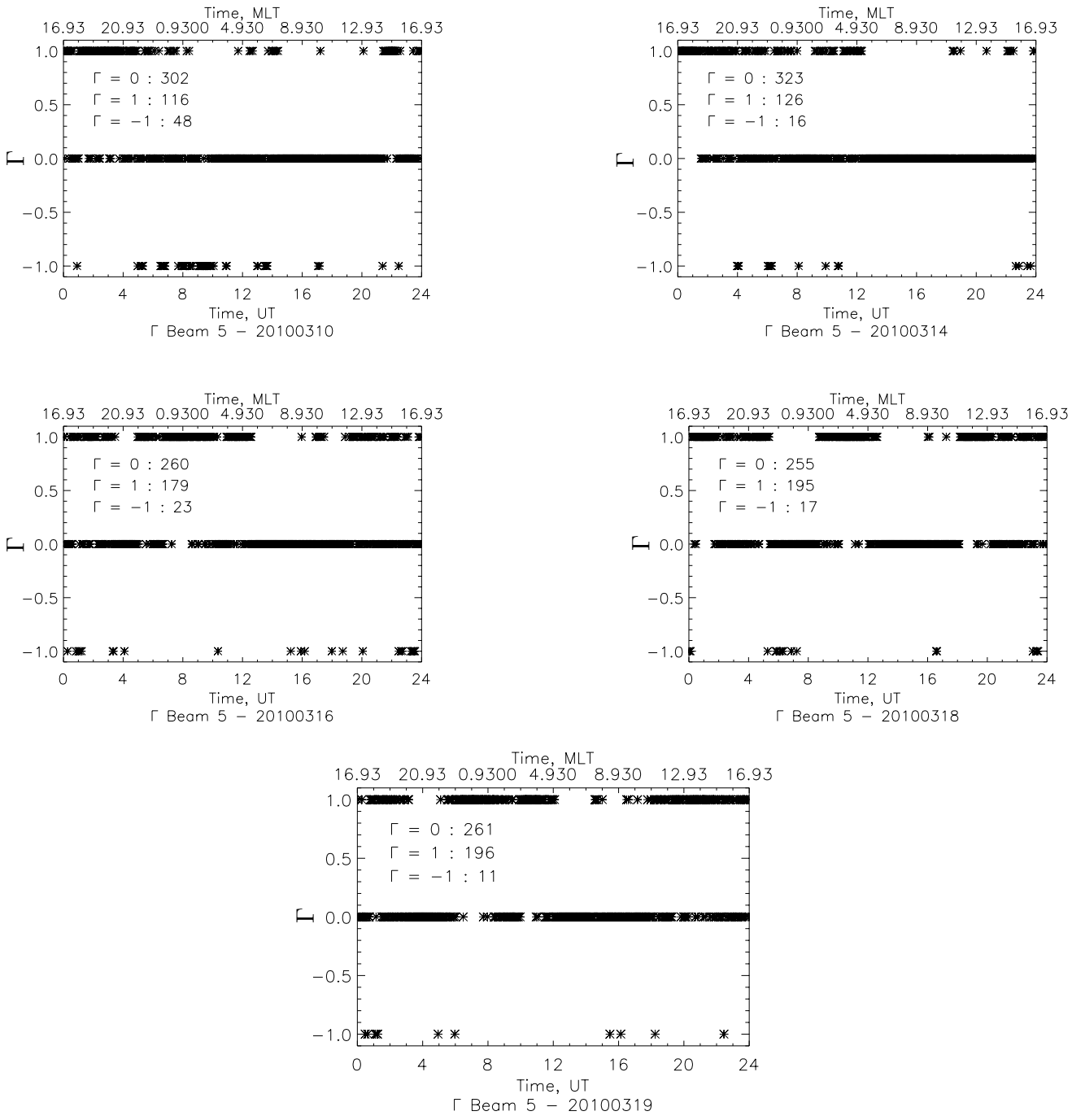

Figure 4.24: A plot of Γ for Rankin Inlet beam 5, as a function of time (UT and MLT) for March 10, 14, 16, 18, and 19, 2010. The tally for each value of Γ is also provided.

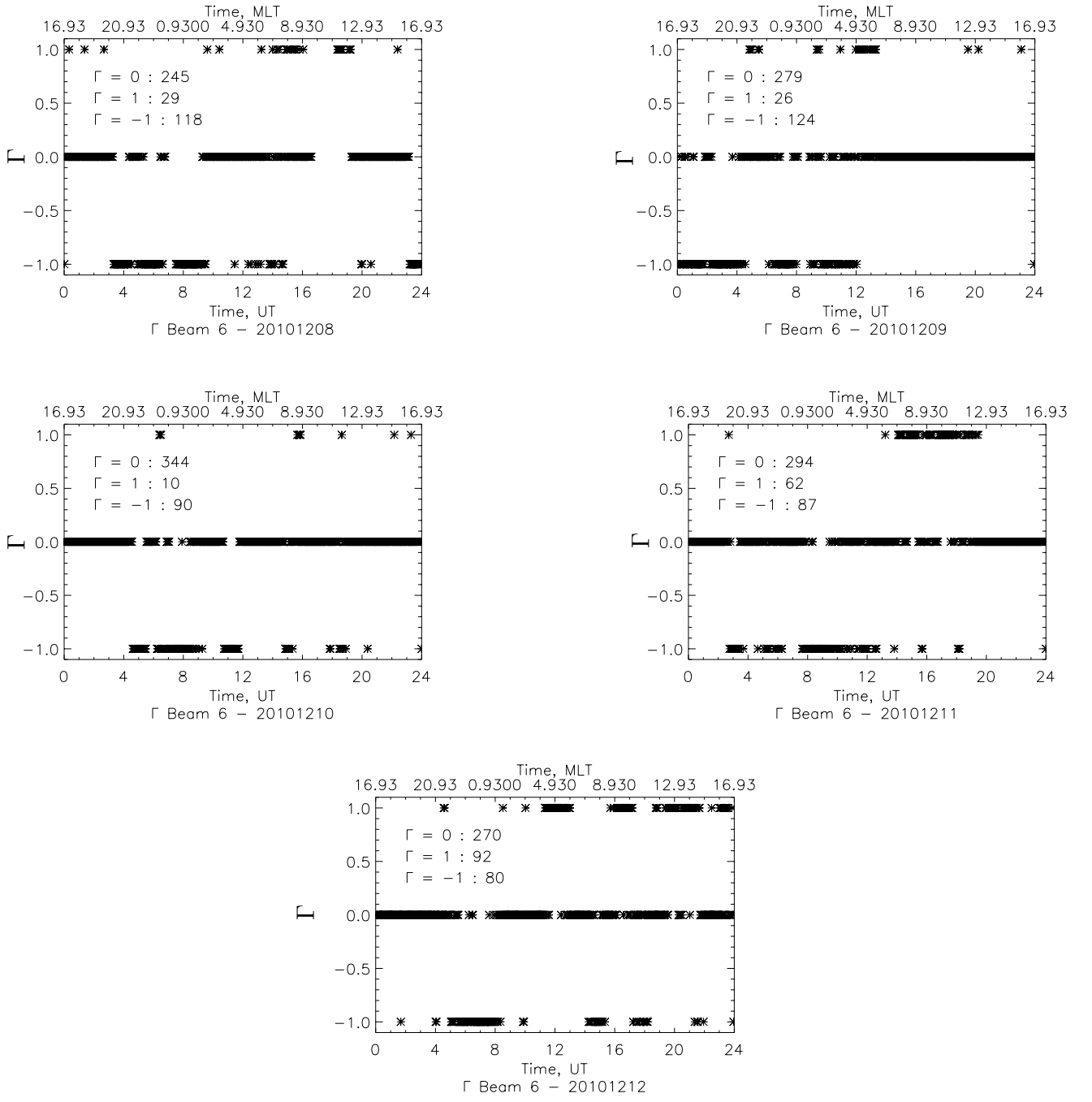

Figure 4.25: A plot of Γ for Rankin Inlet beam 6, as a function of time (UT and MLT) for December 8, 9, 10, 11, and 12, 2010. The tally for each value of Γ is also provided.

24% of the SuperDARN echoes ($\Gamma = -1$) detected in December, 2010, did not have a patch associated with them. Like the March dataset, most of these cases occurred in the 05:00 to 12:00 UT time segment. As shown in Figure 4.11, the number of detected patches declined significantly during this time segment, which is a different result than what was seen with the March dataset.

Simultaneity of PI and Rankin Inlet echoes: HF propagation

Up to this point when talking of HF propagation we have only focused on the vertical refraction, i.e., what is displayed in the two dimensional slice in Figure 2.7. We have neglected the lateral refraction of HF radio waves. In general, refraction can have a significant effect on determining the location the scattering volume [*Villain et al.*, 1985]. Typically, the position of a radar target is ascertained using the a priori knowledge of the beam pointing direction and the delay between the transmission and reception of the radar signal. This is a relatively straightforward procedure if the transmitted radio wave propagates in a straight path and does not undergo any significant refraction in the ionosphere. This is the case for ISR radars since their transmission frequency is well above the plasma frequency of the ionosphere. But, as explained earlier, in Section 2.2.1, this is not the case for SuperDARN. Its radar beams refracts in the vertical and the horizontal [e.g., *Koustov et al.*, 2008]. Even though the propagation delay of the signal can still be determined accurately, uncertainty in the location the scattering volume is introduced by the mere notion that the ray path is distorted due to refraction. This is illustrated by the black contours in Figure 2.7, which are range gate markers along the beam. Closer to the HF ray source, the contours are radially distributed nearly isotropically. However, at further distances from the ray source, once the HF ray begins to refract in the modelled ionosphere, the range gate contours become heavily distorted, showing the increase in location uncertainty for HF radars. The only location information available is the propagation delay of the radar signal. All other information such as the n_e profile of the ionosphere along the ray path must be inferred [e.g., *Gillies et al.*, 2009; *Gillies et al.*, 2012], or modelled.

Not only will a HF radar wave refract vertically, it was also refract horizontally, producing even more uncertainty in the location of the scattering target. A good example of this is given

by *Dahlgren et al.* [2012b], who studied a single patch detected with the RISR-N, SuperDARN Rankin Inlet and OMTI. That work can also be found Chapter 5 of this document. Figure 3 in *Dahlgren et al.* [2012b], which is reproduced in Figure 5.3 in Chapter 5, demonstrates the possible effects of refraction of the location accuracy of SuperDARN. The majority of the patch was located within Rankin Inlet beam 7; a portion of the RISR-N and OMTI signature were also located in beam 7. What is interesting is that the backscatter power of the SuperDARN echoes associated with the patch were detected in beams 7, 8 and 9, but were most enhanced in Rankin Inlet beams 8 and 9 – adjacent to the beams in which the patch was determined to be by RISR-N and OMTI. This shows that it is possible for a coherent backscatter signature of an individual patch to appear in multiple SuperDARN beams as well as range gates. This effect may be a byproduct of horizontal refraction; radar waves from Rankin Inlet beam 8 and 9 are being refracted into adjacent beams with contain FAIs generated by the patch. More work is needed to verify this, however. Nonetheless, the generation of backscatter echoes in the adjacent beams has important implications for Γ as it would be a case in which $\Gamma = -1$. This may provide an explanation for some of the $\Gamma = -1$ cases described in Figures 4.24 and 4.25.

Simultaneity of PI and Rankin Inlet echoes: summary and future Work

For the March and December, 2010 datasets, a SuperDARN echo was present without an associated patch 5% and 24% of the time time in Rankin Inlet beams 5 and 6, respectively. Although these results do not fully confirm the notion that the majority of SuperDARN echoes from the polar region originate from patches, they do provide a strong indication that this may be the case.

At this point in time this study is incomplete. More consideration must be given to the HF propagation conditions to verify whether the $\Gamma = 1$ and $\Gamma = -1$ are indeed a byproduct of HF propagation effects. This can be done by expanding the analyzed datasets to include echoes from other radars, such as the Inuvik and Clyde River radars. HF ray trace modelling would also be required. It was mentioned earlier that the Inuvik radar only receives a fraction of the radar echoes from the RISR-N FOV that the Rankin Inlet radar does. As illustrated in Figures 2.9 and 4.21, Rankin Inlet and Inuvik have FOVs that are nearly at right angles

to each other. As it turns out both radars are approximately equidistant from the RISR-N FOV; each has ground range of approximately 1500 to 2000 km from the RISR-N FOV. Thus, the discrepancy in echo count between the two radars is a HF propagation effect and as such should be investigated as it may provide further context to the simultaneity of patches and echoes detected within the RISR-N FOV. For example, the Inuvik radar can be used as a secondary confirmation for SuperDARN echoes (or lack thereof) in a scattering region intersected by the Rankin Inlet radar.

The Clyde River and Rankin Inlet radar FOVs are also at nearly right angles to one another. As Figure 4.21 illustrates, only a portion of the RISR-N FOV is covered by the Clyde River FOV. The ground distance between Clyde River and the RISR-N FOV is approximately 1000 km. This is nearly half the distance between Rankin Inlet/Inuvik and Resolute Bay, and has important implications in terms of HF propagation considerations. The HF ray paths from the Rankin Inlet and Inuvik radars are termed "one and a half hop" paths. For a 1-1/2-hop path, the HF ray propagates up to the ionosphere, refracts back towards the ground at which point it is reflected back towards the ionosphere where it undergoes coherent backscatter (assuming there is a FAI present). The HF rays modelled in Figure 2.7 that satisfy the aspect angle condition at 2000 km ground range are 1-1/2-hop paths. The Clyde River radar is close enough to the RISR-N FOV that the echoes it receives from the region are 1/2-hop ("half-hop") ray paths [G. J. Sofko, personal communication, 2013], meaning that the HF ray is backscattered upon entering the ionosphere for the first time. The HF rays that satisfy the aspect angle condition at approximately 700 km from the ray origin in Figure 2.7 are an example of 1/2-hop paths. One important difference between 1/2- and 1-1/2-hop ray paths is that the latter spends more time in the ionosphere, and is subject to more refraction and dispersion. As a result, the location uncertainty along these ray paths will inherently be higher than the location uncertainty in the 1/2-hop ray paths. Clyde River can also be used in conjunction with the Rankin Inlet and Inuvik radars to confirm the presence of echoes from a common scattering region within the RISR-N FOV.

With all of the aforementioned details in mind an experiment can be performed with the objective of providing a deeper understanding of the interconnection between SuperDARN echoes and patches in the polar ionosphere. The RISR-N radar should be run in a mode

similar to the World Day mode used in March and December, 2010. Furthermore, the radar should be run continuously for several days at a time. This way, a variety of geomagnetic and ionospheric conditions may be investigated. Several iterations of these multi-day experiments should be conducted at different times throughout the year as well, so as to ascertain the influence of seasonal variations. All three SuperDARN radars in the region: Rankin Inlet, Clyde River and Inuvik should also be used to detect and confirm the presence of echoes. In this section, all of the echoes from within the region of the RISR-N FOV bounded by a selected SuperDARN beam were considered, but there is no reason why smaller or larger regions of the RISR-N FOV cannot be considered either. If the majority of SuperDARN echoes from the polar ionosphere are originating from patches, then their simultaneity should be observed in any portion of the RISR-N FOV explored regardless of its size.

4.7 Summary

In this section, an algorithm designed to detect patches within the RISR-N FOV has been developed, the RISR-N algorithm, and shown to be an effective tool for detecting and investigating patches in the polar ionosphere.

In Section 4.4, the algorithm was used to conduct a survey of the patches detected in the RISR-N FOV over 10 days: March 10, 14, 16, 18 and 19, 2010, and December 8, 9, 10, 11 and 12, 2010. Results of this survey include:

1. The n_e of patches varies significantly throughout the day, by as much as an order of magnitude in some cases, e.g., March 10, 2010. A distribution of patch n_e for March and December, 2010 is given in Figures 4.12.

2. The patch population in a strongly "sunlit" ionosphere is much less than a poorly illuminated "dark" ionosphere.

3. The December, 2010, dataset has population of patches with a low n_e that is not seen in March, 2010. This distinct population is attributed to greater n_e depletion in December due to the lack of photoionization.

4. The T_i of patches is relatively consistent throughout a 24 hour period. On average, the T_i of patches in a strongly sunlit ionosphere is only approximately 100 K higher than patches in poorly illuminated conditions.

5. The T_e varies significantly between strongly and poorly sunlit conditions. The T_e of patches in a strongly sunlit ionosphere is approximately twice as large as the T_e of patches in a poorly illuminated ionosphere.

6. The T_e of patches detected in March, 2010, during poorly illuminated conditions is systematically larger than the T_e of patches detected during the same time frame in December, 2010. The difference in T_e was attributed to the increased cooling time of the electron gas in December, 2010.

In Sections 4.5 and 4.6 a patch index, PI, was introduced to quantify what proportion of the RISR-N FOV contains a patch. The PI was then used to investigate the interconnection of SuperDARN echoes originating of the polar ionosphere and patches. With the same datasets used in Section 4.4, it was determined that the occurrence of SuperDARN echoes measured by Rankin Inlet are strongly linked to the presence of patches in its FOV. For March, 2010, only 5% of the dataset featured SuperDARN echoes that did not appear to be associated with a patch. 60% of the echoes were associated with patches. For December, 2010, those numbers were 25% and 66%, respectively. However, more work is need to gauge the influence of HF propagation on these results, and is left for future work.

4.8 Future work

In addition to the future work discussed in Section 4.6.3, there are additional avenues of investigation that should be discussed.

Other patch trends which were not discussed in this chapter should be explored using the RISR-N algorithm, and are left for future work. One such avenue of inquiry includes investigating the many n_e variations observed through the March and December, 2010 datasets. In some instances, such as December 10, 2010, the patch n_e variations appear to be sinusoidal with a fixed frequency. What is driving the n_e of patches to exhibit this pattern? Are these

variations due to a local effect; are alterations in the background ionosphere or thermosphere being reflected in the n_e of the patches? Or, are these oscillations related to the orientation of the IMF, which is strongly coupled to the polar-cap plasma convection pattern (see Figure 1.15) [*Weimer*, 1995]? *Milan et al.* [2002] proposed that the movement from the polar cusp may be a moderator in the n_e of patches entering the polar-cap. Are we witnessing the results of this effect?

The RISR-N algorithm should be modified to include an estimate on the size and shape of a detected patch. It its current state, the RISR-N algorithm does not attempt to compare patch detections in adjacent beams. Since the RISR-N beam configuration is static and well known, it should be possible to infer the shape and size of a patch detected in the RISR-N FOV. This would require the development of a sophisticated algorithm that would compare patch detections in one RISR-N beam to any beam adjacent to it, and so forth. If successful, a survey could be conducted to infer the general shape and size of patches passing through the RISR-N FOV. Admittedly some patch shapes may extend beyond the RISR-N FOV itself. Nonetheless, if the algorithm is successful it could be used to study whether the size and shape of patches is linked to any other geomagnetic or IMF conditions.

Chapter 5

Structuring and Morphology of F-region Ionization Patches

5.1 Introduction

In this chapter, emphasis is placed on the internal structuring and morphology of F-region ionization patches as they convect through the high-latitude and polar-region. This chapter features a thorough investigation of an individual patch detected over Resolute Bay by the RISR-N system, two SuperDARN radars, and the OMTI imager at Resolute Bay. Patches are a well-know source of plasma irregularities, with the GDI instability as their source (see Section 2.2.2). By amalgamating the data from multiple instruments, several aspects of the patch can be monitored as it convects through the ionosphere. For example, irregularities associated with the patch can be investigated by monitoring the coherent backscatter power, or spectral width properties of the of the patch, with SuperDARN. This data can then be complemented by any plasma density or temperature variations detected by RISR-N. Using multi-instrument analysis techniques in the case study presented here, it becomes clear that F-region ionization patches can be extremely complex and dynamic features of the nighttime ionosphere.

The research presented in this chapter was performed alongside Dr. Hanna Dahlgren, currently at the University of Southampton. Its results are presented in *Dahlgren et al.* [2012b]. My participation in this research included compiling and interpreting all of the SuperDARN related data, some of which is plotted in Figures 5.2, 5.3, 5.4, 5.5, 5.8 and 5.12. Figures 5.2, 5.4 and 5.8 were generated by me. In addition to this, I helped author and edit large portions of the manuscript for *Dahlgren et al.* [2012b].

5.2 Previous multi-instrument investigations

Historically, optical imager experiments have been a popular method for patch observations. Due to their large plasma density gradients and speed, patches are subject to the GDI [*Chaturvedi and Ossakow*, 1981; *Moen et al.*, 2002, 2012]. The irregularities produced from the GDI may set-up a Bragg scattering condition, allowing the patches to be detected outside of the optical spectrum, at radio frequencies, by coherent scatter radar systems [e.g., *Rodger et al.*, 1994; *Milan et al.*, 2002; *Carlson et al.*, 2002; *Carlson*, 2004; *Lockwood et al.*, 2005; *Zhang et al.*, 2011; *Hosokawa et al.*, 2010]. Incoherent scatter radar systems [*Moen et al.*, 2006; *Smith et al.*, 2000], ionosondes [*MacDougall and Jayachandran*, 2007], riometers [*Nishino et al.*, 1998] and rocket-borne instruments [*Lorentzen et al.*, 2010] have all contributed to patch research as well. The majority of early patch research only features data from individual instruments. To test the self-consistency of our understanding about dynamic processes at work within and around patches, multi-instrument observations are crucial. Recently, the scientific community has placed more emphasis on the high-latitude and polar cap region, investing in new scientific instrumentation there. Within the last decade, the installation of several all-sky imagers at Resolute Bay, like the OMTI, two SuperDARN sites at Rankin Inlet, Inuvik and Clyde River, and the installation of the RISR-N (as well as RISR-C, which is expected to be operational soon), has increased the opportunity to conduct patch research using a variety of complementary instruments.

Multi-instrument observations of polar cap patches have been carried out by for example *Carlson* [2004]; *Carlson et al.* [2006]. In the patch case-study by *Lorentzen et al.* [2010] observations from a meridian scanning photometer (MSP), rocket borne instrumentation and the European Incoherent Scatter (EISCAT) Svalbard Radar (ESR), as well as derived ionospheric convection patterns from the SuperDARN radars were featured. The use of multiple instruments in that study culminated in a significant contribution to patch research: compelling evidence of a strong link between fast convection flows on the edges of a Poleward Moving Auroral Form (PMAF) near the cusp region, and the formation of polar cap patches. The PMAF was observed optically with the MSP, the ESR and rocket were used to measure the plasma density of the PMAF, and the SuperDARN radar was used to infer plasma flows

in and around the PMAF and patches. It is important to note that each of the instruments used in this work offered unique and complementary measurements.

Some studies have shown that radar echoes are often stronger on the trailing edge of a patch, attributing this to the notion that GDI growth conditions are more favorable there [*Milan et al.*, 2002; *Cerisier et al.*, 1985]. Observations of multiple patches made both optically and with the Rankin Inlet SuperDARN data by *Hosokawa et al.* [2009b], found no evidence to support this. The radar echoes corresponded well with the optical emissions, even though the lifetime of the patch was shorter than the time needed for the GDI to spread through the patch. A process to account for this discrepancy was presented by *Carlson et al.* [2008], who argued that shear-driven instabilities could rapidly structure the patch during its formation, which was also supported by their measurements.

The complexity and dynamic properties of polar cap patches necessitate a systematic approach for their investigation. Previous work gives credence to the value of using multiple instruments for patch studies. However, each instrument is often limited to measurements in one or two dimensions. In the work presented here, we continue to develop the multi-instrument approach by combining patch measurements from an ISR, a coherent scatter radar and optical instruments. The fast beam-steering technique of the phased-array RISR-N provides a novel three-dimensional view of the plasma parameters in a polar cap patch. This technique was demonstrated on a polar cap patch by *Dahlgren et al.* [2012a], who discussed that multiple time-dependent mechanisms can lie behind the high degree of structuring seen in the electron density of the patch. In this chapter, we expand on those results, by further investigating the same event, with more depth and a more extensive suite of instrumentation. Reminiscent of the combined observations by *Hosokawa et al.* [2009b] of a patch with SuperDARN and an all-sky imager, where a good correlation between the HF echoes and the optical response was found, we use the RISR-N radar to obtain data on the actual electron density in the polar cap, to compare with SuperDARN echoes, and optical images. The advantages of direct electron density measurements for polar cap studies are many. Instead of projecting line-of-sight integrated optical emissions onto a two-dimensional plane, which does not always reflect the true location of the denser plasma, a three-dimensional distribution of the electron density can be obtained. The observations are also not weather-

dependent. Previous probing of the plasma properties in the polar cap by ISRs have been conducted by the EISCAT Svalbard Radar and the Sondrestrom radar, during slow azimuth or elevation scans [e.g., *Carlson et al.*, 2002; *Valladares et al.*, 1998]. With the capabilities of the RISR-N radar, the probing is no longer limited to two dimensions, and data can be captured simultaneously from all beam directions.

At 22:10 UT on December 11, 2009, a patch was observed for approximately 10 minutes with both the OMTI and RISR-N instruments. At the same time, and in the same region, radar echoes consistent with a patch were detected by both the SuperDARN sites at Rankin Inlet and Saskatoon. The combined data sets allowed for detailed investigation of the ionospheric properties of the patch, and a high degree of intrinsic structuring and variability was indicated in the patch.

5.3 Instrumentation and analysis techniques

The instrumentation used in this study consists of incoherent and coherent scatter radars and all-sky imagers, which are detailed below.

5.3.1 RISR-N

RISR-N was introduced in detail in Section 2.1.1. In this study, RISR-N was operating a 480 μs long pulse experiment, limiting the line-of-sight range resolution to 72 km. The radar was pointed in a 5 $\times$ 5 beam grid, with a beam separation of 14° on average, corresponding to a coverage of about 300 $\times$ 400 km at an altitude of 300 km. The pointing directions of the beams are illustrated in Figure 5.1, as small rings overplotted on one of the 630.0 nm OMTI images during the time of the event discussed further below. The geographic cardinal directions as well as the radar beam elevation angle are marked by white dashed lines in the figure. By using a trilinear interpolation technique of the data (illustrated in *Dahlgren et al.* [2012a]), based on the techniques described in *Nicolls et al.* [2007] and *Semeter et al.* [2009], a volumetric image of the plasma parameters is obtained at 1 minute resolution.

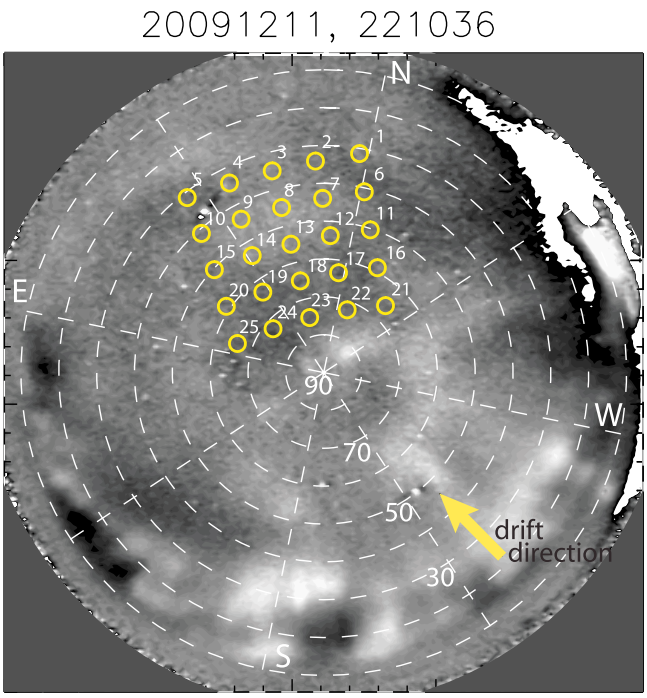

Figure 5.1: OMTI 630.0 nm image on 11 December 2009, at 22:10 UT. The over-plotted small rings show the pointing directions of the 5 × 5 RISR-N beam grid. White dashed lines mark the geographical cardinal directions and elevation angles. The arrow in the bottom right corner shows the general drift direction of the patches from their formation region and through the zenith at Resolute Bay.

5.3.2 SuperDARN data

The SuperDARN radars at Rankin Inlet (62.8°N, 287.0°E), Prince George (54.0°N, 237.4°E), Saskatoon (52.2°N, 253.5°E) and Inuvik (68.4°N, 226.5°E) monitor coherent backscatter from the northern polar cap. For the times from which the radar data was used, the Rankin Inlet radar was operating at 12.2 MHz, the Prince George radar at 10.7 MHz, the Saskatoon radar at 10.8 MHz and the Inuvik radar at 10.5 MHz. Each SuperDARN radar is capable of electronic beam-steering over an azimuth of approximately 55° that is divided into 16 beams. Each beam is subdivided radially into 100 range gates with a radial resolution of 45 km. These SuperDARN radar field-of-views (FOVs) encompass Resolute Bay, providing backscatter power and line-of-sight velocity estimates with a temporal resolution of 2 minutes. The FOVs of the four SuperDARN radars are outlined in black in Figure 5.2, with Rankin Inlet in the center (data colored with grayscale), Saskatoon to the top left (greenscale), Prince

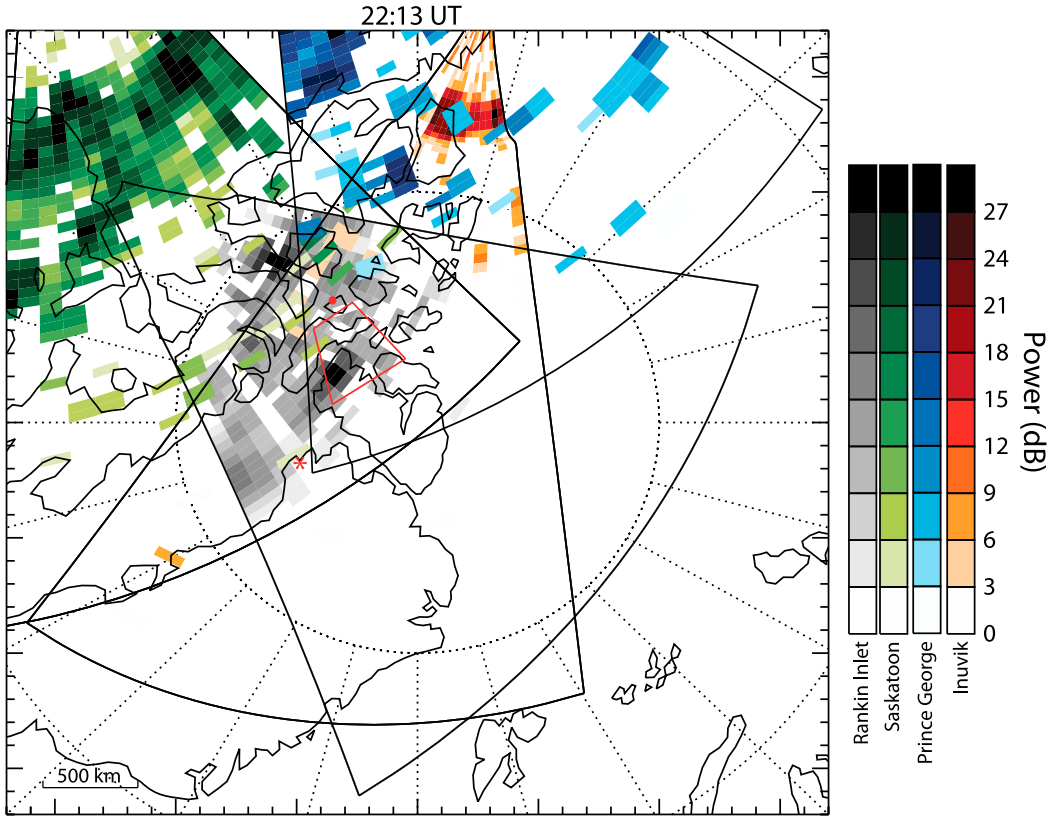

Figure 5.2: Backscatter power echo fan plot from the superDARN radars at Rankin Inlet (gray scale, in center), Saskatoon (green scale, top left), Prince George (blue scale, top center) and Inuvik (red scale, top right), at 22:13 UT. The full FOV of the radars are indicated by black lines. The red tetragon marks the FOVs of RISR-N data at 270 km altitude. The patch of particular interest is seen here with the Rankin Inlet radar, within the FOV of RISR-N. Resolute Bay and Qaanaaq are indicated by a red dot and star, respectively. The direction of the sun is up in the figure.

George to the top center (bluescale) and Inuvik to the top left (redscale). The RISR-N FOV at 270 km altitude is outlined with a red tetragon. The Prince George radar also monitors a region encompassing the cusp during the event discussed here.

5.3.3 Optical imager

One of the OMTI airglow all-sky imagers is located in Resolute Bay. The imager captures a 30 s exposure in 630.0 nm every 2 minutes and regularly 30 s exposures in 557.7 nm. The 630.0 nm red channel is background corrected, by subtracting a one-hour running average for increased contrast. Due to gaps in the imaging sequence, a similar correction cannot be

made for the green 557.7 nm channel. Additional 3 s exposures of N_2^+ at 427.8 nm every 30 s were provided by the NASCAM (Narrow-band All-Sky Camera for Auroral Monitoring) imager owned by the University of Calgary and installed in Resolute Bay.

Data from an all-sky imager installed in Qaanaaq, Greenland (77.5°N, 290.8°E, 85.1°N MLAT) operated by the U.S. Air Force Research Laboratory are also available for this study. The imager captures 55 s exposures in the red line, at 630.0 nm. The FOV is partly overlapping with the FOV of the OMTI and NASCAM imagers, so that it is possible to continue monitoring the patches as they move out of the range of OMTI.

5.4 Observations

The polar cap density enhancements discussed in this paper were observed on 11 December 2009, during a very quiet (Kp = 0) period of negative IMF B_z, and negative and positive IMF B_y and B_x, respectively. Faint plasma structures which drifted anti-sunward from their formation region into the polar cap were seen during a time period of a couple of hours following 18:00 UT. A snapshot of the structures at 630.0 nm taken with the OMTI imager at 22:10:36 UT is shown in Figure 5.1. The patches come into the FOV from the bottom right corner (geographic southwest) and then drift anti-sunward across the FOV to the northeast. The general direction of the drift is marked in the image with an arrow.

One of the patches drifted through the RISR-N FOV around 22:13 UT, producing enhanced echoes in both the incoherent and coherent scatter radars. Figure 5.2 shows the SuperDARN power returns at this time, with data from the Saskatoon, Prince George and Rankin Inlet radar. All three color scales are normalized to 30 dB. A stronger echo (darker region) can be seen in the Rankin Inlet data colocated with the RISR-N FOV. The white regions do not necessarily signify the absence of a radar echo, but are most likely due to problems with the fitting of the measured signal, due to low signal-to-noise ratio. Figure 5.3 shows the correlation between the electron density as measured by RISR-N in a horizontal slice at 270 km altitude (plotted as colored contours in the figure) and the power echo measured by the Rankin Inlet SuperDARN radar (grayscale) at the same time. An enhancement in red line emission could also be detected in the OMTI data, and the location of the emission

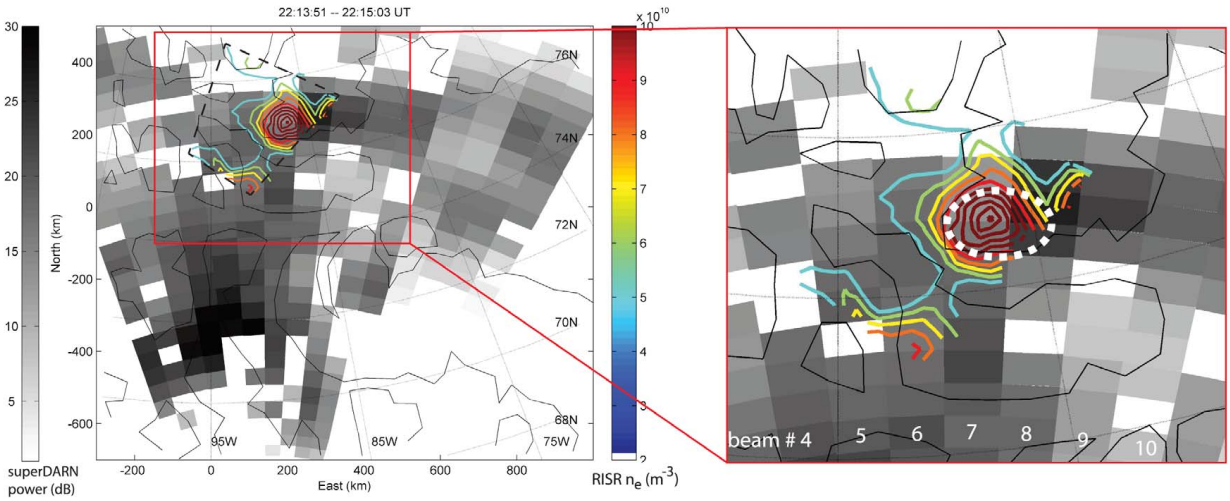

Figure 5.3: RISR-N electron density contour is plotted in color on top of gray scale SuperDARN echoes. The FOV of RISR-N is outlined by a dashed black line. The coherent scatter in SuperDARN is seen next to the plasma density structure. The white dashed oval in the enlarged figure to the right indicates the location of the optical patch seen with the 630 nm channel on OMTI.

is marked in the magnified image by a white dashed oval. In Figure 5.4, range-time plots for backscatter power, velocity and spectral width, from the Rankin Inlet and Saskatoon SuperDARN radar are given. In the former, a transient backscatter power feature – consistent with a patch – can be seen just after 21:50 UT, drifting in a magnetic poleward direction. A similar feature is coincidently detected by the Saskatoon radar.

A three-dimensional composite of horizontal and vertical slices from the RISR-N data is displayed in Figure 5.5 for this patch. The slices at 340 km, 250 km and the vertical slice are produced by extracting cuts of the trilinear interpolation of the radar electron density measurements. The positions of the radar beams are marked on each horizontal slice as black circles. This method of visualization and a discussion of the RISR-N data for this particular event has been previously presented in *Dahlgren et al.* [2012a]. The structure has a peak electron density of 1.5×10^{11} m^{-3}, close to 250 km in altitude. The contemporary 630.0 nm OMTI image is mapped to 200 km altitude rather than 250 km, to keep the figure from being cluttered. The emission ratio brightness of signal over average background is given by the horizontal colorbar at the bottom of the figure. The optical enhancements correspond to the location of the plasma structures seen in the radar data. The coherent scatter from

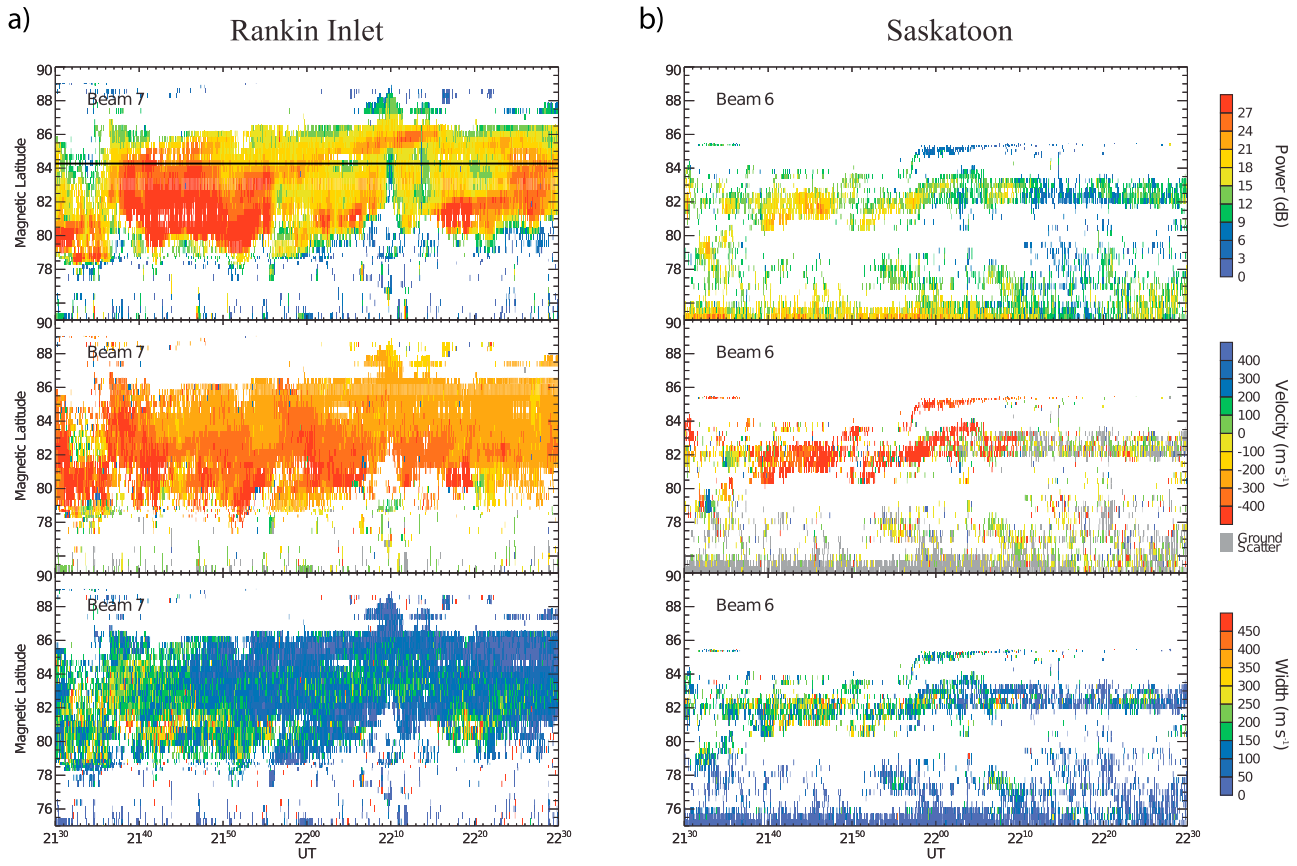

Figure 5.4: a) Range-Time intensity plot of Beam 7 of the SuperDARN radar at Rankin Inlet (top). The latitude of the center of the RISR-N FOV is marked as a black line. (middle) The line-of-sight Doppler velocity and (bottom) the spectral width. b) Same format as in a, for data from Beam 6 of the Saskatoon radar.

the SuperDARN radar is then plotted at 300 km altitude. The strongest echo (up to 30 dB, colorbar to the left in the figure) comes from the region to the northeast of the vertical slice, partly overlapping the RISR-N plasma structure.

The structure at 22:13 UT is seen in the optical data to arrive from the cusp region (the identification of the cusp will be discussed shortly) and then drift anti-sunward and through the RISR-N FOV at a constant speed. The top panel of Figure 5.6 shows the OMTI meridian-aligned keogram for the time period 22:00 – 24:00 UT, where each slanted structure illustrates a poleward drift. The middle and bottom panels show the derived average velocity and direction of the optical enhancements as they pass the zenith of the OMTI imager. At 22:00 UT the structures have an optically measured velocity of close to 300 m/s, in the northeast direction. The speed then increases and the direction becomes more eastward.

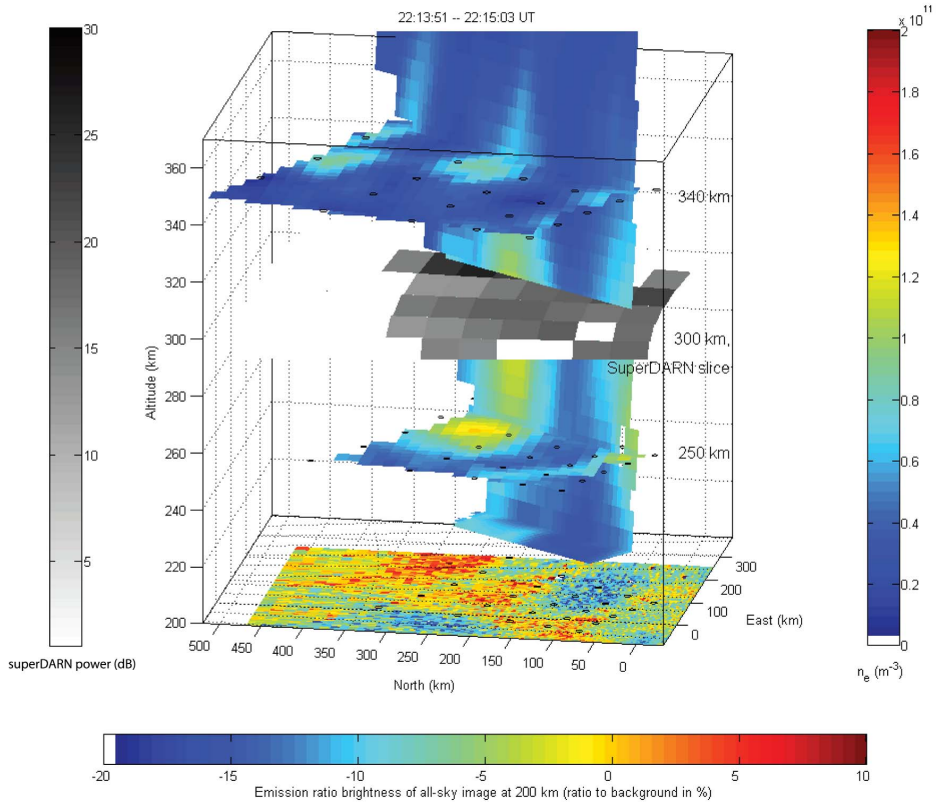

Figure 5.5: Three-dimensional view of an F-region plasma density structure. The slices at 350 km and 250 km as well as the vertical slice show the electron density as derived from RISR-N data. The location of the radar beams are marked as black circles on the horizontal slices. At 300 km altitude, the SuperDARN echo is shown. The simultaneous 630.0 nm OMTI image is projected to 200 km altitude, for which the emission brightness over the background level is indicated with the colorbar below the combined plot. Optical signatures are seen in the location of plasma density enhancements, whereas the coherent echo from SuperDARN is strongest to the side of the plasma structure.

This is consistent with the plasma velocity vectors in the region as constructed from data from the SuperDARN network of HF radars for the same segment of time.

The faint 630.0 nm emissions are also visible in the all-sky data from Qaanaaq, Greenland. At this time, Qaanaaq is located anti-sunward of Resolute Bay and there is some overlap in the FOVs of this imager and the OMTI imager, but unfortunately it was not possible to track a specific patch through both imagers. Even so, red line emission could be seen drifting in the northeast (anti-sunward) direction through the Qaanaaq imager (J. M. Holmes, private communication, 2012).

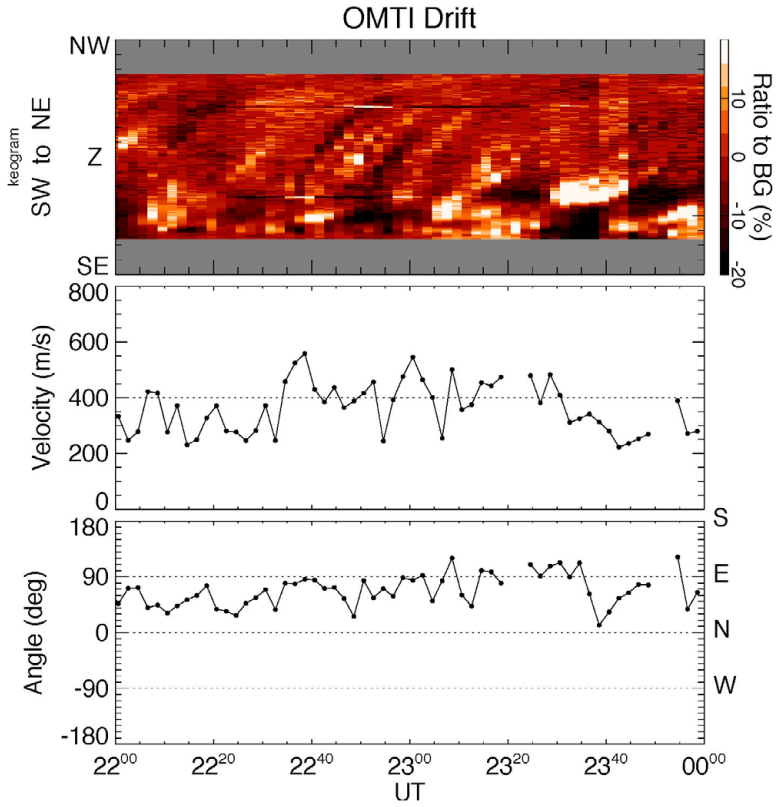

Figure 5.6: (top) OMTI 630.0 nm keogram along the meridian for the times 22:00 - 24:00 UT. (middle and bottom) The drift velocity of the optical enhancements, and their drift angle (east of north), where north is 0 degrees. The structures are drifting predominantly north east, with a velocity of 300 - 400 m/s.

5.5 Discussion

We present simultaneous coherent and volumetric incoherent scatter measurements of polar cap irregularities. The results are compared with optical all-sky measurements in order to clarify the dynamic evolution of polar cap patches, and investigate their intrinsic variability. The weak structures (electron densities of the order of 10^{11} m^{-3}) seen to drift through the RISR-N FOV have spatial sizes of about 100 km $\times$ 100 km $\times$ 100 km, which is small for typical polar cap patches. Similar horizontal sizes are measured from the optical data. The emissions are also very faint, with brightnesses in the all-sky data of only up to 300 R in 630.0 nm and 50 R in 557.7 nm. The NASCAM imager show no or very faint emission in the N_2^+ 427.8 nm wavelength region at around 22:00 UT, which indicates that there is no significant electron precipitation in the polar cap at this time. The structures in the OMTI

imager data appear to originate close to the poleward edge of the auroral oval and drift poleward.

5.5.1 Correlation between radar and optical data

The location of the optical signatures in OMTI correspond well to the enhancements seen in RISR-N for the few hours of contemporary measurements in the two datasets. The coherent backscatter power data from Rankin Inlet SuperDARN radar are indicative of patches in this region during the same time period. In Figure 5.3, the strongest coherent scatter signal originates from the range gates adjacent to the plasma enhancement seen within the RISR-N FOV. The OMTI all-sky data show a faint optical signature collocated with the RISR-N enhancement at this time. An enlargement of the region of interest is shown in Figure 5.3, where the location of the optical structure has been marked with a white dashed oval. This comparison shows that the optical structure seen in OMTI overlaps well with the RISR-N structure, and both features straddle two beams (Beams 7 and 8) in the SuperDARN FOV, with the strongest echo found in Beam 8.

Field aligned irregularities (FAIs) likely produced by the GDI in the plasma set up the Bragg scattering conditions required for coherent backscatter. These FAIs are closely associated with polar cap patches [e.g., *Weber et al.*, 1984; *Rodger et al.*, 1994; *Ogawa et al.*, 1998; *Hosokawa et al.*, 2009b]. An asymmetry between the irregularity intensity on the leading and trailing edge of a patch is a common feature in patch observations [*Milan et al.*, 2002; *Cerisier et al.*, 1985]. This has been used to infer stronger structuring on the trailing edge and weaker structuring on the leading edge of a patch. The GDI is least stabilized where the $\mathbf{E} \times \mathbf{B}$ velocity of the patch is parallel to the density gradient of the patch, and most stabilized when the $\mathbf{E} \times \mathbf{B}$ velocity of the patch is anti-parallel to the density gradient of the patch. It is therefore expected that the FAI intensity and thus the backscatter power would be higher on the trailing edge of patches [*Cerisier et al.*, 1985]. This explanation for the observed asymmetry was further reinforced by *Milan et al.* [2002], who used the CUTLASS SuperDARN radar in Finland together with an ionosonde located on Svalbard to investigate the structuring of polar cap patches near the cusp. *Hosokawa et al.* [2009b] performed combined SuperDARN radar and all-sky optical measurements on several patches

over Resolute Bay. The radar data showed decameter-scale FAIs extending over all of the optically observed polar cap patches, with no preference for the patch edges – contradicting the supposed FAIs preference for the trailing edge of a patch. In their work, *Milan et al.* [2002] and *Ogawa et al.* [1998] speculated that FAI structuring is distributed along the trailing edge of a patch shortly after the formation of the patch. The FAIs then spread over the entire patch during its travel through the polar cap. This was supported by numerical three-dimensional simulations of the nonlinear evolution of instabilities and show that FAI structuring penetrates through the entire patch over a time period of about one hour after its formation [*Gondarenko and Guzdar*, 2004], beginning at the trailing edge of the patch. The patches studied by *Hosokawa et al.* [2009b] were estimated to be only 20 – 25 minutes old as they entered the all-sky FOV at Resolute Bay, and were found to be almost fully structured. In other work, in-situ measurements of 18 patches in the polar cap region by the Dynamics Explorer 2 spacecraft showed that the majority of those patches were either fully structured or were structured at the edges, regardless of the distance between the patch and the cusp where they are believed to have formed [*Kivanç and Heelis*, 1997]. Thus there does not appear to be any connection between the spread of FAIs throughout the patch, and the proximity of the patch to the region of its formation. It has also been suggested that auroral particle precipitation in the cusp can give rise to km scale plasma structuring, onto which the GDI can operate [*Kelley et al.*, 1982; *Moen et al.*, 2012]. *Oksavik et al.* [2010] pointed out that polar patches may undergo substantial rotation as they travel, constantly re-defining the trailing edge of the patch, increasing the rate at which FAIs occupy the entire patch. In a recent paper by *Carlson et al.* [2008], a possible explanation was offered: a velocity-shear instability may rapidly structure a patch as it is formed, upon which the GDIs then grow. SuperDARN observations were used to support this new mechanism by showing several cases of flow shear in the region where patches were formed. However, no clear evidence of velocity flow shears was detected in the cusp region probed by the Prince George SuperDARN radar during the present event.

The location of the cusp is estimated from the plasma velocity plot in Figure 5.7 as the region where the drift velocity arrows turn and change from a sunward to an anti-sunward direction, near 75°N MLAT and 12:30 MLT. This location is also consistent with modeling

for Kp = 0 [*Sigernes et al.*, 2011] and coincident with optical signatures consistent with cusp precipitation and dynamics (e.g., *Milan et al.* [1999] and references therein). The distance from Resolute Bay to the cusp is estimated to be 800 km at 22:00 UT. With an average drift velocity of 300 m/s the patches would be $\sim$ 45 minutes old when they reach the FOV of RISR-N, assuming they were formed in the cusp region. Compared with the patches observed by *Hosokawa et al.* [2009b] we would thus expect the patches in this event to be fully structured by the time they reach Resolute Bay. In Figure 5.3, the SuperDARN data indicates strong backscatter power throughout the plasma density enhancement observed in the RISR-N data; but the strongest SuperDARN echo is located on the eastern edge of and adjacent to the RISR-N structure. This observation further highlights the indifference of FAIs to align along a leading or trailing edge of patch. It is important to note that the spatial resolution of this SuperDARN data is 45 km radially and $\sim$50 km azimuthally, with an estimated accuracy of $\sim$15 km [*Yeoman et al.*, 2001], though the accuracy can be up to 100 km, depending on the HF propagation conditions. Since the RISR-N patch appears to straddle Beams 7 and 8 in the SuperDARN FOV, the coherent backscatter echo may have been shifted into an adjacent range gate, creating the appearance of radar echo power in adjacent range gates. A correlation does exist between the SuperDARN echoes in Beam 7 and the RISR-N and OMTI signatures; however, their power is less than that of the SuperDARN echoes in Beam 8. HF radar backscatter power is not strictly dependent on a large density gradients or the amplitude of the FAIs; other effects must be considered. Radio wave propagation conditions play a major role in coherent backscatter. To undergo coherent backscatter, the wave vector of an incident radar beam has to be close to perpendicular (within a few degrees) with the magnetic field in the scattering volume. At high latitudes the magnetic field lines are nearly vertical. In order for the HF radio waves to meet the aspect angle for coherent backscatter, an HF radio wave must undergo refraction, which is possible due to the dispersive properties of ionospheric plasma. The aspect angle condition can be quite sensitive and it is not uncommon to measure a large variation of backscatter power from adjacent range gates or beams, due to propagation conditions. Ray tracing models show that discrete F-region density enhancements (i.e., patches) have similar properties to converging optical lenses causing radio waves incident on the patch to be focused by the patch

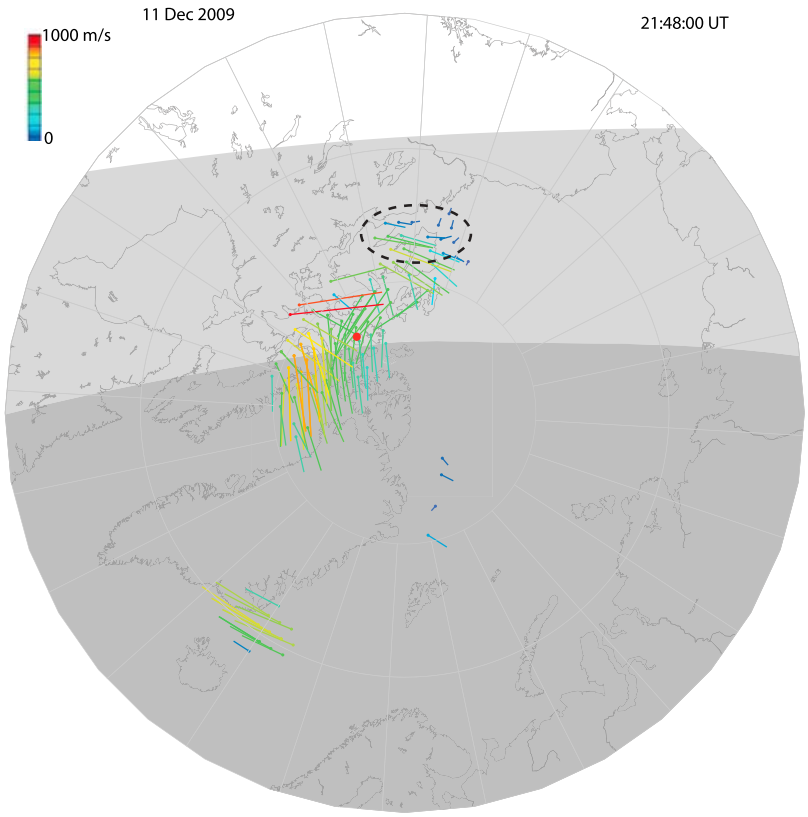

Figure 5.7: Plasma velocity vectors constructed from line-of-sight velocity information from multiple SuperDARN sites using the FIT technique [*Ruohoniemi and Baker*, 1998]. The plasma flow at Resolute Bay (red dot) is predominantly in the northeast direction. The estimated location of the cusp is marked with a black dashed oval. The transitions to the light and dark gray regions mark the day/night terminators at 300 km altitude and on the ground.

and then backscatter on the far side of the patch, with respect to the radar. In SuperDARN data this effect would resemble that of Figure 5.3, in which the strongest backscatter power return in the SuperDARN data is behind the patch in RISR-N and the optical patch in the OMTI data. Therefore, the discrepancy between the locations of the SuperDARN backscatter power and the RISR-N enhancement (Figure 5.3) may be the result of a combination of the HF propagation conditions and the positioning of the patch between two beams within the SuperDARN FOV.

5.5.2 Formation mechanism

The substantial amount of instrumentation available for this event is an important asset when characterizing the properties of the polar cap patches, but also in gaining insight into how the structures were formed. Theory suggests that patches may be formed from photoionized plasma originating from subauroral latitudes. The plasma may be transported into the cusp region by convection streamlines and undergo structuring as they reach the cusp [*Foster*, 1993]. The structuring of plasma within the polar cap or cusp region is attributed to a variety of mechanisms such as: transient reconnection and flux transfer events (FTEs) (see Section 1.4.1 in this work) [*Lockwood and Carlson*, 1992], enhanced recombination rates discretizing dense plasma flows, leading to the plasma depletions between the patches [*Valladares et al.*, 1996], and soft particle precipitation creating plasma density enhancements [*Walker et al.*, 1999]. The polar cap itself can be a source of patches; they have been seen to form in the polar cap due to soft precipitation in a region free of photoionization [*Oksavik et al.*, 2006; *Moen et al.*, 2012]. Observations by *Lorentzen et al.* [2010] have also shown that patches may merge from much larger poleward moving auroral forms (PMAFs). In those observations the newly formed patches subsequently convected into the cusp region.

Observations from OMTI in Figure 5.8a show strong emissions at the 630.0 nm wavelength in the region of the cusp. In the figure, a red dot marks the location of Resolute Bay and the black, dashed oval is roughly the estimated location of the cusp. The SuperDARN radar at Prince George detected an isolated region of backscatter in the same region, which is overplotted with the OMTI data in Figure 5.8b. Both of these observations are consistent with previous work investigating HF radar and optical signatures of the cusp and FTEs [*Milan et al.*, 1999; *Moen et al.*, 2000]. In the OMTI data, the position, direction and velocity of the patch was consistent with the convection flow estimates provided by the SuperDARN coverage, as well as the expected ionospheric response to FTEs under IMF $B_y < 0$ conditions [*Milan et al.*, 1999]. Additional observations from NASCAM also show patches emerging from the same region of high optical emissions (the cusp region) first identified in the OMTI data, drifting along the same convection trajectories.

The range time power plot for Beam 7 from the Rankin Inlet SuperDARN radar (Fig-

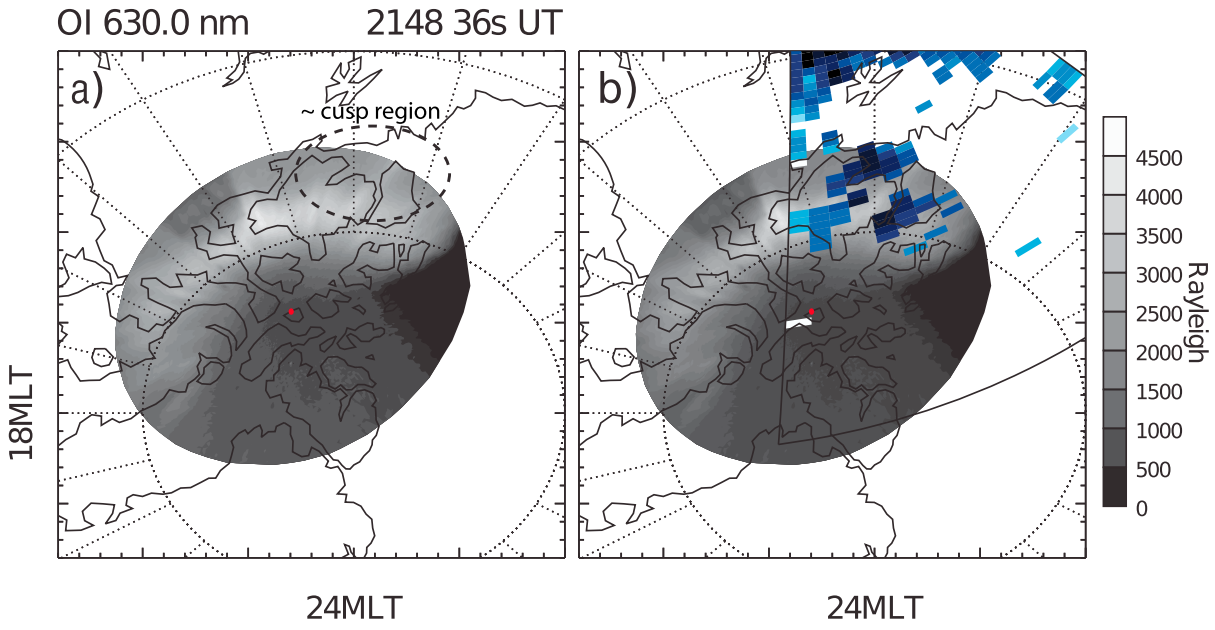

Figure 5.8: a) The 630.0 nm OMTI image at 21:48 UT shows the brighter edge corresponding to the formation region of the patches. The red dot marks the location of Resolute Bay and the black dashed oval the estimated location of the cusp. b) The same OMTI image as in a), with the SuperDARN echoes from the radar in Prince George overplotted. Echoes are seen in the region of the cusp, indicative of the strong electrodynamic processes occurring there.

ure 5.4a, top panel) shows numerous features during a one hour period between 21:30 and 22:30 UT. Magnetic latitude coordinates are provided along the y-axis and a black horizontal line denotes the magnetic latitude of the center of the RISR-N FOV. A strong echo, identified as the patch of interest from Figure 5.3, proceeds from a much larger backscatter feature, starting just prior to 22:00 UT, at ∼82°N MLAT. At 22:13 UT, the backscatter power of the patch increases. The same feature is present in the backscatter data measured with the Saskatoon radar, displayed in Figure 5.4b, but reaches just out of range of this radar at 22:05 UT. The line-of-sight velocity is plotted in the middle panels. The direction of the Doppler velocity is directed away from the radar, with a magnitude of approximately 300 m/s. The velocity features in Figure 5.4 are consistent with those of pulsed ionospheric flows (PIFs). The poleward moving transient feature in Figure 5.4 has a velocity that is larger than the surrounding plasma. This is a signature of FTEs [*McWilliams et al.*, 2001; *Provan et al.*, 2002]. The spectral width, a measure of the spread Doppler velocity components within the

scattering volume, is plotted in the bottom row of panels in Figure 5.4. The spectral width of the patch echoes, expressed in velocity units, are relatively low, between $\sim$ 150 and 200 m/s, but seem to have undergone a subtle evolution from a higher spectral width of 250 – 300 m/s at 79°N MLAT (at about 21:45 UT). The low spectral width and its decrease over time for the patch observed here is again consistent, albeit not as prominent, with the measurements by *McWilliams et al.* [2001] and *Rodger et al.* [1999], where the spectral width of echoes associated with FTEs evolved from large values, near 400 or 500 m/s, to lower values near 100 to 200 m/s.

Several other structures are also seen to reach the same latitudes as the patch, north of Resolute Bay, during an interval of a few hours around 22:00 UT. FTEs between the IMF and the geomagnetic field differ from quasi-stationary reconnection at the dayside magnetopause due to their bursty nature. In the event reported here, bright emission bands are seen in the OMTI optical data to form in the cusp region with 4 – 8 minute intervals, which then break up to smaller structures as they drift to the northeast with the modeled convection streams. This repetition rate is consistent with the mean period of 8 minutes found for FTEs in the statistical study by *Rijnbeek et al.* [1984]. The longitudinal motion of the emissions towards the east, observed by OMTI, is also expected during periods of IMF $B_y < 0$ in the northern hemisphere, due to the curvature force on newly opened field lines [*Sandholt et al.*, 1992; *Lockwood et al.*, 1993].

5.5.3 Variations in patch plasma density profile

Figure 5.9 shows RISR-N data of the temporal evolution of the patch monitored in Figures 5.3 and 5.5. In the top row of panels, electron density contours along a vertical north-south directed slice through the center of the patch are displayed for three subsequent time steps. These slices and their horizontal locations were also discussed in *Dahlgren et al.* [2012a], Figure 3. Each slice in Figure 5.9 is through the center of the patch, and therefore moves with the patch. The northward drift component of the patch is evident in the three time segments. The electron density of the patch is approximately twice that of the background ionosphere. The middle row of panels show the corresponding east-west slice for the same times. The bottom row of panels in Figure 5.9 show the weighted average of the electron

density taken over the whole patch, encompassed by approximately the white dashed circle in Figure 5.3, as a function of altitude during each of these three time intervals. At 22:11 UT (first column), the electron density peaks close to 260 km altitude. During the next minute of integration the density peak moved up in altitude to 320 km and marginally decreased in magnitude. The data from the subsequent minute (starting at 22:13:51 UT) shows an increased electron density, where the peak altitude dropped to 280 km. The observations are not consistent with patch depletion due to recombination with neutrals. The time sequence illustrates a significant variation in the plasma density of the patch over a short period of time. Since the position of the region over which a weighted average of the electron density is being taken (the white dashed line in Figure 5.3) is moving with the patch, the density variations are not due to the motion of a patch through a stationary reference frame. This is also evident from the bottom row of panels, since they depict the total average density over the whole patch, the variations are not the result of horizontal displacement. The sudden electron density enhancements with a lowering of the peak altitude at 22:13:51 UT suggest that the patch may be experiencing some degree of internal turbulence, resulting in a re-distribution of plasma density, possibly initiated by local precipitation, solar irradiance, or another unknown mechanism.

If soft precipitation is present, an increase in the electron temperature, T_e, would be expected, but the T_e/T_i ratio measured by RISR-N did not show any associated enhancements. The O and N_2^+ emission rates would have increased due to precipitation in the region; however, a close study of the NASCAM imager data associated with these emissions show no significant enhancements indicative of electron precipitation.

The altitude at which the patch event takes place on December 11, 2009 is sunlit at 22:10 UT, which corresponds to 14:25 MLT at Resolute Bay. At this time, the atmosphere is sunlit above 200 km (Figure 5.10). Photoionization would therefore be underway in the region in and around the patch. The photo production rates of O^+ are significant enough to cause density increase on the order of 10^{11} m^{-3} during the plotted time-segment [*Tohmatsu and Ogawa*, 1990], but the increase would be over a larger region and not as localized as the observed enhancements. Analysis of the density profiles of the ionosphere surrounding the patch do not indicate any significant plasma density changes, consistent with photoionization.

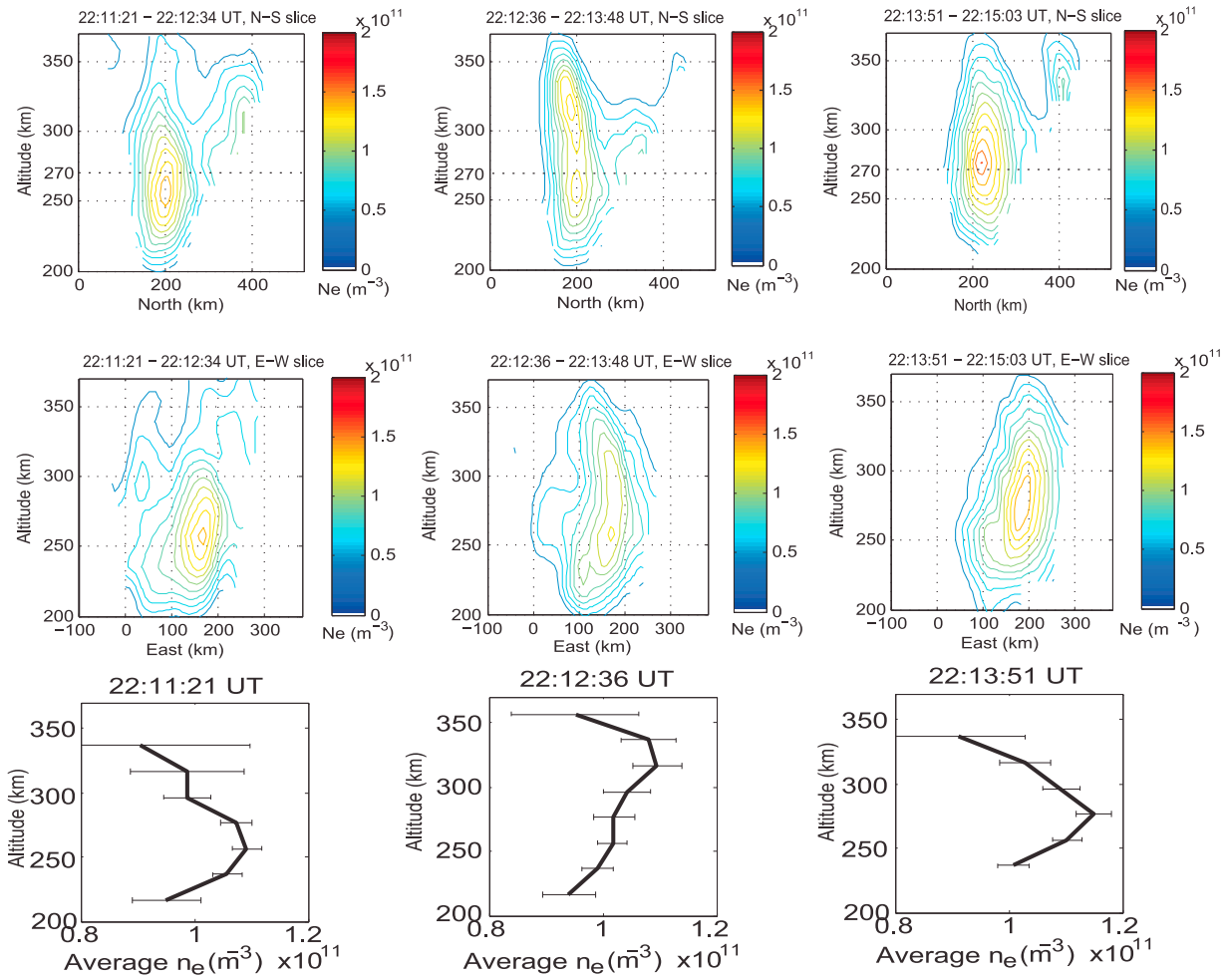

Figure 5.9: (top) Contour plots of vertical north-south aligned slices through the patch, for the times 22:11:21 UT, 22:12:36 UT and 22:13:51 UT. (middle) Same as top, but for an east-west aligned slice. Bottom row of panels: The weighted average vertical density profile of the patch, for each time.

The contours suggest a relatively steady plasma density in the vicinity of the patch over a period of a few minutes.

5.5.4 Interior plasma transport

Plasma drift velocities in the horizontal and anti-parallel directions with respect to the background magnetic field can be derived utilizing inversion techniques from the RISR-N line-of-sight ion drift measurements. The horizontal components are split in northward and eastward and are found to correspond well with the SuperDARN (Figure 5.7) and OMTI data. From

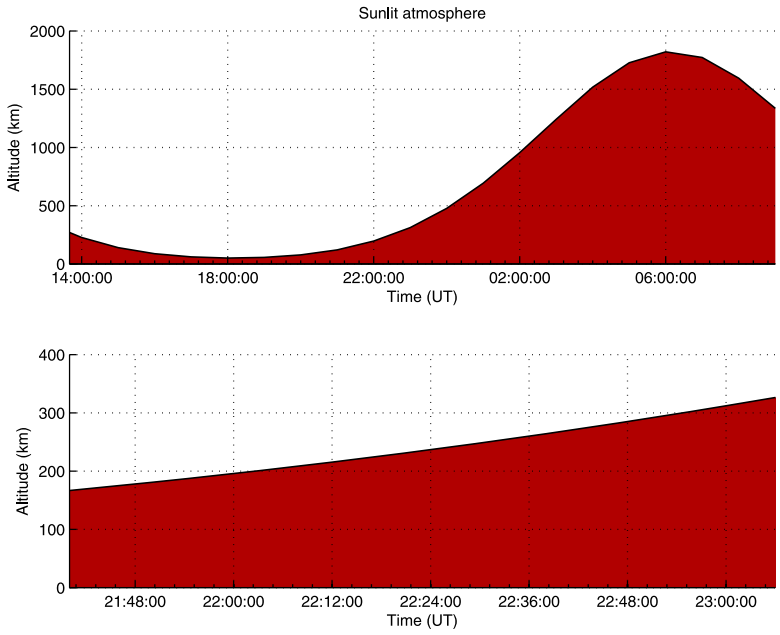

Figure 5.10: The modelled sunlit atmosphere (white) above Resolute Bay shows that the ionosphere is sunlit above 200 km when the patch drifts through the RISR-N FOV at 22:00 UT.

the three dimensional imaging of the patches with RISR-N, we can establish the plasma rest frame in the polar cap ionosphere such that the convection term corresponding to the direction perpendicular to the geomagnetic field, $\nabla_\perp \cdot (n_e \mathbf{v}_{e\perp})$, in the electron continuity equation (which is equivalent to the ion continuity equation, Equation 1.38), can be disregarded. The rate of change of the electron density, n_e, of the patch is therefore only governed by ion production (P_e) via impact ionization, chemical loss terms (L_e) and any electron transport along the magnetic field line, $\frac{\partial}{\partial z}(n_e \mathbf{v}_{e\|})$. The RISR-N data indicates that the patch studied is a closed system with no additional plasma being transported into the region. Despite this, the three profiles in Figure 5.9 show density variations of around 10% which may be explained by an ionization source between 22:11 UT and 22:13 UT, but none was observed.

The magnitude of the plasma density fluctuations in Figure 5.9 exceeds the standard deviation, suggesting a redistribution of plasma within the patch. The anti-parallel ion drift obtained from RISR-N data at 84.2°N MLAT, corresponding to the center of the RISR-N FOV and integrated over all altitudes, is displayed in Figure 5.11. The data suggest that there is little vertical plasma motion in the region, which is further supported by the lack of temperature enhancements due to frictional heating. Upward motion due to neutral winds

are also not expected at this latitude, since the magnetic field lines are close to vertical and perpendicular to the winds. There is a small increase in anti-parallel velocity at 22:12 UT, coinciding with the upward relocation of the electron density peak seen in Figure 5.9, which then moves to lower altitudes again in the subsequent minute. Nonetheless, it is clear that even the extremum of the velocities measured in Figure 5.11 can not account for the large density variations seen in Figure 5.9. This indicates that a large component of the plasma redistribution within the patch may be occurring horizontally. Previous studies [e.g., *Kivanç and Heelis*, 1997; *Hosokawa et al.*, 2009b] have shown that patches are subject to structuring over a range of scale lengths, which may be driven by multiple instabilities [*Basu et al.*, 1990; *Gondarenko and Guzdar*, 2006]. Simulations by *Gondarenko and Guzdar* [2006] illustrate that only a short time is needed for a patch to be fully engulfed with plasma instabilities. In addition, *Carlson et al.* [2008] showed that the irregularities can appear during the formation of the patch, due to shear motion. The observations in Figure 5.9 may be an example of these instabilities and provide a unique ISR observation of density fluctuations within a patch, due to field-aligned irregularities. Previous observations, specifically those by *Kivanç and Heelis* [1997], were performed by satellite and therefore were unable to provide an unambiguous stationary observation of a patch. However, *Hosokawa et al.* [2010] demonstrated that a polar cap patch can be split into two due to larger scale shear motion in the background convection. The presence of a velocity shear in the patch would indicate the existence of a field-aligned current, which might change the vertical structure of the patch.

The variations of plasma distribution shown in Figure 5.9 indicate fluctuations within the patch of both intensity as well as spatial distribution of the electron density, with possible velocity shear. A patch is driven by the $\mathbf{E} \times \mathbf{B}$ drift; therefore if E is structured in altitude then the velocity of the patch could be as well. This is assuming that the electric fields within the patch are significant enough to counteract the influence of the large-scale convection electric field. Reports have been made of plasma density fluctuations combined with electric field fluctuations observed by satellites within several patches [*Basu et al.*, 1990; *Kivanç and Heelis*, 1997]. On this note, *Basu et al.* [1990] observed electric field deviations over a range up to $\sim$ 30 mV/m – magnitudes on par with the convection electric field. It is however questionable if the presence of intense electric field fluctuations within the patch would be

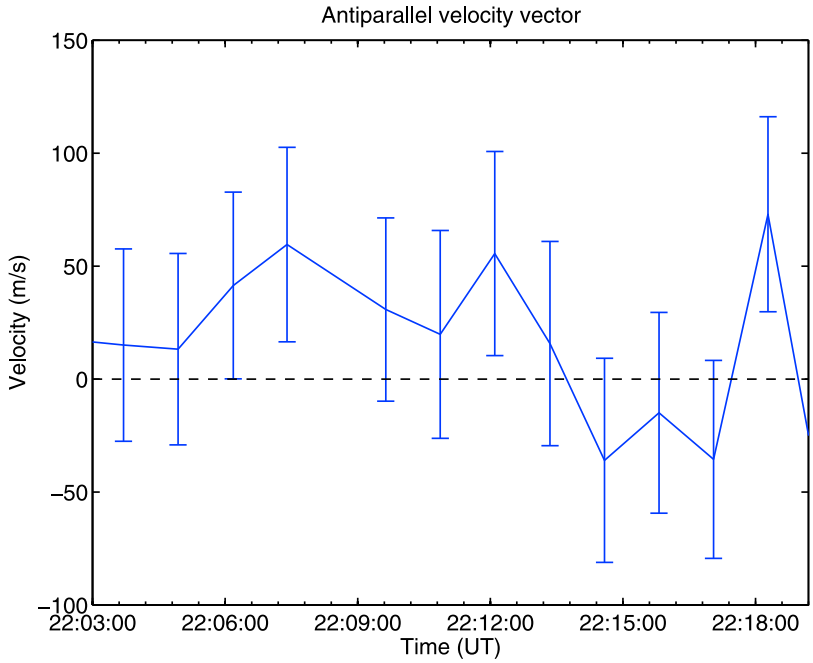

Figure 5.11: Anti-parallel ion drift velocity, derived from the RISR-N data in the center of the RISR-N FOV. A small increase is seen at 22:12 UT, coincident with an upward shift of the electron density peak in the altitude profiles displayed in Figure 5.9.

able to produce such large effects as those shown in Figure 5.9. The optical patches in the OMTI data show no corresponding significant dynamic as they pass the RISR-N FOV. This is to be expected, since the electron density does not change much below 250 km altitude, which is the altitude most of the optical emission originates from. Some variations can be detected in the SuperDARN power, but the changes in the data are not significantly larger than the noise fluctuations.

5.5.5 Multiple patches postulate

A possibility that was not contemplated by *Dahlgren et al.* [2012b] was that the patch under study may have been composed of several patches with scale sizes below the resolvability of RISR-N [J.-P. St.-Maurice, personal communication, 2013]. It was assumed that $Dn_e/Dt = -\nabla_\perp \cdot (n_e \mathbf{v}_{e\perp}) = 0$, and that the traces in Figure 5.9 are measurements made in the frame of reference of the patch. Presumably one or both of those assumptions was false since the n_e profiles showed substantial variations in time; namely, $Dn_e/Dt \neq 0$. In

$Dn_e/Dt = -n_e \nabla \cdot \mathbf{v}_{e\perp} - \mathbf{v}_{e\perp} \cdot \nabla n_e$, the first term on the right hand side is negligible [*Rishbeth and Hanson*, 1974]; only the passage of a drifting density gradient, i.e., a patch, would result in $Dn_e/Dt \neq 0$. This is only true if the measurement is not taken in the reference frame of the drifting gradient. Since the results in Figure 5.9 are measured in the frame of reference of the patch $\mathbf{v}_{e\perp} = 0$, indicating that another factor must be contributing to the n_e fluctuations.

Recall that the traces in Figure 5.9 are spatial averages of measurements from multiple RISR-N beams. The single patch in question could simply be a combination of several patches. If the scale size of the smaller patches is at or below the separation distance of the RISR-N beams, which is this case is of the order of 30 km, then a different patch may have contributed to the overall average in each scan plotted in Figure 5.9. If each patch had a unique plasma density characteristic, this could generate the appearance of a fluctuating plasma density as a different patch entered the RISR-N beams for each successive scan. Each profile plotted in Figure 5.9 could be an average of a different set of patches in each scan.

This is a difficult postulate to confirm due to the coarseness of the resolvability of the RISR-N mode used in this experiment. Other methods such as simulating conditions that would recreate the density profiles in Figure 5.9 would be required to test the postulate. This is left for future work. To test the existence of small scale patches, such as those postulated here, other experimental RISR-N modes with closer beam separations may also be useful. In fact, RISR-N 42-beam mode described in Chapter 6 and the RISR-N algorithm presented in Chapter 4 were both designed with this in mind. Using them to explore the existence of the small scale patches is left for future work.

5.6 Event on 15 December 2009

The RISR-N 5 $\times$ 5 beam experiment was carried out during a few consecutive days in December 2009, during very quiet geophysical conditions. Despite the length of the observations, events with strong electron density enhancements in RISR-N and simultaneously measured echoes in the SuperDARN data from the same region were difficult to find. For this segment of time, most SuperDARN echoes are seen south of Resolute Bay. On 15 December, another

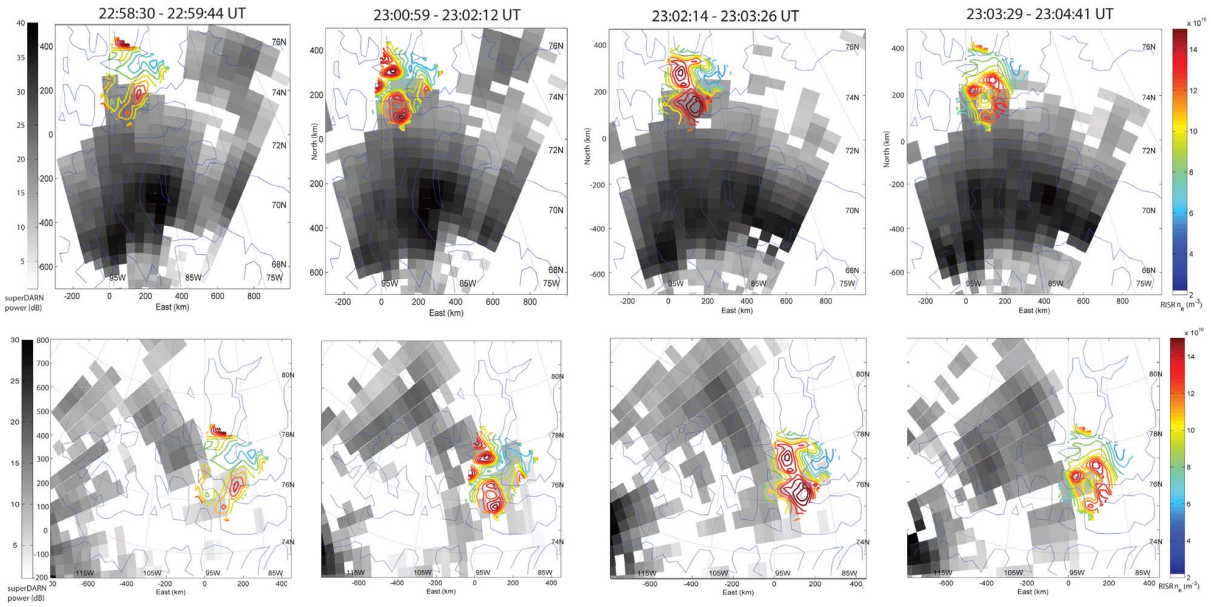

Figure 5.12: A second polar cap patch was observed in the RISR-N data (coloured contour plots) on 15 December 2009, between 22:59 and 23:04 UT. The contemporary SuperDARN echoes are plotted in gray scale, from the (top) Rankin Inlet radar and (bottom) the Inuvik radar (bottom row of panels). The patch drifts through the RISR-N FOV in the northeast direction and breaks up around 23:04 UT. Although the event is faint, a correlation between the coherent and incoherent scatter data can be discerned. The Rankin Inlet SuperDARN radar also measures strong echoes from large structures south of Resolute Bay (around 70° lat).

event of enhanced electron densities was measured with RISR-N, at around 23:00 UT. The Kp index at this time was 1, IMF $B_z < 0$, IMF $B_y < 0$, IMF $B_x > 0$ and the plasma features were seen to drift anti-sunward. Figure 5.12 shows the Rankin Inlet SuperDARN power for three consecutive times in gray scale (with darker regions being stronger echoes). The format is the same as for Figure 5.3, with the RISR-N electron density contour plot at 300 km altitude superimposed in color on the SuperDARN radar data. A patch of less than 200 km in diameter drifted in from the south into the RISR-N FOV, dispersed and diminished as it reached the center of the FOV. No vertical redistribution of plasma like the one noted for the 11 December event could be seen in this data. At the time of this event, the farmost edge of the SuperDARN scatter reached to halfway through the RISR-N FOV, and larger power is recorded throughout the regions where the patch is seen in the RISR-N electron density data. No specific increase in scatter is seen from the edge of the patch. Larger structures are

evident in the radar data from the Rankin Inlet SuperDARN radar, located further south and also drifting anti-sunward at the time. It is possible that these larger patches break up into smaller structures as they drift across the pole [*Hosokawa et al.*, 2010], so that the smaller patch seen by RISR-N is a segment of the larger structure. However, it was not possible to trace the origin of the structure seen in the SuperDARN data.

This event highlights the difficulty in capturing an individual patch with multiple instruments. During this event, the OMTI imager was unusable due to cloud cover over Resolute Bay, leaving only RISR-N and the SuperDARN radars for the observations. Even though RISR-N clearly detected patches, the SuperDARN radars had a more difficult time due to the propagation conditions. Although the event from December 11 demonstrates the validity and usefulness of using multiple instruments to study patches, it should be noted that capturing such a clear event is difficult.

5.7 Conclusions and summary

In this chapter, a thorough investigation of the structuring and morphology of F-region ionization patches was undertaken. Polar cap patches were observed with incoherent and coherent scatter radars as well as all-sky imagers, as they passed over Resolute Bay. Volumetric imaging of the RISR-N data revealed that the electron density enhancements were largest at around 270 km altitude, with some temporal variations. The low electron densities of $\sim 2 \times 10^{11}$ m^{-3} as well as the height of the patches lead to very faint optical emissions, but it was still possible to trace the patches from their formation region in the cusp, across Resolute Bay and continuing into the FOV of the all-sky imager located further north in Qaanaaq, Greenland. The transient nature of the optical emissions in the formation region and SuperDARN measurements of the patch suggest that the patches may have been formed by the FTE mechanism described by *Lockwood and Carlson* [1992]; *Carlson* [2004]; *Lockwood et al.* [2005]; *Zhang et al.* [2011]. It is also possible that the internal structuring was initiated by particle precipitation in the cusp [*Kelley et al.*, 1982; *Moen et al.*, 2012]. A more focused study of one of the plasma patches demonstrates a close colocation of the RISR-N, SuperDARN and the all-sky data, with the same scale sizes of the regions in all data sets. No

evidence of stronger coherent scatter from the trailing edge of the patch is seen, which would be expected for GDI growth on non-rotating, stagnated patches. Instead the irregularities seem to be present throughout the patch, or even strongest on the leading edge. A second event on 15 December 2009 showed a similar correlation, with the measured HF SuperDARN radar scatter taking place throughout the patch. This event is even fainter than the first and the patch is quickly breaking up. Interpretation of the data from these two events should therefore be done with some precaution. Future observations are planned with a specially designed SuperDARN mode with higher spatial resolution over the RISR-N FOV, for a more detailed analysis of similar patches.

From the ISR volumetric data of the individual patch under study, it was indicated that during a short time interval of only a few minutes, significant variations took place, with shape deformations in all spatial directions and velocity shears across the patch. It is noteworthy that these dynamic deformations were observed during a period of Kp = 0. The data indicate that even under these quiet conditions, the patch should not be considered a stagnated feature, but a dynamic and constantly varying structure. This supports the findings by *Oksavik et al.* [2010] who observed rotations of patches during their transit across the polar cap, and suggests that internal motion may also be present, and the patch cannot always be considered a rigid plasma body. It has been learned [*Carlson et al.*, 2008] that irregularity structures in ionospheric patches can be initially driven by the shear instability, not gradient drift, due to strong shears associated with the patch formation process. This leads to structure throughout the patch, a view which our data supports, and establishes the required electron density gradients in the patch to maintain structuring downstream from the high shear formation region. However, our data go beyond this to show that the downstream patch is also actively structured throughout, by dynamics not previously recognized until this work as a further structuring process.

In a novel approach, compared to earlier observations of polar cap patches, optical emissions were not used to first detect the structures; instead the electron density structures measured with the RISR-N radar defined where the patches were located, a method also used in *Dahlgren et al.* [2012a]. The patches were then searched for in the SuperDARN and all-sky imager data. The dimness of the patches would have made their initial detection in

the all-sky imager data difficult. The faint optical emissions could be mapped to the same geomagnetic latitudinal and longitudinal location as the electron density enhancement, but the altitudes of the two signatures will differ, with the electron density being larger at higher altitudes. This is important to note since patches at higher altitudes will not react with neutrals to produce emissions, and therefore could only be detected with radio instruments. An exception to this is patch detection using 777.4 nm O emissions, since that emission occurs between 250 and 350 km altitude as a result of radiative recombination of O^+ and electrons, and is independent of the neutral atmosphere. The emission was used by *Makela et al.* [2001] for F layer topography maps. However, this emission is also normally very faint which makes it a difficult tracer. The ability to conduct multi-instrument patch experiments provides the opportunity to gain further insight into the properties and dynamics of patches and is crucial when trying to understand and investigate their formation, evolution and characteristics. In most cases, like the one reported here, a single instrument cannot provide sufficient measurements to investigate the intricacies of a patch.

Chapter 6

Spatiotemporally resolved electrodynamic properties of a sun-aligned arc over Resolute Bay

The focus of this chapter is plasma density depletions in the polar ionosphere. This chapter has been submitted as a manuscript to *Geophysical Research Letters* as *Perry et al.* [2014], hence its brevity and conciseness. The role of enhanced chemical recombination rates in the generation of plasma density depletions and their subsequent transport through the polar ionosphere is discussed. This generation mechanism was introduced in Section 1.4.2. This chapter is one of the first results of a campaign involving the SuperDARN network, RISR-N system and OMTI imager, organized by myself and Dr. Hanna Dahlgren, who is currently at the University of Southampton.

In this chapter, common volume measurements by the Resolute Bay Incoherent Scatter Radar - North (RISR-N) and Optical Mesosphere and Thermosphere Imagers (OMTI) have been used to clarify the electrodynamic structure of a sun-aligned arc in the polar cap. The plasma parameters of the dusk-to-dawn drifting arc and surrounding ionosphere were extracted using the volumetric imaging capabilities of RISR-N. Multipoint line-of-sight RISR-N measurements of the plasma drift are inverted to construct a time sequence of the electric field and field-aligned current system of the arc. Evidence of dramatic electrodynamic and plasma structuring of the polar cap ionosphere due to the arc is described in detail. One notable feature of the arc is a meridionally extended plasma density depletion on the leading edge of the arc, located partially within a downward field-aligned current region. The depletion is determined to be a byproduct of enhanced chemical recombination operating on a time scale

of 15 minutes. A similarly shaped electric field structure of the order of 150 mV/m, and line-of-sight ion temperatures nearing 3000 K were collocated with the depletion feature.

6.1 Introduction

Sun-aligned arcs are the hallmark of a polar ionosphere under northward interplanetary magnetic field (IMF) conditions [*Carlson and Cowley*, 2005]. The arcs are often referred to as transpolar arcs, of which there are many identifiable types and classifications [*Kullen*, 2012]. *Zhu et al.* [1997] provide an excellent review on the electrodynamic properties of sun-aligned arcs. Many of the models, measurements and conjectures regarding sun-aligned arcs agree on a few features. First, the optical emissions of a sun-aligned arc mark the location of an upward field-aligned current (FAC), carried by precipitating electrons. The magnetospheric source and energization mechanisms of the electrons remains unresolved; both soft and hard precipitation have been measured in the arcs. Corresponding downward FACs have been measured with the arcs [e.g., *Cumnock et al.*, 2011, and references therein], and sometimes multiple FAC pairs are detected. The arcs superpose an electric field on the background polar cap electric field, which can establish velocity shears in the polar cap convection [*Carlson et al.*, 1984; *Koustov et al.*, 2012].

Sun-aligned arcs are intrinsically linked to processes in the magnetosphere and its interaction with the solar wind [*Zhu et al.*, 1993a; *Hosokawa et al.*, 2011; *Fear and Milan*, 2012]. Their interconnection to polar cap dynamics and structuring via magnetosphere-ionosphere (MI) coupling has been thoroughly investigated, although a complete understanding of its mediators and agents remains elusive. *Zhu et al.* [1993b] noted that inhomogeneities in the Pedersen conductivity are non-trivial in MI coupling. They alter the reflection coefficient of the ionosphere, and can cause a rotation between the wave field of an incident and reflected Alfvén wave. For further insight into MI coupling in the polar cap, its impact on the plasma structuring and electrodynamics of the region must be investigated in detail. To accomplish this, accurate and spatiotemporally resolved diagnostics of the ionospheric component of the MI system are required.

The electrodynamics of sun-aligned arcs are measured indirectly by estimating horizontal

electric fields, from Doppler velocity measurements of plasma drifts obtained with radar [e.g., *Carlson et al.*, 1984]. Seminal work in this technique includes *de la Beaujardiere et al.* [1977] who used the Chatanika incoherent scatter radar (ISR) to estimate the current structure of three auroral arcs, with estimates of upward FACs measuring 6 and 9 μA/m^2 for two of them. ISRs also provide valuable diagnostic information of the electron density, n_e, and the ion and electron temperature, T_i and T_e, in the plasma. *Carlson et al.* [1984] measured a four-fold n_e increase within a sun-aligned arc, consistent with plasma production by soft electron precipitation. They also detected significant T_i enhancements in the vicinity of velocity shears associated with the arc, presumably a signature of frictional heating. Using EISCAT, *Opgenoorth et al.* [1990] also identified enhanced T_i values located on the edges of auroral arcs. The location of the enhanced T_i was coincident with significant n_e depletions and strong electric fields (some approaching 125 mV/m) both of which are elements of enhanced chemical recombination rates.

Previous sun-aligned arc research with ISR was conducted using a single, steerable antenna. With the development of the Advanced Modular Incoherent Scatter Radar (AMISR) systems and their electronic beam steering capabilities [*Nicolls et al.*, 2007; *Bahcivan et al.*, 2010], it is now possible to investigate the electrodynamics of polar cap arcs with multiple beams, in a customized beam configuration which can encompass a large volume of the ionosphere. The beam is directed by adjusting the phase of the signals from the many antenna elements on a pulse-to-pulse basis, eliminating the need to mechanically steer a radar dish. In this way, precise, volumetric measurements are provided without spatiotemporal ambiguities when integrating the measurements on the order of minutes [e.g., *Dahlgren et al.*, 2012a; *Dahlgren et al.*, 2012b].

In this chapter, we present a novel experimental perspective to polar cap dynamics and MI coupling by providing the first spatiotemporally resolved images of the organization and morphology of the ionospheric plasma and electric fields for a sun-aligned arc. The data show a clear connection between the structuring in the F-region polar cap ionosphere and the electrodynamics of the sun-aligned arc. In particular, we provide direct estimates of auroral arc electric fields, current systems, and associated plasma density cavities. We demonstrate that these observations are consistent with existing arc models and dynamic plasma structuring

mechanisms. Our observations confirm that intense electric fields and FACs are sufficient enough to ignite strong chemical recombination and current closure processes giving rise to the depletions. These processes have been demonstrated indirectly in the auroral zone [e.g *Zettergren et al.*, 2014]; we report a direct confirmation that they are present in sun-aligned arcs as well.

6.2 Observations and instrumentation

For a more general overview of the sun-aligned arc event described here, including information about the IMF conditions and a postulate on the generation mechanism of the arc, we direct the reader to *Dahlgren et al.* [2014].

6.2.1 OMTI

At 05:04 UT (approximately 22 MLT), February 20, 2012, two closely separated sun-aligned arcs became visible on the duskward edge of the field-of-view (FOV) of the OMTI all-sky imager installed at Resolute Bay, Canada (74.73° N, 265.07° E, geographic) [*Shiokawa et al.*, 1999]. An image of both arcs at 05:10 UT after they entered the FOV of RISR-N is given in Figure 6.1. Both arcs travelled towards dawn (eastward) and were identifiable and collocated at the 557.7 and 630 nm wavelengths. At 05:14 UT, the arcs were near the zenith of the OMTI imager. The leading arc was much less intense than the trailing arc, at both optical wavelengths, and became indistinguishable from the brighter, trailing arc at 05:16 UT. It could not be determined whether the leading arc ceased to exist, or was rendered indistinguishable due to a parallax effect. The brighter arc, hereafter referred to as the "arc", remained visible until 05:26 UT. During its transit, the luminosity of the arc varied between 350 and 450 R in the red- and green-line emissions.

6.2.2 RISR-N

At 05:06 UT, the arc entered the duskward edge of the RISR-N FOV, an AMISR class radar installed at Resolute Bay. RISR-N transmits at 441.9 MHz, providing diagnostic mea-

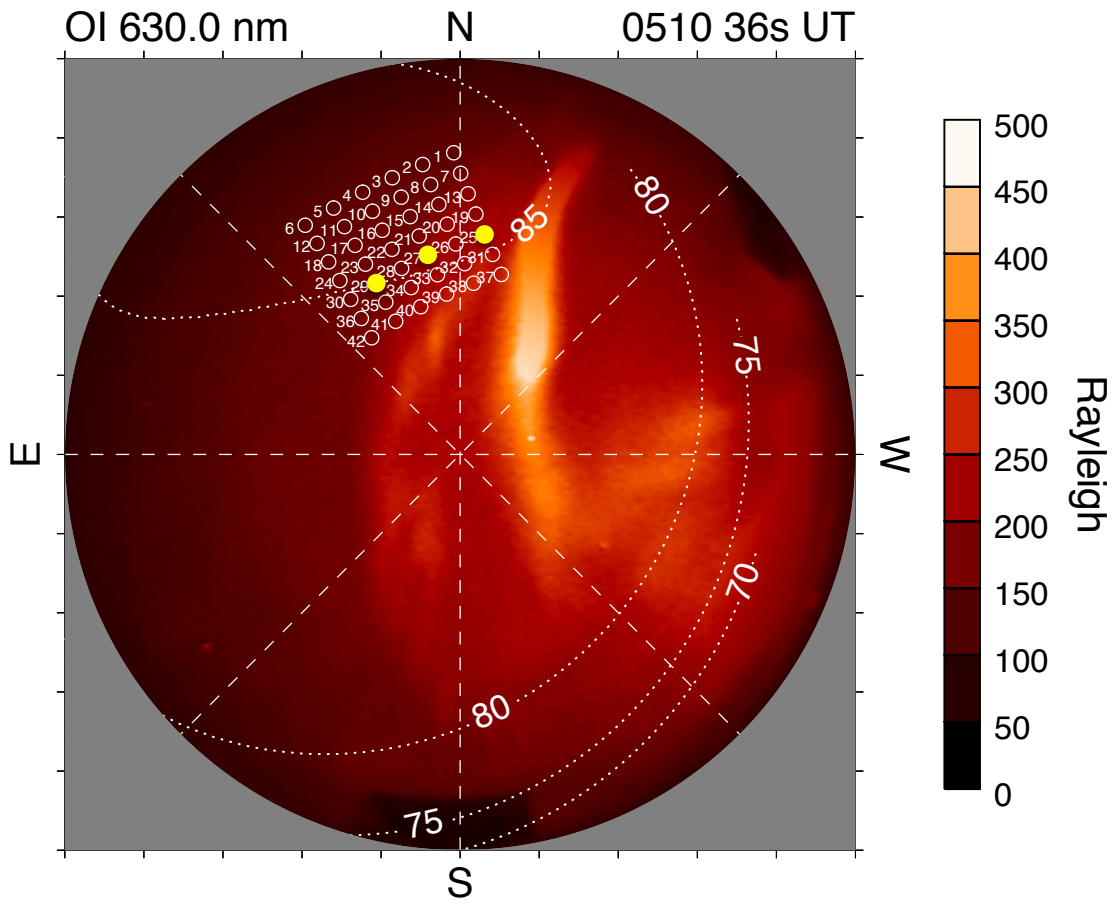

Figure 6.1: The FOV of the OMTI imager at Resolute Bay, with geographic directions, showing emissions at 630 nm at 05:10 UT on February 20, 2012. Also shown is the 6×7 RISR-N grid with numbered beams, and magnetic latitude contours. RISR-N beams 25, 27 and 29 are highlighted in yellow and are aligned northwest to southeast.

surements of the polar ionosphere, including n_e, T_i, T_e, and line-of-sight (LOS) ion velocity measurements, v_{los}. For this study, the RISR-N was operating with a custom 42-beam mode, in a 6×7 grid, which is shown as a grid of white circles in Figure 6.1 (beams 25, 27 and 29 are coloured yellow). The system transmitted interleaved Barker and long-pulse coded radar pulses, giving approximately 750 m and 36 km range resolutions, respectively. The arc moved with an average speed of 250 m/s towards the dawn, and exited the RISR-N FOV at 05:22 UT.

A plot of n_e, $T_{i_{los}}$, T_e, and v_{los} as a function of time, measured in RISR-N beam 29 with the two-minute integrated long-pulse mode is given in Figure 6.2. We have chosen to label the ion temperatures as $T_{i_{los}}$ for reasons that will be explained shortly. A time series of n_e

measured at 285 km altitude in beams 25, 27 and 29, which are along a row in the RISR-N FOV (coloured yellow in Figure 6.1) is plotted in Figure 6.3. In both plots, the time segment during which the optical arc was seen to be within the RISR-N FOV is outlined by a violet, dashed box.

A substantial n_e depletion region is seen in Figures 6.2 and 6.3, centred at approximately 05:12 UT in beam 29. The n_e decreased from 4.6 to almost 1.3×10^{11} m^{-3} in 10 minutes, starting at 05:01 UT. It is clear that the depletion progressed towards dawn, from beam 25 to 29. The depletion feature is marked by a shaded box coloured for each beam in Figure 6.3. At 130 km altitude (not visible in any figure), an increase in n_e from 1 to 3 $\times$ 10^{10} m^{-3} was measured with the long-pulse mode. The enhancement was centred at 05:16 UT which is marked by a yellow shaded box in Figure 6.3. The increase was short lived, and was only present in beam 29 between 05:14 and 05:18 UT. A similar n_e enhancement was also measured with the Barker code mode (not presented here), although those observations are less reliable due to their relatively high measurement uncertainties. A more subtle signature of an n_e increase is indicated by the appearance of n_e values plotted below 200 km altitude in Figure 6.2, starting just after 05:12 UT. They appeared because the n_e had increased to above the minimum plot value in that figure. The n_e enhancement in the lower F region marks the arrival of the electron precipitation region of the optical arc in RISR-N beam 29, which trailed the n_e depletion feature on its dawnward trajectory. The appearance and ordering of the aforementioned signatures are evident in nearly all of the other beams comprising the RISR-N FOV.

During the arc event, both T_e and $T_{i_{los}}$ in beam 29 increased dramatically, each changing from 800 K to above 2500 K over several minutes, starting at 05:01 UT. The $T_{i_{los}}$ enhancement was collocated with the n_e depletion region as it moved through the RISR-N FOV, and maximized at 3000 K for several minutes, starting at 05:15 UT. T_e reached 2500 K at approximately 05:20 UT, and only briefly maintained this temperature. In the majority of the RISR-N beams, the $T_{i_{los}}$ increases were measured into the lower F region, in some cases down to 175 km altitude. The T_e increases displayed a different characteristic, and only generally kept above 250 km altitude.

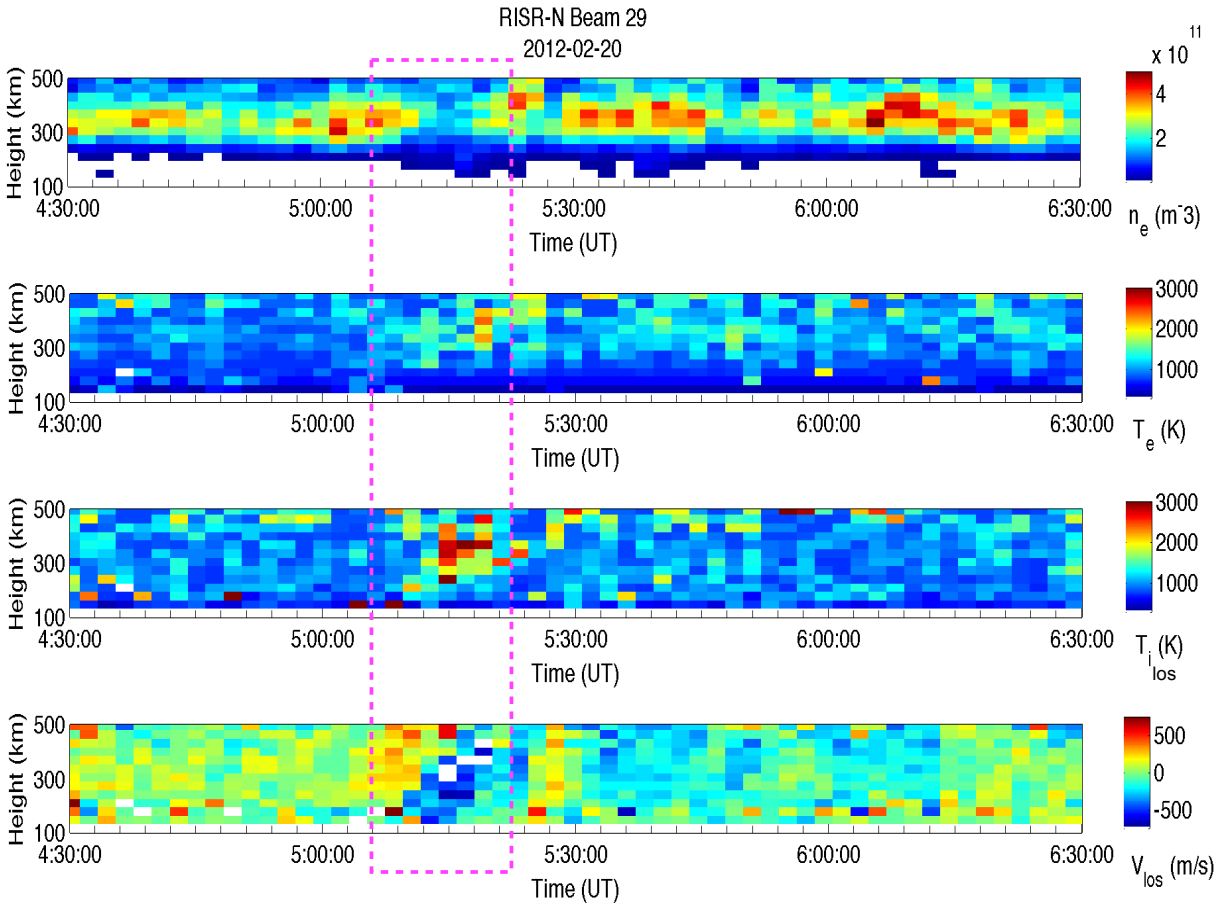

Figure 6.2: RISR-N beam 29 measurements of n_e, T_e, $T_{i_{los}}$, and v_{los}, as a function of altitude along the beam, and time. The time segment in which the sun-aligned arc was within the RISR-N FOV is indicated by the violet, dashed box.

6.3 Analysis

In this chapter, we focus on the plasma and electrodynamic structuring of the arc observed over Resolute Bay. A technique that was recently developed by *Nicolls et al.* [2014] was used to estimate the electric fields within the RISR-N FOV during the arc event. The approach centres on modelling a spatially varying electrostatic potential, ϕ, that reproduces the RISR-N v_{los} measurements. When a suitable ϕ is determined, the electric field, $\mathbf{E}_\perp$, is computed from $\mathbf{E} = -\nabla\phi$. The technique builds and improves on previous work by *Heinselman and Nicolls* [2008] and *Butler et al.* [2010], who developed effective procedures for inverting RISR-N v_{los} measurements into full velocity vectors. However, those previous methods had difficulty

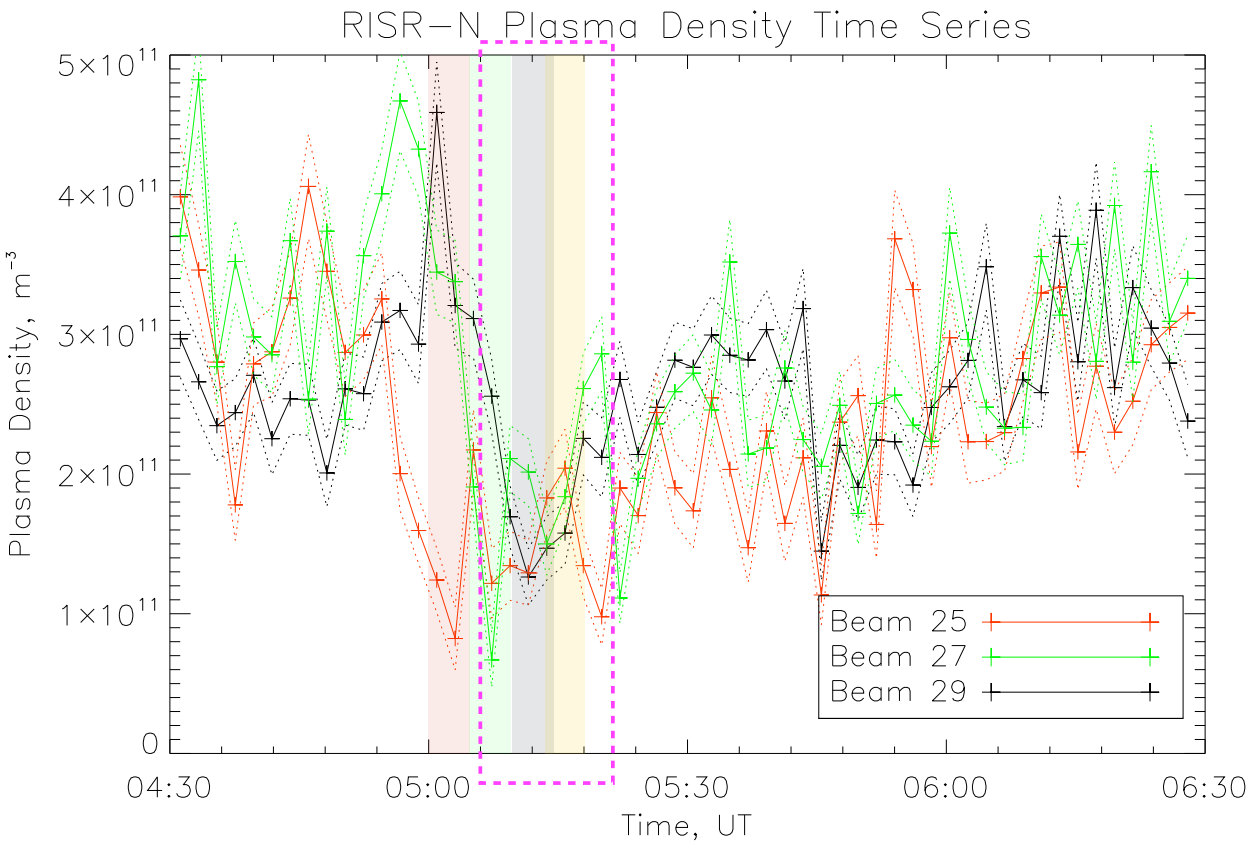

Figure 6.3: A time series of n_e measured at 285 km altitude in RISR-N beams 25 (red), 27 (green) and 29 (black), with associated error bars (dotted lines). The time segment in which the arc was observed within the RISR-N FOV is outlined by a violet, dashed box. The shaded rectangles denote the approximate location of the plasma density depletion in each beam. The yellow shaded rectangle marks the appearance of the lower F-region n_e enhancement.

reproducing vectors in the presence of velocity shears, such as those measured with this event, i.e., the shear appearing just after 05:00 UT in Figure 6.2. The technique introduced by *Nicolls et al.* [2014] and used here is able to mitigate these difficulties.

To obtain estimates for the FAC, $\mathbf{J}_\parallel$, for the arc event, we enforce current closure, $\nabla \cdot \mathbf{J} = 0$, expressed as [*Sofko et al.*, 1995]:

$$\mathbf{J}_\parallel = -\mathbf{\Sigma_P} \nabla \cdot \mathbf{E}_\perp - \mathbf{E}_\perp \cdot \nabla \mathbf{\Sigma_P} - \nabla \mathbf{\Sigma_H} \cdot \mathbf{b} \times \mathbf{E}_\perp, \tag{6.1}$$

in which $\mathbf{b}$ is the geomagnetic field unit vector, and $\mathbf{J}_\parallel \cdot \mathbf{b} > \mathbf{0}$. In this form, only measurements of the height integrated Pedersen and Hall conductivities, Σ_P and Σ_H, and $\mathbf{E}_\perp$

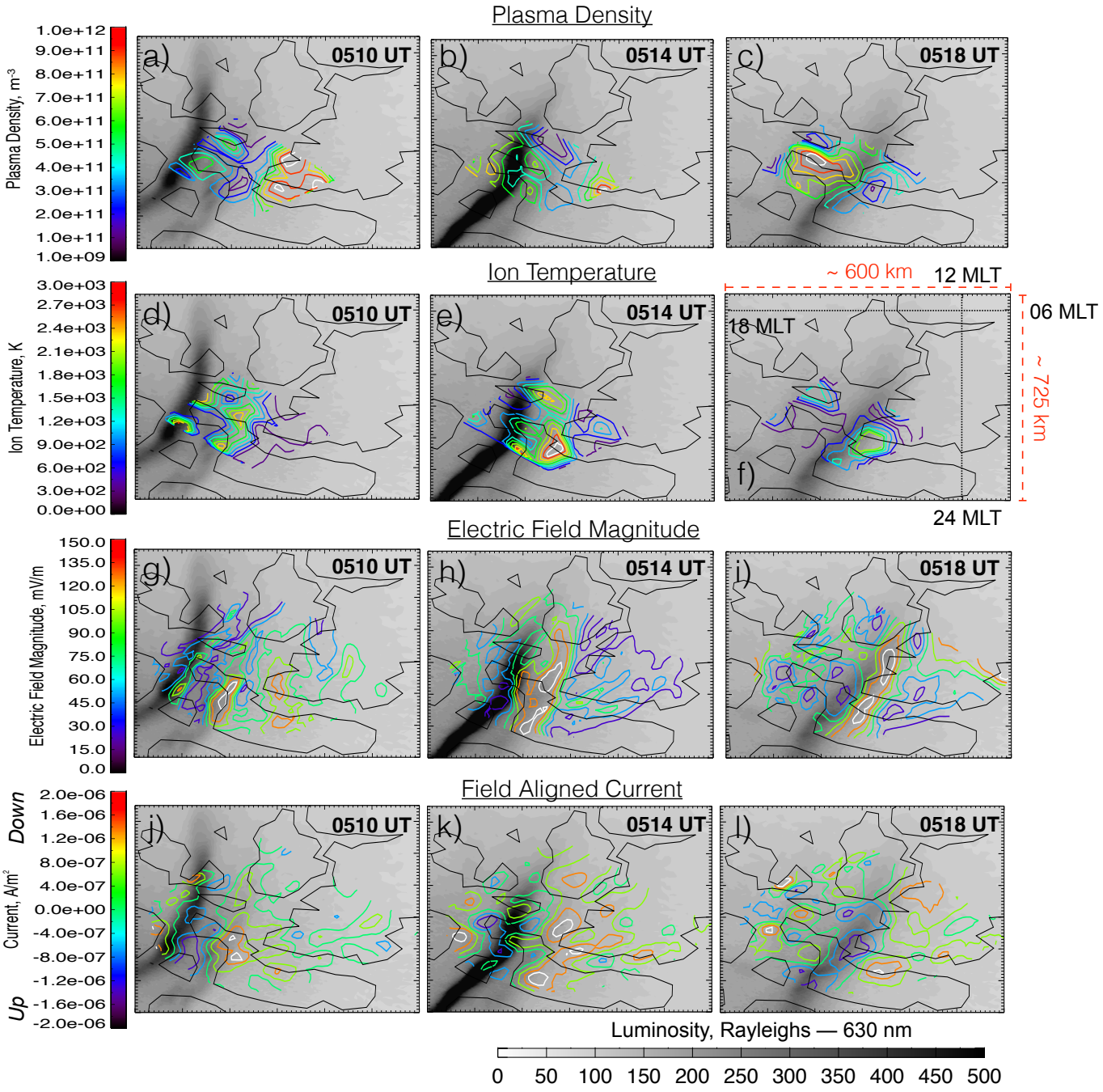

Figure 6.4: Combined plots of the optical data from OMTI (grayscale) and RISR-N contours for n_e (a–c), $T_{i_{los}}$ (d–f), $|\mathbf{E}_\perp|$ (g–i), and $\mathbf{J}_\parallel$ (j–l). Dimensions of the FOV and MLT meridians are indicated in (f).

are needed. The n_e measurements from RISR-N and neutral density estimates from MSIS [*Hedin*, 1991] are used to derive the conductivities. Obtaining an estimate for $\mathbf{E}_\perp$ is done using the procedure previously described. The first term in Equation 6.1 is the dominant term given what we were able to ascertain about the conductivity gradients from the RISR-N data.

6.4 Results and discussion

Contour plots of n_e, $T_{i_{los}}$ and estimates of $|\mathbf{E}_\perp|$ and $\mathbf{J}_\parallel$ are plotted with the OMTI data, in Figure 6.4. The altitude of the contours for n_e and $T_{i_{los}}$ is 325 km. The $|\mathbf{E}_\perp|$ and $\mathbf{J}_\parallel$ contours are constructed from data integrated over several hundred kilometres in altitude and mapped to 300 km altitude. The OMTI data is mapped to 250 km altitude, the normal practice for 630.0 nm emissions.

Structuring in $|\mathbf{E}_\perp|$ due to both arcs is significant and easily identifiable. Between 05:10 and 05:18 UT, meridionally extended $|\mathbf{E}_\perp|$ structures moved towards dawn, coincident with the two optical arcs discussed earlier. At 05:10 UT, three structures with low $|\mathbf{E}|$ were in the FOV. Two of the structures, both with $|\mathbf{E}| \sim 15$ mV/m, were collocated with two optical arcs shown in grayscale. The low $|\mathbf{E}_\perp|$ structures are indicative of the upward $\mathbf{J}_\parallel$ region of an arc; a region of electron precipitation in which plasma production is enhanced, increasing the ionospheric conductivities. With enhanced conductivities $|\mathbf{E}_\perp|$ decreases to uphold current closure. The upward $\mathbf{J}_\parallel$ associated with the low $|\mathbf{E}_\perp|$ structure of the brightest of the arcs is estimated to be approximately 1.5 μA/m^2, and maintains its intensity during the transit of the arc through the RISR-N FOV. Enhancements in n_e due to the electron precipitation were also detected by RISR-N and are evident in Figure 6.2 and Figures 6.4a–c.

During the same time frame, a structure of substantially enhanced $|\mathbf{E}_\perp|$ was also present, moving towards dawn, ahead of the two low $|\mathbf{E}_\perp|$ features previously described. The structure measured $|\mathbf{E}_\perp| \sim$ 150 mV/m at 05:10 UT, and remained above 100 mV/m for several minutes afterwards. The electric field was predominantly directed towards dusk, towards the arc. This structure is the counterpart to the low electric field structure discussed earlier. It partially overlaps with a region of downward $\mathbf{J}_\parallel$. We postulate that the n_e depletion is created in

part by electrons moving upwards, away from the region, thereby lowering the conductivity of the plasma and necessitating an increase in $|\mathbf{E}_\perp|$ to enforce current closure. This will be discussed in more detail shortly. A downward current, $\mathbf{J}_\parallel \sim\ 1.5 - 2.0\ \mu\mathrm{A/m}^2$, was in the vicinity of the enhanced $|\mathbf{E}_\perp|$ structure during the 05:10 to 05:18 UT time segment, as shown in Figure 6.4.

A striking feature of the $|\mathbf{E}_\perp|$, $\mathbf{J}_\parallel$, n_e and $T_{i_{los}}$ contours is the similarity between their shape and that of the optical arc throughout the event. This is most prominent at 05:14 UT when the shape of the optical arc is kinked. This distinct spatial structuring is seen in the $|\mathbf{E}_\perp|$, $\mathbf{J}_\parallel$, n_e and $T_{i_{los}}$ contours as well. This kind of interconnection between the electrodynamic structuring and the optical morphology of arcs is well documented [e.g., *Lanchester et al.*, 1996].

It should be noted that even though T_i is not a vector, when the electric field is strong (50 mV/m or greater) the observed value of T_i will depend strongly on the aspect angle, α, namely the angle between the radar beam and the magnetic field direction. This is due to the significant anisotropic character of the ion velocity distribution in the F region under such circumstances [*St-Maurice and Schunk*, 1979]. It has been shown [*Raman et al.*, 1981] that the line of sight temperature is given by $T_{i_{los}} = T_{i_\parallel} \cos^2 \alpha + T_{i_\perp} \sin^2 \alpha$. Analytical as well as Monte-Carlo calculations of $T_{i_\parallel}$ and $T_{i_\perp}$ have been obtained for various situations of interest [e.g., *Winkler et al.*, 1992]. For example, $T_{i_{los}}$ is of the order of 2000 K less than the actual temperature, T_i, at 125 mV/m for O^+ at 300 km altitude at an aspect angle of 30°. For the RISR-N beams used in the observations presented here the aspect angle varied between 20° for the high beam numbers and 50° for the low beam numbers. It is for this reason that we have chosen the $T_{i_{los}}$ notation when referring to RISR-N measurements.

The downward $\mathbf{J}_\parallel$ region was responsible for considerable structuring of the polar cap ionosphere. This is evidenced by the grouping of the enhanced $|\mathbf{E}_\perp|$, enhanced $T_{i_{los}}$ and depleted n_e features near the downward $\mathbf{J}_\parallel$ region in Figure 6.4, and their simultaneous movements towards dawn. Velocity measurements from the Rankin Inlet SuperDARN radar [*Greenwald et al.*, 1995; *Chisham et al.*, 2007] also confirm velocity signatures consistent with a downward FAC on the leading edge of the arc, moving dawnward. However, the SuperDARN measurements were only line-of-sight, and could not be fitted into full vectors

[e.g., *Ruohoniemi and Baker*, 1998] due to the lack of coverage from other SuperDARN radars at the time. The measured increases in $T_{i_{los}}$ and a significant v_{los} reversal measured by RISR-N and SuperDARN (not shown), which can be seen in bottom panel of Figure 6.2 shortly after 05:00 UT, are symptomatic of frictional heating and augmented chemical recombination reaction rates – an appealing candidate to account for the large n_e depletion [*Doe et al.*, 1995]. Evacuation of plasma via current closure must also be considered as a factor in the depletion [*Doe et al.*, 1993].

Zettergren and Semeter [2012] noted an altitude dependence on chemical recombination and current closure mechanisms in the vicinity of a FAC system. The current closure mechanism dominates in the E region and lower F region, while the chemical recombination mechanism dominates in the F region, at least in the larger-scale currents ($\sim$ 10 km). Combining current closure with chemical recombination can culminate in a positive feedback if the FAC sourced by the magnetosphere is held constant: the decrease in n_e leads to an increase in $|\mathbf{E}_\perp|$ and n_e gradients; this increases the convection flows parallel to the arc, thereby heating up the plasma, depleting n_e even more, forcing another increase in $|\mathbf{E}_\perp|$; etc. For this study, their simulation was modified to model the advecting FAC current system of the arc reported here. The plasma parameters measured by RISR-N were used as constraints to set a uniform background n_e and then a convecting current system was added which produced a peak $T_{i_{los}}$ enhancement roughly matching the data in Figure 6.4. This simulation test reproduced the basic behaviour of the n_e depletion near the upward $\mathbf{J}_\parallel$ region of the arc, as well as the location and order of magnitude for the upward and downward $\mathbf{J}_\parallel$ as estimated from the data.

In Figure 6.4 it is evident that the depletion travels in conjunction with the leading edge of the arc. This would mean that the n_e depletion was generated several minutes before it entered the RISR-N FOV. Results from *Zettergren and Semeter* [2012] support this, as well as the modified simulation outlined above. The convolution of heightened chemical recombination and current closure has the capacity to generate significant depletions of the F-region plasma on the order of 15 minutes in model runs, drastically modifying the state parameters of the ionosphere. Chemical recombination dominates in generating the depletion in this event. Evacuation and recombination of the E and F regions has important implications for

MI coupling in the polar ionosphere, for example, by structuring the Pedersen conductivity, which is an important component in the reflection coefficient of an Alfvén wave [*Zhu et al.*, 1993b]. The traces in Figure 6.3 are very coherent from beam to beam. At 250 m/s the depletion moved between RISR-N beams in roughly two minutes, which was likely why no substantial growth in the depletion can be seen in Figure 6.3 – the depletion moved through the FOV too quickly.

In the hours surrounding the arc event n_e exhibited appreciable variability; several polar cap patches were discernible in the OMTI and RISR-N data. A signature of one of the patches is seen in Figure 6.2 at 05:00 UT, immediately before the n_e depletion and arc were detected. It is conceivable that the quick decrease in n_e associated with the depletion feature was merely the signature of the tail-end of a patch advecting through the RISR-N beam; namely, $\partial n_e/\partial t = -\mathbf{v_p}\cdot\nabla\mathbf{n_e}$, in which $\mathbf{v_p}$ is the velocity of the patch. Even so, other features in Figure 6.3 show that an advecting patch could not be solely responsible for the n_e depletion feature. In Figures 6.2 and 6.3, the depletion marks the absolute minimum in n_e for the two hour period; it is also an absolute minimum for a six hour period surrounding the arc event. Furthermore, the depletion signature extends into the lower F region – into altitudes that are too low for patches. Therefore, other mechanisms such as chemical recombination must have been at play and were a leading contributor to generating the n_e depletion.

6.5 Conclusion

We have used multipoint measurements from RISR-N to, for the first time, resolve the electrodynamics and plasma structuring of a sun-aligned arc in time and space. Estimates of a moderate $\mathbf{J}_\parallel$ associated with the arc were observed, and are on par with previously reported arcs and models. $|\mathbf{E}_\perp|$ approaching 150 mV/m, and $T_{i_{los}}$ of up to 3000 K were also measured in the vicinity of the arc. The arc was responsible for a significant enhancement of the ionospheric electric field and remarkable plasma structuring in the region. One of the most spectacular arc features was a prominent, meridionally extended n_e depletion, located partially within the auroral downward current region on the leading edge of the arc as it progressed towards dawn. The depletion was largely a byproduct of heightened chemical

recombination rates and was generated on a time scale of 15 minutes.

Chapter 7

Summary and Conclusions

The objective of this research was to study large scale plasma density perturbations in the polar ionosphere to gain new insight into their generation mechanisms, transport properties and signatures at optical and radio wavelengths. This was accomplished by studying measurements from radio and optical instruments that have been deployed in the polar region within the past decade. In Section 1.5, six points of inquiry into the role and dynamics of the plasma density perturbations were outlined. Each section of this thesis focused on one or two of these questions. The results from those chapters are now summarized.

Is there a link between the optical signature of F-region ionization patches and their motion in the ionosphere?

This question was the focus of Chapter 3. In that chapter, the link between the vertical motion of two F-region ionization patches and their luminosity were investigated. Equation 3.13 was developed, and describes the luminosity of a patch as a function of its vertical velocity in the neutral atmosphere. Equation 3.13 was shown to adequately describe the optical data of two patches measured by OMTI, that were both moving through the OMTI FOV.

Equation 3.13 describes that the luminosity of a patch with a vertical velocity directed towards the surface of the Earth resembles a parabola in time. Once a patch begins to move downwards, its luminosity will increase, owing to the increased 630 nm emissions due to the enhanced chemical recombination of O^+ with the neutral atmosphere. After a short while, the luminosity will begin to decrease since the O^+ supply of the patch becomes depleted by the enhanced chemical recombination rates.

Results from this chapter link the luminosity of a patch to its velocity through the polar ionosphere, offering new insight into the chemistry of the polar ionosphere at F-region alti-

tudes. The results of this chapter were published in *Perry et al.* [2013]. Future work for this line of research was discussed in detail in Section 3.9.

Using radar, can our existing capabilities in identifying and characterizing F-region ionizations patches be improved?

This question was discussed in detail in the first part of Chapter 4. To address this question an algorithm that detects patches moving through the RISR-N FOV, the RISR-N algorithm, was introduced. The algorithm is founded on the *Crowley* [1996] criterion of a patch: a volume of plasma that has a n_e that is twice that of the background ionosphere. The RISR-N algorithm was shown to be extremely effective at detecting patches over Resolute Bay.

The RISR-N algorithm was then used to conduct a survey of patches detected over Resolute Bay during a total of ten days, five in March and December, 2010, respectively. The state parameters of the patches, i.e., n_e, T_i and T_e, were each analyzed separately. Some general results from the surveys include that less patches were detected during sunlit conditions in the ionosphere. In general, the n_e of patches was less under dark ionosphere conditions, and were lowest in December, 2010. The T_i of patches remains relatively constant in either sunlit or dark ionosphere conditions. The T_e of patches is very sensitive to the solar zenith angle. To our knowledge this survey is the first of its kind for F-region ionization patches.

How strong is the interconnection between the occurrence of high frequency (HF) radar echoes from the polar-ionosphere and the presence of F-region ionization patches there?

This question was the topic of the second part of Chapter 4. Using the RISR-N algorithm developed in the first part of the chapter, SuperDARN echo return from within the RISR-N FOV were analyzed and compared to the presence of patches in that same area. It was determined that in March, 2010, 60% of the SuperDARN echoes originating from a Rankin Inlet beam located within the RISR-N FOV were associated with patches. For December, 2010, that number increased to 66%. In each dataset, only 5% and 24% of the SuperDARN echoes were not associated with patches, respectively. These results give strong support to the notion that the majority of SuperDARN echoes originating from the polar region are

associated with F-region ionization patches. However, more work is needed to gauge the role of HF propagation on these results.

Are patches a dynamic or stagnant feature of the ionosphere? Is there any evidence of internal morphology?

This question was a focal point of Chapter 5 in which a single F-region ionization patch was investigated using SuperDARN, RISR-N and OMTI. The patch was studied as it travelled through the polar ionosphere. Using RISR-N measurements in the frame of reference of the patch, it was determined that the n_e of the patch displayed significant variability in time. This result indicates that patches are not stagnant features.

An alternate theory explaining the extreme variability of the n_e measurements of the patch was also given. It was posited that the patch in question may have been a group of patches with spatial scales below the resolvability of the RISR-N system. Probing this grouping of patches may give the appearance of a varying n_e profile since a different patch may have contributed to the n_e profile of the patch in question in each scan. Further investigations along this front were left for future work. The results of this chapter were published in *Dahlgren et al.* [2012b].

What geophysical phenomena are related to the frictional heating events producing plasma density depletions in the polar ionosphere?

What is the time scale of generating plasma density depletions in the polar-ionosphere via a frictional heating mechanism?

These two questions were addressed in Chapter 6, which investigated a sun-aligned arc that passed through the RISR-N FOV. In this chapter a novel analysis technique was used to invert the line-of-sight ion velocity measurements from RISR-N to infer the electrodynamics of the sun-aligned arc system. The effect of the arc on the F-region ionosphere was also investigated.

The results of the analysis showed that the arc system generated a large meridionally extended n_e depletion on the leading edge of the optical arc. By consulting an auroral arc

model, it was determined that the depletion was a result of enhanced electric fields located on the leading edge of the optical arc. The enhanced electric field created fast flows parallel to the optical arc, thereby increasing the frictional heating and chemical recombination of the ionosphere in this region. The time scale of generating the depletion was determined to be of the order of 15 minutes. In another fascinating result from this chapter, it was revealed that the depletion generated by the sun-aligned arc moved in conjunction with the arc. The results of this chapter were submitted to a peer-reviewed journal under *Perry et al.* [2014].

Final words

One of the more significant results from this thesis was presented in Chapter 4; that is, ionization patches are almost always present in the polar ionosphere and they display a significant amount of variability in terms of plasma state parameters. This reinforces the ongoing paradigm shift in our view of the polar ionosphere which is that the polar ionosphere is not a relatively homogenous region with transient plasma density perturbations, such as patches; on the contrary, homogeneity is atypical in the polar ionosphere. This shift was initiated in previous work studying plasma density variations in the high-latitude ionosphere using radio and optical instruments, and has been bolstered here with the addition of measurements of plasma density and temperature. Also, the lack of complementary datasets in previous work may have led to an underestimation of the level of structuring in the polar ionosphere by large scale plasma density perturbations. This has been rectified by the use of multi-instrument studies in this work. Results from Chapter 3 may provide a reason as to why this underestimation may have not been realized earlier. Optical data has been featured most often in patch studies. Since the luminosity of a patch is interconnected with its altitude and vertical velocity, many patches may have been missed due to their high altitude and lack of vertical motion, making them too dim to detect optically as they passed through the polar ionosphere.

This has important implications for the global communications infrastructure in the Arctic region. The HF band is an important frequency range for military and civilian communications and monitoring systems, including those for aviation and maritime traffic. As shown

in this thesis, plasma density perturbations can affect HF radio wave propagation. On one hand this may benefit HF communications by enabling refraction in an otherwise tenuous ionosphere, extending the effective range of radio communications. However, the perturbations may also have an adverse effect on radio communications since the perturbations seed field-aligned irregularities which present a scattering cross section for HF radio waves. Other research has detailed the negative effects of density perturbations on the higher frequency radio bands, such as those used for GPS and other satellite communications.

More work is needed to understand the drivers behind the population of patches and depletions in the ionosphere. With the tools and techniques introduced in this thesis, along with theory and computer simulations, and other instruments such as ionosondes and GPS receivers, we can pursue a goal of understanding the polar ionosphere to a point, for example, in which forecasts of plasma density perturbations are possible. This would be a profound milestone in our comprehension of the coupling between solar processes and the terrestrial environment, i.e., Space Weather.

References

Akasofu, S.-I., The development of the auroral substorm, *Planet. Space Sci.*, *12*(4), 273–282, doi:http://dx.doi.org/10.1016/0032-0633(64)90151-5, 1964.

Alcaydé, D., Incoherent Scatter, *Tech. Rep. November 1997*, EISCAT Scientific Association, 2001.

Alfvén, H., On the Existence of Electromagnetic-Hydrodynamic Waves, *Ark. Mat. Astron. Fys.*, *29B*, 1942.

Appleton, E. V., and G. Builder, The ionosphere as a doubly-refracting medium, *Proc. Phys. Soc.*, *45*(2), 208, doi:10.1088/0959-5309/45/2/307, 1933.

Bahcivan, H., R. Tsunoda, M. Nicolls, and C. Heinselman, Initial ionospheric observations made by the new Resolute incoherent scatter radar and comparison to solar wind IMF, *Geophys. Res. Lett.*, *37*(15), L15,103, doi:10.1029/2010GL043632, 2010.

Bahcivan, H., M. J. Nicolls, and G. Perry, Comparison of SuperDARN irregularity drift measurements and F-region ion velocities from the resolute bay ISR, *J. Atmos. Solar-Terrestrial Phys.*, *105106*(0), 325–331, doi:http://dx.doi.org/10.1016/j.jastp.2013.02.002, 2013.

Basu, S., S. Basu, E. MacKenzie, W. R. Coley, J. Sharber, and W. Hoegy, Plasma Structuring by the Gradient Drift Instability at High Latitudes and Comparison with Velocity Shear Driven Processes , *J. Geophys. Res.*, *29*, 195–207, doi:10.1029/93RS01515, 1990.

Baumjohann, W., and R. A. Treumann, *Basic Space Plasma Physics*, Imperial College Press, 1997.

Bilitza, D., International reference ionosphere 2000, *Radio Sci.*, *36*(2), 261–275, doi: 10.1029/2000RS002432, 2001.

Bilitza, D., and B. Reinisch, International Reference Ionosphere 2007: Improvements and new parameters, *Adv. Sp. Res.*, *42*(4), 599–609, doi: 10.1016/j.asr.2007.07.048, 2008.

Bowles, K. L., Observation of Vertical-Incidence Scatter from the Ionosphere at 41 Mc/sec, *Phys. Rev. Lett.*, *1*(12), 454–455, 1958.

Brekke, A., *Physics of the Upper Polar Atmosphere*, Springer Atmospheric Sciences, Springer, 2012.

Brinton, H. C., J. M. Grebowsky, and L. H. Brace, The high-latitude winter F region at 300 km: Thermal plasma observations from AE-C, *J. Geophys. Res.*, *83*(A10), 4767–4776, doi:10.1029/JA083iA10p04767, 1978.

Buchau, J., B. Reinisch, E. Weber, and J. Moore, Structure and dynamics of the winter polar cap F region, *Radio Sci.*, *18*(6), 995–1010, doi::10.1029/RS018i006p00995, 1983.

Buchau, J., E. J. Weber, D. N. Anderson, H. C. Carlson, J. G. Moore, B. W. Reinisch, and R. C. Livingston, Ionospheric structures in the polar cap: Their origin and relation to 250-MHz scintillation, *Radio Sci.*, *20*(3), 325–338, doi:10.1029/RS020i003p00325, 1985.

Burston, R., K. Hodges, I. Astin, and P. T. Jayachandran, Automated identification and tracking of polar-cap plasma patches at solar minimum, *Ann. Geophys.*, *32*(3), 197–206, doi:10.5194/angeo-32-197-2014, 2014.

Butler, T. W., J. Semeter, C. J. Heinselman, and M. Nicolls, Imaging F region drifts using monostatic phased-array incoherent scatter radar, *Radio Sci.*, *45*, RS5013, doi:10.1029/2010RS004364, 2010.

Carlson, H. C., Ionospheric patch formation: Direct measurements of the origin of a polar cap patch, *Geophys. Res. Lett.*, *31*(8), L08,806, doi:10.1029/2003GL018166, 2004.

Carlson, H. C., Sharpening our thinking about polar cap ionospheric patch morphology, research, and mitigation techniques, *Radio Sci.*, *47*(4), RS0L21, doi:10.1029/2011RS004946, 2012.

Carlson, H. C., and S. W. H. Cowley, Accelerated polar rain electrons as the source of Sun-aligned arcs in the polar cap during northward interplanetary magnetic field conditions, *J. Geophys. Res. Sp. Phys.*, *110*(A5), A05,302, doi: 10.1029/2004JA010669, 2005.

Carlson, H. C., V. B. Wickwar, E. J. Weber, J. Buchau, J. G. Moore, and W. Whiting, Plasma characteristics of polar cap F-layer arcs, *Geophys. Res. Lett.*, *11*(9), 895–898, doi: 10.1029/GL011i009p00895, 1984.

Carlson, H. C., K. Oksavik, J. Moen, A. P. van Eyken, and P. Guio, ESR mapping of polar-cap patches in the dark cusp, *Geophys. Res. Lett.*, *29*(10), 24–1–24–4, doi: 10.1029/2001GL014087, 2002.

Carlson, H. C., J. Moen, K. Oksavik, C. P. Nielsen, I. W. McCrea, T. R. Pedersen, and P. Gallop, Direct observations of injection events of subauroral plasma into the polar cap, *Geophys. Res. Lett.*, *33*(5), L05,103, doi:10.1029/2005GL025230, 2006.

Carlson, H. C., K. Oksavik, and J. Moen, On a new process for cusp irregularity production, *Ann. Geophys.*, *26*, 2871–2885, doi:10.5194/angeo-26-2871-2008, 2008.

Cerisier, J., and C. Senior, Merge: A FORTRAN program, *Tech. rep.*, Centre d'Étude des Environnments Terrestres et Planétaires, Cent. Nat. de la Rech. Sci, St-Maur, France, 1994.

Cerisier, J., J. Berthelier, and C. Beghin, Unstable density gradients in the high-latitude ionosphere, *Radio Sci.*, *20*(4), 755 – 761, doi:10.1029/RS020i004p00755, 1985.

Chaturvedi, P. K., and S. L. Ossakow, The current convective instability as applied to the auroral ionosphere, *J. Geophys. Res. Sp. Phys.*, *86*(A6), 4811–4814, doi: 10.1029/JA086iA06p04811, 1981.

Chen, F. F., *Introduction to Plasma Physics and Controlled Fusion: Volume 1: Plasma Physics*, 2nd ed., Springer US, 2010.

Chen, Y., L. Liu, and W. Wan, Does the F10.7 index correctly describe solar EUV flux during the deep solar minimum of 20072009?, *J. Geophys. Res. Sp. Phys.*, *116*(A4), A04,304, doi: 10.1029/2010JA016301, 2011.

Chisham, G., I. J. Coleman, M. P. Freeman, M. Pinnock, and M. Lester, Ionospheric signatures of split reconnection X-lines during conditions of IMF Bz < 0 and $|By| \sim |Bz|$: Evidence for the antiparallel merging hypothesis, *J. Geophys. Res. Sp. Phys.*, *107*(A10), 1323, doi:10.1029/2001JA009124, 2002.

Chisham, G., et al., A decade of the Super Dual Auroral Radar Network (SuperDARN): scientific achievements, new techniques and future directions, *Surv. Geophys.*, *28*(1), 33–109, doi:10.1007/s10712-007-9017-8, 2007.

Coley, W. R., and R. A. Heelis, Adaptive identification and characterization of polar ionization patches, *J. Geophys. Res. Sp. Phys.*, *100*(A12), 23,819–23,827, doi: 10.1029/95JA02700, 1995.

Coley, W. R., and R. a. Heelis, Structure and occurrence of polar ionization patches, *J. Geophys. Res.*, *103*(A2), 2201, doi: 10.1029/97JA03345, 1998.

Committee on a Decadal Strategy for Solar and Space Physics (Heliophysics); Space Studies Board; Aeronautics and Space Engineering Board; Division of Earth and Physical Sciences; National Research Council, Solar and space physics: A science for a technological society, *Tech. rep.*, 2013.

Cousins, E. D. P., and S. G. Shepherd, A dynamical model of high-latitude convection derived from SuperDARN plasma drift measurements, *J. Geophys. Res. Sp. Phys.*, *115*(A12), A12,329, doi:10.1029/2010JA016017, 2010.

Cowley, S. W. H., Magnetosphere-ionosphere interactions: A tutorial review, in *Magnetospheric Current Systems*, *Geophys. Monogr. Ser.*, vol. 118, pp. 91–106, AGU, Washington, DC, doi:10.1029/GM118p0091, 2000.

Cowley, S. W. H., and M. Lockwood, Excitation and decay of solar wind-driven flows in the magnetosphere-ionosphere system, *Ann. Geophys.*, *10*, 103–115, 1992.

Crowley, G., Critical review of ionospheric patches and blobs, *URSI Review of Radio Science 19931996, (Ed) Stone, W. R.*, *Oxford University Press*, doi:10.1029/2000RS002558, 1996.

Crowley, G., H. C. Carlson, S. Basu, W. F. Denig, J. Buchau, and B. W. Reinisch, The dynamic ionospheric polar hole, *Radio Sci.*, *28*(3), 401–413, doi:10.1029/92RS02878, 1993.

Cumnock, J. A., G. Le, S. Imber, J. A. Slavin, Y. Zhang, and L. J. Paxton, Space Technology 5 multipoint observations of transpolar arcrelated field-aligned currents, *J. Geophys. Res. Sp. Phys.*, *116*(A2), A02,218, doi: 10.1029/2010JA015912, 2011.

Dahlgren, H., J. L. Semeter, K. Hosokawa, M. J. Nicolls, T. W. Butler, M. G. Johnsen, K. Shiokawa, and C. Heinselman, Direct three-dimensional imaging of polar ionospheric structures with the resolute bay incoherent scatter radar, *Geophys. Res. Lett.*, *39*, doi:10.1029/2012GL050895, 2012a.

Dahlgren, H., G. W. Perry, J. L. Semeter, J.-P. St.-Maurice, K. Hosokawa, M. J. Nicolls, M. Greffen, K. Shiokawa, and C. Heinselman, Space-time variability of polar cap patches: Direct evidence for internal plasma structuring, *J. Geophys. Res.*, *117*(A9), doi:10.1029/2012JA017961, 2012b.

Dahlgren, H., G. Perry, J.-P. St Maurice, T. Sundberg, K. Hosokawa, J. L. Semeter, M. J. Nicolls, and K. Shiokawa, 3D imaging reveals electrod ynamics of polar cap aurora, *Astron. Geophys.*, *55*(5), 5.26–5.28, doi:10.1093/astrogeo/atu215, 2014.

de la Beaujardiere, O., R. Vondrak, and M. Baron, Radar observations of electric fields and currents associated with auroral arcs, *J. Geophys. Res.*, *82*(32), 5051–5062, doi: 10.1029/JA082i032p05051, 1977.

Doe, R. A., M. Mendillo, J. F. Vickrey, L. J. Zanetti, and R. W. Eastes, Observations of nightside auroral cavities, *J. Geophys. Res. Sp. Phys.*, *98*(A1), 293–310, doi: 10.1029/92JA02004, 1993.

Doe, R. A., J. F. Vickrey, and M. Mendillo, Electrodynamic model for the formation of auroral ionospheric cavities, *J. Geophys. Res. Sp. Phys.*, *100*(A6), 9683–9696, doi: 10.1029/95JA00001, 1995.

Drayton, R. A., A. V. Koustov, M. R. Hairston, and J.-P. Villain, Comparison of DMSP cross-track ion drifts and SuperDARN line-of-sight velocities, *Annales Geophysicae*, *23*, 2479–2486, doi:10.5194/angeo-23-2479-2005, 2005.

Fear, R. C., and S. E. Milan, The IMF dependence of the local time of transpolar arcs: Implications for formation mechanism, *J. Geophys. Res. Sp. Phys.*, *117*(A3), A03,213, doi: 10.1029/2011JA017209, 2012.

Fejer, B. G., D. T. Farley, B. B. Balsley, and R. F. Woodman, Vertical structure of the VHF backscattering region in the equatorial electrojet and the gradient drift instability, *J. Geophys. Res.*, *80*(10), 1313–1324, doi:10.1029/JA080i010p01313, 1975.

Fiori, R. A. D., Application of spherical cap harmonic analysis to plasma convection mapping at high latitudes, Ph.D. thesis, University of Saskatchewan, 2011.

Fiori, R. A. D., D. H. Boteler, A. V. Koustov, G. V. Haines, and J. M. Ruohoniemi, Spherical cap harmonic analysis of Super Dual Auroral Radar Network (SuperDARN) observations for generating maps of ionospheric convection, *J. Geophys. Res. Sp. Phys.*, *115*(A7), A07,307, doi:10.1029/2009JA015055, 2010.

Forbes, J. M., S. E. Palo, and X. Zhang, Variability of the ionosphere, *J. Atmos. Solar-Terrestrial Phys.*, *62*(8), 685–693, doi:http://dx.doi.org/10.1016/S1364-6826(00)00029-8, 2000.

Foster, J. C., Ionospheric signatures of magnetospheric convection, *J. Geophys. Res.*, *89*(A2), 855–865, doi:10.1029/JA089iA02p00855, 1984.

Foster, J. C., Storm time plasma transport at middle and high latitudes, *J. Geophys. Res.*, *98*, 1675–1689, doi:10.1029/92JA02032, 1993.

Foster, J. C., et al., Multiradar observations of the polar tongue of ionization, *J. Geophys. Res.*, *110*(A9), A09S31, doi:10.1029/2004JA010928, 2005.

Fried, B. D., and S. D. Conte, *The Plasma Dispersion Function: The Hilbert Transform of the Gaussian*, Academic Press, 1961.

Garner, T. W., T. L. Killeen, A. G. Burns, J. D. Winningham, and W. R. Coley, Examination of the oxygen red line signature of a polar cap ionization patch as seen from the Dynamics Explorer 2 satellite, *Radio Sci.*, *31*, 607–618, doi:10.1029/96RS00617, 1996.

Gillies, R. G., G. C. Hussey, G. J. Sofko, K. A. McWilliams, R. A. D. Fiori, P. Ponomarenko, and J.-P. St.-Maurice, Improvement of SuperDARN velocity measurements by estimating the index of refraction in the scattering region using interferometry, *J. Geophys. Res. Sp. Phys.*, *114*(A7), A07,305, doi:10.1029/2008JA013967, 2009.

Gillies, R. G., G. C. Hussey, G. J. Sofko, and K. McWilliams, A statistical analysis of SuperDARN scattering volume electron densities and velocity corrections using a radar frequency shifting technique, *J. Geophys. Res.*, *117*(A08320), doi:10.1029/2012JA017866, 2012.

Gondarenko, N. A., and P. N. Guzdar, Plasma patch structuring by the nonlinear evolution of the gradient drift instability in the high-latitude ionosphere, *J. Geophys. Res.*, *109*(A18), A09301, doi:10.1029/2004JA010504, 2004.

Gondarenko, N. A., and P. N. Guzdar, Nonlinear three-dimensional simulations of mesoscale structuring by multiple drives in high-latitude plasma patches, *J. Geophys. Res.*, *111*(8), A08302, doi:10.1029/2006JA011701, 2006.

Goodwin, L. V., F-region Dusk Ion Temperature Spikes at the Equatorward Edge of the High Latitude Convection Region, Master's thesis, University of Saskatchewan, 2013.

Gordon, W. E., Incoherent Scattering of Radio Waves by Free Electrons with Applications to Space Exploration by Radar, doi:10.1109/JRPROC.1958.286852, 1958.

Greenwald, R. A., et al., DARN/SuperDARN, *Space Sci. Rev.*, *71*(1-4), 761–796, doi: 10.1007/BF00751350, 1995.

Gudadze, N. B., G. G. Didebulidze, L. N. Lomidze, G. S. Javakhishvili, M. A. Marsagishvili, and M. Todua, Different long-term trends of the oxygen red 630.0 nm line nightglow intensity as the result of lowering the ionosphere f2 layer, *Annales Geophysicae*, *26*(8), 2069–2080, doi:10.5194/angeo-26-2069-2008, 2008.

Haerendel, G., G. Paschmann, N. Sckopke, H. Rosenbauer, and P. C. Hedgecock, The frontside boundary layer of the magnetosphere and the problem of reconnection, *J. Geophys. Res. Sp. Phys.*, *83*(A7), 3195–3216, doi:10.1029/JA083iA07p03195, 1978.

Hamacher, D. W., Aurorae in australian aboriginal traditions, *Journal of Astronomical History and Heritage*, *16*, 207–219, 2013.

Hargreaves, J. K., *The Solar-Terrestrial Environment: An Introduction to Geospace - the Science of the Terrestrial Upper Atmosphere, Ionosphere, and Magnetosphere*, Cambridge Atmospheric and Space Science Series, Cambridge University Press, 1992.

Hartree, D. R., The propagation of electromagnetic waves in a stratified medium, *Math. Proc. Cambridge Philos. Soc.*, *25*(01), 97, doi:10.1017/S0305004100018600, 1929.

Hedin, A. E., Extension of the MSIS Thermosphere Model into the middle and lower atmosphere, *J. Geophys. Res. Sp. Phys.*, *96*(A2), 1159–1172, doi:10.1029/90JA02125, 1991.

Heinselman, C. J., and M. J. Nicolls, A Bayesian approach to electric field and E -region neutral wind estimation with the Poker Flat Advanced Modular Incoherent Scatter Radar, *Radio Sci.*, *43*(5), doi: 10.1029/2007RS003805, 2008.

Heppner, J. P., and N. C. Maynard, Empirical high-latitude electric field models, *J. Geophys. Res. Sp. Phys.*, *92*(A5), 4467–4489, doi:10.1029/JA092iA05p04467, 1987.

Hill, G. E., Sudden enhancements of f-layer ionization in polar regions, *Journal of the Atmospheric Sciences*, *20*(6), 492–497, 1963.

Hosokawa, K., K. Shiokawa, Y. Otsuka, A. Nakajima, T. Ogawa, and J. D. Kelly, Estimating drift velocity of polar cap patches with all-sky airglow imager at Resolute Bay, Canada, *Geophys. Res. Lett.*, *331*, L15,111, doi:10.1029/2006GL026916, 2006.

Hosokawa, K., K. Shiokawa, Y. Otsuka, T. Ogawa, J.-P. St-Maurice, G. J. Sofko, and D. A. Andre, Relationship between polar cap patches and field-aligned irregularities as observed with an all-sky airglow imager at Resolute Bay and the PolarDARN radar at Rankin Inlet, *J. Geophys. Res.*, *114*(A13), A03,306, doi:10.1029/2008JA013707, 2009a.

Hosokawa, K., T. Kashimoto, S. Suzuki, K. Shiokawa, Y. Otsuka, and T. Ogawa, Motion of polar cap patches: A statistical study with all-sky airglow imager at Resolute Bay, Canada, *Journal of Geophysical Research*, *114*(A4), A04,318, doi:10.1029/2008JA014020, 2009b.

Hosokawa, K., J.-P. St-Maurice, G. Sofko, K. Shiokawa, Y. Otsuka, and T. Ogawa, Reorganization of polar cap patches through shears in the background plasma convection, *J. Geophys. Res.*, *115*, A01,303, doi:10.1029/2009JA014599, 2010.

Hosokawa, K., J. I. Moen, K. Shiokawa, and Y. Otsuka, Decay of polar cap patch, *J. Geophys. Res.*, *116*(A15), A05,306, doi:10.1029/2010JA016297, 2011.

Hosokawa, K., S. Taguchi, Y. Ogawa, and T. Aoki, Periodicities of polar cap patches, *J. Geophys. Res. Sp. Phys.*, *118*(1), 447–453, doi: 10.1029/2012JA018165, 2013a.

Hosokawa, K., S. Taguchi, Y. Ogawa, and J. Sakai, Two-dimensional direct imaging of structuring of polar cap patches, *J. Geophys. Res. Sp. Phys.*, *118*(10), 6536–6543, doi: 10.1002/jgra.50577, 2013b.

Hosokawa, K., S. Taguchi, K. Shiokawa, Y. Otsuka, Y. Ogawa, and M. Nicolls, Global imaging of polar cap patches with dual airglow imagers, *Geophys. Res. Lett.*, pp. n/a–n/a, doi: 10.1002/2013GL058748, 2013c.

Johnson, C. Y., Ion and neutral composition of the ionosphere., *Annals of the IQSY*, *5*, 197–213, 1969.

Jones, A. V., *Aurora*, Geophysics and Astrophysics Monographs, Springer Netherlands, 1974.

Kazimirovsky, E. S., and V. D. Kokourov, The Tropospheric and Stratospheric Effects in the Ionosphere, *J. Geomagn. Geoelectr.*, *43*(Supplement1), 551–562, doi: 10.5636/jgg.43.Supplement1_551, 1991.

Kelley, M. C., *The Earth's Ionosphere: Plasma Physics & Electrodynamics*, International Geophysics, 2nd ed., Elsevier Science, 2009.

Kelley, M. C., *The Earths Electric Field: Sources from Sun to Mud*, Elsevier Science, 2013.

Kelley, M. C., J. F. Vickrey, C. W. Carlson, and R. Torbert, On the origin and spatial extent of high-latitude F region irregularities, *J. Geophys. Res. Sp. Phys.*, *87*(A6), 4469–4475, doi:10.1029/JA087iA06p04469, 1982.

Keskinen, M. J., and S. L. Ossakow, Nonlinear evolution of plasma enhancements in the auroral ionosphere, 1, Long wavelength irregularities, *J. Geophys. Res. Sp. Phys.*, *87*(A1), 144–150, doi:10.1029/JA087iA01p00144, 1982.

Keskinen, M. J., and S. L. Ossakow, Theories of high-latitude ionospheric irregularities: A review, *Radio Sci.*, *18*(6), 1077–1091, doi:10.1029/RS018i006p01077, 1983.

Kitamura, N., Y. Ogawa, Y. Nishimura, N. Terada, T. Ono, A. Shinbori, A. Kumamoto, V. Truhlik, and J. Smilauer, Solar zenith angle dependence of plasma density and temperature in the polar cap ionosphere and low-altitude magnetosphere during geomagnetically quiet periods at solar maximum, *J. Geophys. Res. Sp. Phys.*, *116*(A8), A08,227, doi:10.1029/2011JA016631, 2011.

Kivanç, Ö., and R. A. Heelis, Structures in ionospheric number density and velocity associated with polar cap ionization patches, *J. Geophys. Res.*, *102*, 307–318, doi:10.1029/96JA03141, 1997.

Kivelson, M. G., and C. T. Russell, *Introduction to Space Physics*, Cambridge atmospheric and space science series, Cambridge University Press, 1995.

Knudsen, W. C., Magnetospheric convection and the high-latitude F2 ionosphere, *J. Geophys. Res.*, *79*(7), 1046–1055, doi:10.1029/JA079i007p01046, 1974.

Koustov, A., K. Hosokawa, N. Nishitani, T. Ogawa, and K. Shiokawa, Rankin Inlet PolarDARN radar observations of duskward moving Sun-aligned optical forms, *Ann. Geophys.*, *26*(9), 2711–2723, doi: 10.5194/angeo-26-2711-2008, 2008.

Koustov, A. V., K. Hosokawa, N. Nishitani, K. Shiokawa, and H. Liu, Signatures of moving polar cap arcs in the F-region PolarDARN echoes, *Ann. Geophys.*, *30*(3), 441–455, doi: 10.5194/angeo-30-441-2012, 2012.

Kubota, M., H. Fukunishi, and S. Okano, Characteristics of medium- and large-scale TIDs over Japan derived from OI 630-nm nightglow observation, *Earth, Planets Sp.*, *53*(7), 741–751, doi:10.1186/BF03352402, 2001.

Kullen, A., Transpolar Arcs: Summary and Recent Results, in *Auror. Phenomenol. Magnetos. Process. Earth Other Planets*, pp. 69–80, American Geophysical Union, doi: 10.1029/2011GM001183, 2012.

Lanchester, B. S., K. Kaila, and I. W. McCrea, Relationship between large horizontal electric fields and auroral arc elements, *J. Geophys. Res. Sp. Phys.*, *101*(A3), 5075–5084, doi: 10.1029/95JA02055, 1996.

Li, S., and L. Hui, Parallel AMR Code for Compressible MHD or HD Equations, *Tech. rep.*, Los Alamos National Loboratory, 2006.

Lockwood, M., and H. C. Carlson, Production of polar cap electron density patches by transient magnetopause reconnection, *Geophys. Res. Lett.*, *19*(17), 1731–1734, doi: 10.1029/92GL01993, 1992.

Lockwood, M., H. C. Carlson, Jr., and P. E. Sandholt, Implications of the altitude of transient 630-nm dayside auroral emissions, *J. Geophys. Res.*, *981*, 15,571–15,587, doi:10.1029/93JA00811, 1993.

Lockwood, M., J. Moen, A. P. van Eyken, J. A. Davies, K. Oksavik, and I. W. McCrea, Motion of the dayside polar cap boundary during substorm cycles: I. Observations of pulses in the magnetopause reconnection rate, *Ann. Geophys.*, *23*(11), 3495–3511, doi: 10.5194/angeo-23-3495-2005, 2005.

Lorentzen, D. A., N. Shumilov, and J. Moen, Drifting airglow patches in relation to tail reconnection, *Geophys. Res. Lett.*, *31*(2), L02,806, doi:10.1029/2003GL017785, 2004.

Lorentzen, D. A., J. Moen, K. Oksavik, F. Sigernes, Y. Saito, and M. G. Johnsen, In situ measurement of a newly created polar cap patch, *J. Geophys. Res.*, *115*(A14), A12,323, doi:10.1029/2010JA015710, 2010.

Lotko, W., The magnetosphereionosphere system from the perspective of plasma circulation: A tutorial, *J. Atmos. Solar-Terrestrial Phys.*, *69*(3), 191–211, doi: 10.1016/j.jastp.2006.08.011, 2007.

Lyons, L. R., Y. Nishimura, H.-J. Kim, E. Donovan, V. Angelopoulos, G. Sofko, M. Nicolls, C. Heinselman, J. M. Ruohoniemi, and N. Nishitani, Possible connection of polar cap flows to pre- and post-substorm onset PBIs and streamers, *J. Geophys. Res. Sp. Phys.*, *116*(A12), A12,225, doi:10.1029/2011JA016850, 2011.

MacDougall, J., and P. T. Jayachandran, Polar patches: Auroral zone precipitation effects, *J. Geophys. Res. Sp. Phys.*, *112*(A5), A05,312, doi: 10.1029/2006JA011930, 2007.

MacDougall, J. W., and P. T. Jayachandran, Polar cap convection relationships with solar wind, *Radio Sci.*, *36*(6), 1869–1880, doi: 10.1029/2001RS001007, 2001.

Maeda, S., Y. Ogawa, K. Hosokawa, S. Nozawa, S.-i. Oyama, T. Tsuda, and A. Brekke, Ion heating in high-speed flow channel within the duskside cell of the polar cap ion convection under large IMF- B y condition, *J. Geophys. Res.*, *114*(A11), A11,307, doi: 10.1029/2009JA014300, 2009.

Makela, J. J., M. C. Kelley, S. A. González, N. Aponte, and R. P. McCoy, Ionospheric topography maps using multiple-wavelength all-sky images, *J. Geophys. Res. Sp. Phys.*, *106*(A12), 29,161–29,174, doi:10.1029/2000JA000449, 2001.

Mantas, G. P., H. C. Carlson, and C. H. LaHoz, Thermal response of the F region ionosphere in artificial modification experiments by HF radio waves, *J. Geophys. Res. Sp. Phys.*, *86*(A2), 561–574, doi:10.1029/JA086iA02p00561, 1981.

McFarland, M., D. Albritton, F. Fehsenfeld, E. Ferguson, and A. Schmeltekopf, Flow-drift technique for ion mobility and ion-molecule reaction rate constant measurements. II. Positive ion reactions of N^+, O^+, and H_2^+ with O_2 and O^+ with N_2 from thermal to ~ 2 eV, *J. Chem. Phys.*, *59*(12), 6620, doi: 10.1063/1.1680042, 1973.

McWilliams, K. A., T. K. Yeoman, and S. W. H. Cowley, Two-dimensional electric field measurements in the ionospheric footprint of a flux transfer event, *Ann. Geophys.*, *18*, 1584–1598, doi:10.1007/s00585-001-1584-2, 2001.

Meek, J. H., Sporadic ionization at high latitudes, *J. Geophys. Res.*, *54*(4), 339–345, doi: 10.1029/JZ054i004p00339, 1949.

Mende, S. B., J. H. Doolittle, R. M. Robinson, R. R. Vondrak, and F. J. Rich, Plasma drifts associated with a system of Sun-aligned arcs in the polar cap, *J. Geophys. Res. Sp. Phys.*, *93*(A1), 256–264, doi:10.1029/JA093iA01p00256, 1988.

Milan, S. E., M. Lester, S. W. H. Cowley, J. Moen, P. E. Sandholt, and C. J. Owen, Meridian-scanning photometer, coherent HF radar, and magnetometer observations of the cusp: a case study, *Ann. Geophys.*, *17*, 159–172, doi:10.1007/s00585-999-0159-5, 1999.

Milan, S. E., M. Lester, and T. K. Yeoman, HF radar polar patch formation revisited: summer and winter variations in dayside plasma structuring, *Ann. Geophys.*, *20*(4), 487–499, doi:10.5194/angeo-20-487-2002, 2002.

Milan, S. E., J. S. Gosling, and B. Hubert, Relationship between interplanetary parameters and the magnetopause reconnection rate quantified from observations of the expanding polar cap, *J. Geophys. Res.*, *117*(A3), A03,226, doi:10.1029/2011JA017082, 2012.

Moen, J., P. E. Sandholt, M. Lockwood, W. F. Denig, and U. P. Lvhaug, Events of enhanced convection and related dayside auroral activity, *J. Geophys. Res.*, *100*, 23,917–23,934, doi:10.1029/95JA02585, 1995.

Moen, J., H. C. Carlson, S. E. Milan, N. Shumilov, B. Lybekk, P. E. Sandholt, and M. Lester, On the collocation between dayside auroral activity and coherent HF radar backscatter, *Ann. Geophys.*, *18*(12), 1531–1549, doi:10.1007/s00585-001-1531-2, 2000.

Moen, J., I. K. Walker, L. Kersley, and S. E. Milan, On the generation of cusp HF backscatter irregularities, *J. Geophys. Res. Sp. Phys.*, *107*(A4), SIA 3–1–SIA 3–5, doi:10.1029/2001JA000111, 2002.

Moen, J., H. C. Carlson, K. Oksavik, C. P. Nielsen, S. E. Pryse, H. R. Middleton, I. W. McCrea, and P. Gallop, Eiscat observations of plasma patches at sub-auroral cusp latitudes, *Ann. Geophys.*, *24*(9), 2363–2374, doi:10.5194/angeo-24-2363-2006, 2006.

Moen, J., X. C. Qiu, H. C. Carlson, R. Fujii, I. W. Mccrea, B. Crescent, W. Ruislip, and H. A. Uk, On the diurnal variability in F2-region plasma density above the EISCAT Svalbard radar, *Ann. Geophys.*, *26*(1974), 2427–2433, doi:10.5194/angeo-26-2427-2008, 2008.

Moen, J., K. Oksavik, T. Abe, M. Lester, Y. Saito, T. A. Bekkeng, and K. S. Jacobsen, First in-situ measurements of HF radar echoing targets, *Geophys. Res. Lett.*, *39*(7), L07,104, doi:10.1029/2012GL051407, 2012.

Moen, J. r., K. Oksavik, L. Alfonsi, Y. Daabakk, V. Romano, and L. Spogli, Space weather challenges of the polar cap ionosphere, *J. Sp. Weather Sp. Clim.*, *3*, doi:10.1051/swsc/2013025, 2013.

Muldrew, D. B., F-layer ionization troughs deduced from Alouette data, *J. Geophys. Res.*, *70*(11), 2635–2650, doi:10.1029/JZ070i011p02635, 1965.

Nicolls, M. J., C. J. Heinselman, E. A. Hope, S. Ranjan, M. C. Kelley, and J. D. Kelly, Imaging of Polar Mesosphere Summer Echoes with the 450 MHz Poker Flat Advanced Modular Incoherent Scatter Radar, *Geophys. Res. Lett.*, *34*(20), L20,102, doi:10.1029/2007GL031476, 2007.

Nicolls, M. J., R. Cosgrove, and H. Bahcivan, Estimating the Vector Electric Field using Monostatic, Multi-beam Incoherent Scatter Radar Measurements, *Radio Sci.*, p. 2014RS005519, doi: 10.1002/2014RS005519, in press, 2014.

Nishino, M., S. Nozawa, and J. Holtet, Daytime ionospheric absorption features in the polar cap associated with poleward drifting f-region plasma patches, *Earth, Planets, and Space*, *50*(2), doi:107 – 117, 1998.

Noja, M., C. Stolle, J. Park, and H. Lühr, Long term analysis of ionospheric polar patches based on CHAMP TEC data, *Radio Sci.*, Accepted Article, doi:10.1002/rds.20033, 2013.

Ogawa, T., N. Nishitani, M. Pinnock, N. Sato, H. Yamagishi, and A. S. Yukimatu, Antarctic HF radar observations of irregularities associated with polar patches and auroral blobs: A case study, *J. Geophys. Res.*, *103*, 26,547–26,558, doi:10.1029/98JA02044, 1998.

Oksavik, K., J. M. Ruohoniemi, R. A. Greenwald, J. B. H. Baker, J. Moen, H. C. Carlson, T. K. Yeoman, and M. Lester, Observations of isolated polar cap patches by the European Incoherent Scatter (EISCAT) Svalbard and Super Dual Auroral Radar Network (SuperDARN) Finland radars, *J. Geophys. Res.*, *111*(A10), A05310, doi:10.1029/2005JA011400, 2006.

Oksavik, K., V. L. Barth, J. Moen, and M. Lester, On the entry and transit of high-density plasma across the polar cap, *J. Geophys. Res.*, *115*(A12), A12,308, doi:10.1029/2010JA015817, 2010.

Opgenoorth, H., I. Häggström, P. Williams, and G. Jones, Regions of strongly enhanced perpendicular electric fields adjacent to auroral arcs, *J. Atmos. Terr. Phys.*, *52*(6-8), 449–458, doi:10.1016/0021-9169(90)90044-N, 1990.

Parker, E. N., and M. Krook, Diffusion and severing of magnetic lines of force, *Astrophys. J.*, *124*, 214, doi:10.1086/146216, 1956.

Pedersen, T. R., B. G. Fejer, R. A. Doe, and E. J. Weber, Incoherent scatter radar observations of horizontal F region plasma structure over Sondrestrom, Greenland, during polar cap patch events, *Radio Sci.*, *33*(6), 1847–1866, doi: 10.1029/98RS01702, 1998.

Pedersen, T. R., B. G. Fejer, R. A. Doe, and E. J. Weber, An incoherent scatter radar technique for determining two-dimensional horizontal ionization structure in polar cap F region patches, *J. Geophys. Res.*, *105*(A5), 10,637–10,655, doi:10.1029/1999JA000073, 2000.

Perry, G. W., J.-P. St.-Maurice, and K. Hosokawa, The interconnection between cross-polar cap convection and the luminosity of polar cap patches, *J. Geophys. Res.*, *118*(11), 7306–7315, doi:10.1002/2013JA019196, 2013.

Perry, G. W., H. Dahlgren, M. J. Nicolls, M. Zettergren, J.-P. St.-Maurice, J. L. Semeter, T. Sundberg, K. Hosokawa, S. K., and S. Chen, Spatiotemporally resolved electrodynamic properties of a sun-aligned arc over Resolute Bay, *Geophys. Res. Lett.*, submitted, 2014.

Ponomarenko, P. V., F. W. Menk, C. L. Waters, and M. D. Sciffer, Pc3-4 ULF waves observed by the SuperDARN TIGER radar, *Ann. Geophys.*, *23*(4), 1271–1280, doi:10.5194/angeo-23-1271-2005, 2005.

Ponomarenko, P. V., J.-P. St-Maurice, C. L. Waters, R. G. Gillies, and A. V. Koustov, Refractive index effects on the scatter volume location and Doppler velocity estimates of ionospheric HF backscatter echoes, *Ann. Geophys.*, *27*(11), 4207–4219, doi:10.5194/angeo-27-4207-2009, 2009.

Ponomarenko, P. V., J.-P. St. Maurice, G. C. Hussey, and A. V. Koustov, HF ground scatter from the polar cap: Ionospheric propagation and ground surface effects, *J. Geophys. Res. Sp. Phys.*, *115*(A10), A10,310, doi:10.1029/2010JA015828, 2010.

Provan, G., S. E. Milan, M. Lester, T. K. Yeoman, and H. Khan, Letter to the editor simultaneous observations of the ionospheric footprint of flux transfer events and dispersed ion signatures, *Annales Geophysicae*, *20*(2), 281–287, doi:10.5194/angeo-20-281-2002, 2002.

Raman, R. S. V., J. P. St-Maurice, and R. S. B. Ong, Incoherent scattering of radar waves in the auroral ionosphere, *J. Geophys. Res. Sp. Phys.*, *86*(A6), 4751–4762, doi:10.1029/JA086iA06p04751, 1981.

Richards, P. G., Seasonal and solar cycle variations of the ionospheric peak electron density: Comparison of measurement and models, *J. Geophys. Res. Sp. Phys.*, *106*(A7), 12,803–12,819, doi:10.1029/2000JA000365, 2001.

Rijnbeek, R. P., S. W. H. Cowley, D. J. Southwood, and C. T. Russell, A survey of dayside flux transfer events observed by ISEE 1 and 2 magnetometers, *J. Geophys. Res.*, *89*, 786–800, doi:10.1029/JA089iA02p00786, 1984.

Rishbeth, H., and W. B. Hanson, A comment on plasma pile-up in the F-region, *J. Atmos. Terr. Phys.*, *36*(4), 703–706, doi:http://dx.doi.org/10.1016/0021-9169(74)90094-4, 1974.

Rishbeth, H., and M. Mendillo, Patterns of F2-layer variability, *J. Atmos. Solar-Terrestrial Phys.*, *63*(15), 1661–1680, doi:http://dx.doi.org/10.1016/S1364-6826(01)00036-0, 2001.

Robinson, R., R. Tsunoda, and J. F. Vickrey, Sources of F region ionization enhancements in the nighttime auroral zone, *J. Geophys. Res.*, *90*(A8), 7533–7546, 1985.

Roble, R. G., The calculated and observed diurnal variation of the ionosphere over Millstone Hill on 2324 March 1970, *Planet. Space Sci.*, *23*(7), 1017–1033, doi:http://dx.doi.org/10.1016/0032-0633(75)90192-0, 1975.

Rodger, A. S., M. Pinnock, J. R. Dudeney, K. B. Baker, and R. A. Greenwald, A new mechanism for polar patch formation, *J. Geophys. Res.*, *99*(A4), 6425–6436, doi:10.1029/93JA01501, 1994.

Rodger, A. S., M. Pinnock, J. R. Dudeney, and K. B. Baker, Riometer and HF radar signatures of polar patches, *Radio Science*, *34*, 501–508, doi:10.1029/1998RS900005, 1999.

Ruohoniemi, J. M., and K. B. Baker, Large-scale imaging of high-latitude convection with Super Dual Auroral Radar Network HF radar observations, *J. Geophys. Res.*, *103*, 20,797 – 20,811, 1998.

Ruohoniemi, J. M., and R. A. Greenwald, Statistical patterns of high-latitude convection obtained from Goose Bay HF radar observations, *J. Geophys. Res. Sp. Phys.*, *101*(A10), 21,743–21,763, doi:10.1029/96JA01584, 1996.

Ruohoniemi, J. M., and R. A. Greenwald, Dependencies of high-latitude plasma convection: Consideration of interplanetary magnetic field, seasonal, and universal time factors in statistical patterns, *J. Geophys. Res. Sp. Phys.*, *110*(A9), A09,204, doi: 10.1029/2004JA010815, 2005.

Ruohoniemi, J. M., R. A. Greenwald, K. B. Baker, J. P. Villain, and M. A. McCready, Drift motions of small-scale irregularities in the high-latitude F region: An experimental comparison with plasma drift motions, *J. Geophys. Res. Sp. Phys.*, *92*(A5), 4553–4564, doi: 10.1029/JA092iA05p04553, 1987.

Russell, C. T., The polar cusp, *Adv. Space Rec.*, *25*, 1413–1424, doi:10.1016/S0273-1177(99)00653-5, 2000.

Russell, C. T., and J. G. Luhmann, Earth: Magnetic field and magnetosphere, in *Encyclopedia of Planetary Sciences*, edited by J. H. Shirley and R. W. Fainbridge, Chapman and Hall, New York, USA, 1997.

Sandholt, P. E., M. Lockwood, W. F. Denig, R. C. Elphic, and S. Leont'ev, Dynamical auroral structure in the vicinity of the polar cusp - Multipoint observations during southward and northward IMF, *Ann. Geophys.*, *10*, 483–497, 1992.

Schindler, K., and G. Hornig, Magnetic Reconnection, in *Encyclopedia of Astronomy and Astrophysics*, Nature Publishing Group, 2001.

Schunk, R. W., and A. Nagy, *Ionospheres: Physics, Plasma Physics, and Chemistry*, Cambridge atmospheric and space science series, Cambridge University Press, 2000.

Semeter, J., C. J. Heinselman, J. P. Thayer, R. A. Doe, and H. U. Frey, Ion upflow enhanced by drifting F-region plasma structure along the nightside polar cap boundary, *Geophys. Res. Lett.*, *30*(22), 2139, doi:10.1029/2003GL017747, 2003.

Semeter, J., T. Butler, C. Heinselman, M. Nicolls, J. Kelly, and D. Hampton, Volumetric imaging of the auroral ionosphere: Initial results from PFISR, *J. Atmos. Solar-Terr. Phys.*, *71*, 738–743, doi:10.1016/j.jastp.2008.08.014, 2009.

Sheffield, J., *Plasma scattering of electromagnetic radiation*, Academic Press, 1975.

Shepherd, S. G., and J. M. Ruohoniemi, Electrostatic potential patterns in the high-latitude ionosphere constrained by SuperDARN measurements, *J. Geophys. Res. Sp. Phys.*, *105*(A10), 23,005–23,014, doi:10.1029/2000JA000171, 2000.

Shiokawa, K., Y. Katoh, M. Satoh, M. K. Ejiri, T. Ogawa, T. Nakamura, T. Tsuda, and R. H. Wiens, Development of Optical Mesosphere Thermosphere Imagers (OMTI), *Earth, Planets Sp.*, *51*(7-8), 887–896, doi:10.5636/eps.51.887, 1999.

Shiokawa, K., Y. Katoh, M. Satoh, M. Ejiri, and T. Ogawa, Integrating-sphere calibration of all-sky cameras for nightglow measurements, *Adv. Sp. Res.*, *26*(6), 1025–1028, doi: 10.1016/S0273-1177(00)00052-1, 2000.

Shiokawa, K., Y. Otsuka, and T. Ogawa, Propagation characteristics of nighttime mesospheric and thermospheric waves observed by optical mesosphere thermosphere imagers at middle and low latitudes, *Earth, Planets Sp.*, *61*(4), 479–491, doi:10.1186/BF03353165, 2009.

Sigernes, F., M. Dyrland, P. Brekke, S. Chernouss, D. A. Lorentzen, K. Oksavik, and C. S. Deehr, Two methods to forecast auroral displays, *J. Space Weather Space Clim.*, *1*, A03, 2011.

Simon, A., Instability of a Partially Ionized Plasma in Crossed Electric and Magnetic Fields, *Phys. Fluids*, *6*(3), 382, doi:10.1063/1.1706743, 1963.

Siscoe, G., Solar System Magnetohydrodynamics, in *Solar-Terrestrial Phys. SE - 2*, *Astrophysics and Space Science Library*, vol. 104, edited by R. L. Carovillano and J. M. Forbes, pp. 11–100, Springer Netherlands, doi:10.1007/978-94-009-7194-3_2, 1983.

Skolnik, M. I., *Introduction to Radar Systems*, 3 ed., Tata McGraw Hill, 2003.

Smith, A. M., S. E. Pryse, and L. Kersley, Polar patches observed by esr and their possible origin in the cusp region, *Ann. Geophys.*, *18*(9), 1043–1053, doi:10.1007/s00585-000-1043-5, 2000.

Smith, E., and D. M. Gottlieb, Solar flux and its variations, *Space Science Reviews*, *16*(5-6), 771–802, doi:10.1007/BF00182600, 1974.

Sofko, G. J., R. Greenwald, and W. Bristow, Direct determination of large-scale magnetospheric field-aligned currents with SuperDARN, *Geophys. Res. Lett.*, *22*(15), 2041–2044, doi: 10.1029/95GL01317, 1995.

Sojka, J. J., W. J. Raitt, and R. W. Schunk, Plasma density features associated with strong convection in the winter high-latitude F region, *J. Geophys. Res.*, *86*(A8), 6908–6916, doi: 10.1029/JA086iA08p06908, 1981.

Sojka, J. J., M. D. Bowline, R. W. Schunk, D. T. Decker, C. E. Valladares, R. Sheehan, D. N. Anderson, and R. A. Heelis, Modeling polar cap F-region patches using time varying convection, *Geophys. Res. Lett.*, *20*(17), 1783–1786, doi:10.1029/93GL01347, 1993.

Sojka, J. J., M. D. Bowline, and R. W. Schunk, Patches in the polar ionosphere: UT and seasonal dependence, *J. Geophys. Res. Sp. Phys.*, *99*(A8), 14,959–14,970, doi: 10.1029/93JA03327, 1994.

St.-Maurice, J.-P., and W. B. Hanson, Ion frictional heating at high latitudes and its possible use for an in situ determination of neutral thermospheric winds and temperatures, *J. Geophys. Res.*, *87*(A9), 7580–7602, doi:10.1029/JA087iA09p07580, 1982.

St-Maurice, J.-P., and R. W. Schunk, Ion velocity distributions in the high-latitude ionosphere, *Rev. Geophys.*, *17*(1), 99–134, doi: 10.1029/RG017i001p00099, 1979.

St.-Maurice, J. P., and D. G. Torr, Nonthermal rate coefficients in the ionosphere: The reactions of O+ with N2, O2, and NO, *J. Geophys. Res. Sp. Phys.*, *83*(A3), 969–977, doi:10.1029/JA083iA03p00969, 1978.

Sweet, P. A., The neutral point theory of solar flares, in *Electromagnetic Phenomena in Cosmic Physics*, edited by B. Lenhert, pp. 123–134, Cambridge Univ. Press, New York, USA, 1958.

Taguchi, S., K. Hosokawa, Y. Ogawa, T. Aoki, and M. Taguchi, Double bursts inside a poleward-moving auroral form in the cusp, *J. Geophys. Res. Sp. Phys.*, *117*(A12), A12,301, doi:10.1029/2012JA018150, 2012.

Tohmatsu, T., and T. Ogawa, *Compendium of Aeronomy*, Developments in Earth and Planetary Sciences, Springer, 1990.

Tsunoda, R. T., High-latitude F region irregularities: A review and synthesis, *Rev. Geophys.*, *26*(4), 719–760, doi:10.1029/RG026i004p00719, 1988.

Valladares, C. E., S. Basu, J. Buchau, and E. Friis-Christensen, Experimental evidence for the formation and entry of patches into the polar cap, *Radio Sci.*, *29*(1), 167–194, doi: 10.1029/93RS01579, 1994.

Valladares, C. E., D. T. Decker, R. Sheehan, and D. N. Anderson, Modeling the formation of polar cap patches using large plasma flows, *Radio Sci.*, *31*, 573–593, doi:10.1029/96RS00481, 1996.

Valladares, C. E., D. T. Decker, R. Sheehan, D. N. Anderson, T. Bullett, and B. W. Reinisch, Formation of polar cap patches associated with north-to-south transitions of the interplanetary magnetic field, *J. Geophys. Res. Sp. Phys.*, *103*(A7), 14,657–14,670, doi:10.1029/97JA03682, 1998.

Varney, R. H., S. C. Solomon, and M. J. Nicolls, Heating of the sunlit polar cap ionosphere by reflected photoelectrons, *J. Geophys. Res. Sp. Phys.*, *119*(10), 8660–8684, doi: 10.1002/2013JA019378, 2014.

Villain, J. P., G. Caudal, and C. Hanuise, A Safari-Eiscat comparison between the velocity of F region small-scale irregularities and the ion drift, *J. Geophys. Res. Sp. Phys.*, *90*(A9), 8433–8443, doi:10.1029/JA090iA09p08433, 1985.

Villain, J. P., R. André, C. Hanuise, and D. Grésillon, Observation of the high latitude ionosphere by HF radars: interpretation in terms of collective wave scattering and characterization of turbulence, *J. Atmos. Terr. Phys.*, *58*(89), 943–958, doi: http://dx.doi.org/10.1016/0021-9169(95)00125-5, 1996.

Walker, I. K., J. Moen, L. Kersley, and D. A. Lorentzen, On the possible role of cusp/cleft precipitation in the formation of polar-cap patches, *Ann. Geophys.*, *17*(10), 1298–1305, doi:10.1007/s00585-999-1298-4, 1999.

Wayne, R. P., *Chemistry of atmospheres. An introduction to the atmospheres of Earth, the planets, and their satellites.*, 1985.

Weber, E. J., J. Buchau, J. G. Moore, J. R. Sharber, R. C. Livingston, J. D. Winningham, and B. W. Reinisch, F layer ionization patches in the polar cap, *J. Geophys. Res.*, *89*, 1683–1694, doi:10.1029/JA089iA03p01683, 1984.

Weber, E. J., J. A. Klobuchar, J. Buchau, H. C. Carlson, R. C. Livingston, O. de la Beaujardiere, M. McCready, J. G. Moore, and G. J. Bishop, Polar cap F layer patches: Structure and dynamics, *J. Geophys. Res. Sp. Phys.*, *91*(A11), 12,121–12,129, doi: 10.1029/JA091iA11p12121, 1986.

Weimer, D. R., Models of high-latitude electric potentials derived with a least error fit of spherical harmonic coefficients, *J. Geophys. Res.*, *100*(A10), 19,595–19,607, doi: 10.1029/95JA01755, 1995.

Winkler, E., J. P. St-Maurice, and A. R. Barakat, Results From improved Monte Carlo calculations of auroral ion velocity distributions, *J. Geophys. Res. Sp. Phys.*, *97*(A6), 8399–8423, doi: 10.1029/91JA03104, 1992.

Yamada, M., R. Kulsrud, and H. Ji, Magnetic reconnection, *Reviews of Modern Physics*, *82*(1), 603–664, doi:10.1103/RevModPhys.82.603, 2010.

Yeoman, T. K., D. M. Wright, A. J. Stocker, and T. B. Jones, An evaluation of range accuracy in the Super Dual Auroral Radar Network over-the-horizon HF radar systems, *Radio Sci.*, *36*, 801–813, doi:10.1029/2000RS002558, 2001.

Zettergren, M., and J. Semeter, Ionospheric plasma transport and loss in auroral downward current regions, *J. Geophys. Res. Sp. Phys.*, *117*(A6), A06,306, doi: 10.1029/2012JA017637, 2012.

Zettergren, M., K. Lynch, D. Hampton, M. Nicolls, B. Wright, M. Conde, J. Moen, M. Lessard, R. Miceli, and S. Powell, Auroral ionospheric F region density cavity formation and evolution: MICA campaign results, *J. Geophys. Res. Sp. Phys.*, *119*(4), 3162–3178, doi: 10.1002/2013JA019583, 2014.

Zhang, Q.-H., et al., On the importance of interplanetary magnetic field |By| on polar cap patch formation, *J. Geophys. Res. Sp. Phys.*, *116*(A5), A05,308, doi: 10.1029/2010JA016287, 2011.

Zhang, Q.-H., et al., Direct Observations of the Evolution of Polar Cap Ionization Patches, *Science*, *339*(6127), 1597–1600, doi:10.1126/science.1231487, 2013.

Zhu, L., J. J. Sojka, R. W. Schunk, and D. J. Crain, A time-dependent model of polar cap arcs, *J. Geophys. Res. Sp. Phys.*, *98*(A4), 6139–6150, doi: 10.1029/92JA01600, 1993a.

Zhu, L., J. J. Sojka, R. W. Schunk, and D. J. Crain, Influence of horizontal inhomogeneity in the ionosphere on the reflection of Alfvén waves, *Geophys. Res. Lett.*, *20*(4), 313–316, doi: 10.1029/93GL00079, 1993b.

Zhu, L., R. Schunk, and J. Sojka, Polar cap arcs: a review, *J. Atmos. Solar-Terrestrial Phys.*, *59*(10), 1087–1126, doi: 10.1016/S1364-6826(96)00113-7, 1997.